UNIVERSIDAD
DE LA REPUBLICA
URUGUAY

Radiation techniques for urban thermal simulation with the Finite Element Method

José Pedro Aguerre Alonso

Doctorado en Informática
Facultad de Ingeniería
Universidad de la República - PEDECIBA informática

Montevideo – Uruguay
Marzo de 2020

UNIVERSIDAD
DE LA REPUBLICA
URUGUAY

Radiation techniques for urban thermal simulation with the Finite Element Method

José Pedro Aguerre Alonso

Tesis de Doctorado presentada al Programa de Posgrado en Informática, Facultad de Ingeniería de la Universidad de la República, como parte de los requisitos necesarios para la obtención del título de Doctor en Informática.

Directores:
Dr. Ing. Eduardo Fernández
Dr. Benoit Beckers

Director académico:
Dr. Ing. Sergio Nesmachnow

Montevideo – Uruguay
Marzo de 2020

Aguerre Alonso, José Pedro

Radiation techniques for urban thermal simulation with the Finite Element Method / José Pedro Aguerre Alonso. - Montevideo: Universidad de la República, PEDECIBA informática, Facultad de Ingeniería, 2020.

XXIII, 193 p. 29, 7cm.

Directores:

Eduardo Fernández

Benoit Beckers

Director académico:

Sergio Nesmachnow

Tesis de Doctorado – Universidad de la República, Programa en Informática, 2020.

Referencias bibliográficas: p. 179 – 193.

I. Fernández, Eduardo, Beckers, Benoit, . II. Universidad de la República, Programa de Posgrado en Informática. III. Título.

INTEGRANTES DEL TRIBUNAL DE DEFENSA DE TESIS

Dr. Alberto Pardo (Presidente)

Dr. Cyril Caliot (Revisor)

Dr. Mateu Sbert (Revisor)

Dr. Gonzalo Abal

Dr. Alfredo Canelas

Montevideo – Uruguay
Marzo de 2020

Esta tesis está dedicada a
José Agustín Aguerre SJ (Coqui).
Tío, jesuita, científico,
formador del espíritu crítico y
referente personal del diálogo
entre ciencia y fe.

Agradecimientos

En primer lugar quisiera agradecer a mis tutores de tesis Eduardo y Benoit por haberme guiado en este arduo camino. Al venir de áreas diferentes, se han complementado de buena manera y han permitido que desarrolle una tesis en informática con particular sensibilidad por la física urbana. Han sabido transmitirme la pasión por la ciencia y me han ayudado no solo desde un punto de vista técnico y teórico, sino también desde lo metodológico, demostrandome la importancia del trabajo meticuloso.

Quisiera dedicar un párrafo a mis compañeros de trabajo con los que he compartido estos tres años. A los colegas estudiantes de la UPPA (Jairo, Raphael, Antoine, Elena y Nicolas), que me han recibido con gran afecto y me han hecho sentir como en casa. A ellos les agradezco particularmente todo el trabajo realizado, sin el que esta tesis no podría existir. Al Prof. Christian La Borderie por dedicar parte de su valioso tiempo para introducirme en Cast3m. A Gonzalo Besuievsky por la buena vibra y el entusiasmo mostrado hacia mi trabajo. A mis amigos y compañeros del Instituto de Computación (Rodrigo, Ignacio, Guillermo, Renzo, etc.), por hacer el día a día más disfrutable. A los estudiantes del PEDECIBA informática por haber confiado en mi para que los represente, labor que he realizado con mucho cariño.

Por otro lado, quisiera realizar algunos agradecimientos a nivel personal. A Florentina, Mamá, Papá y Javier por haberme acompañado durante mi doctorado. Por ofrecerme ese apoyo incondicional que me hace sentir libre de hacer lo que me gusta. Agradezco también a todos mis amigos y amigas que tanto aprecio y que siempre han querido lo mejor para mi y los míos.

Por último, es necesario agradecer formalmente a las instituciones que han financiado mi formación doctoral. A la UdelaR por proveerme la beca de doctorado CAP y por haber cubierto gastos de mis pasantías en Francia con fondos CSIC y PEDECIBA. Al Urban Physics Joint Laboratory por haber financiado parcialmente todos mis viajes y estadias en la UPPA. A la ANII (Agencia Nacional de Investigación e Innovación) por haber brindado apoyo salarial mediante el Sistema Nacional de Investigadores y proyectos del Fondo Sectorial de Energía.

RESUMEN

Las sociedades modernas están cada vez más organizadas en ciudades. Más de la mitad de la población mundial vive en asentamientos urbanos en la actualidad. En este contexto, los trabajos a escala arquitectónica y de edificio deben extender su alcance al ambiente urbano. Uno de los mayores desafíos de estos tiempos consiste en entender todos los intercambios térmicos que suceden en la ciudad. La parte radiativa es la menos desarrollada; su caracterización y su interacción con edificaciones ha ganado la atención de la física de edificios, la arquitectura y la ingeniería ambiental. Como herramienta de conexión entre estas áreas, la física urbana es un área que resulta importante para atacar estudios de tal naturaleza.

Los estudios térmicos urbanos están intrínsicamente asociados a trabajos multidisciplinarios. Llevar a cabo mediciones a escala real resulta difícil, y el desarrollo de prototipos de menor escala es complejo. Por lo tanto, la simulación computacional es esencial para entender el comportamiento de la ciudad y para evaluar modificaciones proyectadas. La mejora metodológica y algorítmica de las simulaciones es una de las mayores líneas de trabajo para la física computacional y muchas áreas de las ciencias de la computación. El área de la computación gráfica ha abordado la adaptación de algoritmos de rendering para cómputo de iluminación natural, utilizando modelos de radiación basados en la física y aplicándolos sobre escenas arquitectónicas.

El Método de Elementos Finitos (MEF) ha sido ampliamente utilizado para análisis térmico. La madurez alcanzada por soluciones de software MEF permite tratar grandes modelos con un alto nivel de detalle y complejidad geométrica. Sin embargo, el cómputo del intercambio radiativo en este contexto implica un desafío computacional, y obliga a empujar los límites de las descripciones físicas conocidas. Algunas técnicas de computación gráfica pueden ser adaptadas a MEF para estimar las cargas solares. En el espectro de radiación térmica, los requisitos de memoria necesarios para almacenar la interacción entre los elementos crecen debido a que todas las superficies urbanas se transforman en fuentes emisoras de radiación.

En esta tesis se presenta una metodología basada en MEF para el análisis térmico de escenas urbanas. Un conjunto de técnicas de radiación (para radiación solar y térmica) son desarrolladas e integradas en el software MEF Cast3m. Los algoritmos de radiosidad y ray tracing son utilizados para el cómputo radiativo. Se presentan varios estudios que utilizan diferentes modelos de ciudades. Los resultados obtenidos mediante MEF son comparados con temperaturas medidas por medio de termografías urbanas. Se utilizan técnicas de post-procesamiento para renderizar imágenes térmicas, que permiten concluir que la metodología propuesta produce resultados precisos para los casos analizados. Asimismo, su buen desempeño computacional posibilita realizar este tipo de estudios en computadoras personales.

Palabras claves:
Física urbana, Radiación, Método de Elementos Finitos, Termografía, Radiosidad, Ray tracing.

ABSTRACT

Modern societies are increasingly organized in cities. In the present times, more than half of the world's population lives in urban settlements. In this context, architectural and building scale works have the need of extending their scope to the urban environment. One of the main challenges of these times is understanting all the thermal exchanges that happen in the city. The radiative part appears as the less developed one; its characterization and interaction with built structures has gained attention for building physics, architecture and environmental engineering. Providing a linkage between these areas, the emerging field of urban physics has become important for tackling studies of such nature.

Urban thermal studies are intrinsically linked to multidisciplinary work approaches. Performing full-scale measurements is hard, and prototype models are difficult to develop. Therefore, computational simulations are essential in order to understand how the city behaves and to evaluate projected modifications. The methodological and algorithmic improvement of simulation is one of the main lines of work for computational physics and many areas of computer science. The field of computer graphics has addressed the adaptation of rendering algorithms to daylighting using physically-based radiation models on architectural scenes.

The Finite Element Method (FEM) has been widely used for thermal analysis. The maturity achieved by FEM software allows for treating very large models with a high geometrical detail and complexity. However, computing radiation exchanges in this context implies a hard computational challenge, and forces to push the limits of existing physical models. Computer graphics techniques can be adapted to FEM to estimate solar loads. In the thermal radiation range, the memory requirements for storing the interaction between the elements grows because all the urban surfaces become radiation sources.

In this thesis, a FEM-based methodology for urban thermal analysis is presented. A set of radiation techniques (both for solar and thermal radiation) are developed and integrated into the FEM software Cast3m. Radiosity and ray tracing are used as the main algorithms for radiation computations. Several studies are performed for different city scenes. The FEM simulation results are compared with measured temperature results obtained by means of urban thermography. Post-processing techniques are used to obtain rendered thermograms, showing that the proposed methodology produces accurate results for the cases analyzed. Moreover, its good computational performance allows for performing this kind of study using regular desktop PCs.

Keywords:
Urban physics, Radiation, Finite Element Method, Thermography, Radiosity, Ray tracing.

Thesis development

Scientific context

This thesis was developed in the context of collaboration between two research groups: (a) the *computer graphics group* from Universidad de la República (UdelaR), Uruguay, and (b) the *Urban Physics Joint Laboratory* from Université de Pau et des Pays de l'Adour (UPPA), France. Group (a) provides computational methods regarding radiation exchange and daylighting, while (b) develops physical models and measuring techniques at the urban scale. During the three-year period of development of this thesis, I completed six research stages (of one-month duration each) at the UPPA in France, where I collaborated with researchers and students.

One of the lines of work covered by the aforementioned collaboration between the groups is urban thermography simulation. This line of work is a multidisciplinary field, combining knowledge from computer graphics, building physics, mechanics and environmental engineering, and architecture. Hence, many people participated in the development of this work. In the first place, a thermography campaign was carried out by Elena Garcia-Nevado in the city of Bayonne, France. She proposed a simple simulation test case (geometry, material properties, boundary conditions) with the help of Raphael Nahon, who provided the sky short and long-wave models. A finite element model was developed to simulate the test case, and the comparison between measured and simulated data was performed with the help of Raphael and Elena. In the next year, Jairo Acuña designed a detailed geometrical model representing the scene captured in the campaign. The model was designed for finite element analysis, and Nicolas Duport helped to enter it in the FEM software Cast3m. The simulations with the new 3D model led to the use of a more accurate long-wave emissivity description to render urban thermograms. This work was developed with the help of Jairo and Elena.

Personal contributions

The contents of this thesis were published in four journal articles (one of which is currently under review), and one international conference paper:

1. Aguerre, J. P., Fernández, E., Besuievsky, G., and Beckers, B. (2017). *Computing urban radiation: A sparse matrix approach*. Graphical Models, 91, 1-11. Elsevier.
2. Aguerre, J. P., Fernández, E., and Beckers, B. (2019). *Importance-driven approach for reducing urban radiative exchange computations*. Building Simulation, 12-2, 231-246. Springer.
3. Aguerre, J. P., Nahon, R., Garcia-Nevado, E., La Borderie, C., Fernández, E., and Beckers, B. (2019). *A street in perspective: Thermography simulated by the finite element method*. Building and Environment, 148, 225-239. Elsevier.
4. Aguerre, J. P., Nahon, R., Fernández, E., and Beckers, B. (2019). *Improving FEM computations for the simulation of thermograms at the urban scale*. Proceedings of Building Simulation 2019: 16th Conference of IBPSA.
5. Aguerre, J. P., Garcia-Nevado, E., Paz y Miño, J., Fernández, E., and Beckers, B. *Physically-based simulation and rendering of urban thermography*. Submitted to ACM Transactions on Graphics (TOG).

Due to the particular scientific context and the thesis format, it is important to highlight my own contributions to these publications. I have selected the five articles where I am the first author from among the list of publications in which I participated in these years.

The preliminary works of this thesis are summarized in my masters dissertation, entitled "Efficient representations of large radiosity matrices". The final part of my masters led to the first publication of my phd thesis (1), in which I implemented all the presented radiosity methods and developed the experimental work using a set of procedurally generated urban models. This work was included in this thesis because it contains fundamental concepts about sparse matrices in radiative computations, which were used in the other publications. After this work, I extended the radiation methods using the concept of importance and adding specular behavior of materials (2). In this article I was responsible for the development of the algorithms, the experimental results, and the validation with the RADIANCE software.

A first complete finite element analysis of the urban heat transfer problem was presented in (3). I integrated the partial works developed by the co-authors into one set of algorithms to execute the test case, obtaining the first simulated thermograms. I developed the methods in Cast3m and C++/OpenGL for short-wave radiation exchange. I executed the test case as provided by the co-authors, including two variations considering different diffusivity properties and short-wave reflectances. A continuation of this work was published in (4), where I implemented and executed a new convection scheme for internal air temperature in Cast3m, following the models provided by Raphael Nahon. I also adapted the Cast3m code to use sparse matrix representations in the long-wave radiation computations.

Finally, in (5), I worked in introducing the detailed 3D model of the Bayonne street into Cast3m. I proposed and developed a new reflectivity scheme for long-wave radiation using ray tracing (with the Embree library). I implemented a ray tracing code to post-process the results of the Cast3m simulation, allowing to render thermograms and to consider different long-wave material characteristics.

Other publications

This is the list of other publications in which I participated as a co-author in these years but are not included in my thesis:

1. Beckers, B., Aguerre, J. P., Besuievsky, G., Fernández, E., Nevado, E. G., Laborderie, C., and Nahon, R. (2019). *Visualizing the infrared response of an urban canyon throughout a sunny day*. In Sustainable Building for a Cleaner Environment, 277-284. Springer.
2. Bugeat, A., Aguerre, J. P., Beckers, B., and Fernández, E. (2019). *A Multi-Scale Consideration of Daylight in a Real Urban Context*. Proceedings of Building Simulation 2019: 16th Conference of IBPSA.
3. Besuievsky, G., Fernández, E., Aguerre, J. P., and Beckers, B. (2019). *A radiosity-based methodology considering urban environments for assessing Daylighting*. Proceedings of CISBAT 2019. Ecole Polytechnique Fédérale de Lausanne.

Contents

1 Introduction **1**

1.1 Background . . . 1
1.2 Motivation and objectives . . . 3
1.3 Thesis structure and related publications . . . 5

2 Heat transfer basics **7**

2.1 Basic laws . . . 7
2.2 The heat conduction equation . . . 8
2.3 Initial and boundary conditions . . . 9
2.4 Thermal radiation . . . 10
2.4.1 Blackbody . . . 11
2.5 Properties of radiative surfaces . . . 13
2.5.1 Emission and absorption . . . 13
2.5.2 Reflection . . . 16
2.5.3 Transmission . . . 17
2.5.4 Relation between radiative properties . . . 18
2.5.5 Radiation view factors . . . 19
2.6 Convection . . . 20
2.7 Full heat balance equation . . . 20
2.8 Thermal cameras . . . 21

3 Numerical heat transfer **23**

3.1 Heat conduction methods . . . 23
3.1.1 The Finite Element Method . . . 24
3.1.2 Time discretization with FDM . . . 29
3.2 Radiation methods . . . 30
3.2.1 Short-wave simulation . . . 30
3.2.2 Daylighting . . . 35
3.2.3 Long-wave simulation . . . 39
3.3 Complete heat transfer computational model . . . 45
3.3.1 Short-wave radiation module . . . 45
3.3.2 FEM module . . . 50
3.3.3 Long-wave methods . . . 53

3.3.4 Detailed 3D geometry . . . 56

4 Computing Urban Radiation: A Sparse Matrix Approach 61
4.1 Introduction . . . 61
4.2 Related work . . . 62
4.2.1 The Radiosity Problem . . . 62
4.2.2 Correlation between scene characteristics and $\mathbf{F}$ properties . . . 63
4.2.3 Neumann Series . . . 64
4.2.4 Urban Radiative Methods . . . 65
4.3 Our Proposal . . . 65
4.3.1 Why not factorizing? . . . 65
4.3.2 Studying the Sparsity of a City's Form Factors Matrix . . . 66
4.3.3 An Approximation of $\mathbf{M} = (\mathbf{I} - \mathbf{RF})^{-1}$ . . . 67
4.3.4 Daylight Simulation . . . 68
4.4 Experimental Analysis . . . 69
4.4.1 Example of City Models . . . 69
4.4.2 Sparsity Results for $\mathbf{F}$ and $\tilde{\mathbf{M}}$ . . . 69
4.4.3 Execution Times . . . 71
4.4.4 Radiosity Results . . . 71
4.5 An alternative optimization considering discarded elements . . . 73
4.6 Orography . . . 76
4.7 Conclusions and future work . . . 78

5 Importance-driven approach for reducing urban radiative exchange computations 81
5.1 Introduction . . . 81
5.2 Related work . . . 83
5.2.1 The radiosity algorithm . . . 83
5.2.2 Importance in radiosity . . . 84
5.2.3 Radiation computation on an urban scale . . . 86
5.3 An efficient approach for handling big urban models . . . 87
5.3.1 Computing the importance vector . . . 87
5.3.2 Selecting and subdividing patches in the city mesh . . . 88
5.3.3 Extension for treating specular surfaces . . . 89
5.3.4 Handling multiple target patches . . . 91
5.3.5 Importance for other radiometric units . . . 92
5.4 Experimental analysis . . . 93
5.4.1 Implementation and execution platform . . . 94
5.4.2 Validation with standard radiosity . . . 94
5.4.3 Testing the algorithm for multiple target patches . . . 96
5.4.4 Test case with specular components . . . 98
5.4.5 Example of application: irradiance over a wall in Venice . . . 98
5.4.6 Validation with a standard ray tracing engine . . . 101
5.5 Conclusions and future work . . . 103

6 A street in perspective: Thermography simulated by FEM 105
6.1 Introduction . . . 105
6.2 Modeling physical base . . . 106
6.2.1 Conduction . . . 107
6.2.2 Radiation . . . 107
6.2.3 Convection . . . 108
6.3 Test case description . . . 108
6.3.1 Site and experimental set-up . . . 108
6.3.2 Experimental set-up . . . 109
6.3.3 Environmental and boundary conditions . . . 110
6.4 Computational model . . . 113
6.4.1 Characteristics of the mesh . . . 113
6.4.2 Pre-computations . . . 114
6.4.3 FEM for heat transfer . . . 115
6.5 Simulation results . . . 118
6.5.1 Simulated thermograms . . . 119
6.5.2 Temperature evolution for 3 points . . . 122
6.6 Modifying the urban scene . . . 124
6.6.1 Impact of the thermal inertia . . . 124
6.6.2 Impact of the reflectance . . . 125
6.7 Conclusions . . . 126

7 Improving FEM computations for the simulation of thermograms at the urban scale 129
7.1 Introduction . . . 129
7.2 Methods . . . 130
7.2.1 Transient heat transfer . . . 130
7.2.2 FEM for spatial discretization of conduction . . . 131
7.2.3 FDM for time discretization . . . 132
7.2.4 Convection . . . 132
7.2.5 Adding support for windows . . . 134
7.2.6 Long wave radiation . . . 135
7.2.7 Short wave radiation . . . 135
7.3 Test case and model . . . 136
7.4 Results and discussion . . . 138
7.4.1 Computational performance . . . 140
7.5 Conclusion . . . 141

8 Physically-based simulation and rendering of urban thermography 143
8.1 Introduction . . . 143
8.2 Physical basis . . . 145
8.3 Literature review . . . 147
8.3.1 Urban thermal simulation . . . 147
8.3.2 Previous works . . . 148
8.4 Simulation Methodology . . . 149

8.4.1 Short-wave radiation . . . 151
8.4.2 Long-wave radiation . . . 151
8.4.3 Thermography rendering . . . 155
8.5 Case of study . . . 158
8.5.1 3D geometry . . . 158
8.5.2 Measurement campaign and parameter set-up . . . 159
8.5.3 Emissivity estimations . . . 160
8.6 Implementation . . . 161
8.7 Results and discussion . . . 162
8.7.1 Impact of directional emissivity . . . 163
8.7.2 Time sequence of measured and rendered thermograms . . . 165
8.8 Conclusion . . . 170

9 Conclusions and future work **171**
9.1 Conclusions . . . 171
9.1.1 Radiation techniques . . . 171
9.1.2 FEM for urban thermal analysis . . . 172
9.1.3 Thermography and infrared rendering . . . 173
9.1.4 Computational performance . . . 173
9.2 Future works . . . 174
9.2.1 Geometry for FEM . . . 174
9.2.2 Integration of fluid dynamics . . . 175
9.2.3 Large-scale studies . . . 175

Bibliography **179**

List of symbols

symbol	definition	units
T	Temperature	K (kelvins)
q, ϕ, φ	Heat flux	Wm^{-2}
k	Thermal conductivity	$\mathrm{Wm}^{-1}\mathrm{K}^{-1}$
α	Thermal diffusivity	$\mathrm{m}^2\mathrm{s}^{-1}$
c_p	Specific heat capacity	$\mathrm{J\ kg}^{-1}\mathrm{K}^{-1}$
c_v	Volumetric heat capacity	$\mathrm{Jm}^{-3}\mathrm{K}^{-1}$
ρ_m	Density, specific mass	$\mathrm{kg\ m}^{-3}$
h	Convective heat transfer coefficient	$\mathrm{Wm}^{-2}\mathrm{K}^{-1}$
ε	Emissivity	
τ	Transmissivity	
ρ, r	Reflectivity	
ε^h	Total hemispherical emissivity	
n	Number of patches/elements in the geometry mesh	
B, J	Radiosity	Wm^{-2}
$\widetilde{B}$	Approximation of B	
E	Irradiance, emitted radiant flux	Wm^{-2}
L	Radiant flux density	$\mathrm{Wm}^{-2}\mathrm{sr}^{-1}$
ψ	Importance	
ψ_s	Specular importance	
θ	Initial source of importance	
B_r	Reflected radiosity	Wm^{-2}
P	Incident power	W
$\mathbf{I}$	$n \times n$ identity matrix	
$\mathbf{R}$	Diagonal matrix with reflectivity indexes	
$\mathbf{F}$	Form factors matrix	
$\mathbf{RF}$	Matrix result of the product $\mathbf{R} \cdot \mathbf{F}$	
$\mathbf{M}$	Inverse of the radiosity matrix $(\mathbf{I} - \mathbf{RF})^{-1}$	
$\mathbf{C}$	Capacitance matrix	JK^{-1}
$\mathbf{K}$	Conductivity matrix	WK^{-1}
f	Load vector	W

Table 1: Symbol notation with definition and units.

Chapter 1

Introduction

1.1 Background

Solar radiation is the primary source of energy in the planet. The Sun emits radiation mostly at short wavelengths ($\lambda < 4\mu$m). Radiation travels at the speed of light through the outer space vacuum. The atmosphere reflects and absorbs part of the radiation that reaches the planet and transmits the remaining fraction towards the Earth's surface. The surface is heated up by this energy and starts emitting radiation at longer wavelengths.

At the macro-scale, the energy budget of the Earth-atmosphere system can be described with the diagram in Figure 1.1. Of the Sun's total radiative energy reaching the system (100%), 30% is reflected by the atmosphere and the planet's surface, 23% is absorbed by the atmosphere and 47% is absorbed by the ground. Since the system must be in thermal equilibrium, the absorbed energy (70%) has to be re-emitted into the outer space. Of this 70%, 12% corresponds to long-wave emission of the ground that passes the atmosphere, and 58% is the long-wave emission of the atmosphere. The local equilibrium between ground and atmosphere is maintained through long-wave exchanges, sensible heat and latent heat.

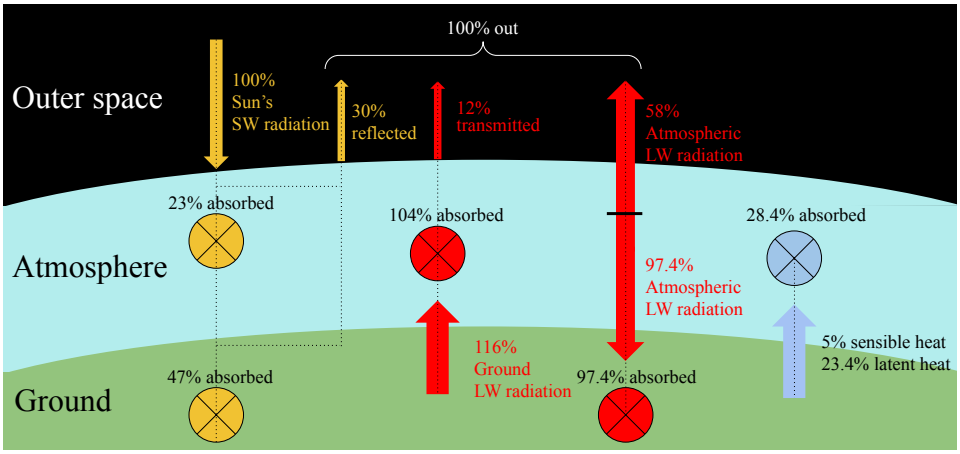

Figure 1.1: Earth's radiation energy budget. A fraction of the Sun's radiation (yellow) passes through the atmosphere and reaches the objects in the surface of the planet. These objects emit thermal radiation (red) to other surfaces and back into the atmosphere. Values extracted from [Beckers, 2013c].

At the meso-scale, the objects in the planet's surface exchange radiation between each other in many forms, because the air is transparent in many portions of the spectrum. The short-wave parts that are not absorbed by the materials are reflected and forwarded towards other surfaces. The emitted long-wave radiation is intercepted and absorbed by other objects. These exchanges happen in a context of multi-physical heat interactions that includes conduction, convection and other phenomena.

Needless to say, life could not exist on Earth without radiation. For humans, the potential benefits of this energy are still a subject of study [Devabhaktuni et al., 2013]. Habitable spaces such as houses or buildings are affected by solar radiation as a heat source, and long-wave radiation as a cooling facility with the exposition to the cold sky. In the recent decades, buildings' energy efficiency has become a major topic of interest [Gillingham et al., 2009]. In this context, the characterization of radiation and its interaction with built structures has gained attention for building physics, architecture and environmental engineering [Oliveti et al., 2003; Rahimi and Sabernaeemi, 2010]. Occupants' thermal comfort also depends greatly on the radiation budget and thermal properties of the scene [Hall, 2010].

Modern societies are more highly organized in dense built environments called cities. In the present times, more than half of the world's population lives in urban settlements. Moreover, 60% of the population is projected to live in cities by 2030 [United Nations, 2018]. City planners have the major challenge of providing a regulatory framework that allows for the aforementioned demographic increase without reducing the already low life quality of citizens [Cramer et al., 2004]. In this context, architectural and building scale studies have the need of extending their scope to the urban environment. Emerging as a tool for this necessity, the nascent field of urban physics [Beckers, 2013a] has become important for providing a linkage between environmental and building physics.

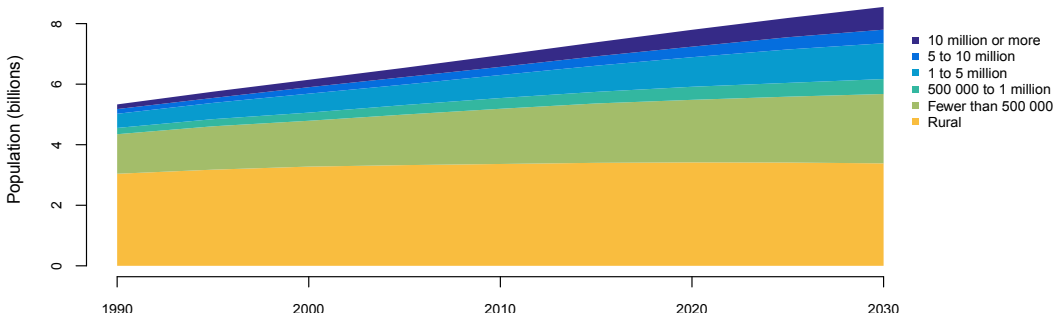

Figure 1.2: World's population by size class of settlement, 1990-2030. Extracted from [United Nations, 2018]

The development of computer science and hardware advances has always been strongly influenced by the field of physics. The original high-end computers, and more recently personal computers, have been constantly used for the resolution of physical problems. New numerical methods have led to the design of new hardware devices, and *vice versa*. The methodological improvement of algorithms, as well as the adaptation of existing ones to modern architectures are the main lines of work for computational physics, high performance computing, computer graphics, and many other subareas of computer science.

Urban physics are devoted to the study of physical phenomena at the urban scale. Computational simulations are the main tool for performing studies at the city scale. Examples of this kind of works

are computational fluid dynamics [Van Hooff and Blocken, 2010], energy performance simulations [Hénon et al., 2012], daylighting analysis [Saratsis et al., 2017], and geometric procedural modeling [Garcia-Dorado et al., 2017]. Adapting existing methods to urban environments requires handling big geometries, modeling multi-physical phenomena, and developing new measuring strategies to validate the simulation results.

1.2 Motivation and objectives

There is a multiplicity of motivations that drive the development of this thesis. Urban thermal studies are intrinsically linked to multidisciplinary work approaches [Beckers, 2013a]. Cities are multi-scale environments subject to a diverse variety of restrictions driven by nature's laws, but also boosted by society's laws, because they are (or must be) designed to provide a certain quality of life to their inhabitants. Some of the phenomena that an accurate thermal study must address are (Figure 1.3): the geometric and material definition of the scene, the conductivity properties of the objects, external air temperatures and heat exchange coefficients, internal temperatures associated with the occupants' behavior, short-wave radiation fluxes considering anisotropic sky radiance distribution, and long-wave fluxes linked to sky temperatures. In this context, thermal engineers, environmental scientists, architects, city planners, designers, and computer scientists must join forces to encompass skilled and well-motivated studies that allow for the maximum benefit of urban societies.

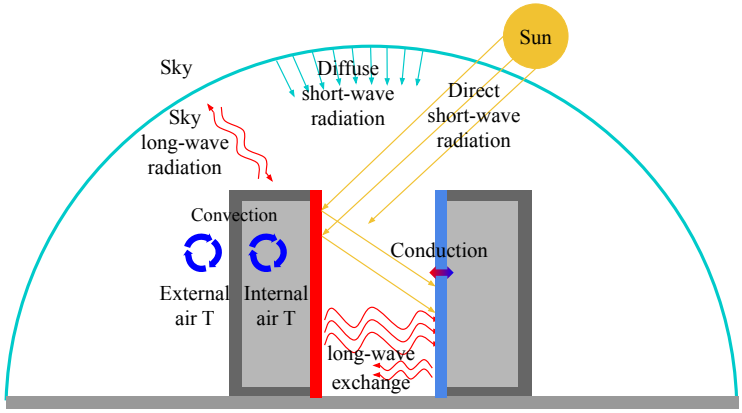

Figure 1.3: Diagram of heat exchanges in an urban thermal study.

This thesis is mainly dedicated to the study of radiation techniques in the context of urban computational heat transfer. For the short-wave spectrum, many works have been developed by the daylighting community [Mardaljevic, 2000; Reinhart, 2014; Reinhart et al., 2006]. The analysis of natural light availability in interior spaces requires the estimation of sky radiances [Perez et al., 1993], the correct treatment of the exterior environment [Fernández et al., 2016a], the simulation of openings [McNeil and Lee, 2013], and the evaluation of light exchanges inside the room [Fernández et al., 2016b]. The used methods must be adapted to study exterior daylighting and short-wave loads, especially because the computational requirements are high when dealing with large city models. With this challenge comes the first goal of this thesis, which is the adaptation of global illumination algorithms to the city scale.

On the long-wave radiation side, fewer works have been developed by the community. Daylighting and short-wave analysis are independent of surface temperature and heat transfer, while long-wave is not. Every surface above the absolute zero emits radiation, and hence long-wave analysis must incorporate heat transfer methods. At the building scale, the most used engines are based in electric-analogy approximations [Asawa et al., 2008; Kramer et al., 2012]. This approach provides simplified modeling strategies to allow for better algorithmic performance [Reinhart and Davila, 2016], but it is difficult to evaluate their accuracy. Long-wave exchanges are roughly simplified using sky view factor or related techniques [Evins et al., 2014].

More accurate heat transfer simulation methods are those used by the mechanical engineering community, which are based on splitting the geometry into small parts to guide the discretization of the physical equations modeled. Finite difference [Croft and Lilley, 1977], finite volume, and finite element method (FEM) [Lewis et al., 2004] techniques are the most used ones. The second objective of this thesis is the use of FEM in the context of urban heat transfer, providing better and more accurate simulation conditions, but also engaging into a much harder computational challenge. The adaptation of short and long-wave radiation techniques to FEM is an immediate necessity to address the previous goal.

Urban physicists also study measurement techniques at the city scale. In recent years, the heat transfer behavior of the city has been evaluated by means of infrared thermography (Figure 1.4). The idea consists in using a thermal camera to capture a set of images of the urban surfaces throughout a time period [Beckers and Garcia-Nevado, 2018]. This process allows for obtaining a spatialized view of the temperature distribution of the scene that helps monitoring buildings and city elements [Vollmer and Möllmann, 2017]. Thermography has the big advantage of being a non-invasive inspection tool, but the physical interpretation of thermal images is a challenging task [Datcu et al., 2005].

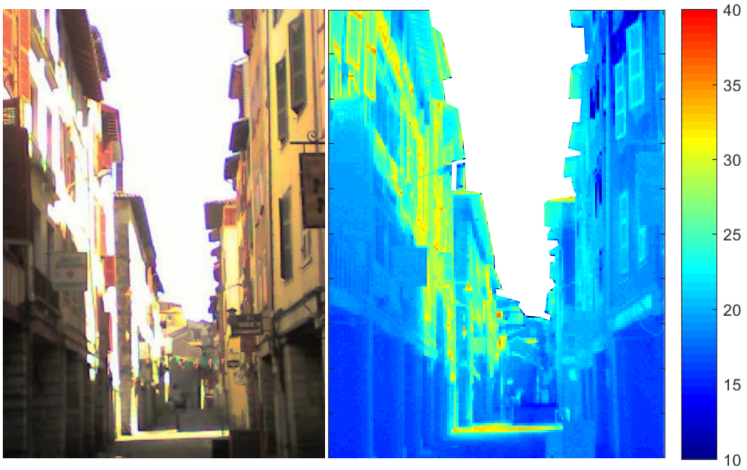

Figure 1.4: Image and corresponding thermogram of a street using a perspective view. Data extracted from [Beckers and Garcia-Nevado, 2018].

Extracting the real temperature of the urban surface from the one estimated by the thermal camera implies understanding the behavior of thermal radiation in the scene. The presence of complex geometries, the collection of material varieties, and the sky long-wave emission complicates the matter in such way that it becomes hard to obtain reliable results by only observing the time-sequence

of images. Urban thermal simulation appears as the ideal tool to complement thermography studies, because a clean comparison between measured and simulated results allows for a mutual reliability assessment. Therefore, another objective of this thesis is to provide computational methods for simulating thermal images, and to compare them with measurements. Finite element analysis seems to be the appropriate tool for this purpose because it offers results that are as refined as the mesh used. Computer graphics techniques can also help in simulating thermograms by adapting rendering methods to long-wave radiation.

1.3 Thesis structure and related publications

This thesis is divided into three main parts, each one containing two or more chapters. The first part is composed of two chapters. Chapter 2 provides an introduction to the core physical and computational notions of this thesis. The first sections describe some basic heat transfer laws, and the next two sections cover thermal radiation and related properties of radiative surfaces. Finally, thermal cameras and thermography measuring techniques are introduced. In Chapter 3, a state of the art in numerical heat transfer is outlined first, covering heat conduction methods and radiation techniques. In the next section, a first complete FEM model is shown along with its calibration results.

The second part of this thesis corresponds to the development of short-wave methods for urban studies, and it is divided in two chapters (Chapters 4 and 5). These chapters are derived from the following journal publications:

- Aguerre, J. P., Fernández, E., Besuievsky, G., and Beckers, B. (2017). *Computing urban radiation: A sparse matrix approach*. Graphical Models, 91, 1-11. Elsevier.
- Aguerre, J. P., Fernández, E., and Beckers, B. (2019). *Importance-driven approach for reducing urban radiative exchange computations*. Building Simulation, 12-2, 231-246. Springer.

Chapter 4 starts with the introduction and related work about radiosity and urban radiative methods. Next, a new method is proposed based on the use of sparse view factors matrices to solve urban radiation. The method is tested for several urban geometries, where different discretization levels of the meshes are analyzed. This work prepares the adaptation of the developed techniques into FEM, and the correspondent conclusions are outlined. In Chapter 5, an approach for reducing the computational effort of the previous method is presented. The technique is based on the concept of *importance*, so a section of related work is developed. The technique is then described and tested over larger urban geometries, including non-diffuse materials. A comparison of the proposed method with the RADIANCE daylighting software package is performed.

The third part of this thesis covers the use of FEM for urban heat transfer. It is divided in three chapters (Chapters 6, 7 and 8), derived from two journal publications and one international conference paper:

- Aguerre, J. P., Nahon, R., Garcia-Nevado, E., La Borderie, C., Fernández, E., and Beckers, B. (2019). *A street in perspective: Thermography simulated by the finite element method*. Building and Environment, 148, 225-239. Elsevier.

- Aguerre, J. P., Nahon, R., Fernández, E., and Beckers, B. (2019). *Improving FEM computations for the simulation of thermograms at the urban scale*. Proceedings of Building Simulation 2019: 16th Conference of IBPSA.
- Aguerre, J. P., Garcia-Nevado, E., Paz y Miño, J., Fernández, E., and Beckers, B. *Physically-based simulation and rendering of urban thermography*. Submitted to ACM Transactions on Graphics (TOG).

Chapter 6 presents a FEM-based methodology for urban thermal simulation. A simplified test case is outlined, and the computational model is developed. The resulting surface temperatures for the simplified geometry are compared with a thermographic campaign performed in the city of Bayonne, France. After the comparison and validation of the results, several tests are presented by modifying the parameters of the simulation, such as the thermal inertia and short-wave reflectances of walls. In Chapter 7, the computational model is further enhanced by improving the calculation of the boundary conditions. A new method is used to compute internal air temperatures, and sparse matrices are introduced to accelerate the long-wave radiation module. The new methods are applied to the previous simplified test case and the results are compared with the same measurement campaign. In Chapter 8, the same scene is simulated using a highly detailed geometry and a set of long-wave emissivity and reflectivity models are introduced for long-wave calculations. After the computation of surface temperatures, a rendering module is added, where computer graphics techniques are used to synthesize thermal images.

Finally, Chapter 9 is dedicated to summarizing the most important conclusions of the work developed in this thesis, along with the definition of some lines of future works.

Chapter 2

Heat transfer basics

Heat is defined as the transfer of thermal energy, determined by the temperature of bodies. Heat transfer happens in three main modes [Lewis et al., 2004]:

- Conduction heat transport occurs within bodies, when nearby molecules exchange energy without their actual motion, or when free electrons move around. Greater temperature differences imply greater conduction fluxes, where heat is conducted from hot to cold parts of the body.
- Convection is related to the movement of liquids and gases. Molecules moving from hot to cold regions carry energy, and this phenomenon is known as *natural* convection. Its counterpart, namely *forced* convection, is caused by external forces, such as wind or fluid currents.
- Thermal radiation is heat transferred in the form of electromagnetic waves through a material medium or vacuum. All surfaces with a temperature above the absolute zero emit radiation at different wavelengths. Radiation is emitted from the surface of the body, and it travels in straight lines until reaching another surface, where it is absorbed, reflected and transmitted.

It is important to define the notion of *heat flux*, also denoted as *thermal flux* or *heat flux density*. It is a vector quantity that defines the flow of energy per unit of area per unit of time, and it is measured in W m^{-2}.

There are two different problems studied by heat transfer analysis. The first one, called *steady-state* heat transfer, implies that temperature does not depend on time. It can be seen as a system in which infinite time passed and temperature equilibrium was reached. The second problem, *transient* heat transfer, allows for the evolution of temperature as a function of space and time. In this case, the boundary conditions can be different at each timestep, and the temperature varies with time.

2.1 Basic laws

The amount of transferred energy is quantified using heat flux equations. Fourier's law expresses the heat flux related to conduction. Its one-dimensional form is expressed as:

$$q_{cond} = -k\nabla T \tag{2.1}$$

where q_{cond} is the vector of heat flux, k is the thermal conductivity of the material (W $m^{-1}K^{-1}$), and ∇T is the temperature gradient ($\frac{\partial T}{\partial x}$ in Km^{-1}).

Newton's law of cooling gives the heat flux by convection:

$$q_{conv} = h(T - T_a) \tag{2.2}$$

where T_a is the fluid temperature, and h ($Wm^{-2}K^{-1}$) is the convection heat transfer coefficient. This constant expresses the thermodynamic driving force related to convection.

For an ideal radiation emitter body, namely *blackbody*, Stefan law describes the radiative heat flux leaving the surface:

$$q_{rad} = \sigma T^4 \tag{2.3}$$

where σ is the Stefan-Boltzmann constant (5.6703×10^{-8} $Wm^{-2}K^{-4}$) and T must be expressed in Kelvin degrees. Real-world bodies emit a fraction of the blackbody radiation, given by its total hemispherical emissivity ε:

$$q_{rad} = \varepsilon \sigma T^4 \tag{2.4}$$

2.2 The heat conduction equation

The energy balance in a differential volume is given by the equivalence between: i) the incoming and the generated energy, and ii) stored and outgoing energy [Lewis et al., 2004]. This equivalence implies that energy cannot be created or destroyed; it can only be transformed or transferred. Temperature is a measure of the kinetic energy of the particles that make up the body, and it is a function of space and time.

In Cartesian three-dimensional coordinates (x, y, z), the heat conduction equation is derived by applying the energy conservation law in a differential control hexahedral volume of sides dx, dy, dz. The heat flux for the three directions is described by applying Taylor series to the differential volume:

$$\begin{aligned} Q_{x+dx} &= Q_x + \frac{\partial Q_x}{\partial x} dx \\ Q_{y+dy} &= Q_y + \frac{\partial Q_y}{\partial y} dy \\ Q_{z+dz} &= Q_z + \frac{\partial Q_z}{\partial z} dz \end{aligned} \tag{2.5}$$

Another way of expressing the heat flux for each direction is using Fourier's law (Eq. 2.1):

$$\begin{aligned} Q_x &= -k_x dy\ dz \frac{\partial T}{\partial x} \\ Q_y &= -k_y dx\ dz \frac{\partial T}{\partial y} \\ Q_z &= -k_z dx\ dy \frac{\partial T}{\partial z} \end{aligned} \tag{2.6}$$

where k_x is the thermal conductivity in the x direction.

The energy generated within the differential volume must also be considered. It is described as:

$$G dx\ dy\ dz \tag{2.7}$$

where G is the heat source term per unit of volume.

Heat transfer is also dependent of time. The rate of change in energy storage is described as:

$$\rho_m c_p dx\ dy\ dz \frac{\partial T}{\partial t} \tag{2.8}$$

where ρ_m (kg m^{-3}) and c_p (J kg^{-1} K^{-1}) are the mass density and specific heat, properties of the body. Applying the energy balance to the differential volume, it can be stated that:

$$\begin{gathered} Q_x + Q_y + Q_z + G dx\ dy\ dz = \\ Q_{x+dx} + Q_{y+dy} + Q_{z+dz} + \rho_m c_p dx\ dy\ dz \frac{\partial T}{\partial t} \end{gathered} \tag{2.9}$$

Substituting Eqs. 2.5 and 2.6 into Eq. 2.9, the transient heat conduction equation is obtained:

$$\frac{\partial}{\partial x}\left[k_x \frac{\partial T}{\partial x}\right] + \frac{\partial}{\partial y}\left[k_y \frac{\partial T}{\partial y}\right] + \frac{\partial}{\partial z}\left[k_z \frac{\partial T}{\partial z}\right] = \rho_m c_p \frac{\partial T}{\partial t} - G \tag{2.10}$$

The previous equation is a second-order partial differential equation, where the conductivity properties vary directionally. Considering isotropic behavior of conductivity (i.e. k_x=k_y=k_z=k), no internal heat generation ($G = 0$), and expressing the left size of Eq. 2.10 with the temperature Laplacian ΔT, the equation results in the following:

$$k\Delta T = \rho_m c_p \frac{\partial T}{\partial t} \tag{2.11}$$

2.3 Initial and boundary conditions

The heat conduction differential equation requires a set of initial and boundary conditions to be solved. Two types of boundary conditions can be imposed [Zienkiewicz et al., 1977]:

- Dirichlet condition (imposed temperature):

$$T = T_b \text{ on part of the boundary } \Gamma_b$$

- Neumann condition (imposed flux):

$$\bar{q} = -k\frac{\partial T}{\partial n} - h(T - T_a) \text{ on part of the boundary } \Gamma_q$$

The vector n denotes the outward normal to the boundary Γ_q. The total boundary is defined as $\Gamma = \Gamma_b \cup \Gamma_q$. Both boundary conditions cannot be defined at the same point, because a flux imposition over a point with fixed temperature would not have any effect. Hence, $\Gamma_b \cap \Gamma_q = \varnothing$. Since the heat conduction equation is of the second order, two boundary conditions are sufficient to solve it. $\bar{q}$ describes other boundary heat fluxes entering the system.

A typical application of boundary conditions when simulating heat exchange in a 3D geometry is that conductive phenomena happens within 3D volumes, whereas boundary exchanges such as convection and radiation occur at part of the planar surfaces that enclose the 3D geometry. Figure 2.1 presents a diagram that shows a 2D domain Π with its boundary Γ and heat transfer phenomena.

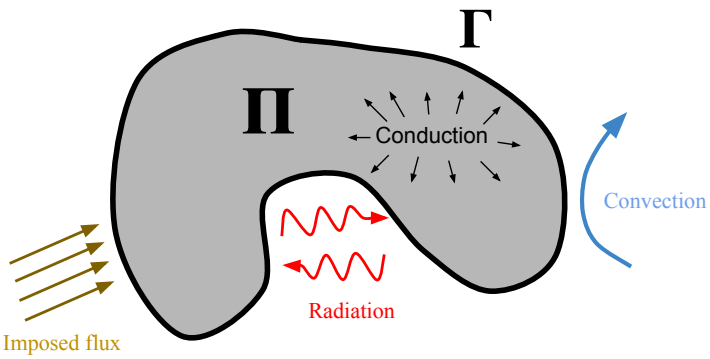

Figure 2.1: Description of domain, boundary, and heat transfer phenomena.

Time t appears as a first order term in Eq. 2.11, so an initial value is enough to solve the equation. The initial conditions are described as:

$$T = T_0 \text{ at } t = 0 \text{ over the domain } \Pi \tag{2.12}$$

2.4 Thermal radiation

Every body emits and absorbs radiation. Radiation is the only heat transfer mode that does not require a medium to propagate. This fact allows, for instance, sunlight to travel through space and reach the earth surface. The speed of propagation of radiation electromagnetic waves through the vacuum is determined by the speed of light ($c_0 = 2.9979{\times}10^8$ m/s). The waves are characterized by their frequency v and wavelength λ, where $v = c_0/\lambda$. Radiation waves receive different names depending on λ, as observed in Figure 2.2. Thermal radiation corresponds to wavelengths between 0.1μm and 100μm, which includes visible light ($0.4 - 0.8\mu$m), infrared ($> 0.8\mu$m) and ultraviolet ($< 0.4\mu$m) [Howell et al., 2015].

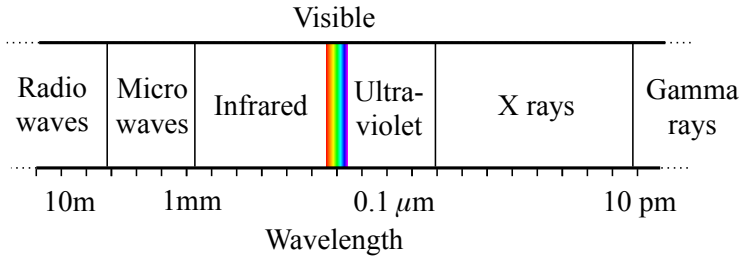

Figure 2.2: Radiation spectrum according to Modest [2003].

To characterize radiation, it is important to define the notion of *radiance* [Sillion et al., 1994]. This magnitude represents the radiant flux density emitted, reflected, transmitted or received by a given surface per unit solid angle (steradian, sr), and it is measured in $\text{Wm}^{-2}\text{sr}^{-1}$:

$$L(T, \vec{\omega}) = \frac{\partial^3 Q}{\partial t \, \partial \vec{\omega} \, \partial A \, cos\theta} \tag{2.13}$$

where T is the temperature of the differential area of surface A, $\vec{\omega}$ is the direction of the emitted radiation, θ is the angle between $\vec{\omega}$ and the normal vector of the area, and Q is the radiant energy (in J).

The spectral distribution of radiation is defined as the radiant flux density per solid angle for a given frequency v (measured in $\mathrm{Wm^{-2}sr^{-1}hz^{-1}}$), and it is expressed as:

$$L_v(T,\vec{\omega}) = \frac{\partial^3 Q_v}{\partial t\ \partial\vec{\omega}\ \partial A\ cos\theta} \tag{2.14}$$

2.4.1 Blackbody

The study of the radiative behavior of a body is usually based on the notion of *blackbody* radiation. A blackbody is defined as an ideal body that absorbs all the incident radiation. At local thermodynamic equilibrium, a blackbody emits the same amount of radiation that it absorbs, and hence it is said that it emits a maximum amount of radiation. Because it is independent of the angle of incidence, the radiance of a blackbody satisfies the following law:

$$L(T,\vec{\omega}) = L^o(T) \tag{2.15}$$

The spectral distribution of blackbody radiation for a given temperature is described by Planck's law [Howell et al., 2015]. This law was proposed by Max Planck in 1900, who derived it from thermodynamic statistics and electromagnetic wave theory:

$$L_v^o(T) = \frac{2hv^3}{c_0^2\left[\exp\left(\frac{hv}{kT}\right)-1\right]} \tag{2.16}$$

where h is the Planck constant ($\approx 6.62{\times}10^{-34}$ J s), and k is the Boltzmann constant ($\approx 1.38{\times}10^{-23}$ J $\mathrm{K^{-1}}$). An analogous relation can be expressed based on radiation wavelength λ instead of frequency v:

$$L_\lambda^o(T) = \frac{2hc_0^2}{\lambda^5\left[\exp\left(\frac{hc_0}{kT\lambda}\right)-1\right]} \tag{2.17}$$

where $L_v^o(T)$ is measured in $\mathrm{Wm^{-2}sr^{-1}Hz}$ and $L_\lambda^o(T)$ in $\mathrm{Wm^{-3}sr^{-1}}$.

The maximum spectral radiance for a blackbody is given by Wien's displacement law, which states that the peak of the spectral radiance curve occurs at:

$$\lambda_{max} = \frac{b}{T} \tag{2.18}$$

where b is a constant of proportionality with a value of $\approx 2898\mu mK$. This constant can be obtained by a derivation in λ of Planck's relation. The evolution of the emissive power of a blackbody with respect to wavelength and for different temperatures is observed in Figure 2.3.

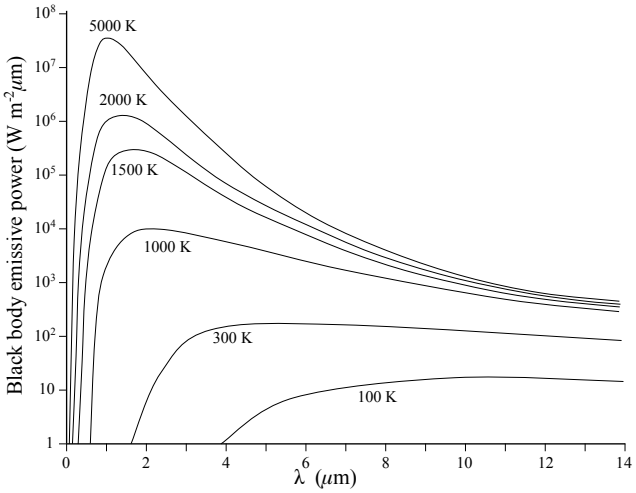

Figure 2.3: Spectral blackbody emissive power curves for different temperatures. Data extracted from [Radhouani and Daouas, 2013]

Eq. 2.16 can be integrated over the whole spectrum to obtain the total radiance of a blackbody:

$$L^o(T) = \int_{v=0}^{\infty} L_v^o(T)dv = \frac{2h}{c_0^2}\int_{v=0}^{\infty} \frac{v^3}{\left[\exp\left(\frac{hv}{kT}\right)-1\right]}dv \tag{2.19}$$

Now, the variable $x = \frac{hv}{kT}$ is introduced, which leads to the following relation:

$$L^o(T) = \frac{2h}{c_0^2}\left(\frac{kT}{h}\right)^4 \int_{x=0}^{\infty} \frac{x^3}{e^x-1}dx \tag{2.20}$$

Since the integral on the right side is equal to $\frac{\pi^4}{15}$, the total radiance is:

$$L^o(T) = \frac{\sigma T^4}{\pi} \tag{2.21}$$

where σ is the Stefan-Boltzmann constant, $\sigma = \frac{2\pi^5 k^4}{15c_0^2h^3} \approx 5.6703 \times 10^{-8}$ Wm^{-2}K^{-4}. Finally, the total radiative density flux emitted by a blackbody is given by Stefan's law [Howell et al., 2015]:

$$\phi^o(T) = \pi L^o(T) = \sigma T^4 \tag{2.22}$$

The Sun as a blackbody The Sun may be assimilated to a blackbody at 5777 K, emitting radiation at short wavelengths (less than 4μm). Part of the radiation reaching the atmosphere is absorbed by the clouds (23%) and the Earth (47%), and returned essentially in radiation with long wavelengths (greater than 4 μm) [Beckers, 2013c]. Figure 2.4 shows the spectral distribution of solar irradiance (received radiant density flux) outside the atmosphere, along with the distribution for a blackbody. After passing the atmosphere, this distribution changes, because the chemical properties of the atmosphere make it not transparent for some portions of the radiation spectrum (Figure 2.9).

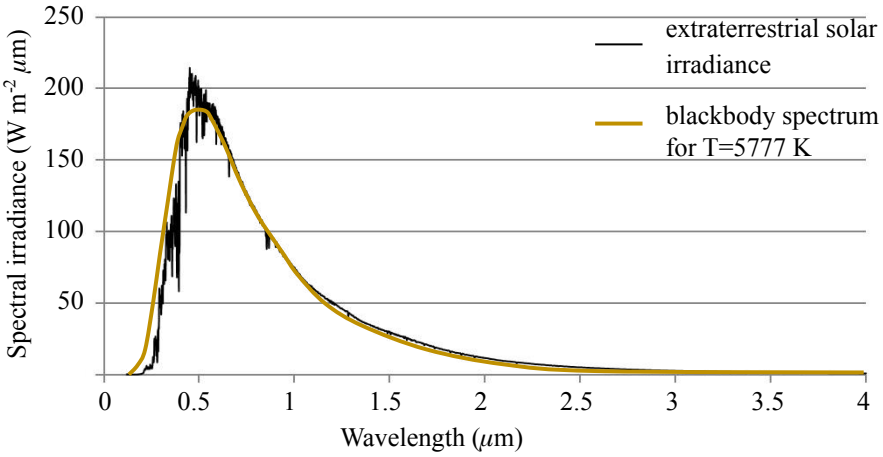

Figure 2.4: Spectral irradiance of the sun compared to that of a blackbody at 5777K. Data extracted from [Paulescu and Badescu, 2013].

2.5 Properties of radiative surfaces

Every non-black radiative surface absorbs and emits radiation at smaller rates than black bodies [Radhouani and Daouas, 2013]. On the other hand, it reflects and transmits part of the incident radiation. The behavior of a radiative surface is described using the following characteristics: emission, absorption, reflection and transmission (Figure 2.5).

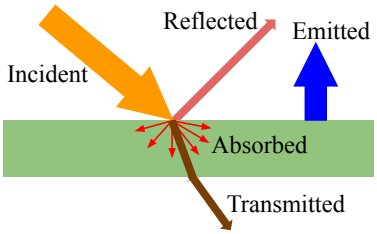

Figure 2.5: Behavior of a radiative surface

2.5.1 Emission and absorption

Radiative surfaces can emit different amounts of radiation depending on temperature, spectral region and direction. This property is described by the magnitude named directional spectral emittance:

$$M_v(T,\vec{\omega}) = \frac{\partial^3 Q}{\partial t\, \partial\vec{\omega}\, \partial A} \tag{2.23}$$

Comparing Eq. 2.23 with Eq. 2.14, the following relation is derived, relating spectral radiance with spectral emittance:

$$M_v(T,\vec{\omega}) = L_v(T,\vec{\omega})cos\theta \tag{2.24}$$

It can be seen that emittance depends on the cosine of the angle between the surface normal and the outgoing direction.

The emission characteristics of a surface are usually described using the concept of *emissivity*, which is a result of comparing its real radiant emittance to that of a blackbody. The directional spectral emissivity of a surface is obtained with:

$$\varepsilon_v(T,\vec{\omega}) = \frac{M_v(T,\vec{\omega})}{M_v^o(T)} \tag{2.25}$$

where $M_v^o(T)$ is the blackbody spectral emittance. Integrating $\varepsilon_v(T,\vec{\omega})$ over the whole spectrum and over the hemisphere, one obtains the total hemispherical emissivity $\varepsilon(T)$.

The *absorptivity* of a surface is the fraction of the incident radiant energy that is absorbed by it. This concept is initially unrelated to the ideal blackbody, and it is more complex than emissivity because the characteristics of the incident radiation must be considered in the calculations. The directional spectral absorptivity is defined as:

$$\alpha_v(T,\vec{\omega}) = \frac{\partial^3 Q_v^a(T,\vec{\omega})}{\partial^3 Q_v^i(\vec{\omega})} = \frac{\partial^3 Q_v^a(T,\vec{\omega})}{L_v(\vec{\omega})cos\theta\ \partial A\ \partial\vec{\omega}\ \partial t} \tag{2.26}$$

where Q_v^i is the incident radiative energy per square meter per steradian per second, and Q_v^a the correspondent absorbed energy. Note that Q_v^i does not depend on temperature. Integrating $\alpha_v(T,\vec{\omega})$ over the whole spectrum and over the hemisphere, one obtains the total hemispherical absorptivity $\alpha(T)$. None of these properties are intrinsic to the surface, because they depend on the characteristics of the incident radiation.

Kirchhoff's law Let us consider an element with differential area dA placed in a closed black cavity where only radiation phenomena is present (i.e. without conduction or convection conditions). At thermal equilibrium, all the cavity is at the same temperature. Under these conditions, the absorbed and emitted energies on the differential area must be equal for every direction, to maintain the energy balance with the rest of the black cavity. This relation is given by *Kirchhoff's law of thermal radiation*:

$$\varepsilon_v(T,\vec{\omega}) = \alpha_v(T,\vec{\omega}) \tag{2.27}$$

This relation is true for every radiative body at thermodynamic equilibrium, which allows explaining why radiation heat transfer does not violate the *Second Law of Thermodynamics* [Howell et al., 2015].

Gray body A gray body is defined as a body in which the directional emissivities and absorptivities do not vary for different spectral regions. Since Kirchhoff's law is true for all directions and for all frequencies, it can be said that, for gray bodies, the total directional emissivity is equal to the total directional absorptivity:

$$\varepsilon(T,\vec{\omega}) = \alpha(T,\vec{\omega}) \tag{2.28}$$

For the case of a gray body that emits diffusely (i.e. emissivity is equal for all directions), it can be said that the total hemispherical emissivity is equal to the total hemispherical absorptivity:

$$\varepsilon(T) = \alpha(T) \tag{2.29}$$

Semigray bodies A common assumption in studies involving solar radiation is to consider two well-defined spectral regions: short and long wavelengths. In this case, materials are often called *semigray* [Howell et al., 2015], which means that they have two different set of properties that are uniform within each region. In other words, they can be considered to be gray surfaces with a given directional absorptivity at short wavelengths, and as gray surfaces with other directional absorptivity values for long wavelengths.

Directional emissivity properties The characterization of radiation properties for construction materials is still a subject of study [Peeters et al., 2016]. Usually, besides semigray approximations, the temperature dependence of these characteristics is neglected. Optically smooth materials are those where the surface imperfections and roughness are much smaller than the wavelength of the incident radiation. The behavior of optically smooth non-conductor materials such as glass can be described using *electromagnetic wave theory* [Modest, 2003]. Fresnel's relations are used to obtain directional emissivity curves depending on the refractive index of the medium, represented by symbol n:

$$\varepsilon(\theta) = 1 - 0.5\left[\left(\frac{n^2 cos\theta - \sqrt{n^2 - sin^2\theta}}{n^2 cos\theta + \sqrt{n^2 - sin^2\theta}}\right)^2 + \left(\frac{cos\theta - \sqrt{n^2 - sin^2\theta}}{cos\theta + \sqrt{n^2 - sin^2\theta}}\right)^2\right] \tag{2.30}$$

A common assumption is that the emissivity depends only on the zenith angle of view, i.e. it has the same behavior for different directions in the azimuth angle. Figure 2.6 shows examples of Fresnel emissivity curves using different n values. Nonconductors show a high emittance for most directions, which drops to zero at grazing angles.

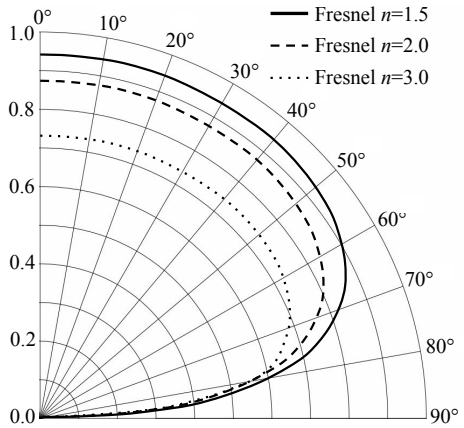

Figure 2.6: Ideal directional emissivity models using Fresnel equations, with n the refractive index of the medium.

With the previous specification of directional emissivity, the total hemispherical emissivity is calculated by an integration on the zenith angle:

$$\varepsilon = 2\int_0^{\pi/2} \varepsilon(\theta)\, cos\theta\, sin\theta\, d\theta \tag{2.31}$$

2.5.2 Reflection

If a surface does not absorb all the incoming radiation, then a fraction of it is reflected and/or transmitted. Reflection properties are harder to study than emission or absorption, because they depend on the incoming direction of radiation, $\vec{\omega}_i$, as well as on the outgoing direction $\vec{\omega}_r$. In this section, the temperature dependence of reflection properties is neglected for clarity reasons, but it could be integrated in the same way as for gray body emission. The fraction of the incoming spectral radiance that is reflected in each direction is called *bidirectional spectral reflectivity*, and it is defined as:

$$\rho_v(\vec{\omega}_i, \vec{\omega}_r) = \frac{\partial L_v^r(\vec{\omega}_i, \vec{\omega}_r)}{L_v(\vec{\omega}_i) cos\theta_i \, \partial\vec{\omega}_i} \tag{2.32}$$

where $L_v^r(\vec{\omega}_i, \vec{\omega}_r)$ is the radiance reflected in direction $\vec{\omega}_r$ and $L_v(\vec{\omega}_i)$ is the total radiance reaching the surface in directions within the solid angle $\partial\vec{\omega}_i$. The cosine dependence of this property implies that, when integrating over all the incident directions, the total reflected intensity is correctly weighted by the incident direction.

Helmholtz reciprocity law [Clarke and Parry, 1985] can be used to prove that the bidirectional reflectivity is a symmetric function, i.e. $\rho_v(\vec{\omega}_i, \vec{\omega}_r)$ is equal to $\rho_v(\vec{\omega}_r, \vec{\omega}_i)$ for all $\vec{\omega}_i$ and $\vec{\omega}_r$.

An integration over the reflected hemisphere allows obtaining the *directional spectral reflectivity*, which is a measure of the fraction of the incident radiation (from a single direction) that is reflected into the entire hemisphere:

$$\rho_v(\vec{\omega}_i) = \frac{\int_{\vec{\omega}_r=2\pi} \partial L_v^r(\vec{\omega}_i, \vec{\omega}_r) cos\theta_r \, d\vec{\omega}_r}{L_v(\vec{\omega}_i) cos\theta_i \, \partial\vec{\omega}_i} \tag{2.33}$$

Now, considering the whole radiation spectrum, one can obtain the *total directional reflectivity* by the following formula:

$$\rho(\vec{\omega}_i) = \frac{\int_{v=0}^{\infty} \rho_v(\vec{\omega}_i) L_v(\vec{\omega}_i) \, dv}{\int_{v=0}^{\infty} L_v(\vec{\omega}_i) \, dv} \tag{2.34}$$

Reflectivity models Despite the fact that a large number of bidirectional reflectivity functions are used in physics, optics and computer graphics, there are three widely accepted simplified models that are usually used in radiation studies (Figure 2.7).

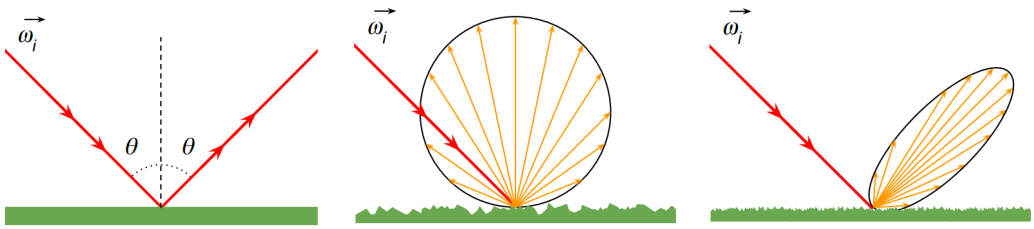

(a) Specular. (b) Diffuse. (c) Glossy.

Figure 2.7: Simplified reflectivity models.

Specular reflections imply a mirror-like behavior, which means that radiation is reflected only in the direction that is symmetric to the incident ray. This kind of approximation is used for smooth surfaces, where the radiation wavelength is much larger than the roughness of the material. On the

other hand, purely diffuse reflections, also known as *Lambertian* reflections, model the directional reflectivity following Lambert's cosine law. In this case, the reflectivity is independent of the incident direction. The material's micro-surface roughness can cause the effect of diffuse reflection at the macro scale. An intermediate model, namely *glossy* reflectivity [Jensen, 2001], is based on a mixture of the two previous models, and allows following directions near the symmetric specular direction, using different lobe sizes to model different kinds of materials.

For short-wave radiation, many construction materials tend to be very rough (e.g. concrete, wood, or clay), which leads to the usage of the diffuse reflectivity model. Nevertheless, the same surfaces can present a very different behavior at longer wavelengths, which allows modeling them with specular or glossy approximations.

2.5.3 Transmission

The transmission of radiation happens in non-opaque media, such as transparent materials like glass. The fraction of radiation that is transmitted at an interface is called *transmissivity*. The definition of this concept follows a very similar approach than reflectivity. Transmission also depends on both incident and outgoing directions. The latter corresponds to the direction at which the radiation is transmitted after crossing the surface.

The fraction of the incoming spectral radiance that is transmitted in each direction is called *bidirectional spectral transmissivity*, and it is defined as:

$$\tau_v(\vec{\omega}_i, \vec{\omega}_t) = \frac{\partial L_v^t(\vec{\omega}_i, \vec{\omega}_t)}{L_v(\vec{\omega}_i) cos\theta_i \, \partial\vec{\omega}_i} \tag{2.35}$$

where $L_v^t(\vec{\omega}_i, \vec{\omega}_t)$ is the radiance transmitted in direction $\vec{\omega}_t$ and $L_v(\vec{\omega}_i)$ is the total radiance reaching the surface in directions within the solid angle $\partial\vec{\omega}_i$.

The *directional spectral transmissivity* corresponds to the fraction of the incident radiation coming from direction $\vec{\omega}_i$ and for a given frequency v that is transmitted into the entire opposed hemisphere:

$$\tau_v(\vec{\omega}_i) = \frac{\int_{\vec{\omega}_t=2\pi} \partial L_v^t(\vec{\omega}_i, \vec{\omega}_t) cos\theta_t \, d\vec{\omega}_t}{L_v(\vec{\omega}_i) cos\theta_i \, \partial\vec{\omega}_i} \tag{2.36}$$

The *total directional reflectivity* is the transmitted fraction for an incoming direction and the whole spectrum:

$$\tau(\vec{\omega}_i) = \frac{\int_{v=0}^{\infty} \tau_v(\vec{\omega}_i) L_v(\vec{\omega}_i) \, dv}{\int_{v=0}^{\infty} L_v(\vec{\omega}_i) \, dv} \tag{2.37}$$

Snell's law The transmission properties for electromagnetic waves is a subject of study of many research areas. The analysis of light passing through the boundary between two transparent isotropic media led to the formulation of Snell's law [Howell et al., 2015]. This law states that the direction of the waves is affected by the change of media (Figure 2.8), and that the ratio between the refractive indices of both media (n_1/n_2) is equal to the ratio between the sines of the angle of incidence and of the outgoing direction:

$$\frac{sin\theta_1}{sin\theta_2} = \frac{n_1}{n_2} \tag{2.38}$$

When light travels from a medium with a higher refractive index to one with a lower refractive

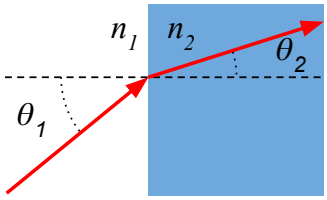

Figure 2.8: Components of Snell's law of refraction between two media with different refractive indices.

index, there is a phenomenon called *total internal reflection* that implies that light does not passes to the second medium. The largest possible angle of incidence for transmission to happen between two given media is called *critical angle*.

Atmospheric transmissivity The Earth's atmosphere is a transparent medium that transmits a fraction of the radiation coming from the Sun, and a fraction of radiation coming from the surface of the planet. Each of the chemical components that are present in the atmosphere absorbs radiation from different parts of the thermal spectrum, resulting in the spectral distribution of the transmissivity that is presented in Figure 2.9.

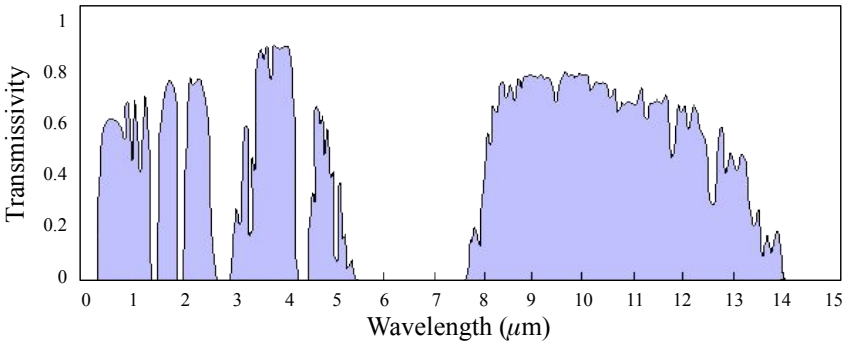

Figure 2.9: Spectral transmissivity of the atmosphere. Data extracted from [Salisbury and D'Aria, 1992].

It can be seen that there are some intervals of the thermal radiation spectrum that present high transmissivity values (e.g. between 8μm and 14μm). This phenomenon is known as the *infrared atmospheric window* [Vollmer and Möllmann, 2017], which indicates that part of the radiation emitted by the Earth's surface is transmitted to space at larger rates, implying fewer absorption, and thus lower atmospheric temperatures.

2.5.4 Relation between radiative properties

The previously introduced radiative properties (emissivity, absorptivity, reflectivity and transmissivity) are defined as fractions of some other magnitudes such as blackbody radiation or incident radiance. Therefore, because they are all dimensionless ratios, they all take values in the [0,1] interval. This fact indicates that there is an evident relation between them. For example, in opaque materials, all of the transmitted radiation is absorbed by the medium, which means that absorptivity equals transmissivity. For any surface at radiative equilibrium, the application of Kirchhoff's law

allows obtaining the following relation:

$$\alpha_v(\vec{\omega}_i) + \rho_v(\vec{\omega}_i) + \tau_v(\vec{\omega}_i) = 1 \tag{2.39}$$

This equation indicates that the sum of spectral directional absorptivity, reflectivity and transmissivity is equal to 1. The same deduction can be proved true hemispherically:

$$\alpha_v + \rho_v + \tau_v = 1 \tag{2.40}$$

Finally, over the whole radiation spectrum, the relation is preserved:

$$\alpha + \rho + \tau = 1 \tag{2.41}$$

2.5.5 Radiation view factors

Radiation transfer studies in complex environments must address the radiative exchange between the different parts of the geometry. This exchange is determined by the emitted and reflected portions. For instance, in the case of short-wave radiation, the scene is mainly a reflector of light emitted by few sources (the sun, artificial sources). In long-wave studies, all the surfaces become emitters, and reflected radiation becomes a fraction of the overall exchange.

The concept of *view factor* [Cohen and Wallace, 1993] is a geometrical relation that depicts the fraction of the energy leaving a surface that arrives at another surface. Other terminology for the same concept is *form factor*, *shape factor* and *configuration factor*. View factors are typically used under non-participating media assumptions, i.e. when the exchange is virtually unaffected by the medium. Although they can be used for arbitrary material properties, they are mostly applied to gray surfaces with diffuse emission and reflection properties. Many science fields have used this approach (lighting engineering, applied optics, etc), but it was originally designed for heat transfer studies [Howell et al., 2015].

Consider two infinitesimal areas dA_i and dA_j, separated by a distance r, then the view factor between them is calculated as the total energy leaving dA_i and intercepted by dA_j divided by the total diffuse energy leaving dA_i. This is expressed by:

$$F_{dA_i - dA_j} = \frac{cos\theta_i cos\theta_j}{\pi r^2} V_{(i,j)} dA_j \tag{2.42}$$

where θ_i is the angle between the normal of dA_i and the vector in the direction of dA_j, and $V_{(i,j)}$ is a visibility term that is equal to 1 if dA_i is visible from dA_j, and 0 otherwise [Cohen and Wallace, 1993]. This equation defines the differential area to differential area view factor, and it is the simplest form of the view factor. When studying scenes with a finite number of isothermal surfaces, it is of interest to define the form factor between a differential area and a finite surface, and between to arbitrary finite surfaces. The former is simply obtained by adding an integral in Eq. 2.42:

$$F_{dA_i - A_j} = \int_{A_j} \frac{cos\theta_i cos\theta_j}{\pi r^2} V_{(i,j)} dA_j \tag{2.43}$$

In order to introduce the total area of A_i into the definition, it is convenient to assume that the intensity leaving A_i is equal for every point of the surface. Then, the area-to-area view factor is

defined by:

$$F_{A_i-A_j} = \frac{1}{A_i}\int_{A_i}\int_{A_j}\frac{cos\theta_i cos\theta_j}{\pi r^2}V_{(i,j)}dA_j dA_i \tag{2.44}$$

For this expression, a law of reciprocity is usually defined, relating the view factors between two arbitrary surfaces:

$$A_i F_{A_i-A_j} = A_j F_{A_j-A_i} \tag{2.45}$$

Another important property is the summation relation, which depicts that for a scene composed of N elements, the sum of all the view factors from A_i is less than or equal to 1:

$$\sum_{j=1}^{N} F_{A_i-A_j} <= 1 \tag{2.46}$$

The previous sum is equal to 1 for the case of a closed scene where all the elements only see elements, i.e. they do not see the void.

2.6 Convection

Convection is the heat transfer phenomena related to the observable movement of fluids [Yunus et al., 2003]. When the key problem is determining the heat transfer at a surface exposed to a flowing fluid, convection simulations are fundamental for obtaining precise results. In an urban thermal problem, the air is the fluid in contact with the surfaces. The simulation of fluid dynamics is still a very expensive problem in terms of computational complexity, mostly because of the precision needed in the discretization step of the computation, i.e. the meshes must be composed of millions of nodes. For this purpose, we simplify the convection assuming the simulated day is calm (not windy), and that the air fluid is static at varying temperatures. The equation that represents the heat flux by convection is presented in Eq. 2.47, which is given by Newton's law of cooling.

$$\dot{q} = h(T - T_{air}) \tag{2.47}$$

In Eq. 2.47, $\dot{q}$ is the heat flux associated to convection, T_{air} is the air temperature, and T is the temperature of the studied point. h is the convection heat transfer coefficient, measured in W m^{-2} K^{-1}.

2.7 Full heat balance equation

The urban energy balance problem can be formulated as a conduction-dominant transient problem, where the conductivity properties of the scene greatly influence its thermal behavior through time. Nevertheless, several boundary conditions must be considered in an urban study, which complicates the analysis and the involved computational methods [Garcia-Dorado et al., 2017; Maréchal et al., 2010]. The transient energy balance is described using Fourier's law of heat conduction [Lewis et al., 2004]:

$$\begin{gathered}\rho_m c_p \frac{\partial T}{\partial t} = k\Delta T \;\text{ subject to: }\; T = T_b \;\text{ on }\; \Gamma_b, \\ \text{and }\; -k\frac{\partial T}{\partial n} + q_s + h(T - T_{air}) + \varepsilon\sigma(T^4 - T_{env}^4) = 0 \;\text{ on }\; \Gamma_q\end{gathered} \tag{2.48}$$

This equation is a non-linear second-order partial differential equation. The first part represents heat conduction, while the subsequent terms account for boundary conditions. Dirichlet conditions are imposed temperatures T_b in the interface Γ_b. Neumann conditions are imposed fluxes in Γ_q, in the form of absorbed short-wave radiation q_s (W m^{-2}), long-wave radiative exchange, and convective heat transfer exchanged with the air. The vector n denotes the outward normal to the boundary Γ_q. T is the temperature of the surface in K, t represents time, while Δ is the Laplace operator. ρ_m (kg m^{-3}), c_p (J kg^{-1} K^{-1}) and k (W m^{-1} K^{-1}) are the mass density, specific heat, and conductivity of the material. h is the convective heat transfer coefficient in W m^{-1} K^{-1}, and T_{air} is the air temperature. ε is the emissivity of the material, and T_{env} is the average temperature of the environment. An initial temperature T_0 at t = 0.0s is necessary for solving this differential equation.

2.8 Thermal cameras

The analysis of heat transfer has been historically addressed through a wide variety of measurement techniques and experiments. Since centuries ago, the most typical laboratory tool used for thermal studies is the thermometer, which allows to track local temperature variations of a body. After the discovery of thermal radiation, thermodynamic engineers started the development of non-invasive measurement techniques that allow measuring the radiative flux to transform it into *brightness* temperature. This technique has the advantage of being non-invasive but provides results that are harder to interpret without the proper knowledge of radiation physics. In the last decades, thermal cameras have become more available to the civil public, and have led to the birth of a new field of science, so-called *infrared thermal imaging* [Vollmer and Möllmann, 2017].

Thermal cameras are composed of a collection of infrared sensors that gather the incoming infrared radiative flux arriving in directions within the field of view (FOV) of the lens. Far-infrared thermal cameras measure radiation with a wavelength between 7 and 14 μm. The measured radiation is composed of a mixture of three different components: radiation emitted by the captured object, radiation emitted by other bodies and reflected by the object, and radiation emitted by the atmosphere (air) between the camera and the object (Figure 2.10).

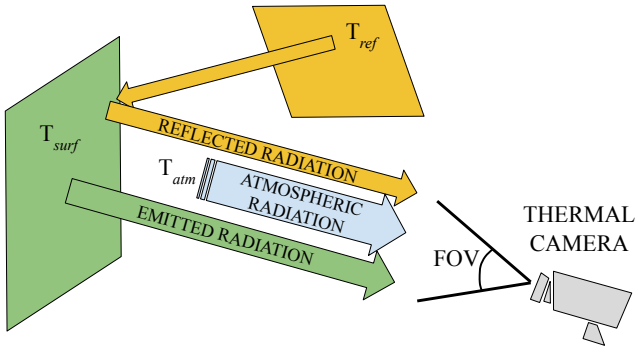

Figure 2.10: Components of the radiation captured by a thermal camera.

A simplified physical model is then used by the camera software to estimate the temperature of the captured surfaces. This model is based on the measured radiative flux and some data that must be entered to the camera: the directional emissivity ε and reflected temperature T_{ref} of each pixel,

the air temperature, and the relative humidity. The measured radiative flux is first used to estimate a total radiant flux ϕ_{in}, following the spectral distribution of a blackbody. Then, ϕ_{in} is modeled as:

$$\phi_{in} = \tau_{atm}\Big(\varepsilon\Phi^{black}(T_{surf}) + (1-\varepsilon)\Phi^{black}(T_{ref})\Big) + (1-\tau_{atm})\Phi^{atm}(T_{atm}) \tag{2.49}$$

where T_{surf} is the unknown surface temperature, and τ_{atm} is the atmospheric transmittance estimated using an atmospheric model with the input data. $\Phi^{black}(T)$ is the radiative flux of a blackbody at temperature T, and $\Phi^{atm}(T_{atm})$ is the radiative flux coming from an atmosphere at temperature T_{atm}, output of the atmospheric model.

$\Phi^{black}(T_{surf})$ is extracted from the previous equation in the following way:

$$\Phi^{black}(T_{surf}) = \frac{\phi_{in}}{\tau_{atm}\varepsilon} - \frac{1-\varepsilon}{\varepsilon}\Phi^{black}(T_{ref}) - \frac{1-\tau_{atm}}{\tau_{atm}\varepsilon}\Phi^{atm}(T_{atm}) \tag{2.50}$$

From Eq. 2.22 it is known that $\Phi^{black}(T_{surf}) = \sigma T_{surf}^4$ and $\Phi^{black}(T_{ref}) = \sigma T_{ref}^4$. Also, for a sufficiently close measurement distance, the atmospheric radiation can be neglected ($\tau_{atm} = 1$). Therefore, the surface temperature T_{surf} is calculated as:

$$T_{surf} = \sqrt[4]{\frac{\phi_{in}}{\sigma\varepsilon} - \frac{1-\varepsilon}{\varepsilon}T_{ref}^4} \tag{2.51}$$

The model used by the thermal camera is very sensible to the input data (e.g. directional emissivity, reflected temperatures), whose estimation is usually very difficult. Therefore, the estimated temperatures shown in thermal images are not always accurate estimations of the real temperatures. For the very special case where the input emissivity is set to be 1 and the atmospheric radiation is neglected, the output temperatures are called *apparent surface temperatures*.

Chapter 3

Numerical heat transfer

The study of heat transfer in bodies with complex geometries becomes a hard task to do analytically. In this context, computational methods have been developed to assess thermal studies at building and urban scales. This chapter outlines methods for heat transfer analysis, with special emphasis in heat conduction and radiation methods. Next, the FEM-based computational model developed in this thesis is presented, and the results of its application on a first urban study are shown.

3.1 Heat conduction methods

The heat balance expressed in Eq. 2.48 is usually solved using different computational methods that can be grouped into three main approaches.

Electric-analogy methods [Asawa et al., 2008; Kramer et al., 2012] are the most widely used. The basic idea is to model conduction through the building components with a network of resistors and capacitors. Software solutions like EnergyPlus [Crawley et al., 2001] and CitySim [Robinson et al., 2009] use electric-analogy solvers. The modeling process requires experienced users to build the proper network for each test case [Kämpf and Robinson, 2007], however the simplified nature of the models provide a balance between accuracy and algorithmic performance [Reinhart and Davila, 2016]. Because of the associated geometrical simplifications, these methods are not well suited for a detailed analysis of the spatial distribution of the surface temperatures, which is required in thermography simulations.

The finite difference method (FDM) [Croft and Lilley, 1977] allows for a much better interpretation of the results in a spatialized way. FDM are discretization methods that solve differential equations by approximating derivatives with difference equations. Many software solutions based on FDM, such as ENVI-met [Bruse, 2004], require the urban geometry to be meshed with regular and equally sized elements to perform the simulation [Huttner, 2012], which forces to use a very large number of elements in urban studies.

The Finite Element Method (FEM) [Lewis et al., 2004] provides a more flexible meshing scheme, because elements with different sizes and shapes can be integrated into the same simulation. Moreover, the selection of proper *shape functions* can ensure realistic temperature evolutions within each element, allowing for the reduction of the mesh size. Several FEM software solutions (e.g. COMSOL multiphysics [COMSOL Inc., 2018], ANSYS [Stolarski et al., 2018], and Cast3m [Charras and

Di Paola, 2011]) can be used for urban thermal studies [Evangelisti et al., 2018; Hénon et al., 2012].

Once the simulation method has been chosen, it is necessary to define the boundary and initial conditions of the problem, and to select the proper methods to incorporate them in the system. Regarding the convection energy exchanges, there are two options: predicting wind movements using Computational Fluid Dynamics (CFD) at the city scale [Van Hooff and Blocken, 2010], or setting convection coefficients based on thermal regulations or on experimental correlations from literature. CFD are particularly necessary when simulating strong forced convection conditions (e.g. strong winds) that have a significant effect on the urban surface temperatures. However, CFD simulations demand intensive computational requirements, as well as additional software integration. Under calm wind conditions, setting an approximate value of h from literature references or empirical correlations has proved to be accurate enough for thermal simulations [Mirsadeghi et al., 2013].

3.1.1 The Finite Element Method

The Finite Element Method can be used to discretize Fourier's law of heat transfer, which is first expressed without convective and radiative boundary conditions:

$$k\Delta T + G = \rho_c c_p \frac{\partial T}{\partial t} \tag{3.1}$$

FEM provides a solution to partial differential equations through a system of algebraic equations with a finite number of unknowns (nodes in the domain) [Lewis et al., 2004]. The discretization stage is applied to subdivide the initial problem into smaller parts, denoted as "finite elements". The resulting system of equations is then solved by numerical algebra, aiming to minimize the error function involved.

In FEM the temperature can vary across the elements. This variation is described by a polynomial of first, second or higher order, which means that the temperature can vary following linear, parabolic and other functions. The functions that describe the behavior of the interpolation are called *shape functions*, and they influence the results obtained through FEM.

Let us assume that the domain is discretized into elements (for instance lines in 1D, triangles in 2D, or tetrahedra in 3D). These elements are defined by N nodes connected through edges. If we assume that the temperature at each node is known, then N local shape functions can be defined in order to interpolate the temperature at any point in the elements. For example, in 1D, the temperature at a certain point p inside an element is defined by the temperatures at the two nodes (i and j) that form the element:

$$T(p) = N_i(p)T_i + N_j(p)T_j \tag{3.2}$$

In this equation, N_i and N_j are the local shape functions corresponding to nodes i and j. These functions are zero at any point of the domain that falls outside the elements that contains the respective node. Also, the functions are equal to one if evaluated at the node that defines them.

The general form of Eq. 3.2 is presented next, defining the temperature at any point within the

domain in terms of the shape functions and the nodal temperatures:

$$\hat{T}(p,t) = \sum_{j=1}^{N} T_j(t) N_j(p) \quad \forall p \in \Pi \tag{3.3}$$

Here, p represents any point inside the domain Π, and t is the instant of time in consideration. Note that the term T_j only depends on time because the position of nodes is fixed throughout the simulation, while the term N_j only depends on the point to evaluate. Another important consideration is that $\hat{T}$ approximates the exact temperature.

Now, substituting T by $\hat{T}$ in Eq. 3.1, we get the following equation, where *res* expresses the residual of the approximation in function of p and t:

$$k\Delta\hat{T}(p,t) + G - \rho_c c_p \frac{\partial \hat{T}(p,t)}{\partial t} = res(p,t) \tag{3.4}$$

The problem has been transformed into residual problem, where the aim is to select the nodal temperatures T_j that minimize the residual. This minimization can be accomplished by the Weighted Residual Method (WRM), where a set of $W_j(r)$ independent weighting functions are selected and the residual is made orthogonal to each of them. The above differential equation is replaced by its equivalent weak form:

$$\int_{\Pi} \Big(k\Delta\hat{T}(p,t) + G - \rho_c c_p \frac{\partial \hat{T}(p,t)}{\partial t} \Big) W_i(p) d\Pi = \int_{\Pi} res(p,t) W_i(p) d\Pi = 0 \tag{3.5}$$

This equation is called weak form because of its lower differentiability requirements. There are many possible approaches for the selection of W_j, which define different WRM schemes. One of the most used in FEM is the Galerkin method, where the weighting functions are the same as the shape functions, thus $W_j = N_j \quad \forall j \in 1..N$. This selection has the advantage that each N_j is zero in most of the domain, which makes the resulting matrix for solving the unknowns T_j to be very sparse. The Galerkin form of the energy equation for each of the weighting functions is expressed in Eq. 3.6, now with the $\hat{T}$ terms replaced by the right-hand expression in Eq. 3.3.

$$\int_{\Pi} \left(k\Delta\Big(\sum_{j=1}^{N} T_j(t) N_j(p) \Big) + G - \rho_c c_p \frac{\partial\Big(\sum_{j=1}^{N} T_j(t) N_j(p) \Big)}{\partial t} \right) N_i(p) d\Pi = 0 \tag{3.6}$$

The evaluation of Eq. 3.6 for each nodal point in the domain results in N equations that depend on the nodal temperatures T_j. This process defines the system of equations that needs to be solved in order to find the unknown temperatures, and thus to obtain an approximated solution for the heat equation.

Note that the Laplacian operator differentiates the inner summation only by means of space (independent of time), so the term $T_j(t)$ can be extracted from the derivative. Similarly, the term $N_j(p)$ can be taken out of the time-dependent derivative. Also, the derivative of a summation is equal to the summation of the derivative of each term. These rearrangements result in the following simplified form of the equation:

$$\int_{\Pi} \left(k \sum_{j=1}^{N} T_j(t) \Delta N_j(p) + G - \rho_c c_p \sum_{j=1}^{N} N_j(p) \frac{\partial T_j(t)}{\partial t} \right) N_i(p) d\Pi = 0 \tag{3.7}$$

Following Green's lemma and applying integration by parts in the first term of the integral, the equation is transformed into:

$$
\begin{aligned}
-\int_{\Pi}\left(k\sum_{j=1}^{N}T_j(t)\nabla N_j(p)\nabla N_i(p)-N_i(p)G+\rho_c c_p\sum_{j=1}^{N}N_j(p)N_i(p)\frac{\partial T_j(t)}{\partial t}\right)d\Pi \\
+\int_{\Gamma_q}N_i(p)k\frac{\partial T}{\partial n}\,d\Gamma_q=0
\end{aligned}
\tag{3.8}
$$

Applying Neumann boundary conditions (Sec. 2.3), multiplying both sides by $N_i(p)$, and integrating in the above equation, we get:

$$
\begin{aligned}
-\int_{\Pi}\left(k\sum_{j=1}^{N}T_j(t)\nabla N_j(p)\nabla N_i(p)+\rho_c c_p\sum_{j=1}^{N}N_j(p)N_i(p)\frac{\partial T_j(t)}{\partial t}\right)d\Pi+\int_{\Pi}N_i(p)G d\Pi \\
-\int_{\Gamma_q}N_i(p)h\Big(\sum_{j=1}^{N}T_j(t)N_j(p)-T_a\Big)\,d\Gamma_q-\int_{\Gamma_q}N_i(p)q\,d\Gamma_q=0
\end{aligned}
\tag{3.9}
$$

Two final changes remain to be applied to the equation. In the first place, the integral of a summation is equal to the sum of the integrated summands, so the first term can be simplified. In the second place, the convective term can be separated into two terms, in order to put all the terms that multiply T_j together. Then, the following equation is the final form of the heat equation discretized via Galerkin method:

$$
\begin{aligned}
\sum_{j=1}^{N}\Big(\int_{\Pi}k\nabla N_j(p)\nabla N_i(p)d\Pi+\int_{\Gamma_q}hN_i(p)N_j(p)\,d\Gamma_q\Big)T_j(t) \\
+\sum_{j=1}^{N}\Big(\int_{\Pi}\rho_c c_p N_j(p)N_i(p)d\Pi\Big)\frac{\partial T_j(t)}{\partial t}= \\
\int_{\Pi}N_i(p)G d\Pi+\int_{\Gamma_q}N_i(p)hT_a\,d\Gamma_q-\int_{\Gamma_q}N_i(p)q\,d\Gamma_q
\end{aligned}
\tag{3.10}
$$

Eq. 3.10 is satisfied for each node i. Hence, the evaluation over all the nodes defines N equations, each of them controlled by a summation of N terms. This defines a system of equations whose matrix form is observed in Eq. 3.11.

$$
\mathbf{C}\Big\{\frac{\partial T}{\partial t}\Big\}+\mathbf{K}\{T\}=\{f\}
\tag{3.11}
$$

In this equation, $\mathbf{C}$ is the capacitance matrix (mass matrix in elasticity) and $\mathbf{K}$ is the conductivity matrix (stiffness matrix in elasticity). $\{T\}$ is the vector of unknowns, and $\{\mathrm{f}\}$ is called the load vector. $\left\{\frac{\partial T}{\partial t}\right\}$ is the vector of temperature derivatives over time, which remains to be discretized. Eq. 3.12 shows the value of each element of the matrices.

$$
\begin{aligned}
\mathbf{C}_{ij}&=\int_{\Pi}\rho_c c_p N_j N_i d\Pi \\
\mathbf{K}_{ij}&=\int_{\Pi}k\nabla N_j\nabla N_i d\Pi+\int_{\Gamma_q}hN_jN_i\,d\Gamma_q \\
\{f\}_i&=\int_{\Pi}N_i G d\Pi+\int_{\Gamma_q}N_i hT_a\,d\Gamma_q-\int_{\Gamma_q}N_i q\,d\Gamma_q
\end{aligned}
\tag{3.12}
$$

The matrix $\mathbf{K}$ is symmetric, and positive definite [Lewis et al., 2004]. Moreover, this matrix is usually very sparse, because the i^{th} row (corresponding to the i^{th} node) has elements different than zero only in the positions of the correspondent adjacent nodes. The construction of these matrices involves the differentiation of the local shape functions, which is a simple task because these functions are usually polynomials. Next, integration over the whole domain for some terms and over the boundary for other terms is necessary. This task cannot be performed analytically in elements with complex geometrical shapes, but numerical approaches such as the Gaussian Quadrature can be used.

It is worth saying that the construction of $\mathbf{K}$ and $\mathbf{C}$ matrices is usually accomplished by computing element matrices and then assembling the results into the global matrices. Element matrices are obtained through local integration over each element. The global integration is equal to the summation of all the local integrals, because the domain is discretized in such way that the elements do not overlap. This approach is useful from a computational perspective, because many computations can be performed independently and then joined into the global result.

Mesh for FEM

A major concern of FEM analysis is the creation of meshes. The geometries that represent objects to be simulated must be discretized into a finite set of polygons. For instance, meshing strategies based on CAD have been widely studied in mechanics [de Cougny and Shephard, 1996]. In order to work with FEM, the generated mesh must be conformal, i.e free of intersections, overlapping, and where no node of an element is on an edge or face of another element, meaning that adjacent elements share full edges. It is often difficult to overcome this constraint when dealing with complex geometries [Rassineux and Beckers, 2016]. Figure 3.1 shows two different meshes for a building wall joining the street. The mesh in the left is not conformal because there is overlapping and nodes that fall in the edge of other elements, and the right mesh is perfectly conformal. While the mesh in the left can be used, for instance, in daylighting studies, it cannot be used to represent the conduction between the wall and the street with FEM. This example shows how conformal meshing is more restrictive.

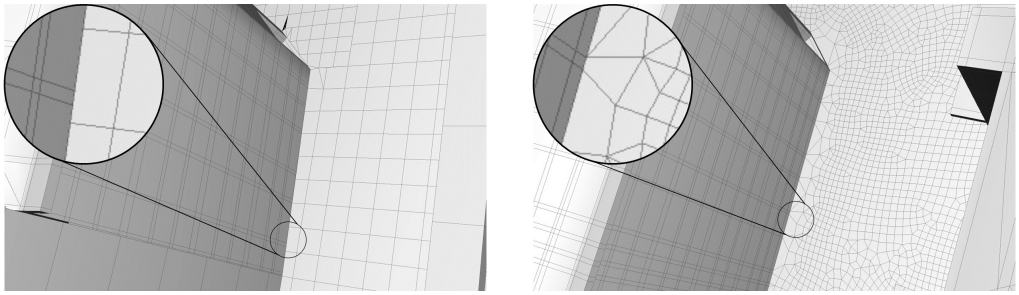

(a) Non-conformal mesh (b) Conformal mesh

Figure 3.1: Two different 3D meshes for the geometry of a building wall and street.

There are two main types of meshing strategies for FEM: 1) structured meshing generates a mesh where all the inner nodes have the same number of elements around them, and 2) unstructured meshing produces irregular results that do not necessarily satisfy the previous constraints (Figure 3.2). The former allows for better simulation conditions but it is more difficult to use in complex

geometries.

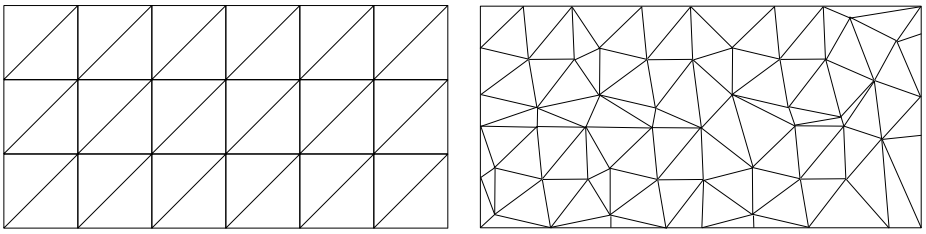

Figure 3.2: Structured and unstructured 2D mesh of triangles.

There are several types of elements that can be used in a FEM simulation, depending on the geometry to be modeled and the phenomena to be analyzed. The selected shape functions determine the number of nodes in each element. For example, linear triangles have 3 nodes n_1, n_2, n_3, and are built in such way that the evolution of temperature along one edge (n_1, n_2) is linear, considering the temperatures at those nodes. On the other hand, in quadratic triangles, one node is added to each edge (adding nodes n_{12}, n_{23}, n_{31}), where the temperature in the edge (n_1, n_{12}, n_2) now follows a parabolic function considering the temperatures of the three nodes that compose the edge.

Figure 3.3 shows some examples of 2D linear and quadratic elements with nodes, and some linear 3D elements. Linear quads have 4 nodes, while quadratic quads have 8 nodes. For 3D volumes, the usual options available are tetrahedra (4 or 10 nodes), hexahedra (8 or 20 nodes), or triangular prisms (6 or 15 nodes).

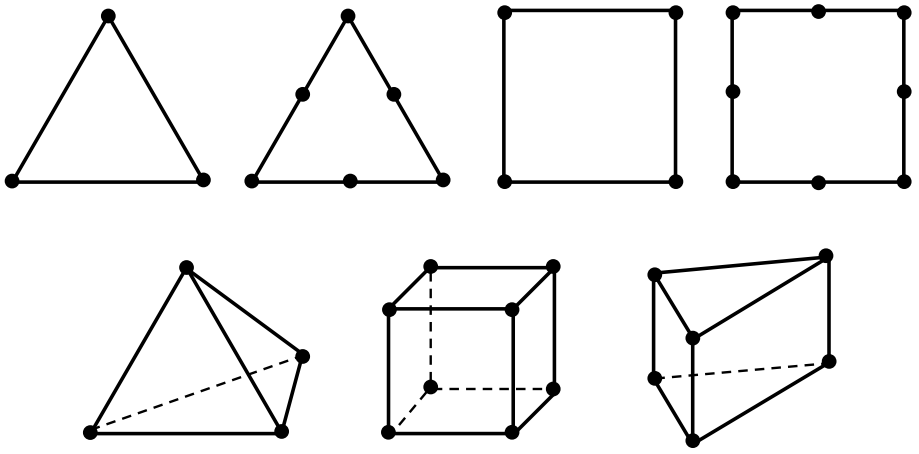

Figure 3.3: Different kinds of 2D and 3D elements in FEM.

Several works have proposed algorithms to refine or coarsen a mesh, following a given criterion (shape, size, etc) [Shamir, 2008]. Typically, these techniques extract a set of elements that share the same node or edge and remesh the outer contour [Chappuis et al., 2004]. Mesh refinement can be a useful strategy to improve the precision FEM calculations, implying higher computational requirements due to working with a larger number of elements.

3.1.2 Time discretization with FDM

The system of equations presented in Eq. 3.11 has a time-dependent term that remains to be discretized. This discretization can be accomplished through many approaches. In this section the Finite Difference Method is used, which is a simple technique and produces accurate results for time discretization [Lewis et al., 2004].

The first step is to divide the whole time frame of the simulation into M equispaced time steps, $t_1, t_2, ..., t_M$. The term Δt is the length of each time interval, so $\Delta t = t_{i+1} - t_i$. Lets assume that temperature for a given node varies linearly inside each time interval. Then, temperature at time t can be calculated via linear interpolation between the two nearest time steps:

$$T_t = \alpha_t T_{t_{i+1}} + (1 - \alpha_t) T_{t_i} \tag{3.13}$$

Here, α_t is the coefficient that determines the time t in which the temperature wants to be evaluated inside the interval defined by $[t_i, t_{i+1}]$. Time derivatives also need to be approximated for the method to be used in FEM calculations. Following Taylor series, it can be stated that:

$$T_{t_{i+1}} = T_{t_i} + \Delta t \frac{\partial T_{t_i}}{\partial t} + \frac{\Delta t^2}{2} \frac{\partial^2 T_{t_i}}{\partial^2 t} + ... \tag{3.14}$$

Discarding higher order terms, then:

$$\frac{\partial T_{t_i}}{\partial t} \approx \frac{T_{t_{i+1}} - T_{t_i}}{\Delta t} \tag{3.15}$$

From Eq. 3.11, it should be pointed out that matrices $\mathbf{C}$ and $\mathbf{K}$ are assumed to be constant in the simulation, because the geometry and material properties are fixed. Nevertheless, the load vector f is different for each timestep, for example because it depends on the environmental temperature at each timestep. Once again assuming a linear variation within a time interval, the load can be calculated in the following way:

$$f_t = \alpha_t f_{t_{i+1}} + (1 - \alpha_t) f_{t_i} \tag{3.16}$$

Substituting Eqs. 3.13, 3.15, and 3.16 in Eq. 3.11, the following system is obtained:

$$\mathbf{C}\Big\{\frac{T_{t_{i+1}} - T_{t_i}}{\Delta t}\Big\} + \mathbf{K}\big\{\alpha_t T_{t_{i+1}} + (1 - \alpha_t) T_{t_i}\big\} = \big\{\alpha_t f_{t_{i+1}} + (1 - \alpha_t) f_{t_i}\big\} \tag{3.17}$$

Rearranging the above equation, we obtain the system of equations to find $T_{t_{i+1}}$ given T_{t_i} and the load vectors:

$$\big(\mathbf{C} + \alpha_t \Delta t \mathbf{K}\big)\big\{T_{t_{i+1}}\big\} = \big(\mathbf{C} - (1 - \alpha_t)\Delta t \mathbf{K}\big)\big\{T_{t_i}\big\} + \Delta t\big\{\alpha_t f_{t_{i+1}} + (1 - \alpha_t) f_{t_i}\big\} \tag{3.18}$$

Variations in the parameter α_t lead to different transient schemes. Typical values for this constant are $\alpha_t = 0.5$ (Crank-Nicolson method), $\alpha_t = 0.66$ (Galerking method), etc. Selecting any value different than zero leads to an implicit scheme, which forces to know vectors f_{t_i} and $f_{t_{i+1}}$ for computing temperature $T_{t_{i+1}}$. In some problems, particularly in non-linear calculations, an implicit scheme forces the use of iterative methods to find $f_{t_{i+1}}$. Otherwise, using $\alpha_t = 0$ determines a fully

explicit scheme, usually called *forward difference* or *forward Euler* method.

3.2 Radiation methods

Studying radiation using analytical methods becomes impractical under complex geometries, because it is very difficult to address the inter-element visibility and the occlusions, even for simple element primitives. Other sophisticated phenomena such as directionally dependent properties, light polarization, participating media and subsurface scattering further complicates the matter. For these reasons, radiation numerical solutions have been subject of study for several fields [Dutre et al., 2006; Howell et al., 2015]. Radiation physics have relied on computational methods since the first computers appeared, being the first area to design radiation algorithms. In the 60's and 70's decades, the simulation of heat transfer in spaceships and satellites promoted the development of radiation computations for both visible and thermal radiation. In the 80's and 90', the computer graphics community addressed the adaptation of previously designed algorithms for photorealistic rendering. The movie animation industry took benefit of these advances in the next decades. On a more recent trend, daylighting engineers have used physically-based radiation models for the analysis of natural lighting and its interaction with architectural scenes, leading to the study of the properties of materials at the visible spectrum.

In this thesis, the radiation methods are categorized into short-wave and long-wave. The former category has been mostly influenced by the developments in light rendering, while the latter is related to thermal physics. Both categories imply considering different design details, mostly related to the study of different radiation wavelengths.

3.2.1 Short-wave simulation

The behavior of light transport in a scene can be described using the so-called *rendering equation*, presented by Kajiya in 1986 [Kajiya, 1986], which has been used by the computer graphics community as the basis for many algorithms. One of the many forms of this equation is the following:

$$L^{out}(x,\vec{\omega}_{out}) = M(x,\vec{\omega}_{out}) + \int_{\Omega} \rho(x,\vec{\omega}_{out},\vec{\omega}_{in}) L^{in}(x,\vec{\omega}_{in})\ cos\theta\ d\vec{\omega}_{in} \tag{3.19}$$

where:

- $L^{out}(x,\vec{\omega}_{out})$ is the total radiance in point x going in the camera direction $\vec{\omega}_{out}$.
- $M(x,\vec{\omega})$ is the total emittance in point x, in direction $\vec{\omega}_{out}$.
- $\int_{\Omega}$ is the integral over the entire hemispherical directions Ω.
- $\rho(x,\vec{\omega}_{out},\vec{\omega}_{in})$ is the bidirectional reflectance distribution function in x, which is the fraction of light incident from direction $\vec{\omega}_{in}$ that is reflected in direction $\vec{\omega}_{out}$.
- $L^{in}(x,\vec{\omega}_{in})$ is the total radiance reaching x from direction $\vec{\omega}_{in}$.
- θ is the angle between the normal vector in x and the incident vector $\vec{\omega}_{in}$.

Starting from a 3D scene, a description of the illumination conditions, and the position of the camera, the previous equation is solved for each pixel of the synthetic image. The total incoming radiance L^{out} is calculated for each pixel based on a different set of values for x and $\vec{\omega}_{out}$. If three

different calculations are performed, separating radiance into three wavelength bands (red, green, and blue), a colored image is obtained.

The rendering equation allows to describe light transport using an integral formulation that considers material properties and visibility, enabling a very precise description of the objects. This formulation has a recursive nature, because the calculation of the outgoing radiance from a point requires evaluating the incoming radiation at that point, which is at the same time outgoing radiance from the directly visible points. Hence, solving the equation numerically implies using recursive algorithms, in which the number of recursive steps is directly related with the number of light bounces. The numerical approaches developed for this purpose are categorized considering the integration method used [Sillion et al., 1994]. Integration by Monte Carlo and quadrature rules led to *ray tracing*, while expressing the problem with a finite element formulation led to *radiosity*.

Ray tracing

The basic idea of the ray tracing algorithm is that light travels in straight lines, where its energy is stored in packets called photons. A ray is a geometrical primitive defined by an origin point and a direction vector. Tracing a ray implies finding its closest intersection with the scene. Hence, the idea of ray tracing methods is to follow the paths of photons in order to simulate the behavior of light and its interaction with the geometry.

In its most basic form, a ray tracing algorithm consists in tracing multiple rays from the light source, follow their paths with multiple reflections until reaching the camera lens. This approach is naive from a computational perspective, because one is forced to trace a large number of rays that do not reach the lens and end up not having an effect in the results. For this reason, a typical solution is to use what is called a *backward* ray tracing approach, where the rays are casted from the camera instead of the light source. For example, *Whitted ray tracing* [Whitted, 1979] is a ray-based algorithm in which, after finding the intersection of each primary ray with the scene, shadow rays are traced from the intersected point to the light sources, in order to determine if the area is in shadow. If not in shadow, the local ambient, diffuse, and specular illumination components are computed for each pixel, and other rays are recursively casted symmetrically to simulate reflections. The final color is composed of the local illumination and the reflections. Alternatively, refracted rays can be added to the algorithm in a very similar way. This algorithm is illustrated in Figure 3.4.

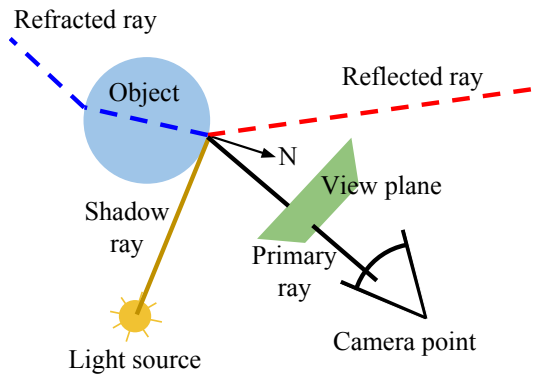

Figure 3.4: Main components of the Whitted ray tracing algorithm.

A more complex approach is the *Monte Carlo path tracing* algorithm [Lafortune, 1996], which uses a Monte Carlo method to solve the integral in Eq. 3.19. Instead of tracing one ray for each pixel, several rays are casted, each one following a different path. The color of the pixel is the average of the colors retrieved by the traced paths. Both stochastic and stratified distributions can be used to sample the domain of the integral. Probability density functions are used to sample the BRDFs. This algorithm is much more complex than the previous one, but it allows to model a vast amount of material behaviors such as diffuse materials, caustics, area light sources, and color bleeding. The computational performance is affected by the number of traced rays, which can easily scale to thousands of rays per pixel to obtain accurate results, especially in the presence of multiple diffuse surfaces.

Bi-directional strategies have been proposed for rendering with ray tracing, where rays are traced from both the light sources and the camera. *Bi-directional path tracing*, *Metropolis light transport* [Veach and Guibas, 1997] and *Photon mapping* [Jensen, 2001] are examples of these kinds of methods. These algorithms follow a shooting and gathering approach, where light is shot from the sources, interacts with the scene, and is then gathered by the camera process to render the image.

In the last years, ray tracing libraries have been developed by hardware manufacturers, looking to offer easier development environments and good computational performance by exploiting parallelism. NVIDIA OptiX [Parker et al., 2010] and Intel Embree [Wald et al., 2014] are the most successful ones, each one offering its own set of advantages. As of 2019, NVIDIA has shipped its first GPU architecture including RTX co-processors [Wald et al., 2019], which is a dedicated piece of hardware specially designed for solving ray tracing primitives.

Radiosity

The radiosity method [Goral et al., 1984a] is a global illumination technique based on the use of a set of finite elements and designed for scenes composed of purely diffuse surfaces. The term "radiosity" stands for the total radiative flux (emitted and reflected) leaving a surface per unit area (W/m^2).

The assumption of Lambertian surfaces simplify the BRDF term in the rendering equation, which is transformed into the "radiosity equation" (Eq. 3.20).

$$J(x) = E(x) + \rho(x) \int_{\Omega} J(x')G(x,x')dA' \tag{3.20}$$

where $J(x)$ and $E(x)$ are the radiosity and emission values at point x, $\rho(x)$ is the reflectivity coefficient of the material, and $G(x,x')$ is a geometric factor that relates the visibility between two points x and x'.

The continuous radiosity equation can be transformed into a sum of values by discretizing the geometry of the scene into a finite set of elements called patches. This formulation allows expressing the problem with the following set of linear equations:

$$J_i = E_i + R_i \sum_{j=1\ldots n} J_j \mathbf{F}(i,j) \quad , \quad \forall i \in \{1 \ldots n\}$$

This set of linear equations is expressed algebraically in Equation 3.21 (known as the Discrete Radiosity Equation).

$$(\mathbf{I} - \mathbf{RF})J = E, \tag{3.21}$$

where $\mathbf{I}$ is the identity matrix, $\mathbf{R}$ is a diagonal matrix containing the reflectivity index of each patch, J is the unknown radiosity vector, and E is the emission vector. $\mathbf{F}(i,j)$ is a number between 0 and 1 expressing the view factor between patch i and j (see Sec. 2.5.5). This value indicates the fraction of the light power going from i to j. The form factor matrix is a $n \times n$ matrix, where n is the number of patches in the scene.

View factors calculation The calculation of view factors was originally of interest for heat transfer studies, where analytical solutions were obtained before the use of computers. In fact, the radiosity algorithm was used in thermal studies several decades before computer graphics started using it for rendering. In the context of FEM, radiosity is still the main algorithm for solving thermal radiation exchange in 3D geometries [COMSOL Inc., 2018; Stolarski et al., 2018].

Computing view factors is relatively complex due to the presence of a double integral (Eq. 2.44), and because the visibility between each patch needs to be calculated. The process is memory demanding because the number of view factors to process is n^2. The most used techniques are based on sampling the hemisphere around the source point. For example, one way of solving the integral is using Monte Carlo to sample the hemisphere, retrieving the intersections of every ray. Another approach is to project the scene surfaces into planes instead of a hemisphere, which ensures the same view factor value, but is lighter to compute using specialized rasterization hardware.

Cohen and Greenberg [1985] proposed the hemi-cube algorithm to compute the view factors. This method uses the Z-buffer algorithm as a simple solution to the visibility problem. Each patch is projected into the hemicube, and if more than one of them is to be drawn at the same region, only the nearest is kept and the depth is updated for that pixel. The memory array used to store this information is called the depth buffer.

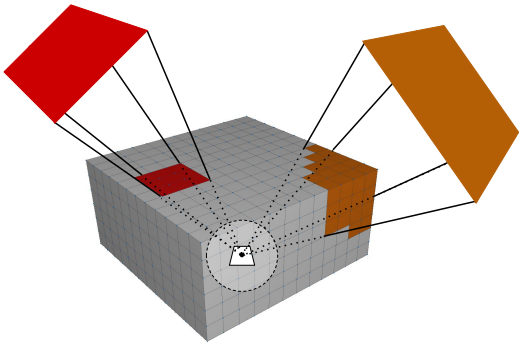

Figure 3.5: Hemicube algorithm.

The hemi-cube algorithm computes the view factors between patch i and the rest of the elements of the scene (the i-th row of $\mathbf{F}$). This is accomplished by rendering five projections of every patch onto the five surfaces of a half cube (see Figure 3.5), using the Z-buffer technique. At the end of the process, each pixel of the hemi-cube contains the information of visible patches. In particular, the color of each pixel denotes the corresponding rendered patch. The final view factor $\mathbf{F}(i,j)$ is equal to the proportion of pixels covered by polygon j in the hemi-cube centered at patch i.

Another approach used to compute view factors is based on Monte-Carlo integration. Ray casting is a suitable tool for geometric solution of the double integral [Cohen and Wallace, 1993]. The idea

is to cast rays instead of rendering the hemicube. Moreover, rays can be casted from any point of the patch instead of only from the barycenter, which can increase the precision of the method. Given two patches i and j, k pair of points $[x_i, x_j]$ are randomly selected, where x_i belongs to patch i and x_j to patch j. The form factor is calculated by evaluating the visibility of the geometrical term with k rays, and also considering the distance between the points and the angle between the ray and the normal vectors. Each ray is traced between the pair $[x_i, x_j]$, and the intersection with the scene is computed. This method becomes more accurate as k grows, but this also means a performance decay. The advent of modern GPUs that implement ray-primitive intersections by hardware [Wald et al., 2019] can be a good alternative to improve the efficiency of this method.

In its most simple form, $\mathbf{F}$ is stands for a purely diffuse behavior of materials. The inclusion of a wider variety of lighting effects implies computing "extended form factors" which are useful for simulating phenomena such as specular reflections and refractions [Sillion and Puech, 1989]. The specular part of the calculation is better suited for a recursive ray-based approach, allowing multi-bounces and arbitrary glossy BRDFs.

Solving the linear system After computing $\mathbf{F}$, there are several strategies used to solve the radiosity linear system, which can be classified into direct and iterative methods. Direct methods focus on finding the inverse of the radiosity matrix: $\mathbf{M} = (\mathbf{I} - \mathbf{RF})^{-1}$, which represents a global transport operator relating the emitted light with the final radiosity of the scene, $J = \mathbf{M}E$. Recently, factorization strategies have been applied to the computation of the inverse, which have led to reduce the memory requirements of radiosity for scenes with big spatial coherence (meaning low numerical rank factorizations) [Fernández and Besuievsky, 2012].

Another approach is to compute J by solving the linear system of equations iteratively, using methods such as Jacobi or Gauss-Seidel ([Cohen and Wallace, 1993]). Eq. 3.22 presents the radiosity iterative resolution. Each iteration adds the radiosity of a new light bounce to the global radiosity result. This iteration is repeated until $\|J^{(i+1)} - J^{(i)}\|$ is less than a given threshold.

$$J^{(i+1)} = \mathbf{RF}J^{(i)} + E \ , \ \text{where } J^{(0)} = E \tag{3.22}$$

The convergence of the iterative methods is ensured because the radiosity matrix $(\mathbf{I} - \mathbf{RF})$ is diagonally dominant [Cohen and Wallace, 1993].

Radiosity or ray tracing? This question has been subject of many discussions. Radiosity was the first algorithm to be adapted for rendering, and its influence in the computer graphics community was very large. This fact can be seen for example in one of the founding articles of the global illumination field [Kajiya, 1986], where the rendering equation is defined and radiosity is the first algorithm described for solving it. The arrival of ray tracing allowed for the simulation of other material properties besides diffuse reflections, and this fact was fundamental for the subsequent development of a wide variety of ray-based approaches to solve the rendering problem.

In the current years, radiosity has lost its original attention, and ray tracing has gained all the focus of the computer graphics community. Nevertheless, in other fields such as finite element analysis, radiosity is still being used, because its adaptation to meshed geometries is natural. Radiosity

has been extended for treating other material properties [Sillion and Puech, 1989], but this alternative is useful for only a small number of non-diffuse surfaces.

The answer to the question "radiostiy or ray tracing?" is usually simplified by only looking at the problem formulation and the material properties. If the geometry is not static, i.e. it changes as a function of time, then radiosity is not well-suited, because it implies a recalculation of the view factors matrix at each timestep. On the other hand, if the geometry does not change, and if diffuse materials dominate the problem, then radiosity looks like the correct solution. The reality shows that even in those scenarios, ray tracing is selected.

For problems with a static geometry, a first diffuse bounce of light is computed in similar ways by both ray tracing and radiosity: sampling the hemisphere with rays or pixels and retrieving the information of the directly seen surfaces. This is again an advantage for ray tracing. Nevertheless, when multiple bounces of diffuse light have to be accounted with a certain level of precision, then ray tracing starts to be prohibitively slow, because a large number of rays must be casted to sample the second and successive bounces with high accuracy. By construction, the view factors matrix contains all the information for a first diffuse bounce, and successive matrix multiplications allow for modeling multiple bounces with great precision and fewer computational requirements.

In conclusion, the very special case of static geometries and multiple diffuse bounces seems better suited for radiosity, while other problems are more solvable with ray tracing. The urban radiation exchange problem is typically characterized by the first conditions, and therefore seems more suitable for radiosity, especially if multiple light bounces are important.

3.2.2 Daylighting

Daylighting methods have been developed for simulating the interaction of daylight in interior building and exterior urban spaces [Reinhart and Herkel, 2000]. During daytime hours, the sky is the only emitter of short-wave radiation, which allows assuming that the scene geometry is only a reflector of light coming from the sky. An accurate treatment of the sky emission is addressed by daylighting methods, which can be used for both illumination availability calculation and for the computation of short-wave loads [Beckers and Beckers, 2014].

The previously described global illumination algorithms are suitable for daylighting calculations. Some adaptations have been developed to consider the particular details of natural light [Mardaljevic, 2000]. On the one hand, the sky must be discretized into a set of tiles with uniform luminance in order to obtain a sky mesh that simplifies the computation of the diffuse part of the emission. The direct component (i.e. the sun) can be integrated into this discretization if the tiles are sufficiently small. Otherwise, the direct and diffuse components are treated separately. On the other hand, a anisotropic sky model must be used to predict the luminance of each sky tile from a set of input data, which are typically the global and direct horizontal luminances. An analogous approach can be used for short-wave radiances.

Sky discretization Tregenza [1987] proposed a partition of the hemisphere into 145 tiles by defining 8 bands (rings) parallel to the horizon. Each band is divided into a different number of cells. The cells are selected based on circles of the same size that cover the vault without overlapping. The solid angle covered by the resulting cells varies, as well as the width-height ratios. An accurate

treatment of the direct component is not possible with this coarse division. Hence, Reinhart [2000] proposed to extend this model by dividing each cell into 16 subpatches, except at the zenith. The resulting discretization is composed of 2305 tiles, and has proven to be accurate enough for including the solar component into daylighting studies [Bourgeois et al., 2008; Reinhart, 2014].

Beckers and Beckers [2014] presented a method that allows for a manual determination of the number of cells in the sky partition. The main idea of this partition is to generate homogeneously shaped cells by looking at the size of its greatest possible inscribed circular cap. The strategy of maximizing the ratio of cap area over cell area is used to obtain the sky discretization. The ability to determine the exact number of sky cells used is the main advantage provided by this method.

The three described sky discretization techniques are shown in Figure 3.6, using equidistant projections for a better analysis of the results. Subfigures (a) and (b) present similar results, but it can be observed that (c) provides a more regular scheme, especially in the zenith cells, where (b) produces several small elements.

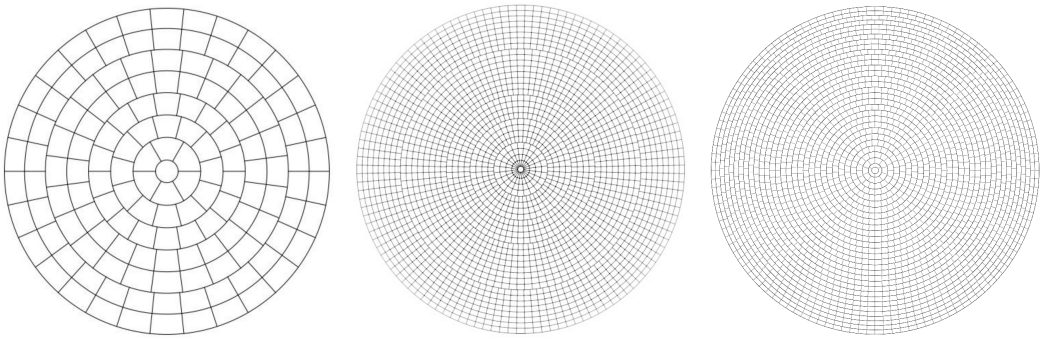

(a) Tregenza, 145 cells (b) Reinhart, 2305 cells (c) Beckers, 2305 cells

Figure 3.6: Equidistant projections of different sky discretization.

All-Weather sky model Several anisotropic sky models are available in the literature, which can consider different kinds of meteorological conditions [Freitas et al., 2015]. In the 90's decade, Richard Perez and his team presented several models to predict solar energy and daylighting from a set of inputs. These models are widely used by the daylighting community. They are based on conversion and radiance distribution algorithms, operating with a similar structure. Least-square approximations were used over experimental data to adjust the involved coefficients in function of insolation conditions.

The All-Weather Model developed by Pérez et al. [1993] is a sky model that predicts the luminance in any point of the sky. The model takes several inputs, wherein the two most important are the diffuse and direct irradiances. The problem of predicting luminance from only two irradiance values (i.e. two real numbers) is a complex problem, because there are several factors that affect the calculations. Computing the position of the sun is relatively simple, but it only addresses part of the information to consider. Complex phenomena such as the sky conditions in terms of clouds must be considered in the calculations. In this way, overcast or clear conditions are accurately managed by several models [Hay and Davies, 1980; Hottel and Woertz, 1942], but considering partly cloudy skies is much more difficult.

Pérez et al. [1993] proposed a mathematical model that uses five adjustable coefficients (a, b, c, d, and e) to handle insolation conditions, in order to estimate the atmospheric influence. These coefficients were adjusted using non-linear least-squares over a large set of experimental data, resulting in a set of tables that relate the sky clearness and brightness with the coefficients. This approach leads to a high accuracy in the model, which has become a state-of-the-art technique for computing accurate sky luminance [Igawa et al., 2004; Mardaljevic, 2000].

The inputs of the model are the horizontal diffuse irradiance E_{ed}, the normal incident direct irradiance E_{es}, time of day, time of year, location, and the zenith angle of the point in the sky to be estimated ζ. E_{ed} and E_{es} are usually experimental data. ζ depends on the geographical place where the luminance is to be predicted and can be deduced via solar geometry. The experimental data must be associated to the same day, time and zone. Figure 3.7 shows other angles that are important in the model: Z is the solar zenith angle, and γ the angle between the sky point and the sun.

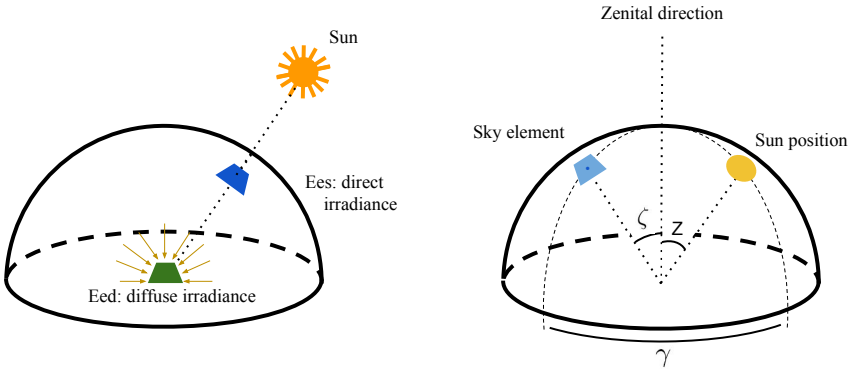

(a) Direct and diffuse irradiance values measured experimentally.

(b) Three angles that play an important role in the model.

Figure 3.7: Components of the sky luminance model.

The first step is to parameterize the insolation conditions from the input data. These conditions are described as a 3D space, taking into account solar zenith angle Z, sky brightness Δ, and clearness ϵ. Eqs. 3.23 and 3.24 describe these two parameters, where E_{es}^0 is the normal extraterrestrial irradiance (usually approximated to 1367 W/m^2), and m the optical mass air (which depends on solar altitude). Sky clearness describes the turbidity of the sky, while sky brightness measures the thickness of clouds:

$$\epsilon = \frac{(E_{ed} + E_{es})/E_{ed} + 1.041Z^3}{1 + 1.041Z^3} \tag{3.23}$$

$$\Delta = mE_{ed}/E_{es}^0 \tag{3.24}$$

In the second step, these three parameters are used to determine five adjustable coefficients using a set of predefined tables that can be found in the original paper [Perez et al., 1993]. Each of the adjustable coefficients has its own meaning in the sky luminance calculation, and are named with characters from a to e. The coefficients are used within a mathematical expression (Eq. 3.25) that

outputs the relative luminance l_v. This value represents the luminance of the sky cell relative to an arbitrary reference sky cell.

$$l_v = [1 + a\ exp(b/cos\,\zeta)] \times [1 + c\ exp(d\gamma) + e\ cos^2\gamma] \tag{3.25}$$

The absolute luminance L_v, output of the model, can be obtained with a normalization of the modeled sky to diffuse illuminance E_{vd} (Eq. 3.26, where ω is the solid angle differential element measured in steradian). This value is measured experimentally or modeled from irradiance Eed [Perez et al., 1990].

$$L_v = \frac{l_v\ E_{vd}}{\int_{2\pi} l_v(\zeta,\gamma) cos\ \zeta d\omega} \tag{3.26}$$

A very similar approach can be used to obtain radiances instead of luminances. The former is needed for computing short-wave fluxes, while the latter is used in daylighting computations.

Computing light exchange After the sky dome is subdivided into cells, and the emission value for each cell is estimated, global illumination algorithms are used to compute the illuminance or irradiance coming to a point of interest (usually called sensor) in a 3D scene, considering radiation bounces and many other phenomena. The most used code to perform this operation is RADIANCE [Ward, 1994], which is a set of ray-based programs to compute interior daylighting. Exterior city models can be used as occluders and reflectors of light.

The Daylight Coefficient (DC) approach, originally proposed by Tregenza [Tregenza and Waters, 1983], allows computing irradiance in a set of sensors using backward ray tracing. The matrix of DC is a $s \times m$ matrix, with s the number of sensors and m the number of sky cells. To compute each of the entries of the matrix, rays are casted from the sensors, following a limited number of bounces until reaching the sky. The contribution of all the rays coming from sensor s_i that reach cell m_j are summed to obtain the total contribution of the cell into the sensor's irradiance, which is stored in the entry (i, j) of the matrix.

In the case of specular materials, the direction of reflected rays is easy to obtain. For diffuse materials, a random direction is selected, which forces to use a big number of samples to obtain accurate solutions when multiple diffuse materials are present. The computational performance of the DC calculation depends linearly on the number of sensors, and on the number of traced rays. The confidence intervals of the solution are proportional to the inverse of the square root of the number of rays [Tregenza and Waters, 1983]. Irradiance caching [Jones and Reinhart, 2014; Ward et al., 1988] can be used to speed up DC calculation. After the precomputation of DCs, thousands of sky conditions are evaluated in short times using matrix operations.

Three-phase and Five-phase methods [Geisler-Moroder et al., 2017; McNeil and Lee, 2013] follow a similar approach for simulating complex fenestration systems. The first phase computes the contribution of the exterior (sky and urban context) into the fenestration. Recently, such simulations have been accelerated through GPU techniques [Jones, 2017; Overby et al., 2016].

Radiosity has also been used for light exchange computation. LICASO [Lighting Analysts,

2019] is a climate-based annual daylight simulation software entirely built on radiosity, which provides the calculation of annual daylight metrics. Ashdown et al. [Ashdown et al., 2017] compared LICASO with RADIANCE-based software DAYSIM and claim that three orders of magnitude speedups can be reached under low relative errors in the computation of such metrics.

3.2.3 Long-wave simulation

Long-wave radiation simulation is not as widely studied as its short-wave counterpart. The emission of long-wave radiation depends on the temperatures of the surface involved in the calculation. At the same time, the temperature of the surfaces also depends on the incoming long-wave radiation. These two facts imply a self-dependence in the calculation of surface temperature. Moreover, alternative methodologies must be used to solve the non-linear system of equations, which complicates the computations [Coulon, 2006].

Usually, long-wave methods are embedded in thermal calculation systems, playing the role of boundary condition in the conduction problem. The previous issues are tackled by linearizing the flux and using last timestep temperatures to compute the current timestep radiation, treating it as an imposed flux [EnergyPlus, 2012]. This approach does not ensure flux equilibrium because the temperatures can differ greatly between the previous and current timesteps. Figure 3.8 shows the average relative error in long-wave fluxes generated by using the timestep lag strategy, as presented by [Evins et al., 2014]. Large errors were observed for timesteps bigger than 30 minutes. Using short timesteps helps reducing radiative flux differences but implies an increment in the computational costs.

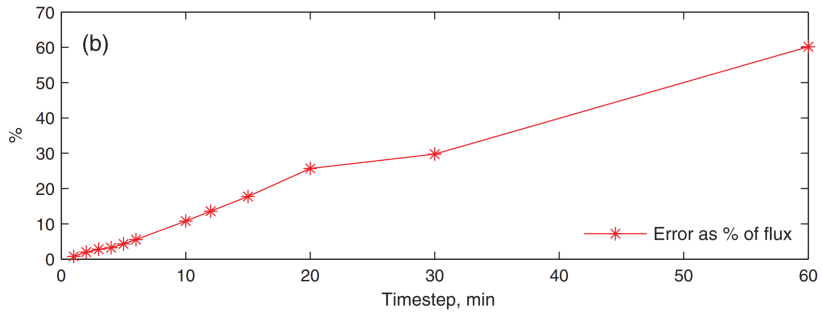

Figure 3.8: Average relative error in long-wave fluxes due to timestep lag. Extracted from [Evins et al., 2014].

A major difference between short and long wave radiation at urban environments is that infrared radiation is emitted by every surface in the city, which brings the question of how to model multiple emitters and their energy exchange. In this context, radiosity seems to fit into the requirements, because the view factors matrix allows multiple emitters in a natural way.

The long-wave problem at urban scale is characterized by a big temperature difference between the urban surfaces and the sky, which presents much colder temperatures. This fact implies defining two matters: the sky temperature model and the radiative exchange method.

Long-wave sky models

The impact of the atmospheric radiation on the surface of the city is significant [Nunez and Oke, 1976]. Typically, the long-wave balance in the ceiling of a building is negative, which means that it emits more radiation than it absorbs. This process is known as sky cooling process, which is especially considerable at night. The urban outdoor thermal comfort is also affected by this fact [Lindberg et al., 2008].

The atmosphere may be assimilated to a blackbody at a varying sky temperature T_{sky}. Another approach is considering it as a gray body at the air temperature T_a, with an emissivity ε_{sky} that depicts its ability to absorb and emit long-wave radiation. These formulations are expressed as:

$$\phi_{sky} = \sigma T_{sky}^4 = \varepsilon_{sky} \sigma T_a^4 \tag{3.27}$$

Ångström [1915] was the first to present a model for the estimation of the atmospheric radiation on a horizontal plane as a function of the air temperature, the water vapor pressure V_p (hPa) and the cloud coverage CC (oktas):

$$\phi_{sky} = 0.82 - 0.25 \times 10^{0.0945 V_p} \Big(1 + 0.21 \frac{CC}{8}^{2.5}\Big) \sigma T_a^4 \tag{3.28}$$

As in short-wave radiation, the long-wave radiation distribution is anisotropic, which means that the sky temperature varies with the zenith angle. For instance, under clear sky conditions the zenith is at colder temperatures than the horizon. Therefore, anisotropic models have been developed, which are important to urban studies because the occlusion of the city implies that sometimes only parts of the sky are seen from a given point.

Bliss [1961] presented a model for the variation of the sky emissivity with the zenith angle θ, which is described by the following formula:

$$\varepsilon_{sky}^{\theta} = 1 - \big(1 - \varepsilon_{sky}\big)^{1/(1.8 cos\theta)} \tag{3.29}$$

where ε_{sky} is the global sky emissivity that can be determined with Ångström formula. Bliss model was constructed for clear sky conditions, which limits its use under other climate conditions.

Martin and Berdhal [1984] proposed another model that shows good results for all other conditions. This model is described by:

$$\varepsilon_{sky}^{\theta} = 1 - \big(1 - \varepsilon_{sky}\big) e^{b(1.7 - 1/cos\theta)} \tag{3.30}$$

where b is a varying parameter. The selection of a proper b value is usually done by integrating the previous equation in the whole hemisphere. By construction, this integration should return the global emissivity ε_{sky}. For each experimental case, the value of b that minimizes the difference between the global emissivity and that estimated from the previous integral, is selected.

Nahon et al. [Nahon et al., 2019] presented a study that tests the accuracy of these two models under different sky conditions. Thermography measurements were performed to obtain an estimated sky temperature, and the results were compared to the modeled temperatures.

The thermal camera measures radiation in the spectral range of 7 to 13 μm, which is part of the atmospheric window (as explained in Sec. 2.5.3). Therefore, the captured apparent temperature of

the sky must be corrected to obtain the real sky temperature. The longwave radiant power reaching the camera is estimated by integrating Planck's law between 4 and 100 μm, using: 1) the thermography temperature inside the atmospheric windows (between 4.5 to 4.8 μm and between 8 to 14 μm) and 2) the air temperature on the remaining spectrum [Kruczek, 2015b]. Figure 3.9 shows some results presented in this work, kindly provided by the main author.

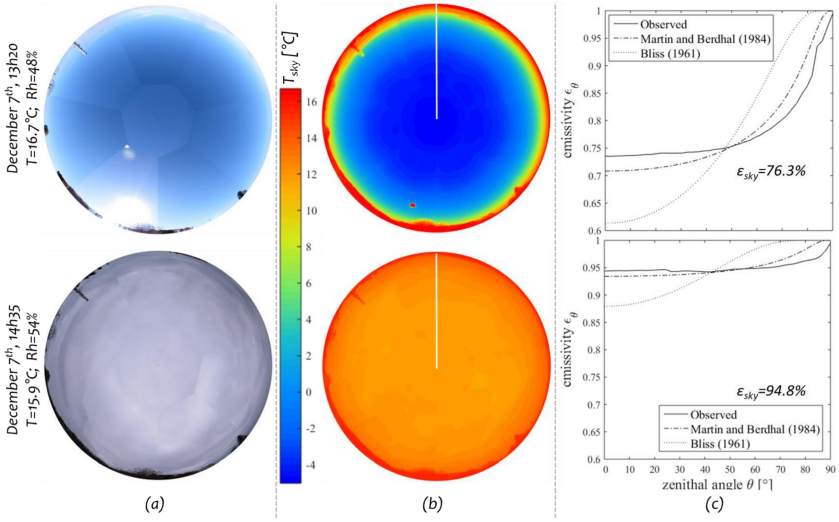

Figure 3.9: Results for clear and dark overcast skies, showing (a) photographs, (b) corrected thermograms, and (c) comparison with modeled sky temperatures. Extracted from [Nahon et al., 2019]

The results show that Martin and Berdhal model correlates particularly well with the observed temperatures at different sky conditions. This kind of study has not yet been extended with the use of larger sets of measured data, such as it has been done in the short-wave counterpart [Freitas et al., 2015].

Long-wave exchange methods

Building energy simulation programs usually solve radiation exchange within the urban environment using Sky View Factor (SVF) based approaches. The SVF is a geometrical metric that indicates the ratio of the radiation received by a planar surface to the radiation emitted by the entire hemisphere [Brown et al., 2001]. Figure 3.10 shows an example of SVF in an urban environment. Because there is a big temperature difference between the sky and the urban surfaces, the SVF can be used to estimate long-wave radiation balances. The sky, as well as the urban context, is assumed to be at a uniform temperature.

EnergyPlus [Crawley et al., 2004] computes the SVF by casting 144 ray samples from each node involved in the calculations. Rays that intersect with the exterior geometry imply an occlusion of the sky. The obtained value is used along with the tilt angle of the surface to calculate the SVF. Then, a linearized heat transfer coefficient [EnergyPlus, 2012] is computed as:

$$h_{sky}^{rad} = \frac{\varepsilon\sigma \mathrm{SVF}(T_{surf}^4 - T_{sky}^4)}{T_{surf} - T_{sky}} \tag{3.31}$$

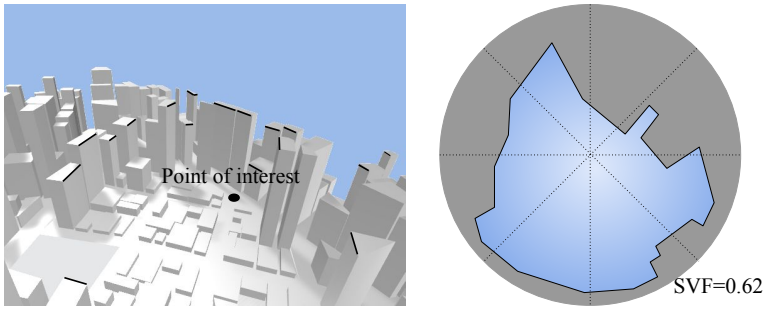

Figure 3.10: Sky View Factor calculation in an urban environment.

This coefficient is used to compute the net radiation flux as:

$$\phi_{lw} = h_{sky}^{rad}(T_{surf} - T_{sky}) + h_{air}^{rad}(T_{surf} - T_{air}) \tag{3.32}$$

where h_{air}^{rad} is the complement of h_{sky}^{rad}, considering the rest of the surfaces (ground and buildings) at the temperature of the air T_{air}. A timestep lag is used in EnergyPlus, where the temperature of last timestep is used to compute h_{sky}^{rad}. Short timesteps must be used to avoid larger errors in the results.

In the SVF approach, the sky and the urban context are assumed to be at uniform temperatures, which brings accuracy problems when anisotropic radiation distributions exist [Miller et al., 2015]. As an alternative to the SVF approach, Robinson and Stone [2005] presented the simplified radiosity algorithm for urban environments. Given a city geometry composed of n patches, and a sky model represented by p elements, the main obstructions between each surface and every sky direction are grouped together. The original system of equations is then reduced to $n \times p$.

A second level of complexity for long-wave exchange simulations consists of accounting for the diffuse exchanges between the elements of the scene. In this context, radiosity becomes the most used technique for computing long-wave radiation in FDM or FEM systems. Integrating a sky model with anisotropic temperature distribution allows for a more accurate characterization of the long-wave radiative balance than with SVF, but it has to be implemented manually, since most of this software are not adapted for urban calculations.

In programs that work with radiosity and a fine discretization of the geometry, the storage of the view factors matrix is highly memory demanding. An efficient alternative is to use a coarser mesh for long-wave exchanges [Péniguel and Rupp, 2004]. In this case, a correspondence between the elements of the fine mesh and those of the coarse mesh must be stated. In each iteration, the temperature of the coarse elements is computed from the correspondent fine elements, and, after the long-wave calculation, the computed flux is distributed.

Greater detail in radiation exchange simulations requires modeling the optical properties of materials, which implies the integration of more complex graphical methods [Modest, 2003]. Van Eekelen [2013] presented a FEM approach to simulate satellite surface temperature considering non-gray surfaces and specular reflections. By using different simulation configurations, the author showed that the thermo-optical properties of the surfaces are an important tool for the thermal control of a satellite. Snyder et al. [1998; 1997] and Li et al. [1999] introduced a variety of Bidirectional Reflectance Distribution Function (BRDF) models for studying land surface temperatures. Wu et al. [2015] proposed a mid-wavelength BRDF and compared it with a thermal image of a set of

buildings.

Integration with FEM

With diffuse-gray assumptions, the flux at a given point in the boundary is then expressed by:

$$q_r = \varepsilon\sigma(T^4 - T_{env}^4) \tag{3.33}$$

where ε_i is the emissivity of the surface varying between 0 and 1, σ is the Stefan-Boltzmann constant, T is the temperature at the boundary point measured in K, and T_{env} is average temperature of the environment. The total emitted radiation from point p is $e_p = \varepsilon_p\sigma T_p^4$. Adding this new flux to the Neumann boundary conditions, we get:

$$\bar{q} + k\frac{\partial T}{\partial n} + h(T - T_a) + \varepsilon\sigma(T^4 - T_{env}^4) = 0$$

Eq. 3.33 can be expressed in terms of two magnitudes: radiosity J, which is the radiant flux leaving (emitted and reflected) the point in the domain, and irradiance E, which is the total radiant flux arriving at the point [Coulon, 2006]. These magnitudes can be calculated in the following way:

$$\begin{aligned} J_i &= \varepsilon\sigma T_i^4 + (1-\varepsilon)E_i \\ E_i &= \sum_{j=1}^{N} F_{ij}J_j \end{aligned} \tag{3.34}$$

where N is the number of elements that that exchange radiosity, and F_{ij} is the view factor between elements i and j. This is a unitless value that expresses the fraction of light power going from i to j. The total radiant heat flux is then reduced to subtract the total income flux from the total outcome flux:

$$q_r = J_i - E_i \tag{3.35}$$

In matrix form, the vector J of radiosities for all nodes is computed solving the linear system of equations in Eq. 3.36, with R and ξ being two diagonal matrix of reflectivity and emissivity values ($R_{ii} = 1 - \varepsilon_i$ and $\xi_{ii} = \varepsilon_i$), and F the square view factors matrix.

$$J = (\mathbf{I} - \mathbf{RF})^{-1}\xi(\sigma T^4) \tag{3.36}$$

where (σT^4) is the vector of the fourth power of temperatures. The vector Q of radiant fluxes is then computed by:

$$Q = (\mathbf{I} - \mathbf{F})(\mathbf{I} - \mathbf{RF})^{-1}\xi(\sigma T^4) \tag{3.37}$$

The algebraic system in Eq. 3.37 is highly non-linear because of the term T^4. In order to solve the radiant flux along with the conduction and convection from the previous section, an iterative scheme is necessary. In the first place, it is worth saying that Eq. 3.37 is expressed for isothermal radiative elements, while the conductivity matrix $\mathbf{K}$ from Eq. 3.11 is expressed for the nodes. It is sufficient to multiply Q by a diagonal matrix of elementary surfaces $\mathbf{S}$ to couple both matrices. In

order to apply this equation to the FEM system of conduction, it is sufficient to express Eq. 3.37 as a system that depends on the vector of temperatures T. For this purpose, note that:

$$\underbrace{\begin{bmatrix} \sigma T_1^4 \\ \sigma T_2^4 \\ \vdots \\ \sigma T_n^4 \end{bmatrix}}_{\sigma T^4} = \underbrace{\begin{bmatrix} \sigma T_1^3 & 0 & 0 & \dots & 0 \\ 0 & \sigma T_2^3 & 0 & \dots & 0 \\ \vdots & \vdots & \vdots & & \vdots \\ 0 & 0 & 0 & \dots & \sigma T_n^3 \end{bmatrix}}_{\sigma \mathbf{T}^3} \underbrace{\begin{bmatrix} T_1 \\ T_2 \\ \vdots \\ T_n \end{bmatrix}}_{T} \tag{3.38}$$

A new matrix of radiant "conduction" is then formed, where the fluxes can be computed by $Q = \mathbf{K}_r(T) \times T$:

$$\mathbf{K}_r(T) = \mathbf{S}(\mathbf{I} - \mathbf{F})(\mathbf{I} - \mathbf{RF})^{-1}\xi(\sigma \mathbf{T}^3) \tag{3.39}$$

The system in Eq. 3.11 is now transformed into:

$$\mathbf{C}\left\{\frac{\partial T}{\partial t}\right\} + (\mathbf{K} + \mathbf{K}_r(T))\{T\} = \{f\} \tag{3.40}$$

The iterative scheme expressed in Eq. 3.41 can be used to solve the non-linear system, where $T^{[k]}$ is the vector of temperatures at iteration k. Beware with the notation: here we are talking about iterations in the solver and not about timesteps in the simulation. In fact, this non-linear system has to be solved for each timestep. The initial temperature $T^{[0]}$ can be initialized with last timestep temperature.

$$\mathbf{C}\left\{\frac{\partial T}{\partial t}\right\} + (\mathbf{K} + \mathbf{K}_r(T^{[k]}))\{T^{[k+1]}\} = \{f\} \tag{3.41}$$

The previous approach can have significant computational costs depending on the model to simulate. The matrix $\mathbf{K}$ was a very sparse matrix, and now $(\mathbf{K} + \mathbf{K}_r)$ may be full. Also, performing the inversion of matrix $(\mathbf{I} - \mathbf{RF})$ can be prohibitively expensive.

De-coupling the radiosity system Another approach that can be taken to include radiative exchanges in the model is to treat radiation in the same way as convection, but recalculating the h coefficient at each timestep [De Veubeke and Hugge, 1972; Péniguel and Rupp, 2004]. Each iteration of the new solver follows these steps:

1. Solve the radiosity linear system independently:

$$(\mathbf{I} - \mathbf{RF})J^{[k]} = \varepsilon\sigma(T^{[k]})^4$$

2. Calculate the irradiance for all elements:

$$E_i^{[k]} = \sum_{j=1}^{N} F_{ij} J_j^{[k]}$$

3. Now, computing the mean environmental temperature (see Eq. 3.33) is possible:

$$T_{env}^{[k]} = (1/\sigma E^{[k]})^{1/4}$$

4. The radiant flux, expressed in Eq 3.33 is now linearized and treated as a convection flux:

$$\begin{aligned} q_r &= h^{[k+1]}\Big(T^{[k+1]} - T_{env}^{[k]}\Big) \\ \text{with } h^{[k+1]} &= \varepsilon\sigma\Big((T^{[k]})^2 + (T_{env}^{[k]})^2\Big)\Big(T^{[k]} + T_{env}^{[k]}\Big) \end{aligned} \tag{3.42}$$

The resulting h coefficients are used in the FEM process in the same way as convective flux to compute $T^{[k+1]}$. This process can be seen as less coupled than the first method described, because the radiosity system is solved independently, and then the results can be adapted to the solver without introducing new full matrices. Moreover, the inverse of the radiosity matrix is not necessary, since the radiosity system can be solved iteratively.

3.3 Complete heat transfer computational model

The idea of this section is to present the computational model developed in this thesis for analyzing urban heat transfer. The development of this model has been incremental and modular, as it is observed in the next chapters. The results of executing the model in a simplified test geometry is shown, and some partial results are analyzed. The next chapters provide more details about implementation and a deeper experimental analysis of the methodology, but this introduction serves as a basis for the reader to follow the incremental development of the model in the same way as it was performed. All the simulations shown in this section were executed on a standard desktop PC (Intel core i7 processor, NVIDIA GTX 1070, and 16GB of RAM memory).

3.3.1 Short-wave radiation module

The first implemented module was the radiosity engine, using C++/OpenGL for view factors calculations, and MATLAB for matrix operations. This module allowed for the computation of diffuse lighting and radiation exchange. It was adapted to daylighting computations using a discretized sky dome and input global irradiance data. Chapter 4 shows the performance of this module under large city geometries.

Two variables were adjusted in the development of this module: the number of sky cells used and the number of light reflections. To show some intermediate results of these adjustments, a simplified geometry that represents an urban canyon is used, composed of four boxes, one for each street block (Figure 3.11). The geometry is meshed using patches of size 1.5m x 1.5m, as described in Chapter 6, with a total of 28395 elements.

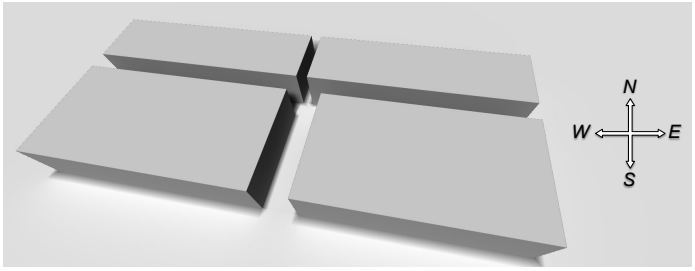

Figure 3.11: Geometry representing an urban canyon.

Chapter 4 shows that there is a strong correlation between the geometrical characteristics of a city and the density of its view factors matrix. The high occlusion factor in the inter-elements visibility of a city enables the reduction of the memory requirements by using sparse matrix representations. Without sparse matrices, the maximum number of elements that fits into the 16GB of memory available in the desktop PC used is reduced to $\approx 45k$ elements. With sparse matrices, this limit can be extended to hundreds of thousands, depending on the geometrical shape of the model. Meshing the model presented in Figure 3.11 with an element size of 1.5m x 1.5m leads to a view factors matrix that requires around 6GB of memory using full matrix representations. Using sparse format, the same matrix requires only 1GB with sparse format. This change also allows for a significant reduction in the total execution time.

The selected boundary conditions correspond to a spring day (April 23^{rd}, 2017) in the city of Bayonne, France. A day with clear sky is selected. Figure 3.12 presents the global horizontal irradiance, showing a smooth behavior related with the high sky clearness. The direct normal and diffuse horizontal irradiances are calculated using the clear sky model described by Liu and Jordan [1960]. This data serves as input to the All-Weather sky model by Perez [1993], to estimate the anisotropic distribution of sky radiances.

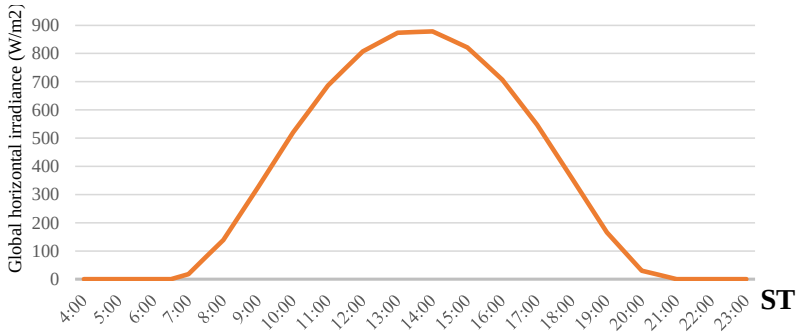

Figure 3.12: Global horizontal irradiance.

After the anisotropic emission of the sky is estimated, the next step is to compute the short-wave exchange between the surfaces. The geometry is assumed to be composed of totally diffuse materials, allowing to use the standard radiosity algorithm. Three kinds of reflection coefficients are considered in this study: 0.54 for walls, 0.33 for roofs, and 0.41 for the street.

The first study to address is the effect of using different number of sky tiles on the short-wave results. For this purpose, the radiosity for each patch is computed using a very large number of light bounces, to avoid errors associated with this variable. The sky is discretized with Beckers and Beckers [2014] partition, and the results for different number of tiles are analyzed, particularly using 145, 500, 2400, and 5000 tiles. The computed short-wave loads for three points inside the canyon are studied (Figure 3.13). N stands for north-facing point, S for south-facing, and G for ground point. Figure 3.14 presents the solar trajectories for the three points selected. The south-facing point receives much more direct sunlight than the other points throughout the day that is analyzed.

Figure 3.15 shows the calculated absorbed radiation for the selected points, using different number of sky tiles. The results show very similar profiles for 2400 and 5000 sky tiles, specially at the south-facing and ground points. The north-facing point receives less light, with a larger reflected portion. This fact reduces the error of using a smaller number of sky tiles, as can be observed in

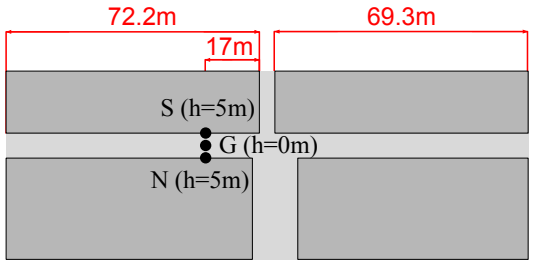

Figure 3.13: Location of three points selected to analyze short-wave loads.

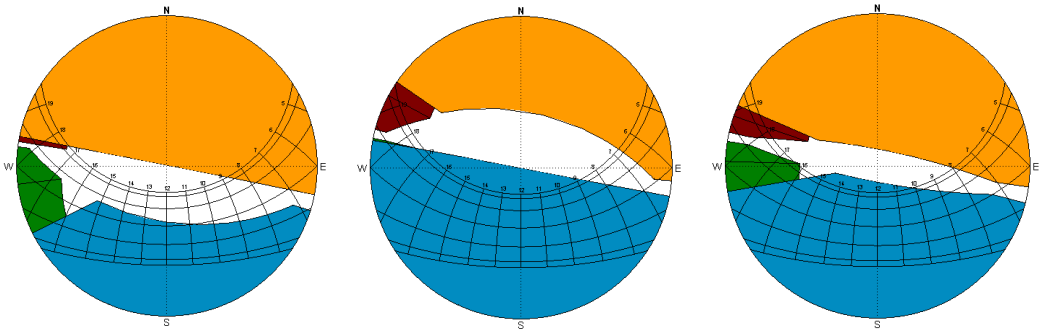

(a) Point S (b) Point N (c) Point G

Figure 3.14: Solar trajectories for the three points selected, in Bayonne, France. Generated with Heliodon2 [Beckers and Masset, 2006]. Each block of buildings is represented with a different color.

the plots. Using 145 or 500 tiles implies larger errors, mainly because of the error generated in the representation of the Sun's direct component. For example, in the plot of the south-facing point with 145 sky tiles, a big noise is produced in the computed absorbed radiation because the direct component is represented by a large sky patch.

The second study corresponds to analyzing the impact of diffuse radiation bounces in the short-wave loads. The same three points than above are selected, and the loads are computed using 2400 sky tiles, and considering four cases: only direct radiation, one bounce, two bounces and third and successive bounces. The results are presented in Figure 3.16. When the sunlight strikes directly (e.g. at the south point around noon), the direct component represents around 80% of the absorbed radiation. On the other hand, at the north-facing point, the first and second bounces provides around 65% of the total. For all the cases, the third and successive bounces represent around 25% of the absorbed radiation. This fact justifies considering them in the calculations, even considering that the test case does not present a highly occluded environment.

Chapter 5 adds two important contributions to this model. On the one hand, specular material properties are considered using extended form factors. On the other hand, the results of the module are validated with RADIANCE. The work developed in Chapter 5 introduced the use of importance to reduce radiation computations in the context of large city models. This proposal is not used in the next chapter because smaller urban geometries were used, focusing on the street scale.

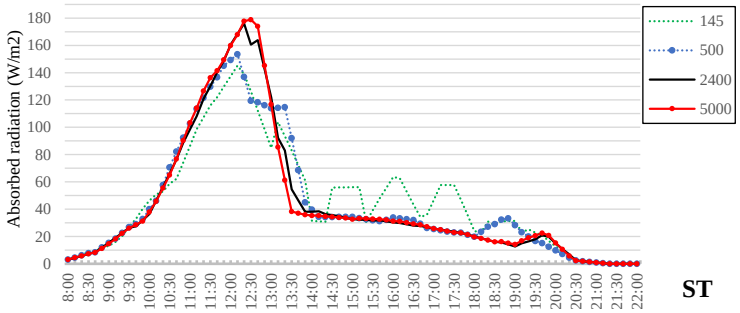

(a) Point S

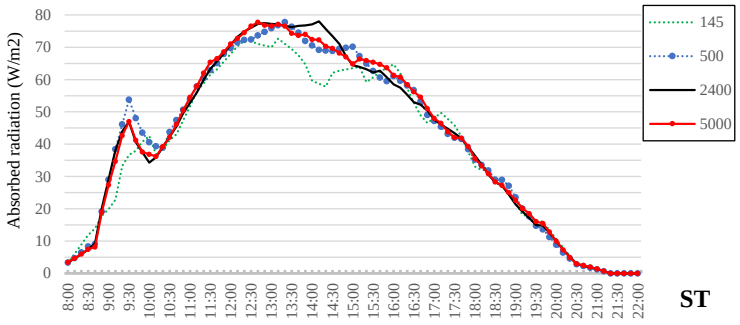

(b) Point N

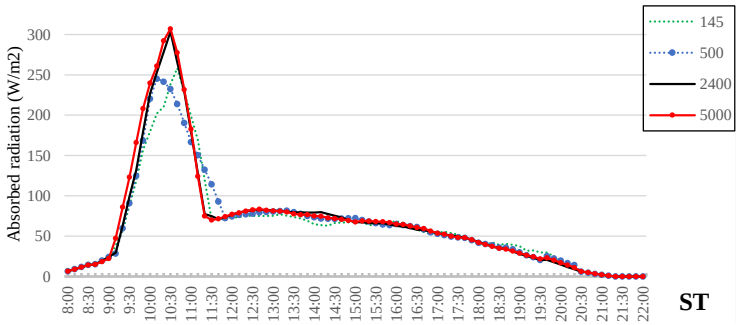

(c) Point G

Figure 3.15: Short-wave loads for the selected points using different number of sky tiles.

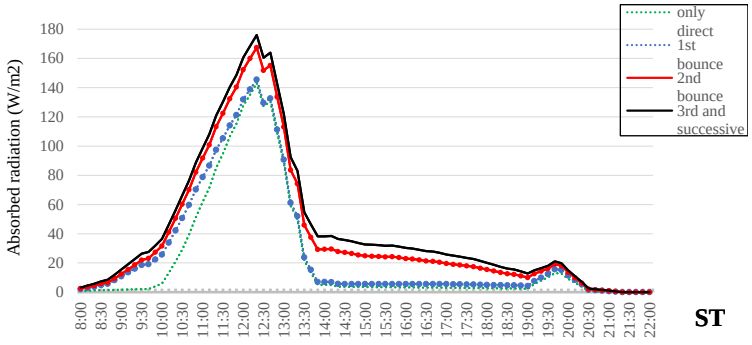

(a) Point S

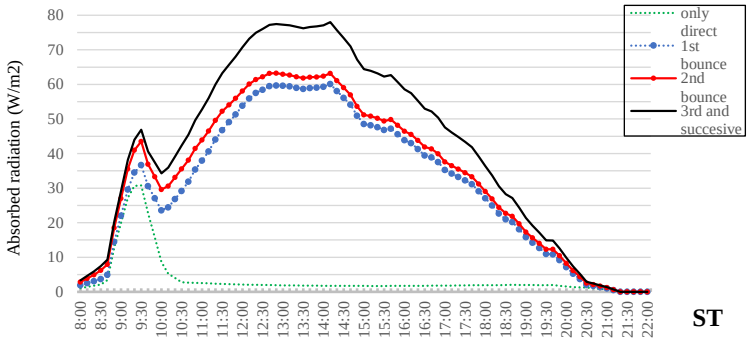

(b) Point N

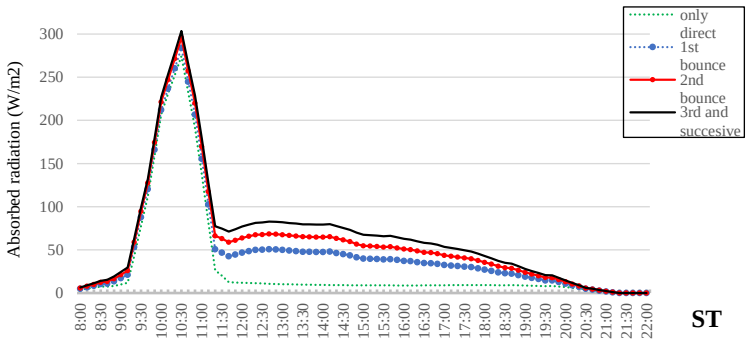

(c) Point G

Figure 3.16: Short-wave loads using different numbers of diffuse radiation bounces.

3.3.2 FEM module

This section presents the module used in Chapters 6 and 7. The short-wave module described above is used to compute the absorbed radiation fluxes, and the FEM software Cast3m is used for heat transfer analysis. Chapter 6 shows the integration of all the boundary conditions needed for this kind of study. Chapter 7 elaborates some modifications into the Cast3m code, in particular to use free internal air temperatures and sparse view factors matrices for long-wave computations.

A simplified test case is used here to show some calibrations for the different stages of the calculation. The test case is presented with greater detail in Chapter 6. The focus here is on conduction (mesh element size, number of layers in the walls) and long-wave radiation (exchange simulation methods).

The selected boundary conditions correspond to a spring day (April 23^{rd}) in the city of Bayonne, France, using the geometry presented in Figure 3.11. A day with clear sky and calm wind conditions is selected. Figure 3.17 shows the evolution of the air temperature in the exterior environment, along with relative humidity and internal air temperature, which is simplified to be constant at 17°C. The wind and humidity values are based on the test case presented in [Garcia-Nevado, 2019]. The outside convection coefficient is fixed at 10 $\mathrm{Wm^{-2}K^{-1}}$, while the interior convection coefficients are set to a value of 0.7 $\mathrm{m^{-2}K^{-1}}$ for the ground, 2.5 $\mathrm{m^{-2}K^{-1}}$ for the vertical walls and 5 $\mathrm{m^{-2}K^{-1}}$ for the roof, as specified in the French thermal regulation [CSTB France, 2012]. The sky temperatures are estimated using Martin and Berdhal [1984] sky model, based on the air temperature and relative humidity.

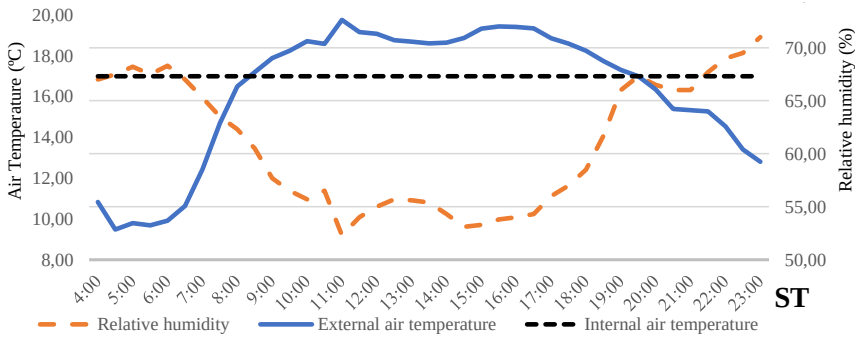

Figure 3.17: Outside air temperature and relative humidity, along with inside air temperature.

Four kinds of surface properties are considered in this study: walls, roofs, floors and street. The thermal and optical properties are described using four parameters: diffuse short-wave reflection coefficient (r), long-wave emissivity ε, thermal conductivity k ($\mathrm{Wm^{-1}K^{-1}}$), and volumetric heat capacity c_v ($\mathrm{Jm^{-3}K^{-1}}$). The definition of surface properties can be found in Figure 6.2. Regarding long-wave radiation, the surfaces are simplified with blackbody emissivity (ε = 1).

The ground temperature at a depth of one meter is set to 11.1°C, corresponding to the mean ground temperature at a depth of one meter in April for the city of Bayonne (Meteonorm global meteorological database [Remund et al., 2010]). The initial conditions correspond to a steady state solution obtained with the initial air temperature. The simulated surface temperatures were compared with those obtained after a simulation period of two days (repeating the same day), and the differences were less than one degree.

Meshing the geometry

Each box that composes the geometry must be meshed to perform FEM calculations. Moreover, the street must be connected to the buildings to ensure the proper conduction simulation conditions. A ground surrounding the structures must be added to allow for accurate radiation boundary conditions. The components of the scene are meshed with volumes for conduction, and surfaces for the envelope that is subject to radiation and convection. The volume is meshed using rectangular hexahedra, which defines an envelope composed of quadrilaterals.

Linear interpolation functions are used for all the elements, because the compatibility between quadratic elements and long-wave radiation is not currently supported by Cast3m. Since the evolution of temperature through the different components may actually be non-linear, the walls are composed of several layers of equally sized elements. This approximation makes the mesh to be more complex but allows estimating the temperatures within the volumes with better precision.

In the first place, the six external faces of the boxes are constructed using several elements at the edges, to account for the layers of the other surfaces that are in contact with it. The correspondent volume is then obtained by extruding the surface. The total volume of the building is constructed by joining the partial volumes and eliminating duplicate nodes. Figure 3.18 presents a diagram of a box with the correspondent mesh for exterior and interior surfaces.

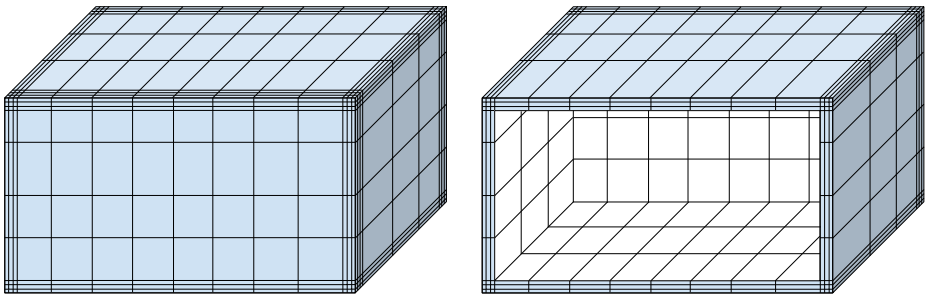

Figure 3.18: Diagram showing a box with the walls meshed using several layers of hexahedra.

After the buildings are meshed, the edges of the bases that face the urban canyon are joined to build the street surface and its volume by extrusion. Finally, a surrounding ground is added using the contour of the bases and the street. The ground mesh gets finer near the buildings, in order to have better precision in that area.

Two main parameters allow to use the described meshing strategy to obtain meshes with different precision: the number of layers, and the size of the quadrilaterals that form the boundary mesh. The rest of the parameters depend on the specification of the geometry, e.g. the tiny elements along the edges are sized accordingly with the wall thickness, as well as the width of each hexahedron.

Figure 3.19 shows the boxes meshed with elements of area 1.5m x 1.5m and four layers in the walls. The four buildings bring a total of 87904 volume elements and an exterior envelope of 21976 quadrilaterals. The street is composed of 2828 volumes and 707 surfaces, while the ground has 22848 and 5712, respectively. The total number of volume elements is 113580, while the exterior envelope is composed of 28395 quadrilaterals.

Table 3.1 shows a summary of the computational model.

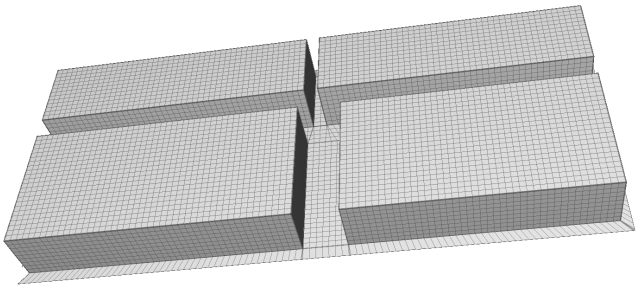

Figure 3.19: Example of mesh with 1.5m x 1.5m quadrilaterals and four layers in the thickness of the wall.

Location	latitude: 43° 28' 35" N, longitude: -1° 30' 48.46" W.
Day and time	April 23^{rd}, 2017. 00:00hs to 23:59hs (24 hours).
Air temperatures	Between 9 and 20 °C (Figure 3.17).
Interior temperature	17 °C.
Sky temperature	Estimated using Martin and Berdhal [1984].
Sky radiances	Estimated using Perez [1993].
Sky mesh	Discretized following Beckers and Beckers [2014]
Material properties	Different for walls, street, roofs, and ground (Figure 7.2)
Elements	Quad4 for the exterior surface (radiation and convection). Hexahedral8 volumes for conduction, walls with 4 layers.
Size of the geometry	113580 volumes, 28395 quads.
Simulation	10 minutes steps (144 steps).

Table 3.1: Summary of the properties of the base computational model.

Temperature results with different meshes

In this study, the full heat transfer model is executed, considering short-wave loads, long-wave radiation exchange, convection and imposed temperatures at 1m deep in the ground. The idea is to calibrate the results with respect to the mesh size and number of layers in the wall. The temperature results are analyzed for the same three points than above, to study the thermal behavior of the exterior surfaces.

In the first place, four meshes are generated using four layers in the wall, but with quadrilateral edge sizes of: 0.75m, 1.5m, 3m, and 5m (Figure 3.20).

Using elements of size 0.75m x 0.75m, the total number of elements in the mesh grows to $\approx 80k$. This fact becomes a problem for long-wave calculations within Cast3m, because the view factors matrix follows a quadratic relation with the number of elements, requiring around 50GB of memory under the current implementation of Cast3m that uses full matrix formats. In order to execute this case in the desktop PC of 16GB of RAM, the modifications presented in Chapter 7, where sparse matrices are introduced into Cast3m for long-wave computations, are used. With this improvement, the memory requirements are reduced to 3.2GB. It is also important to highlight that the memory used for storing view factors is always greater than the memory used for the conductivity matrix $\mathbf{K}$, because accounting for the local connectivity between nodes requires much less information than saving the visibility between each pair of elements. The temperatures of the exterior urban surface are plotted in Figure 3.21.

Assuming that the 0.75m mesh is the most accurate one, the 3m and 5m meshes produce higher errors than the one of 1.5m, especially in the north-facing and ground points. The meshes with

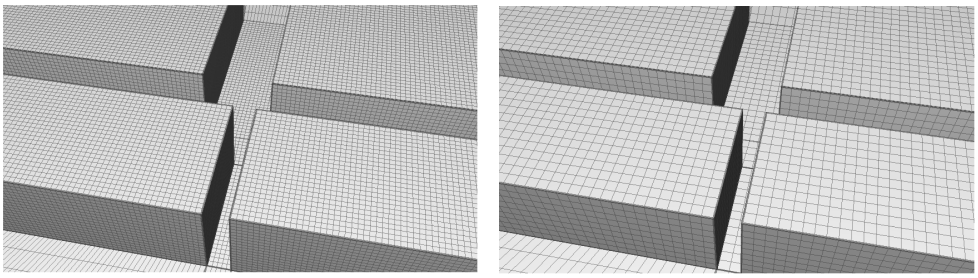

(a) 0.75m x 0.75m - 78842 quads

(b) 1.5m x 1.5m - 28395 quads

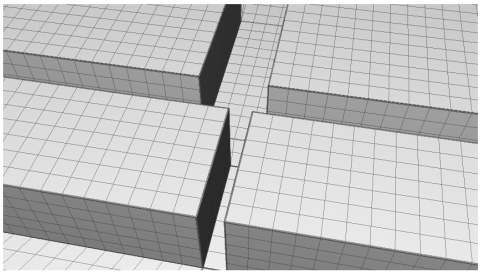

(c) 3m x 3m - 12965 quads

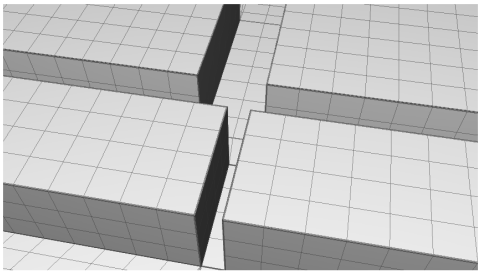

(d) 5m x 5m - 8017 quads

Figure 3.20: Four meshes using different element sizes and corresponding size of the exterior mesh, subject to radiation boundary conditions.

0.75m and 1.5m present smaller discrepancies, with less than 1°C difference for all timesteps. It can be concluded that using an element size of 1.5m x 1.5m allows to obtain accurate results with a significant reduction in the memory requirements (50GB vs 6GB with full matrix format and 3.2GB vs 1GB with sparse format) and therefore a better computational performance.

Another parameter to analyze is the number of layers and its effect on the temperature evolution within the walls. For this purpose, four new meshes are generated, using 1, 2, 4 and 8 layers (see Figure 3.22 for a diagram of the mesh).

The different meshes are executed in FEM model and the temperature within the wall at the south-facing point (see Figure 3.13) is studied. The results are presented in Figure 3.23 for four different hours of the day. In each plot, the leftmost dots indicate the temperature at the exterior surface, which exhibits a wider variation in time than the temperature at the interior surfaces (rightmost dots). The temperature along the selected line shows a non-linear evolution. With 4 and 8 layers, the results are very similar. Using one layer implies higher errors in the interior and exterior temperatures, with differences of up to 3°C. Using 2 layers produces smaller errors in these temperatures, although it does not allow for a good estimation of the internal evolution of the temperature.

3.3.3 Long-wave methods

The next study aims at showing the long-wave radiation computations results for different methods. Two different methods are analyzed: a complete view factor calculation (current implementation of Cast3m [Coulon, 2006], namely CVF), and the Sky View Factor method from EnergyPlus (namely SVF-EP, already described in Section 3.2.3), which considers the city surfaces to be at the air temperature and a uniform sky temperature. This last technique was implemented in Cast3m code for

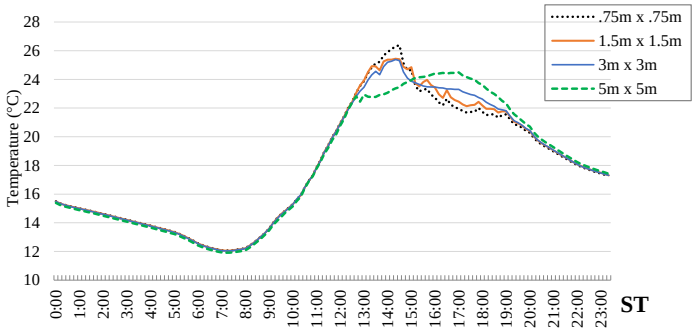

(a) Point S

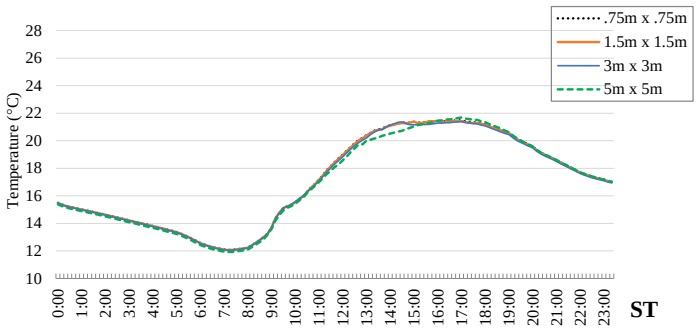

(b) Point N

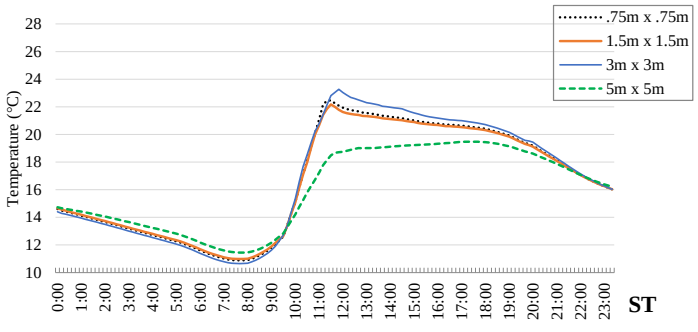

(c) Point G

Figure 3.21: Temperature profiles

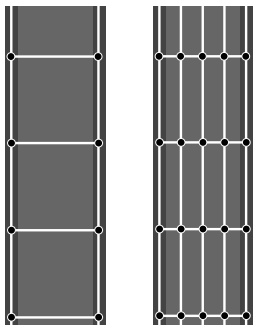

(a) 1 layer (b) 4 layers

Figure 3.22: Diagram showing a traversal section of a wall meshed with 1 and 4 layers of hexahedra.

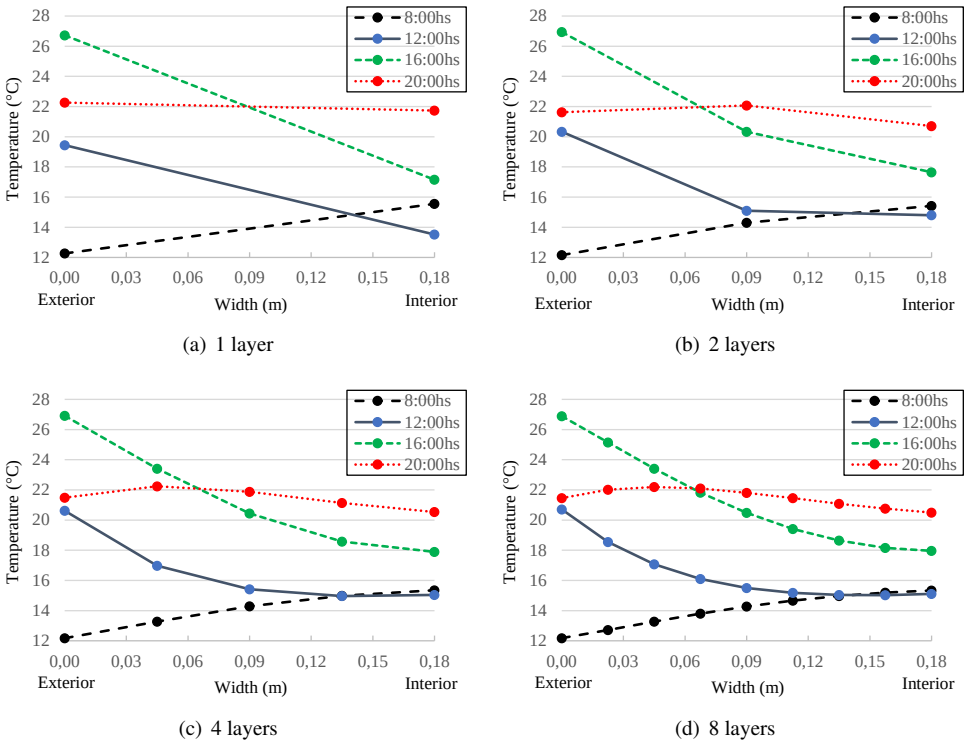

Figure 3.23: Temperature evolution within the wall at the south-facing point.

comparison and calibration purposes, using the average sky temperature estimated by Martin and Berdhal [1984] model as the uniform sky temperature.

The two models are executed for the same test case described above. Since the overall value of long-wave balance is relatively low with respect to other fluxes such as short-wave radiation and convection, the temperature results of using CVF and SVF-EP vary at lower ratios than previous tests. Hence, the results are presented with the total long-wave flux balance values (in W/m^2), which allows for a better interpretation of the differences generated by the methods. The total long-wave balance is obtained after the FEM model is executed by calculating the absorbed minus the emitted long-wave radiation fluxes.

Figure 3.24 shows the obtained results for the three points studied before (see Figure 3.13). In each figure, three plots are presented: the total long-wave balance at the point (*LW balance*), the balance with the sky (*Sky balance*), corresponding to the total flux coming from the sky minus the flux emitted towards the sky, and the long-wave balance with the city (*City balance*), which is the total flux coming from the city minus the flux emitted towards the city. Note that *LW balance* corresponds to the sum of *City balance* and *Sky balance*.

At the south-facing point, the flux balance is negative throughout the entire day, meaning that long-wave radiation has a cooling effect in that point, which is especially hot because of the incoming short-wave flux. Between 14:00 and 18:00, the SVF-EP technique underestimates the exchange with the city surfaces because the air temperature is colder than the front wall, resulting in an overall relative error in the total long-wave balance of around 20% (-48 W/m^2 versus -62W/m^2 at 15:30).

At the north-facing point, the balance is negative in the morning and positive in the afternoon,

mainly because the wall in the front starts receiving direct sunlight and becomes much hotter, emitting more radiation. SVF-EP does not allow for the estimation of this phenomenon, because it only considers the air temperatures. This fact results in a bias of around 20 W/m^2 in the estimation of long-wave balances that can be appreciated in the plot profiles. The temperature difference produced by both models reaches up to 2.5°C.

At the ground point, an error in the estimation of the sky radiation is observed, because the CVF technique considers an anisotropic distribution of the sky temperatures, unlike SVF-EP. The ground point faces the Zenith (the coldest zone of the sky dome) and therefore the effect of sky cooling is enhanced. This phenomenon is not correctly estimated with SVF-EP, which shows lower sky balance absolute values. Moreover, the city balance is underestimated with SVF-EP, because the hot south-facing wall is not considered with this method.

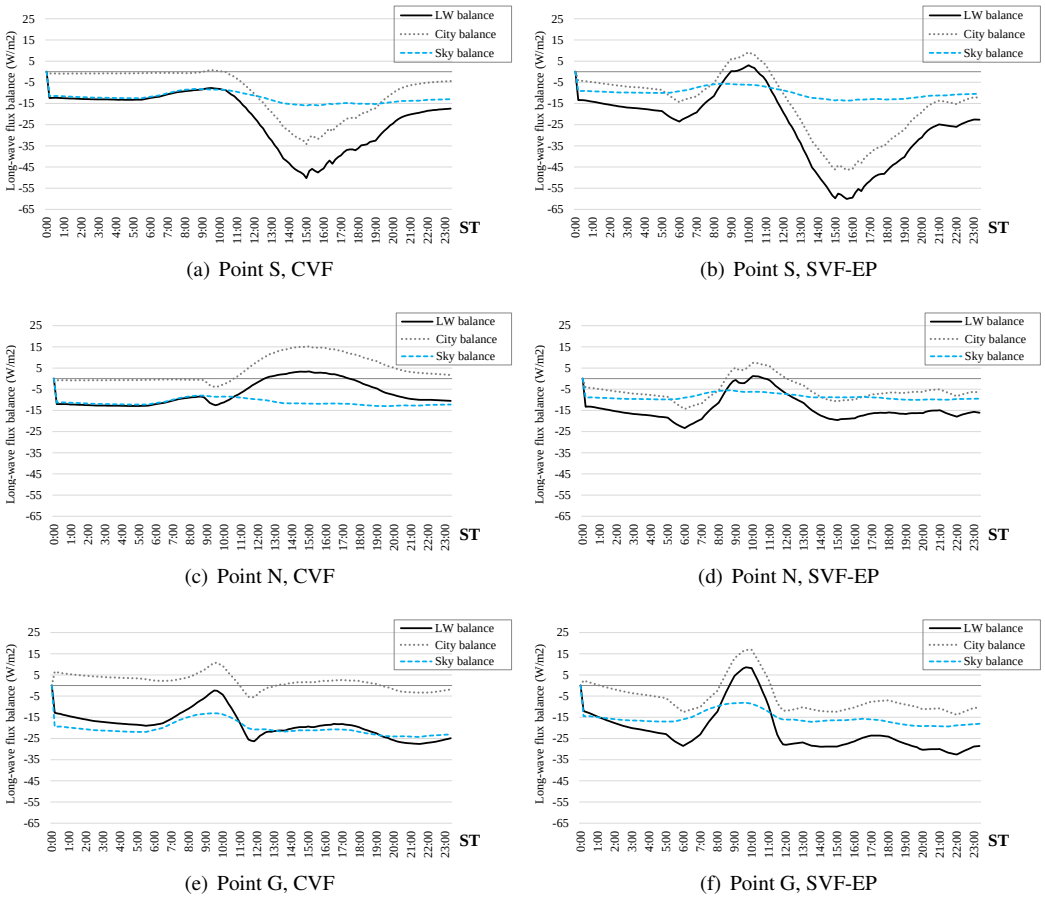

(a) Point S, CVF

(b) Point S, SVF-EP

(c) Point N, CVF

(d) Point N, SVF-EP

(e) Point G, CVF

(f) Point G, SVF-EP

Figure 3.24: Long-wave balance using complete view factors (CVF) and the Sky View Factors technique from EnergyPlus (SVF-EP).

3.3.4 Detailed 3D geometry

In the previous studies, the geometry of the street was composed of four boxes with a uniform set of properties for each wall, with the materials considered as blackbody emitters. This geometry allowed to perform a simplified thermal analysis of the street. Repeating a similar study using a more detailed

3D model and material specification brings many problems that have to be addressed. The first issue is to design a geometry and a mesh compatible with FEM, as well as to insert it into Cast3m. A greater variety of material properties must be introduced, leading to a much complex FEM simulation that includes sophisticated scene characteristics and non-blackbody materials. Chapter 8 introduces a new model (Figure 3.25) composed of a more detailed geometry and material descriptions for the scene used in the previous studies.

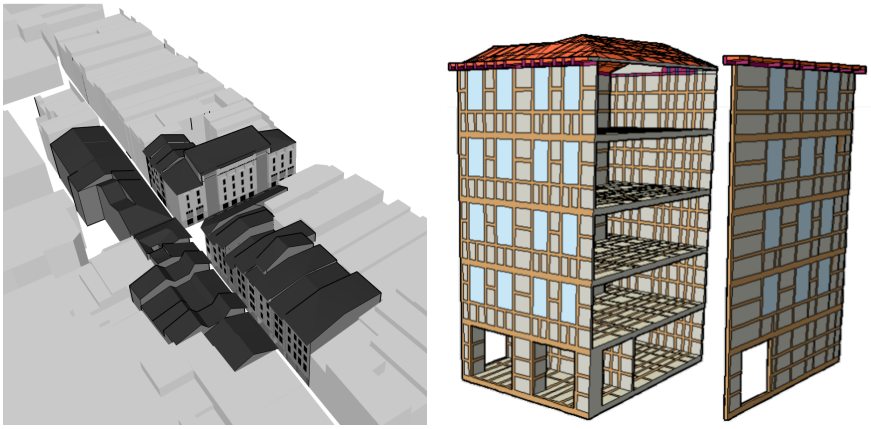

(a) Overall geometry. (b) Building model and mesh detail.

Figure 3.25: Detailed geometric model of Tonneliers street.

It is of great interest to analyze the temperature results of executing the FEM-based model using both simplified and detailed models. For this purpose, the study is repeated under the same boundary conditions (sky temperatures, anisotropic irradiances, etc) but using the new geometry. The results are analyzed for three points (Figure 3.26) selected to represent the same three points that were previously used in the simplified geometry. The new computations are performed with an estimated directional emissivity model and reflectivity function, as presented in Chapter 8. Figure 3.27 shows the solar trajectories in the new geometry, and Figure 3.28 presents the temperature evolutions.

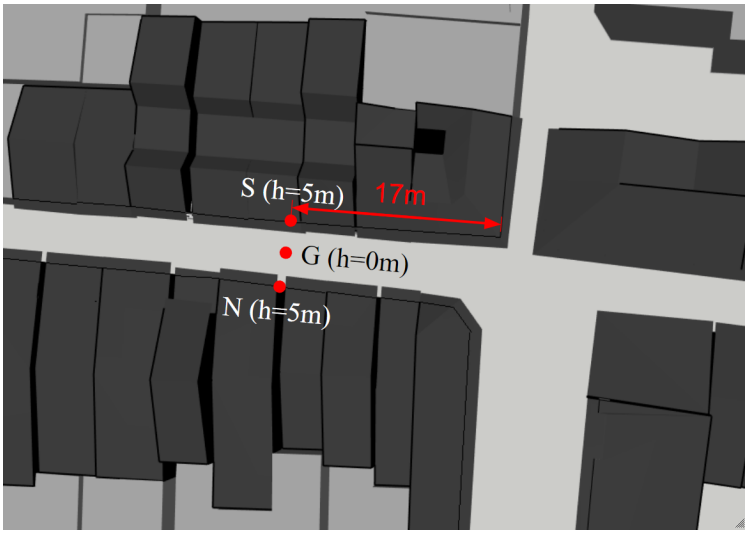

Figure 3.26: Location of the three points selected in the detailed geometry.

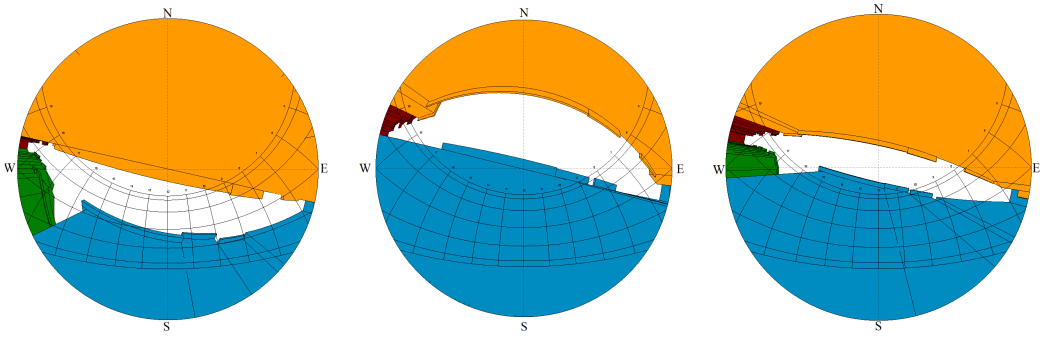

(a) S (b) N (c) G

Figure 3.27: Solar trajectories for the three points selected. Generated with Heliodon2 [Beckers and Masset, 2006].

The temperature profiles show larger biases for the south-facing and ground point. The new geometry contains roof overhangs that block parts of the short-wave fluxes reaching the urban canyon. This fact explains the differences of up to 3.5 °C that is observed in the ground point. The complex shape of the new geometry also provides a more accurate description of the temperature pattern at the south-facing point, where the simplified geometry fails to simulate some shading effects between 14:00 and 17:00. For the north-facing wall, the results are very similar in both cases, mainly because it does not receive direct sunlight.

The simplified study allows to assess the general thermal behavior of the scene, and provides better conditions to evaluate the simulation results, because it is easier to understand and explain the observed patterns in a simple test case. On the other hand, using the complex geometry enables a much detailed study, but increases the complexity of the analysis.

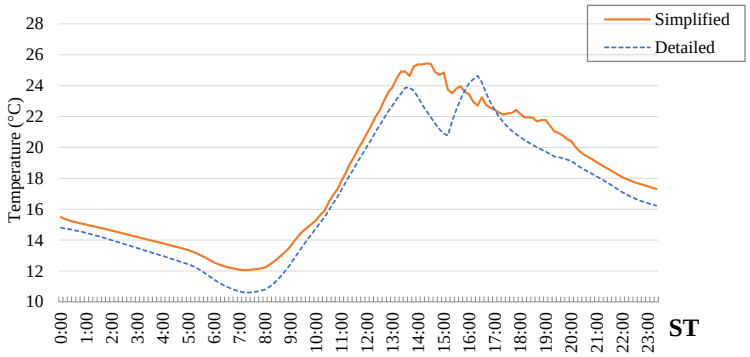

(a) S

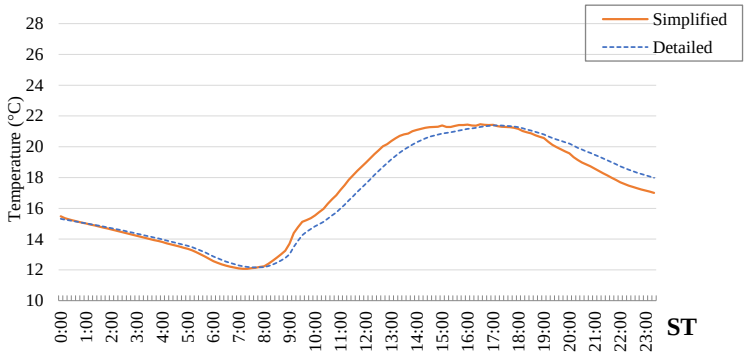

(b) N

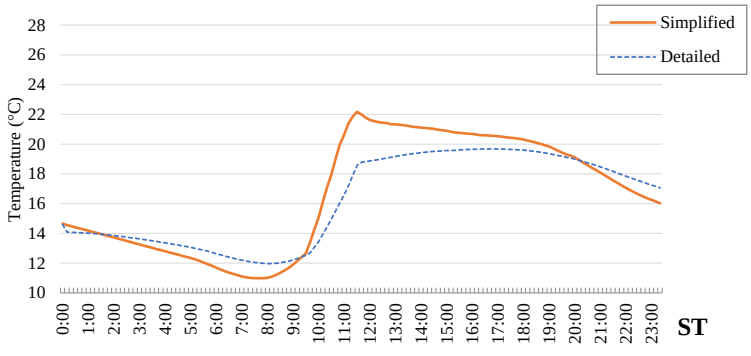

(c) G

Figure 3.28: Temperature profiles for the selected points using the simplified and detailed geometries.

Chapter 4

Computing Urban Radiation: A Sparse Matrix Approach

The contents of this chapter were published in:
Aguerre, J. P., Fernández, E., Besuievsky, G., and Beckers, B. (2017). *Computing urban radiation: A sparse matrix approach*. Graphical Models, 91, 1-11. Elsevier.

Cities numerical simulation including physical phenomena generates highly complex computational challenges. In this paper, we focus on the radiation exchange simulation on an urban scale, considering different types of cities. Observing that the matrix representing the view factors between buildings is sparse, we propose a new numerical model for radiation computation. This solution is based on the radiosity method. We show that the radiosity matrix associated with models composed of up to 140k patches can be stored in main memory, providing a promising avenue for further research. Moreover, a new technique is proposed for estimating the inverse of the radiosity matrix, accelerating the computation of radiation exchange. These techniques could help to consider the characteristics of the environment in building design, as well as assessing in the definition of city regulations related to urban construction.

4.1 Introduction

Due to the increasing need of energy assessment tools at large scale, urban physics simulation has become a major topic of interest. The evaluation of annual solar irradiance and the analysis of the spatial variation over building facades has a relevant interest for urban planning and building design. Computational simulation for radiative transfer on an urban scale is a challenge, because thousands of buildings have to be considered. The main problem is how to deal with the huge amount of data required to represent such models.

One of the mathematical models adapted to predict urban radiation exchange is the use of the radiosity method [Beckers, 2013a; Cohen and Wallace, 1993]. A full solution of this method in a city model may require computing the view factors between all building mesh elements and solving the linear system, which may be an expensive computational task when considering a district model

composed of hundreds of buildings. A possible solution to manage the problem is to simplify the visibility problem [Robinson and Stone, 2005].

We focus on solving the problem taking all visibility information into account. By observing that the form factor matrix that represents all view factors is sparse for this kind of environments, we propose a novel approach for radiative exchange computation that can approximate the inverse of the radiosity matrix. We formulate the problem as a Neumann series [Kontkanen et al., 2006] and approximate the matrix by eliminating unimportant terms. Our study on different kinds of urban model configuration shows that, for models composed of thousands of patches, we can provide an accurate approximation of the inverse radiosity matrix that can also be stored in main memory. The radiosity method exposed here allows reducing the memory and execution time up to two orders of magnitude. This promising result enables processing city models bigger than 100k patches on a standard desktop PC. Moreover, the method can be applied for solving thousands of radiative configurations efficiently, considering many bounces of light and heat radiation. This is useful for light and heat calculations.

4.2 Related work

The two main methodologies for solving the urban radiant exchange problems are ray tracing and radiosity. While the former is widely used in rendering, the radiosity method is more suitable when the surfaces are Lambertian reflectors (such as concrete). One of the advantages of using this method is that it can give results in the whole scene space, which makes it attractive for urban environment analysis. In the rest of this section, we review the radiosity method and the works related to our approach.

4.2.1 The Radiosity Problem

The radiosity method [Goral et al., 1984b] is a technique which allows computing global illumination on scenes with Lambertian surfaces. It has been applied in many areas of design and computer animation [Dutre et al., 2006]. The continuous radiosity equation can be discretized through the use of a finite element methodology. The scene is discretized into a set of patches, leading to express the problem using the following set of linear equations[1]:

$$B_i = E_i + R_i \sum_{j=1\ldots n} B_j \mathbf{F}(i,j) \quad , \quad \forall i \in \{1 \ldots n\}$$

This set of linear equations is expressed in a succinct manner in Equation 4.1.

$$(\mathbf{I} - \mathbf{RF})B = E, \tag{4.1}$$

where $\mathbf{I}$ is the identity matrix, $\mathbf{R}$ is a diagonal matrix containing the reflectivity index of each patch, B is the radiosity vector to be found, and E is the emission vector. $\mathbf{F}(i,j)$ is a number between 0 and 1 expressing the form factor between patch i and j. This value indicates the fraction of the light power going from one to another. Therefore, the form factor matrix is a $n \times n$ matrix, where n

[1] In Chapters 4 and 5, B stands for radiosity. This is the same magnitude that is described with J in the rest of the thesis.

is the number of patches in the scene. $\mathbf{F}$ can be efficiently computed using the hemi-cube algorithm [Cohen and Greenberg, 1985], but its memory requirements ($O(n^2)$) are often an obstacle when working with big models ($n > 50.000$).

Equation 4.1 can be solved using several approaches. For example, the operator $\mathbf{M} = (\mathbf{I}-\mathbf{RF})^{-1}$ can be calculated, which represents a global transport operator relating the emitted light with the final radiosity of the scene, $B = \mathbf{M}E$. When $\mathbf{F}$ has a low numerical rank, factorization techniques can be used to efficiently compute an approximation of $\mathbf{M}$ [Fernández, 2009]. On the other hand, $\mathbf{M}$ can also be approximated using iterative methods such as Neumann series ([Kontkanen et al., 2006]).

Another approach is to compute $\mathbf{B}$ by solving the linear system of equations iteratively, using methods such as Jacobi or Gauss-Seidel [Cohen and Wallace, 1993]. Eq. 4.2 presents the radiosity resolution using the Jacobi iteration. Each iteration adds the radiosity of a new light bounce to the global radiosity result.

$$B^{(i+1)} = \mathbf{RF}B^{(i)} + E \ , \ \text{where } B^{(0)} = E \tag{4.2}$$

4.2.2 Correlation between scene characteristics and F properties

The characteristics of the analyzed scene model have a direct impact on the numerical properties of the associated $\mathbf{F}$ matrix. For example, in scenes with a high spatial coherence, matrices involved in radiosity calculations have a low numerical rank [Fernández, 2009], because close patches have a high probability of being affected similarly by the rest of the scene. This fact enables the application of factorization techniques to compute low rank approximations that can be stored in main memory. On the other hand, in scenes with a high occlusion factor between patches, $\mathbf{F}$ can be efficiently represented using sparse representations. Two patches completely occluded do not exchange energy directly, and if this property is satisfied for most pair of patches on a scene, the form factors matrix has most of its elements equal to 0.

A *sparse matrix* is any matrix with enough zeros that it pays to take advantage of them [Wilkinson, 1971]. Generally, using sparse representations allows saving time or memory (usually both) by exploiting the number of zeros. Furthermore, these kind of matrices are applied in problems where the use of full matrices is not possible due to memory limitations.

The use of sparse matrices in radiosity calculations is still a subject of study. [Gortler et al., 1993] present the Wavelet Radiosity method, which is based on wavelet theory. Expressing the kernel operating in a radiosity function in a wavelet basis leads to a sparse approximation of it. On the other side, [Goel et al., 1991], [Borel et al., 1991] and [Chelle and Andrieu, 1998] solve the radiosity problem using iterative methods (like Gauss-Seidel) taking advantage of the sparsity of the form factors matrix. This property is present in the tested scenes (plant canopies), where there is a high occlusion level between distant polygons.

Studying the correlation between scene characteristics and $\mathbf{F}$ properties can help assessing the election of the correct technique for a given scene or sets of scenes. In this regard, there are scenes where neither sparse nor low-rank matrices are generated. Also, both sparse and low-rank $\mathbf{F}$ matrices could be associated with some kinds of scenes. Figure 4.1 presents a diagram associated with these ideas, using four example models, each one with different properties. A picture of the scene, the sparsity structure of its associated $\mathbf{F}$, and a plot of its singular values are shown.

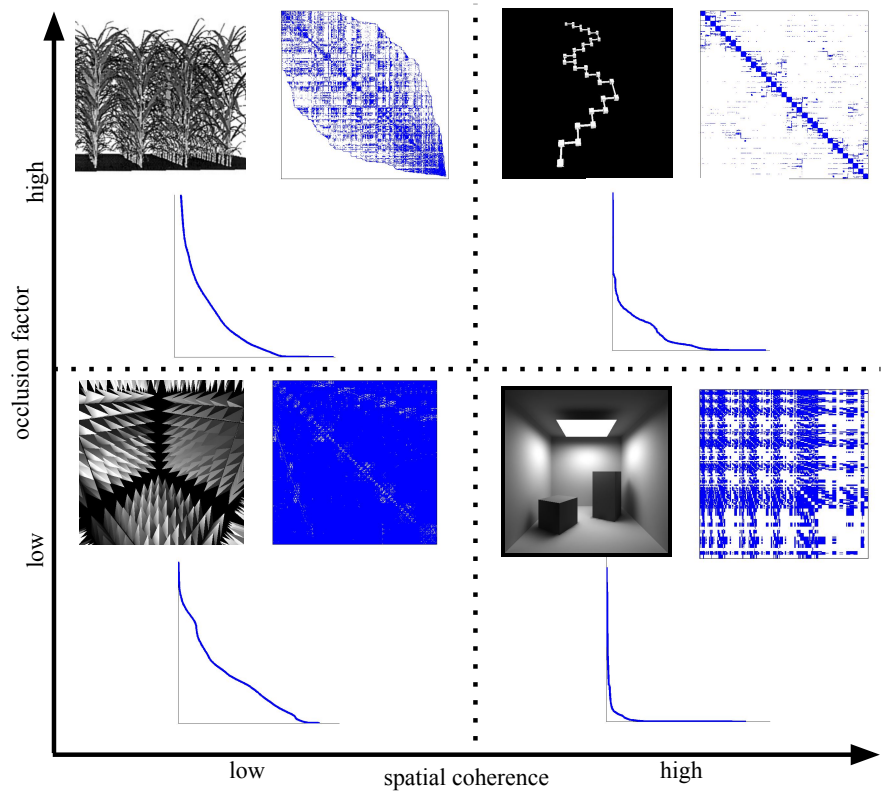

Figure 4.1: Diagram of sparsity and low-rank properties of four example scenes.

The upper left model of Figure 4.1 corresponds to the plant canopy presented in [Chelle and Andrieu, 1998]; the matrix $\mathbf{F}$ is sparse and its associated singular values decay is slow. The lower right scene is the Cornell Box used in [Fernández, 2009]; the matrix $\mathbf{F}$ is full and its numerical rank is low. The other two models were generated to test the existence of other scenes with different properties. The upper right scene is composed of several rooms, and connecting corridors. The rooms are simple boxes composed of a fine mesh, which makes them numerically low-rank by their own. Each room "sees" almost nothing of the others. This makes its form factors matrix sparse, as it can be seen in the figure, but its singular values decay fast enough to be considered numerically low-rank. On the other hand, the lower left scene represents an anechoic chamber, which is a room designed to absorb wave reflections. For this, its walls are filled with pyramids pointing inward. This particular property makes $\mathbf{F}$ to be highly dense and not numerically low-rank. The experimental results presented in Secs. 4.3.1 and 4.4.2 suggest that city models have characteristics similar to plant canopy models.

4.2.3 Neumann Series

Given an Operator $\mathbf{T}$, its Neumann series is a series of the form

$$\sum_{k=0}^{\infty} \mathbf{T}^k$$

The expression $\mathbf{T}^k$ is a mathematical notation that means applying the operator $\mathbf{T}$, k consecutive times. Supposing that $\mathbf{T}$ is a bounded operator and $\mathbf{I}$ the identity operator, if the Neumann series converges, then $(\mathbf{I} - \mathbf{T})$ is invertible and its inverse is the series:

$$(\mathbf{I} - \mathbf{T})^{-1} = \sum_{k=0}^{\infty} \mathbf{T}^k = \mathbf{I} + \mathbf{T} + \mathbf{T}^2 + \mathbf{T}^3 + ...$$

This property can be used to calculate the radiosity [Cohen and Wallace, 1993], by computing an approximate to the inverse of $(\mathbf{I} - \mathbf{RF})$ through l iterations:

$$(\mathbf{I} - \mathbf{RF})^{-1} \approx \mathbf{I} + \mathbf{RF} + (\mathbf{RF})^2 + ... + (\mathbf{RF})^l$$

In this series, $(\mathbf{RF})^i$ contains the information of the i^{th} bounce of light between the surfaces in the scene. The main computational cost of this approach is the multiplication of matrices. Thus, if $\mathbf{RF}$ is sufficiently big, the method could be too expensive.

[Kontkanen et al., 2006] use a variant of this method to compute a global transport operator for radiance calculations. This operator expresses the relationship between the converged and incoming incident lighting. In this process, the matrices are compressed using the following strategy: at each step, all the coefficients below a certain threshold are removed. This results in sparse matrices, which allow speeding up the calculation. The computation is stopped when all the coefficients in $(\mathbf{RF})^i$ are smaller than the threshold.

4.2.4 Urban Radiative Methods

A previous work for reducing the urban radiosity formulation is the simplified radiosity algorithm (SRA) [Robinson and Stone, 2005]. The basis of the simplification is grouping, for each sky direction, the main obstructions that obscured each surface. Then, for a scene composed of n patches and getting p sky patches, the system matrix can be reduced to a $n \times p$ one, that can both be inverted or used to solve the system iteratively. This method is embedded in the CitySim package [Robinson et al., 2009], a multi-purpose system for urban models simulation. In [Beckers, 2013b], the idea of using well-known finite element techniques, as condensation, is analyzed for being adapted to urban models. In this case, the analysis is done only for longwave radiation.

4.3 Our Proposal

This section presents the main ideas of our work, and proposes an algorithm to compute radiosity solutions exploiting the properties of the studied matrices. Firstly, the sparsity of $\mathbf{F}$ in city environments is analyzed. Secondly, a method to approximate the inverse of the radiosity matrix is proposed. Finally, an experimental analysis is performed to test the proposed ideas.

4.3.1 Why not factorizing?

As stated in previous work [Fernández, 2009], a good approach to accelerate the radiosity calculations is to find a factorization that approximates the form factors matrix generated by the scene.

When there is a high spatial coherence, the factorization allows reducing the amount of data drastically, without losing much information about the model. This factorization is used to approximate the inverse of the radiosity matrix, allowing to compute radiosity solutions efficiently for a static geometry. Nevertheless, this is not always the case for many scenes.

City environments composed of thousands of buildings disposed over a terrain do not have enough spatial coherence to exploit the previous properties. Given a city, each street has a different view of the scene, and the singular values of the corresponding matrix $\mathbf{F}$ usually decay slowly, which prevents the use of factorization techniques to accelerate radiosity calculations. Therefore, other strategies need to be studied in order to work with big city models. To understand these concepts, Figure 4.2 shows the singular values for two different scenes: the Cornell box, which has a high spatial coherence, and an example of a city model (see Fig.4.3(a)). As can be seen, the singular values decay rapidly in the high coherence case, while for the city environment they decay more slowly. For example, to get an error of 0.1, the city needs three times more singular values than the Cornell box.

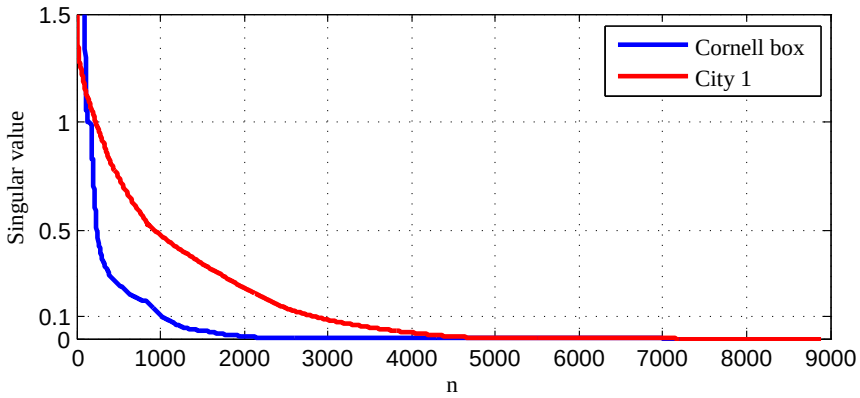

Figure 4.2: Singular values of $\mathbf{F}$ for the Cornell box scene and for City 1.

4.3.2 Studying the Sparsity of a City's Form Factors Matrix

The density factor (sparsity) of a matrix is the fraction of non-zero elements over the total number of elements. In the form factor matrices, this factor depends on the number of patches seen from each patch: if patch j sees few patches, then row j of $\mathbf{F}$ has few elements different than zero, and *vice versa*. Figure 4.3 shows two urban scenes where each patch is colored by checking how many elements are seen from it. For example, the upper elements on the tallest buildings are red while the ones on houses are blue. These results allow to predict that the $\mathbf{F}$ matrix corresponding to a city, where each patch sees few others, is very sparse.

The previous fact derives into the main conjecture of the present work: different kinds of cities have sparse $\mathbf{F}$ matrices with different density factors. This sparsity depends on many aspects. For instance, orography, construction type, buildings disposition and heights are expected to have a great influence on the structure of the matrices. In a first step, we focus on the variation of building heights. A city with big variance on its buildings height (as a typical contemporary downtown with skyscrapers) should generate less sparse matrices than a city with uniformly elevated buildings (as,

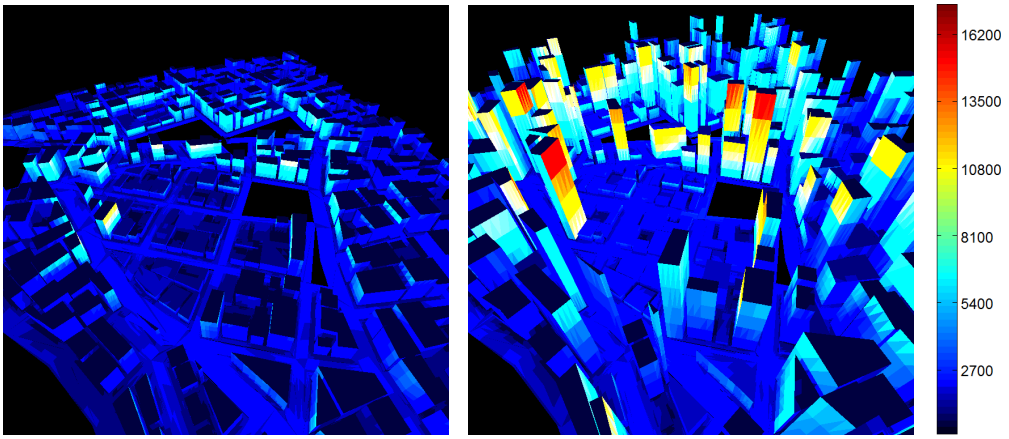

(a) City 1. (b) City 3.

Figure 4.3: Two example of urban scenes. The color of a patch indicates the number of patches that are seen from it. Both models are composed of 142k patches.

for example, Haussmann's Paris [Loyer, 1988]). In following sections the orography is also taken into account.

4.3.3 An Approximation of $\mathbf{M} = (\mathbf{I} - \mathbf{RF})^{-1}$

The inverse of a sparse matrix is usually a full matrix [Duff, 1977], so its calculation is computationally expensive, and has memory limitations for medium to large size matrices. However, in the case of the radiosity matrix, its inverse $\mathbf{M}$ has many elements below a small threshold. This is because the indirect energy exchange between two occluded patches is predominantly small, in such a way that it can be ignored in many cases. Therefore, in relation to $\mathbf{M}$, our proposal consists in finding a sparse approximation ($\tilde{\mathbf{M}} \approx \mathbf{M}$) that allows to compute low-error radiosity values.

In order to compute $\tilde{\mathbf{M}}$ efficiently, we use a method based on the work by Kontkanen [Kontkanen et al., 2006]. As described in Sec. 4.2.3, the algorithm is based on the use of Neumann series and a compression strategy based on removing all elements below a threshold ε. To obtain even sparser matrices, we apply this compression to $\mathbf{RF}$ before starting the process. Algorithm 1 describes the proposed method, where the function "remove" eliminates $|\mathbf{T}(i,j)| < \varepsilon, \forall ij$.

Algorithm 1 Calculate $\tilde{\mathbf{M}}$.

1: $\tilde{\mathbf{M}} = \mathbf{0}$
2: $\mathbf{T} = \mathbf{I}$
3: **while** $\mathbf{T} \neq \mathbf{0}$ **do**
4: $\quad \tilde{\mathbf{M}} = \tilde{\mathbf{M}} + \mathbf{T}$
5: $\quad \mathbf{T} = \mathbf{TRF}$
6: $\quad \mathbf{T} = \text{remove}(\mathbf{T}, \varepsilon)$
7: **end while**

Once the sparse approximation is computed, it is relatively inexpensive to calculate the radiosity

results for k different emissions (Eq. 4.3):

$$\begin{aligned} \tilde{\mathbf{M}} &\approx (\mathbf{I} - \mathbf{RF})^{-1} \\ \tilde{\mathbf{B}} &= \tilde{\mathbf{M}}\mathbf{E} \end{aligned} \tag{4.3}$$

where the i^{th} column of $\mathbf{E}$ is an emission and the i^{th} column of $\tilde{\mathbf{B}}$ is the approximation of its corresponding radiosity result, $\forall i \in 1 \,..\, k$.

4.3.4 Daylight Simulation

Computing urban radiation exchange has increasing interest, since it is used in several fields such as design [Baker and Steemers, 2014], building energy consumption [Hviid et al., 2008] or ecology [Longcore and Rich, 2004]. In this work, we apply the described techniques on urban daylight simulation.

In order to simulate the sky and its interaction with the city, a hemisphere containing the city is added to the model. This hemisphere is divided into m elements, giving to each one its corresponding emittance, so as to simulate the skylight. There are several ways to mesh the sky [Mardaljevic, 2000; Tregenza, 1987], though we use the more traditional division with parallels and meridians (m=132) as a proof of concept.

Once the sky is added to the model, we use the strategy described by Beckers [Beckers, 2013b] to calculate the first bounce of light from the sky in the city. We use this as the urban emission, which allows us to work only with the form factors between patches of the city. For this purpose, the discrete radiosity equation (Eq. 4.1) is re-written in the following way:

$$B = E + \mathbf{RF}B \tag{4.4}$$

Separating the sky (index s) and city (index u) contributions of Eq. 4.4, we get:

$$\begin{bmatrix} B_s \\ B_u \end{bmatrix} = \begin{bmatrix} E_s \\ E_u \end{bmatrix} + \begin{bmatrix} (\mathbf{RF})_{ss} & (\mathbf{RF})_{su} \\ (\mathbf{RF})_{us} & (\mathbf{RF})_{uu} \end{bmatrix} \begin{bmatrix} B_s \\ B_u \end{bmatrix}$$

The sky is considered as a black surface, with zero reflectance, while the city has no emission. Therefore, as $(\mathbf{RF}_{ss}) = 0$, $(\mathbf{RF})_{su} = 0$, and $E_u = 0$:

$$\begin{bmatrix} B_s \\ B_u \end{bmatrix} = \begin{bmatrix} E_s \\ 0 \end{bmatrix} + \begin{bmatrix} 0 & 0 \\ (\mathbf{RF})_{us} & (\mathbf{RF})_{uu} \end{bmatrix} \begin{bmatrix} B_s \\ B_u \end{bmatrix}$$

In the previous equation, $B_s = E_s$. This leads to the following statement:

$$B_u = (\mathbf{RF})_{us}B_s + (\mathbf{RF})_{uu}B_u = (\mathbf{RF})_{us}E_s + (\mathbf{RF})_{uu}B_u$$

Now, grouping the radiosities from both sides:

$$(\mathbf{I} - (\mathbf{RF})_{uu})B_u = (\mathbf{RF})_{us}E_s$$

The left side of this equation is the radiosity matrix ($\mathbf{I} - (\mathbf{RF})_{uu}$) times the radiosity result for the city. Therefore, following Eq. 4.1, the new emission is $E = (\mathbf{RF})_{us}E_s$, which is the first bounce of light coming from the sky into the city.

4.4 Experimental Analysis

The results of the presented set of experiments were conducted on a desktop computer, with Intel quad-core i7 processor and 16 Gbytes RAM. The calculation of each $\mathbf{F}$ matrix was performed using the hemi-cube technique with a resolution of 512 × 512 pixels, where the graphic component was executed on a NVIDIA GeForce-780 GPU processor. The code was implemented on C++, OpenGL, CUDA [Kirk and Hwu, 2010], and MATLAB [MATLAB, 2010].

4.4.1 Example of City Models

The following analysis is performed using three different urban scenes, which are generated from the same cadastral plan. The first model contains only flat houses, the second one low and middle-sized buildings, and the third one is composed of different sized buildings, including tall skyscrapers (see Fig. 4.4). As can be seen, the first model has a small variance on building heights, while the third one has a big variance. The three models are composed of 8897 patches.

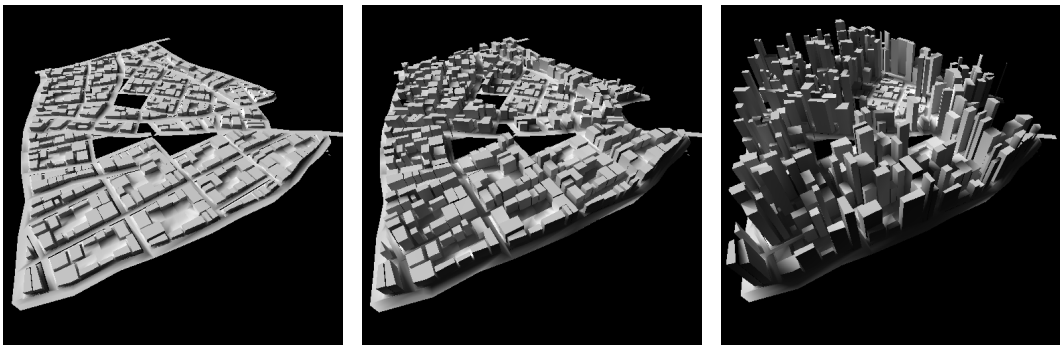

(a) City 1. (b) City 2. (c) City 3.

Figure 4.4: Three different city models generated with height building variation from the same layout.

4.4.2 Sparsity Results for $\mathbf{F}$ and $\tilde{\mathbf{M}}$

We show the sparsity results for the described city models. For each model, three variants are studied: the original (n=8897), dividing each patch into 4 (n=35588) and into 16 (n=142352), where n is the number of patches. This allows analyzing the proposed algorithm for bigger models, as well as the effect of dividing patches in the sparsity factor. The calculation of $\mathbf{F}$ takes about 20s, 90s, and 600s for n=8897, 35588, and 142352, respectively.

First of all, we explore the density of $\mathbf{M}$ matrices (n=8897, inverted with MATLAB) and the distribution of their elements, for different reflectivity indexes $\mathbf{R}$ (Fig. 4.5). It can be appreciated that most of the matrices elements are non-zero, and also that most of them have very small values.

An increment in the value of $\mathbf{R}$ is related to an increment in the values of the matrix elements. The matrices of City 1 have smaller elements than those related to City 3. For example, only 3% of the elements corresponding to City 1 are greater than 10^{-5} for $\mathbf{R}$ <= 0.7, while approximately 10% of the elements in City 3 satisfy this property. In the rest of the paper, a reflectivity index of 0.7 is used. This value is higher than the expected for cities, but it is useful for challenging the sparsity of the matrices $\tilde{\mathbf{M}}$.

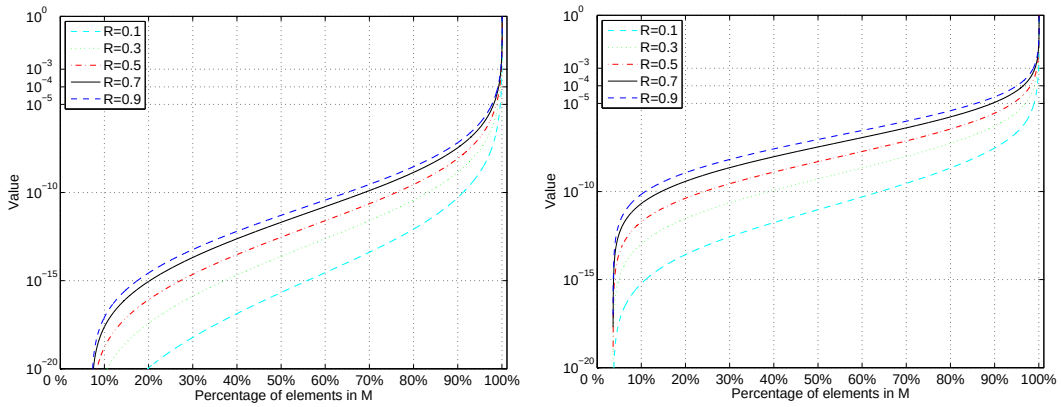

(a) City 1.

(b) City 3.

Figure 4.5: Distribution function of the $\mathbf{M}$ elements, for different reflectivity indexes and cities.

The sparsity results and memory storage for $\mathbf{F}$ and $\tilde{\mathbf{M}}$ matrices can be seen in Table 4.1. As expected, the density factor of $\mathbf{F}$ grows as the city model becomes less homogeneous, which implies the use of a larger memory space. Nevertheless, the density reported in the worst case (City 3 with n = 8897) represents a storage of 1.23% of the total elements of the matrix. On the other hand, the density factors are smaller for finer meshes of the same city model.

The density factor of $\tilde{\mathbf{M}}$ has a similar behavior to that described for $\mathbf{F}$. Also, for all cases, the density increases as the threshold ε becomes smaller. The memory required to store the sparse matrices $\mathbf{F}$ and $\tilde{\mathbf{M}}$ is always lower than its full version, for each of the test cases executed.

		Density	Density of $\tilde{\mathbf{M}}$			Memory size (GB)			Gain	
	n	of $\mathbf{F}$	$\varepsilon = 10^{-3}$	10^{-4}	10^{-5}	Full	$\mathbf{F}$	$\tilde{\mathbf{M}}$ (10^{-5})	$\mathbf{F}$	$\tilde{\mathbf{M}}$ (10^{-5})
City 1	8897	0.68 %	0.22 %	0.61 %	1.48 %	0.60	0.01	0.02	60×	30×
	35588	0.48 %	0.10 %	0.31 %	0.83 %	9.66	0.09	0.17	107×	57×
	142352	0.35 %	0.04 %	0.15 %	0.45 %	154.60	1.05	1.46	147×	106×
City 2	8897	0.84 %	0.30 %	1.01 %	2.58 %	0.60	0.01	0.03	60×	20×
	35588	0.60 %	0.15 %	0.51 %	1.41 %	9.66	0.12	0.28	80×	34×
	142352	0.44 %	0.05 %	0.24 %	0.75 %	154.60	1.34	2.42	115×	64×
City 3	8897	1.23 %	0.55 %	2.07 %	6.24 %	0.60	0.01	0.08	50×	7.5×
	35588	0.87 %	0.20 %	0.88 %	2.98 %	9.66	0.17	0.59	57×	16×
	142352	0.64 %	0.06 %	0.36 %	1.40 %	154.60	1.94	4.52	80×	34×

Table 4.1: Density and memory size of the form factors matrices and the approximated inverse. The gain equals to the full memory size over the sparse memory size.

4.4.3 Execution Times

In order to study the computational performance of the proposed algorithm, we calculate the daylight illumination for a whole year. For this, we use the 3 city models with the 3 mesh variants, along with 3650 sky configurations. The obtained result is compared against the execution times of solving the same radiosity problem iteratively, using the Jacobi iteration (Eq. 4.2).

Table 4.2 shows the obtained execution times for the described test cases. Table 4.3 shows the speedup over the Jacobi based method. It is important to highlight that this speedup is calculated taking into account both time to compute $\tilde{\mathbf{M}}$ and time to compute $\tilde{\mathbf{M}}\mathbf{E}$. That is, speedup = $T_J \big/ (T_{\tilde{\mathbf{M}}} + T_{\tilde{\mathbf{M}}\mathbf{E}})$, where T_J is the execution time needed to calculate the radiosity using Jacobi. For each case, the number of iterations (light bounces) used to compute T_J is the same than the used for $\tilde{\mathbf{M}}$.

As can be appreciated in the tables, the execution times depend highly on the correspondent density factor of $\tilde{\mathbf{M}}$. The sparser this matrix is, the lower the execution times are. For the considered example problem, the proposed algorithm works faster than the Jacobi iteration method for all the test cases.

		Time for $\tilde{\mathbf{M}}$ ($T_{\tilde{\mathbf{M}}}$)			Time for $\tilde{\mathbf{M}}\mathbf{E}$ ($T_{\tilde{\mathbf{M}}\mathbf{E}}$)			Time for Jacobi (T_J)		
	n	$\varepsilon = 10^{-3}$	10^{-4}	10^{-5}	$\varepsilon = 10^{-3}$	10^{-4}	10^{-5}	$\varepsilon = 10^{-3}$	10^{-4}	10^{-5}
City 1	8897	0.17s	0.68s	2.51s	0.52s	1.22s	2.88s	32.78s	51.68s	79.77s
	35588	1.10s	7.08s	32.80s	3.72s	10.20s	26.70s	334.51s	594.43s	993.65s
	142352	7.33s	60.90s	440.00s	26.40s	89.80s	264.00s	3710.30s	6615.73s	14150.40s
City 2	8897	0.26s	1.49s	5.80s	0.71s	1.99s	4.99s	43.84s	76.56s	117.61s
	35588	2.06s	15.20s	79.60s	5.17s	16.20s	45.70s	530.68s	963.98s	1691.55s
	142352	11.80s	136.00s	1180.00s	34.20s	140.00s	442.00s	5704.00s	11509.20s	27411.80s
City 3	8897	0.52s	4.10s	18.40s	1.09s	4.04s	11.90s	72.93s	129.43s	203.01s
	35588	3.35s	38.00s	264.00s	6.91s	29.10s	100.00s	826.96s	1758.02s	3385.20s
	142352	15.80s	306.00s	4070.00s	37.70s	223.00s	837.00s	10058.00s	22323.80s	72132.90s

Table 4.2: Execution times (in seconds) of radiosity calculations for the test cases. Both $T_{\tilde{\mathbf{M}}}$ and T_J are computed using 40 iterations (light bounces).

		Speedup = $T_J \big/ (T_{\tilde{\mathbf{M}}} + T_{\tilde{\mathbf{M}}\mathbf{E}})$		
	n	$\varepsilon = 10^{-3}$	10^{-4}	10^{-5}
City 1	8897	47.5 ×	27.2 ×	14.8 ×
	35588	69.4 ×	34.4 ×	16.7 ×
	142352	110.0 ×	43.9 ×	20.1 ×
City 2	8897	45.2 ×	22.0 ×	10.9 ×
	35588	73.4 ×	30.7 ×	13.5 ×
	142352	124.0 ×	41.7 ×	16.9 ×
City 3	8897	45.3 ×	15.9 ×	6.7 ×
	35588	80.6 ×	26.2 ×	9.3 ×
	142352	188.0 ×	42.2 ×	14.7 ×

Table 4.3: Execution time speedup for radiosity calculations. The acceleration is calculated using the values of T_J, $T_{\tilde{\mathbf{M}}}$, and $T_{\tilde{\mathbf{M}}\mathbf{E}}$ extracted from Table 4.2.

4.4.4 Radiosity Results

In this section we study the impact of the proposed algorithm on the radiosity results. We use 132 different sky configurations, each one with a unique sky tile illuminating the scene, to compute 132

radiosity solutions of the city. Given a patch of the city, the radiosity value calculated for each of the sky configurations is related to the concept of Daylight Coefficient [Tregenza and Waters, 1983]. The linear combinations of the radiosity solutions for the 132 skies allow to find the radiosity of the city for any other sky configuration. Figure 4.4 shows the radiosity values of the three cities for the same sky configuration, when ε=10^{-5}.

Comparison with Jacobi

Table 4.4 shows the relative errors of the 132 radiosities obtained, comparing $\widetilde{B}$=$\widetilde{\mathbf{M}}E$ to the solution (B_J) of the Jacobi iteration methodology (Eq. 4.2). The initial emission is the first bounce of the light emitted from the sky (Sec. 4.3.4). The mean, standard deviation and maximum values are reported. As expected, the error gets smaller as the city homogeneity increases and as the truncation factor decreases. For every case, the standard deviation is small, as well as the maximum error is close to the mean value.

		Relative error of $\widetilde{B}$: $\frac{\|\widetilde{B}-B_J\|}{\|B_J\|}$ (×1000)								
		$\varepsilon = 10^{-3}$			$\varepsilon = 10^{-4}$			$\varepsilon = 10^{-5}$		
	n	μ	σ	Max	μ	σ	Max	μ	σ	Max
City 1	8897	27.80	2.29	29.40	7.83	0.73	8.29	1.88	0.19	2.00
	35588	53.00	3.17	55.70	16.90	1.25	17.90	4.53	0.36	4.78
	142352	48.60	5.09	52.80	15.30	1.88	16.70	4.15	0.57	4.57
City 2	8897	87.70	6.44	95.20	31.70	2.99	34.20	9.50	1.04	10.30
	35588	86.50	9.15	97.80	35.00	5.42	39.80	11.00	2.20	12.80
	142352	134.00	11.70	154.00	61.80	6.24	69.30	23.00	3.41	25.90
City 3	8897	92.60	3.92	98.20	33.30	2.11	35.30	9.86	0.72	10.50
	35588	141.00	8.67	155.00	59.30	4.80	64.20	19.70	1.93	21.40
	142352	189.67	17.74	221.03	99.20	8.45	113.05	42.14	4.77	47.12

Table 4.4: Radiosity errors for the test cases (all numbers are ×1000). Here, $\widetilde{B}$=$\widetilde{\mathbf{M}}E$ and B_J is the result of using the Jacobi iteration methodology.

3^{rd} and successive light bounces

The indirect lighting is an important component of the illumination of the city. Next, a test is performed to measure the precision of the radiosity results without taking the direct and first bounces into account. In Figure 4.6, the average radiosity values for the 132 different sky configurations are shown (for two city models). All the radiosity curves are sorted from lowest to highest values. In both plots, we present the results using the Jacobi iteration method for computing the full radiosity (B_J) and the radiosity considering only the third and successive bounces (S_J). Also, we show the same results using the proposed algorithm for different truncation thresholds. As can be appreciated, the illumination is much higher in B_J than in S_J, because the first two bounces are the main component of the total radiosity. Nevertheless, the rest of the bounces together are not negligible, which means that they cannot be discarded in the calculations. Taking a closer look into the results of the proposed algorithm, it is evident that a higher truncation threshold implies a higher error. When compared to the Jacobi solution, the results seem close enough for most practical applications, when ε=10^{-4} and

10^{-5}. Finally, the absolute errors $\|B - B_J\|$ seem to have similar values to the errors $\|S - S_J\|$, which leads to think that most of the radiosity error is produced after the 2^{nd} bounce.

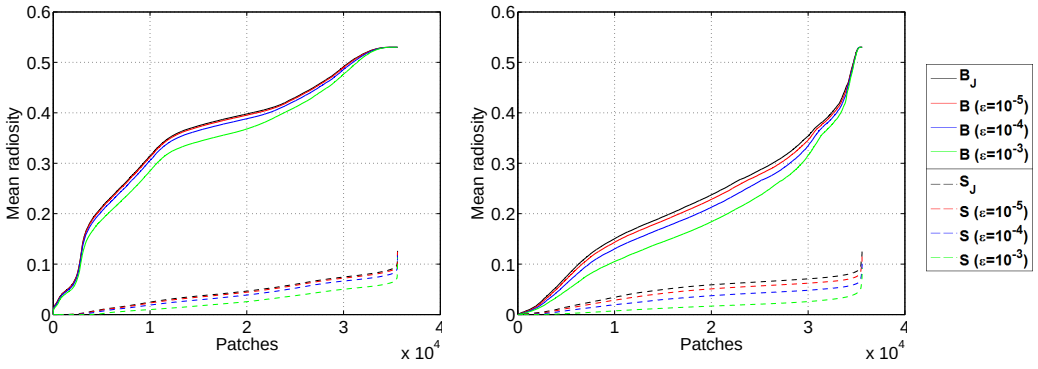

(a) City 1. (b) City 3.

Figure 4.6: Comparison of radiosity results between Jacobi ($\mathbf{B}_j$), third and successive bounces ($\mathbf{S}_j$), and their approximations using different thresholds.

4.5 An alternative optimization considering discarded elements

The described algorithms have shown good results for the tested city models. The sparse radiosity matrix allows to speed up the computations, while the method for approximating its inverse is suitable when the geometry is static and several thousand radiosity calculations must be performed. However, there are still many optimizations to be added to the algorithms. In this section, we propose a corrective technique for improving the precision of radiosity results when using the approximated inverse of the radiosity matrix.

The main error of the algorithm that computes $\tilde{\mathbf{M}}$ is related to the removal of terms below the input threshold. In the previous experimental analysis, these elements were eliminated and not taken into account. In this section, we propose an alternative method for including them in the radiosity calculations, in order to improve the precision of the results.

Let's consider $\mathbf{\Delta}$ to be the error produced by the method to approximate the inverse of the radiosity matrix ($\mathbf{M}$):

$$\mathbf{M} = \mathbf{M} + \mathbf{\Delta} \tag{4.5}$$

By construction, $\mathbf{\Delta}$ can be approximated by accumulating the elements discarded in the Neumann iteration (elements below the input threshold). Then, similarly to Eq. 4.3, the radiosity vector B corresponding to an emission E can be approximated in the following manner:

$$B \approx (\mathbf{M} + \mathbf{\Delta})E = \mathbf{M}E + \mathbf{\Delta}E \tag{4.6}$$

Because of the results shown at Figure 4.5, we can predict that the matrix $\mathbf{\Delta}$ is a full matrix, which prohibits its storage in system memory. Therefore, the term $C = \mathbf{\Delta}E$ needs to be approximated using other techniques.

The i-th element of C is computed in the following way, where $\delta_{i,j}$ are the elements of $\mathbf{\Delta}$, and e_i is the i-th element of E:

$$C_i = \delta_{i,1}e_i + \delta_{i,2}e_i + ... + \delta_{i,n}e_i \ , \ \forall i \in 1..n \tag{4.7}$$

When the values of e_i are similar (for instance, in the city there are many patches receiving direct sky and sun light), they can be approximated by their mean $\mu(E)$=$\sum_{i=1}^{n} e_i$. Therefore, Eq. 4.7 can be substituted by Eq. 4.8.

$$C_i \approx (\delta_{i,1} + \delta_{i,2} + ... + \delta_{i,n})(\frac{e_1 + e_2 + .. + e_n}{n}) = \mu(E) \sum_{j=1}^{n} \delta_{i,j} \tag{4.8}$$

Now, $\mathbf{\Delta}$ is approximated accumulating the discarded elements by row, at each iteration. This is equivalent to accumulate the discarded elements by scene patch, which gives an idea of how much error is produced by the technique at every polygon. Besides, the emission is approximated by its mean value, which can be an inaccurate approach if only few patches are emitters.

Algorithm 2 shows the new scheme, which is very similar to the previous algorithm (Algorithm 1). $\mathbf{\Delta}$ is the matrix that contains all the elements that were removed from $\mathbf{T}$ at each iteration. The operation "sum" performs the summation by row, and the result is accumulated into vector δ.

Algorithm 2 Calculate $\tilde{\mathbf{M}}$ and accumulate discarded elements.

1: $\tilde{\mathbf{M}} = \mathbf{0}$
2: $\delta = \mathbf{0}$
3: $\mathbf{T} = \mathbf{I}$
4: **while** $\mathbf{T} \neq \mathbf{0}$ **do**
5: $\quad \tilde{\mathbf{M}} = \tilde{\mathbf{M}} + \mathbf{T}$
6: $\quad \mathbf{T} = \mathbf{TRF}$
7: $\quad [\mathbf{T}, \mathbf{\Delta}] = \text{remove}(\mathbf{T}, \varepsilon)$
8: $\quad \delta = \delta + \text{sum}(\mathbf{\Delta})$
9: **end while**

The vector δ is calculated at almost no computational cost, and is then applied to compute the radiosity vector. Once $\tilde{\mathbf{M}}$ and δ are computed, and given an emission vector E, the radiosity solution is calculated following Eq. 4.9. Here, $\mu(E)$ means the average emission value.

$$\widetilde{B} = \mathbf{M}E + \delta\mu(E) \tag{4.9}$$

As can be seen, this strategy adds an average energy value to the radiosity of each patch, weighted by the sum of terms discarded when computing $\tilde{\mathbf{M}}$. Next, some experimental analyses are performed to test this technique in daylighting calculations.

The new algorithm is applied to the three city examples presented before (over flat terrain). In the same way than Sec. 4.4.4, we use 132 different sky configurations, each one with a unique sky

element illuminating the scene, to compute 132 radiosity solutions of the city. Table 4.5 shows the relative errors of the 132 radiosities obtained, comparing $\widetilde{B} = \widetilde{\mathbf{M}}E$ to the solution (B_J) of the Jacobi iteration methodology (Eq. 4.2). The mean, standard deviation and maximum values are reported.

		Relative error of $\widetilde{B}$: $\frac{\|\widetilde{B}-B_J\|}{\|B_J\|}$ (×1000)								
		$\varepsilon = 10^{-3}$			$\varepsilon = 10^{-4}$			$\varepsilon = 10^{-5}$		
	n	μ	σ	Max	μ	σ	Max	μ	σ	Max
City 1	8897	11.30	2.10	15.30	2.73	0.53	3.74	0.58	0.11	0.80
	35588	23.00	4.82	32.00	6.31	1.38	8.96	1.51	0.35	2.19
	142352	22.40	4.62	30.70	6.26	1.32	8.69	1.57	0.34	2.20
City 2	8897	43.00	9.69	60.50	13.70	3.01	19.40	3.80	0.85	5.38
	35588	48.30	13.30	67.70	17.20	4.20	23.20	4.98	1.10	6.57
	142352	79.30	24.50	113.00	32.30	9.08	45.20	11.10	2.55	14.80
City 3	8897	42.90	10.60	61.80	13.30	3.11	19.20	3.42	0.85	5.05
	35588	74.10	18.70	105.00	27.30	6.22	38.70	8.15	1.84	11.60
	142352	117.16	38.09	177.58	55.12	16.81	79.35	20.92	5.64	29.41

Table 4.5: Radiosity errors using the new algorithm (all numbers are ×1000). Here, $\widetilde{B} = \mathbf{M}E + \delta\mu(E)$ and B_J is the result of using the Jacobi iteration methodology.

The new results improve the previous ones (see Table 4.4). The mean error is lower for all executed cases, which confirms that the new strategy allows to reduce the relative error in radiosity results. Additionally, despite the fact that the new standard deviations are greater, the maximum error values are still lower than before.

Figure 4.7 shows the relative error for the 132 emissions, using both previous and new algorithms. These plots correspond to City 3 with $n = 35588$, but it is necessary to highlight that the other environments show similar results. It can be observed that the new relative errors are lower than the previous ones, for every emission configuration and ε value.

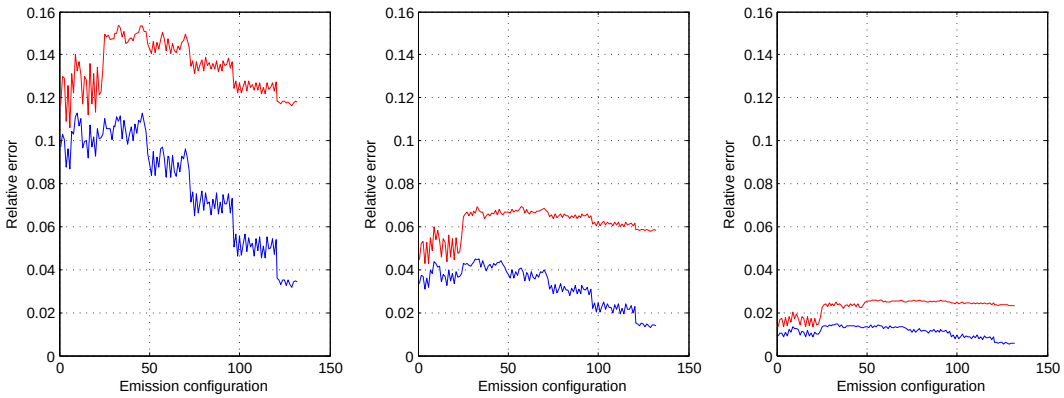

(a) $\varepsilon = 10^{-3}$ (b) $\varepsilon = 10^{-4}$ (c) $\varepsilon = 10^{-5}$

Figure 4.7: Relative error: $\frac{\|\widetilde{B}-B_J\|}{\|B_J\|}$ for the 132 emissions. These results correspond to City 3 with $n = 35588$. The red plot is the error for the original algorithm, while the blue plot is the error for the new algorithm.

4.6 Orography

Orography is the study of the topographic relief of a terrain [Glickman, 2000]. Identifying features and recognizing typical landform patterns are part of the field. It has a major impact on several subjects such as heat exchange, air movement and daylighting [Collier, 2006]. Topographic studies may have different goals: geological exploration, planning and construction for civil engineering projects, or even neuroimaging [Chakraborty, 2005]. This field becomes very important for city planning purposes, because building strategies depend highly on the properties of the surface to construct on. Moreover, in an urban environment, there is a relation between orography and daylighting [Johnson, 1981]. Different terrains lead to different occlusion patterns, which affects the light and heat interaction within the city. In this section, we study the effect of changing the terrain where the city lays. In particular, the density factor of the correspondent form factors matrices is measured.

To perform this study, three different terrains are used: a flat terrain, a hill terrain, and a valley terrain. Then, the three city models presented at Figure 4.4 are skewed according to the terrains shapes, creating six new scenes. Figure 4.8 illustrates the different terrains. Example pictures of the new models are shown in Figure 4.9.

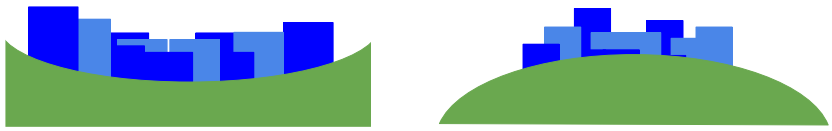

(a) City over valley. (b) City over hill.

Figure 4.8: Illustration of the valley and hill terrains.

As shown in Sec. 4.4.3, the execution times of computing radiosity solutions depends highly on the density factor of the matrix $\mathbf{F}$. Regardless of the strategy to use, this property helps to reduce the memory usage and the number of operations to perform. Figure 4.3 presented the number of patches that are seen from each patch in a flat city, and this affects directly on the sparsity results. The same study can be performed over the new scenes, in order to observe their patch classification graphically. Fig 4.10 presents this result for the three different variations of City 3, using 35588 patches. The valley terrain leads the city patches to see much more elements than over flat or hill terrains. This is because the "U" shape of the landform creates more visibilities between patches.

Next, the sparsity results are reported at Table 4.6, combining terrains, city types and number of patches. Once again, the results show the same behavior as the patch classification shown in Figure 4.10. The valley terrain makes $\mathbf{F}$ much more dense (reaching a maximum value of 14.3%), while the hill landform produces similar results than the flat one. Moreover, for City 3, results using the hill terrain are less dense than using the flat. These results can be explained by taking a look into the different types of patches in the models. For example, in the case of patches belonging to a building's ceiling, the visibility increases drastically in the lower part of a valley terrain, because a big part of the city is now seen from it. On the other hand, the visibility of the ceilings is reduced when they are located at the top of a hill. These facts, along with other similar phenomena, have a direct incidence in the density results for $\mathbf{F}$.

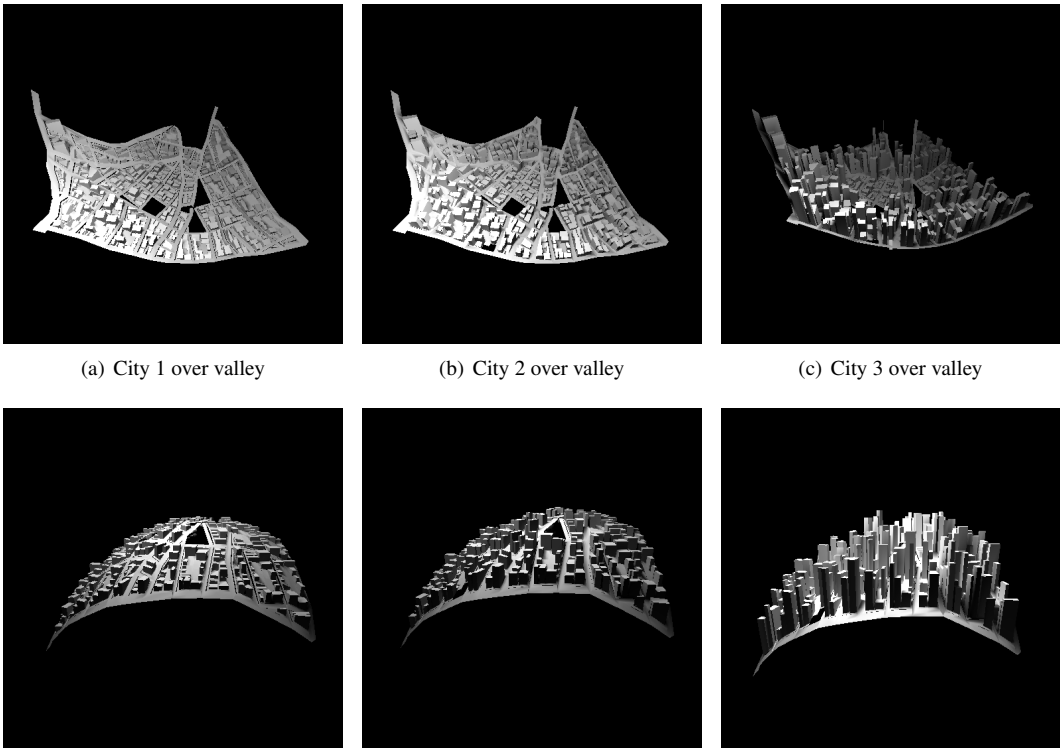

(a) City 1 over valley (b) City 2 over valley (c) City 3 over valley

(d) City 1 over hill (e) City 2 over hill (f) City 3 over hill

Figure 4.9: Six urban scenes generated by posing the three cities into different terrains.

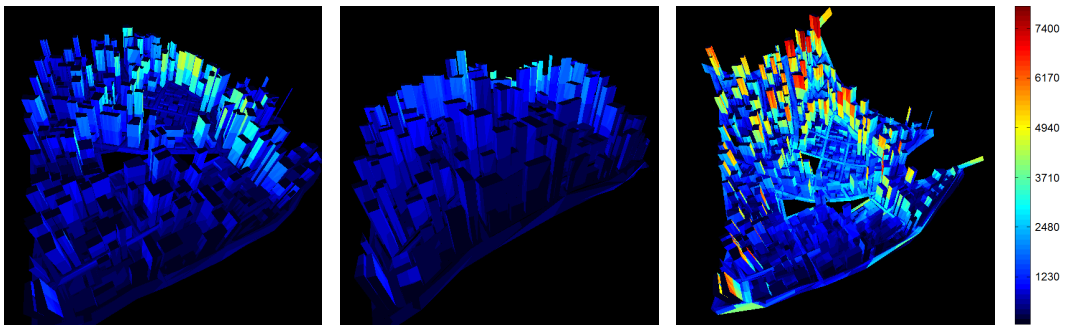

(a) City 3 flat. (b) City 3 over hill. (c) City 3 over valley.

Figure 4.10: Three variations of City 3. The color of a patch indicates the number of patches that are seen from it. All three models are composed of 35k patches.

	n	Flat	Valley	Hill
City 1	8897	0.68%	14.3%	0.87%
	35588	0.48%	9.10%	0.60%
	142352	0.35%	4.87%	0.42%
City 2	8897	0.84%	6.48%	0.96%
	35588	0.60%	4.19%	0.66%
	142352	0.44%	2.48%	0.47%
City 3	8897	1.23%	2.99%	1.14%
	35588	0.87%	1.97%	0.79%
	142352	0.64%	1.31%	0.58%

Table 4.6: $\mathbf{F}$ density factors for different cities, orographies and n values.

4.7 Conclusions and future work

The correlation between the characteristics of a city and the sparsity of its form factors matrix $\mathbf{F}$ shows that the memory requirements of $\mathbf{F}$ can be significantly reduced using sparse representations. Hence, we use a method for approximating the inverse of the radiosity matrix, based on the use of Neumann series. At each series term, all elements below a threshold are removed, which leads to very sparse matrices.

The proposed method was used for daylight simulation. Once a sparse approximation of the inverse of the radiosity matrix is computed, the radiosity corresponding to a sky configuration can be calculated using a single matrix-vector operation. This allows determining the city illumination for a whole year of daylight at reasonable execution times.

The experimental analysis shows that more homogeneous cities produce more sparse $\mathbf{F}$ matrices. The matrices are sparse enough to be stored in the main memory of a desktop computer, considering city scenes that contain up to 140k patches. Another result is that the approximation to the inverse of the radiosity matrix is also sufficiently sparse to be stored in main memory.

The computed matrices were tested for radiosity calculations with several sky configurations. We compared the results with a Jacobi iteration method, and found that the results are sufficiently accurate. Accelerations of up to two orders of magnitude are obtained with less than 0.1 relative error. Moreover, we presented a method using the elements discarded at each Neumann series term for reducing the previous relative errors without introducing a relevant overhead in memory consumption or execution time.

Concerning orography, it was found that the terrain where the city lays has a big influence on $\mathbf{F}$. For example, if the land-form is a valley, $\mathbf{F}$ becomes denser than in a flat terrain. On the other hand, when using hill-type topographies, the results do not vary significantly with respect to flat-type. This study allows concluding that it is possible to work with different types of terrains for city models, but this will have an impact on the execution times and memory consumption of radiosity calculations.

With respect to future work, it should be very important to develop a method for classifying models previous to radiosity calculation, in order to choose the correct method for reducing the memory requirements. Further works should address the study of the form factors associated with real city models, and also taking other characteristics into account, such as the building density. Besides, the simulation of the effect of light over cities can be the empirical basis to the proposal and/or modification of city regulations. Other possible line of work is related to the interior and exterior

design of new city elements, like office buildings and public places, taking into consideration the main characteristics of the surroundings. Finally, the proposed methods can be used for computing global radiation exchange in cities, for heat transfer calculations. This requires the inclusion of other elements, such as those related to the heat equation.

Acknowledgments The work was partially supported by FSE_1_2014_1_102344 project from Agencia Nacional de Investigación e Innovación (ANII, Uruguay) and TIN2014-52211-C2-2-R project from Ministerio de Economía y Competitividad, Spain.

Chapter 5

Importance-driven approach for reducing urban radiative exchange computations

---

The contents of this chapter were published in:
Aguerre, J. P., Fernández, E., and Beckers, B. (2019). *Importance-driven approach for reducing urban radiative exchange computations*. Building Simulation, 12-2, 231-246. Springer.

In the context of large scale urban heat transfer simulation, the prediction of radiative flux at short and long wave spectra is a step necessary to obtain accurate results. From a computational perspective, this task is expensive because realistic conditions require calculations in many sensors, considering multiple radiation bounces, and evaluating many hundred daylighting conditions. Radiosity-based approaches are adequate methods for processing the large number of diffuse surfaces that are usually present in city models. However, the high memory consumption of these algorithms turns them inefficient for handling big geometries, and therefore ray tracing techniques are commonly used.

In this article we present a study on using the *importance* concept to improve the performance of radiosity calculations at the urban scale. The algorithm is able to consider diffuse and specular materials, and it proves to be a viable alternative to ray tracing. Since most of the information contained in big city models is not needed for simulating a selected zone of interest, the computational requirements can be reduced drastically. Several experiments are conducted to test the approach, and promising results are reported.

5.1 Introduction

Solar radiation is the fundamental source of heat and light energy for human life. The potential benefits of radiative energy are still a subject of study [Devabhaktuni et al., 2013]. The evolution of modern societies depends on how this source of energy is handled by architects, engineers, and

city planners. Emerging as a tool for this necessity, urban physics simulations are becoming a major topic of interest, providing a linkage between environmental and building physics. The simulation of physical phenomena related to energy, climate, and demographic change is important for the prediction of urban problems and the development of efficient solutions.

The design process of cities takes advantage of the analysis of urban radiation data for annual periods [Beckers, 2013a]. Forecasting the radiative exchange over an existing or future building helps in the projection of city structures, improving energy availability and climate effects in several ways. This exchange of radiation happens at two different bands. At the short wave spectrum, radiation is emitted by the sun and the sky, and then reflected within the city. At the long wave spectrum, city elements emit and reflect radiation. Materials react differently depending on the spectrum of radiation.

There is a growing interest in urban scale simulations from a computational physics perspective [Blocken, 2015; Muñoz et al., 2018; Strømann-Andersen and Sattrup, 2011]. Recent urban 3D modeling strategies provide access to high-definition city models composed of thousands of buildings [Musialski et al., 2013]. Heat transfer simulation methods, such as Finite Element Methods (FEM) [Lewis et al., 2004], must address the exchange of both short and long wave radiation, which is a challenge when dealing with big urban models. The computational complexity of the algorithms involved and the need for high precision results becomes a major concern.

Radiation computations have been widely studied by the rendering community [Pharr et al., 2016]. Ray-based approaches are successfully used for daylight simulations [McNeil and Lee, 2013; Reinhart et al., 2006; Ward, 1994] but dealing with big environments that are mainly composed of diffuse surfaces implies tracing hundreds of thousands of rays to obtain accurate results. For long wave radiation, strategies such as the Daylight Coefficient [Tregenza and Waters, 1983] would require $O(n^2)$ memory when handling scenes where all the surfaces (n) are emitters. In this regard, a viable alternative is to use the radiosity method [Cohen and Wallace, 1993], which has an algorithmic proximity with FEM, has been adapted for urban daylighting [Beckers, 2013a], and has a lower memory demand when working with city models [Aguerre et al., 2017].

Experience seems to indicate that most of the information contained in urban models is not needed for simulating a smaller part of the city, hereafter referred to as "zone of interest". The reason for this is that most of the elements outside the zone tend to have a smaller influence on the radiation calculation. Thus, the focus is now on finding those patches that have a significance in the calculations.

In this article we present a method for simulating urban radiation over the zone of interest that uses the concept of "importance" [Smits et al., 1992] to reduce the computations. Our proposal shows that the geometrical complexity and highly occluded visibility of city models make them very suitable for importance-driven approaches, which may bring about a renewed interest in this kind of algorithms in the near future. The low density factor of the associated form factors matrix, along with the possibility of discarding most of the city elements without introducing considerable error, allows performing radiative exchange computations over models composed of millions of patches.

symbol	definition
n	number of patches in the city
$\varepsilon_{\min}$	input threshold, minimum importance value
$\varepsilon_{\max}$	input threshold, maximum importance value
s	surface of interest, composed of multiple patches
v_s	scalar function over s
w_i	coefficient related to patch i
Ω_i	weight of initial emitter of importance
B	radiosity vector (W/m^2)
$\widetilde{B}$	approximation to the radiosity vector (W/m^2)
E	emission vector (W/m^2)
ψ	importance vector
ψ_s	specular importance vector
θ	initial source of importance
B_r	reflected radiosity vector (W/m^2)
I_t	total irradiance vector (W/m^2)
P	incident power vector (W)
$\mathbf{I}$	$n \times n$ identity matrix
$\mathbf{R}$	diagonal matrix with reflectivity indexes
$\mathbf{F}$	form factors matrix
$\mathbf{RF}$	matrix result of the product $\mathbf{R} \cdot \mathbf{F}$
Ψ	$n \times k$ matrix of importance for multiple patches
Θ	$n \times k$ matrix of initial source of importance for multiple patches

Table 5.1: Symbol notation.

5.2 Related work

This section describes the main concepts used in this article. Firstly, the radiosity algorithm is outlined, and the idea of importance is defined. Secondly, we address recent daylighting techniques for urban environments, and some applications.

5.2.1 The radiosity algorithm

The radiosity algorithm [Cohen and Wallace, 1993] is a view-independent global illumination technique based on a finite element methodology for solving the rendering equation [Kajiya, 1986]. In the discretization step, the scene is divided into n elements, also called patches. This process leads to a set of linear equations, which are expressed in a succinct manner in Eq. 5.1[1].

$$(\mathbf{I} - \mathbf{RF})B = E, \tag{5.1}$$

In this equation, B and E are vectors containing the radiosity value (W/m^2) of each patch and its initial emission, respectively. $\mathbf{I}$ is the identity matrix, $\mathbf{R}$ is a diagonal matrix containing the reflectivity index of each patch, and $\mathbf{F}$ is the form factors matrix. $\mathbf{F}(i, j)$ is a number between 0 and 1 expressing the form factor between patches i and j (fraction of light power going from one to another). Therefore, $\mathbf{F}$ is a $n \times n$ matrix requiring $O(n^2)$ memory to be stored using full representations. This calculation is a challenging computational problem when the size of n increases [Cohen

[1] In Chapters 4 and 5, B stands for radiosity. This is the same magnitude that is described with J in the rest of the thesis.

and Wallace, 1993].

In its most simple form, $\mathbf{F}$ is built with the assumption that the light power is emitted and reflected isotropically in all directions for each patch. This property leads to a purely diffuse behavior of materials. The inclusion of a wider variety of lighting effects implies computing "extended form factors" [Chen et al., 1991], which are useful for simulating phenomena such as specular reflections and refractions [Immel et al., 1986; Shao et al., 1988; Sillion and Puech, 1989]. The computation of diffuse form factors is usually accelerated using z-buffer techniques (such as the hemicube algorithm [Cohen and Greenberg, 1985]). Nevertheless, the specular part of the calculation of extended form factors is better suited for a recursive ray-based approach, allowing multi-bounces and arbitrary glossy BRDFs [Sillion et al., 1991].

After the computation of $\mathbf{F}$, the radiosity vector B corresponding to a particular emission configuration (E) can be calculated by solving the linear system iteratively. Eq. 5.2 shows the radiosity step using the Jacobi iteration.

$$B^{(i+1)} = \mathbf{RF}B^{(i)} + E \ , \ \text{where } B^{(0)} = E \tag{5.2}$$

Each iteration adds a new reflection of radiation to the global radiosity result. This process is repeated until $\|B^{(i+1)} - B^{(i)}\|$ is less than an expected error threshold. Note that the inclusion of multiple emitters does not affect the computational effort of the algorithm, unlike ray-based approaches. Also, the evaluation of different emissions for a fixed geometry does not require the re-computation of $\mathbf{RF}$.

5.2.2 Importance in radiosity

The concept of "importance" in radiosity was originally introduced by Smits et al. [1992]. The authors presented an algorithm for computing radiosity with respect to a limited number of views. This constraint reduces the computational effort in areas that have a small contribution to the results of the target surfaces.

Importance is a quantity dual to radiosity. It expresses the fraction of energy emitted at patch i that ultimately reaches the target surface j. This quantity is similar to radiosity in many aspects, but it is not the same. While radiosity is a flux density, importance is a dimensionless quantity. Intuitively, importance depicts how much influence a patch has in the radiosity results of other patches. This concept is very useful in scenes where most elements exchange energy with few others, since it helps discarding patches that have little influence in the set of target surfaces.

The mathematical formulation of importance (Eq. 5.3) is expressed using a new linear system, adjoint of the original transport equation (Eq. 5.1). Similarly, Eq. 5.4 shows the resolution of this system using Jacobi iterations. In this equations, θ and ψ are $n \times 1$ vectors: θ contains the initial source of importance, while ψ is the importance vector, dual to B.

$$(\mathbf{I} - \mathbf{RF})^T \psi = \theta, \tag{5.3}$$

$$\psi^{(i+1)} = (\mathbf{RF})^T \psi^{(i)} + \theta \ , \ \text{where } \psi^{(0)} = \theta \tag{5.4}$$

Following Smits et al. [1992], any linear function v in B can be expressed as $v = \theta^T B$, which is also the same as $v = \psi^T E$. Then, for each patch i, $\psi(i)$ gives the contribution by unit of emittance of i to v (see Sec. 5.3.4).

The application of this duality lead to the development of an efficient hierarchical radiosity algorithm, known as "Importance Driven radiosity". The basic concept of this method is that combining radiosity and importance allows to decide which interactions between patches should be refined. For a given emission E, a link between patch i and j is subdivided if the error exceeds a tolerance ε. This error measure is defined as the product of importance, radiosity, and the estimated form factor error. Thus, brightness and importance are considered together, guiding the refinement process to obtain better precision.

The formulation of importance has been used in many other research works, mostly related to realistic image synthesis. Bekaert and Willems [1995] used importance in a progressive refinement radiosity algorithm. The importance is computed incrementally to select the next most contributing patch in the progression, instead of using it for patch subdivision. Christensen et al. [1996] combined importance with wavelet radiance transport and applied the algorithm for computing illumination considering glossy surfaces. Neumann et al. [1996] presented an extension of stochastic ray radiosity algorithm. The extension considers importance to assess the selection of particle paths, giving a higher probability to sample the patches in the region of interest. From the same perspective, Prikryl et al. [2000] combined Neumann's approach with a hierarchical importance-driven radiosity approach: the importance values are used in the probability calculation for power propagation of an element.

In the literature, the scene used to test the algorithms is usually a labyrinth, which is a well-known case of highly occluded environment. When the viewer is located at a point inside the maze, the rest of the scene has a high probability of being occluded by the surrounding walls. Therefore, only few elements influence the radiosity results on a given surface. This concept is graphically shown in Figure 5.1(a). Figure 5.1(b) highlights the effect of specular reflections in the importance results. Besides labyrinth scenes, complex office/room models are often used. A common factor observed is that the use of importance is justified when testing over labyrinth models, because of their occluded nature. Office/room scenes tend to produce lower gains in memory consumption and execution time.

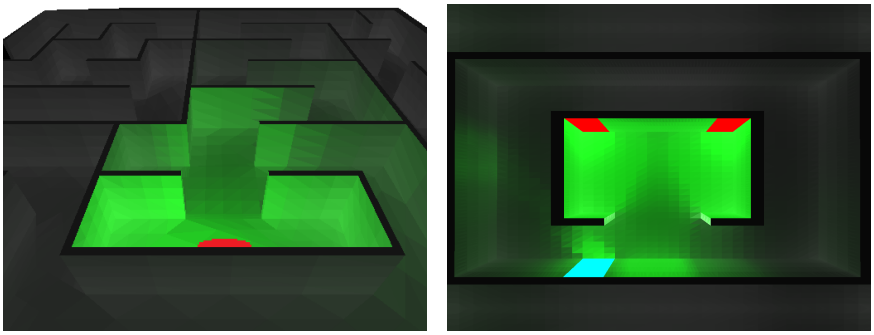

(a) Purely diffuse. (b) Specular surface in sky blue.

Figure 5.1: Example of labyrinth scene. Target surfaces are highlighted in red, while the importance values are shown in a green scale.

Special care should be taken when selecting the initial source of importance. When the zone of interest can be represented by a single patch i, the function $v = \theta^T B$ is equal to $B(i)$. Then, $\theta(j)$ is defined as $\delta_{ij}\ \forall j$, i.e. a vector of zeros with a unique 1 in the correspondent index. In rendering techniques, patch i represents the camera, which will then divide the importance into visible patches with a magnitude proportional to their projected solid angle [Bekaert and Willems, 1995; Christensen et al., 1996; Smits et al., 1992]. Another strategy consists in assigning a 1 to each visible/receiver patch. This procedure must be handled carefully to avoid over-sampling or over-refinement [Pattanaik and Mudur, 1993]. On a different approach, Suykens and Willems [2000] proposed using the minimum error (maximum importance) generated by each receiver patch independently for defining the importance configuration.

Christensen [2003] presented a detailed state-of-the-art review about the use of importance in rendering and other areas. The reader can refer to his work in order to obtain a wider understanding of the concept.

In our work, importance is not combined with radiosity values to guide the refinement process, because multiple emissions must be handled for simulating yearly solar data. Therefore, the selection and refinement of patches is performed in a pre-computation stage only considering importance, and the reduced model is used for computing the radiosity values.

5.2.3 Radiation computation on an urban scale

Radiation exchange is simulated through many strategies. RADIANCE-based approaches [Reinhart and Herkel, 2000] are widely used for interior daylighting, where an exterior city model can be used as occluder and reflector of light. The Daylight Coefficient (DC) approach, originally proposed by Tregenza [Tregenza and Waters, 1983], allows computing illuminance in a set of sensors. The sky dome is subdivided into sky tiles, and the contribution of each sky tile to each sensor is calculated. After the precomputation of DCs, thousands of sky conditions are evaluated in short times using matrix operations. To compute DCs, rays are casted from each sensor. Each ray is followed through a limited number of bounces until reaching the sky. When working with exterior models composed of hundreds of buildings, spatial subdivision techniques such as octrees allow significant acceleration of the calculations. City models commonly contain many diffuse surfaces, which involves casting a big number of rays to converge to accurate solutions. Irradiance caching [Jones and Reinhart, 2014; Ward et al., 1988] can be used to speed up this process.

Three-phase and Five-phase methods [Geisler-Moroder et al., 2017; McNeil and Lee, 2013] follow a similar approach for simulating complex fenestration systems. The first phase computes the contribution of the exterior (sky and urban context) into the fenestration. Recently, such simulations have been accelerated through GPU techniques [Jones, 2017; Overby et al., 2016], making an efficient use of modern hardware.

As an alternative to ray-based approaches, works have been developed using radiosity, so far only considering perfect diffuse surfaces. Robinson and Stone [2005] presented the simplified radiosity algorithm (SRA) for urban computations. Given a city composed of n patches, and a sky model represented by p elements, the main obstructions between each surface and every sky direction are grouped together. The original linear system is then reduced to $n \times p$. This method is embedded in the CitySim package [Robinson et al., 2009]. LICASO [Ashdown et al., 2017] is a climate-based

annual daylight simulation software entirely built on radiosity, which provides a good computational performance and a bounded error scheme. Beckers [Beckers, 2013b] suggested the use of radiosity along with condensation, a well-known finite element technique, to analyze long wave radiation on an urban scale.

In Aguerre et al. [2017], it was shown that the storage of the form factors of a city model is significantly reduced using sparse matrix representations. The high occlusion factor present in urban environments, where a patch i is commonly not seen by most patches j, implies that most $\mathbf{F}(i,j) = 0$. This advantage was used by Fernández et al. [2016a] for opening shapes optimization in a standard office considering the urban context. The illumination is computed for the whole city, which is modeled with a uniform mesh composed of approximately 150k patches. This approach works for small-to-medium sized cities, but it fails when bigger environments need to be simulated because the algorithm is memory demanding.

In this article, we present a novel method for computing urban radiative exchange based on radiosity and importance. The algorithm is a viable alternative to ray-based approaches, because it exploits the specific geometrical properties of urban environments to avoid the excessive memory consumption of previous radiosity works.

5.3 An efficient approach for handling big urban models

Our algorithm works in the following way. In the first place, an importance vector is computed for a coarse mesh, using the sparsity of $\mathbf{F}$ to accelerate the calculations. Then, unimportant patches are discarded in order to reduce the model size, and important patches are subdivided for precision purposes. Finally, radiative exchange is simulated for the target surfaces using multiple sky configurations. In Sec. 5.3.1 and 5.3.2 we start by making the assumption that all the surfaces are diffuse, and the zone of interest is represented by one patch. Sec. 5.3.3 presents an extension of the algorithm to handle specular surfaces and Sec. 5.3.4 defines a novel approach for handling multiple patches as the initial source of importance.

5.3.1 Computing the importance vector

It is likely that most of the information contained in the city model is not needed for simulating radiation over the zone of interest. Thus, the first step for improving the performance of the calculations is to determine the *importance* of each patch.

In this section the algorithm for computing the importance vector (Eq. 5.4) is defined for a single target patch representing the zone of interest, and assuming that all the surfaces are perfectly diffuse. This process is presented in Algorithm 3.

In the previous scheme, θ is a vector containing a 1 in the position of the target patch, and $\psi^{(new)}$ stores the importance vector. The elements of the rows of matrix $\mathbf{F}$ are added throughout the iteration process, computed using the hemicube algorithm [Cohen and Greenberg, 1985]. This approximation allows to only compute the parts of $\mathbf{F}$ that are sensitive in the calculation (see Algorithm 4, where $\varepsilon_{\min}$ is the sensitivity threshold). Moreover, the process becomes more efficient in execution time and memory, because $\mathbf{F}$ is stored using a sparse representation. The algorithm is repeated until the contribution of the step is less than a small threshold t.

Algorithm 3 Importance vector calculation

Input: θ, $\varepsilon_{\min}$
Output: $\psi^{(new)}$

1: $\psi^{(new)} \leftarrow \theta$
2: **repeat**
3: $\psi \leftarrow \psi^{(new)}$
4: $\mathbf{F} \leftarrow$ computeFormFactors($\psi, \varepsilon_{\min}$)
5: $\psi^{(new)} \leftarrow (\mathbf{RF})^T \psi + \theta$
6: **until** $\|\psi^{(new)} - \psi\| < t$

Algorithm 4 $\mathbf{F} \leftarrow$ computeFormFactors(ψ,$\varepsilon_{\min}$)

Input: ψ, $\varepsilon_{\min}$
Output: $\mathbf{F}$

1: **for** $i \mid \psi(i) > \varepsilon_{\min}$ **do**
2: **if** $\mathbf{F}(i,:)$ is not yet computed **then**
3: Compute $\mathbf{F}(i,:)$
4: **end if**
5: **end for**

5.3.2 Selecting and subdividing patches in the city mesh

The major advantage of our approach is the removal of patches that do not have a considerable influence on the radiation calculation, reducing the size of the city models without introducing significant errors in the calculation. Moreover, it allows working with huge city models that otherwise cannot be processed.

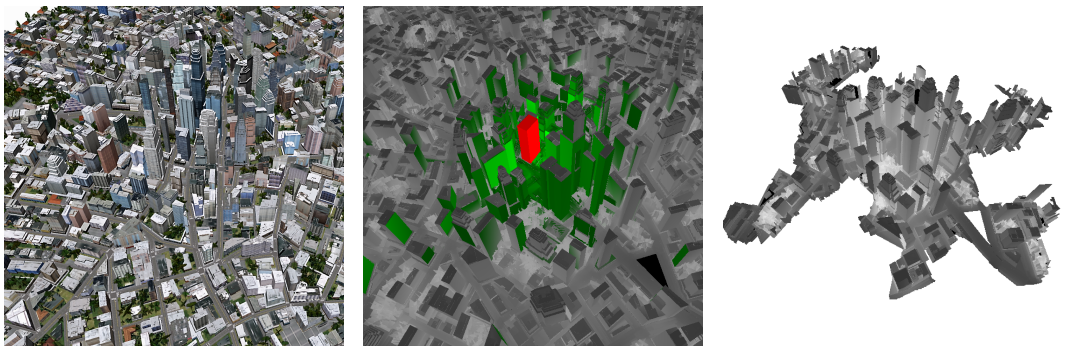

(a) Global view of the input city.

(b) Patches colored by importance (green), selected building (red).

(c) New model: part of the city useful for solar radiation computations.

Figure 5.2: Process of the algorithm shown graphically: (a) input city (b) importance results (c) global view of the city after removing unimportant patches.

The importance values are used for selecting the subset of important patches, and to subdivide the elements in order to improve the precision of the radiosity solutions. This process is described in Algorithm 5, where $\varepsilon_{\min}$ and $\varepsilon_{\max}$ are two input thresholds. $\varepsilon_{\min}$ defines the minimum value of importance for a patch to be considered, while $\varepsilon_{\max}$ is the maximum value of importance before subdividing a patch. The function "refinePatch" subdivides patch i into elements with importance below $\varepsilon_{\max}$, which is a simple task to perform given that the importance of a child element always decreases with its area [Smits et al., 1992].

Algorithm 5 Select and refine patches

Input: M (city model), ψ, $\varepsilon_{\min}$, $\varepsilon_{\max}$
Output: M

```
for i ← 1 to n do
    if ψ(i) < ε_min then
        M ← removePatch(M, i)
    else if ψ(i) > ε_max then
        M ← refinePatch(M, i)
    end if
end for
```

Once the important patches of the city are selected and refined, the matrix $\mathbf{F}$ is computed for the reduced model. This matrix can be used to simulate long wave radiation efficiently, because radiosity can handle multiple emitters without increasing the computations, in contrast with ray-based algorithms. For short wave radiation, we use a Reinhart sky subdivision of 2305 elements [Bourgeois et al., 2008] as the sky model. Typical Meteorological Year [Ebrahimpour and Maerefat, 2010] weather data is used to generate climate-based data. A sky radiance distribution model (Perez et al. [1993]) generates the emission configurations that allow performing whole year simulations on an urban scale over the selected zone of interest through radiosity.

Figure 5.2 shows an example of execution of the algorithm. Given the city model to handle, a patch is selected, and its importance vector is computed. Patches with a considerable influence are selected and subdivided, and the others are discarded. The resultant city model is much smaller than the original, having a direct impact on memory and execution time performance of radiosity calculations.

The differences between the use of importance in the proposed method and the original algorithm presented by Smits et al. [1992] are summarized in the following way:

- In Smits et al. a hierarchical radiosity approach is used, while in this paper a standard adaptive subdivision scheme is presented.
- In Smits et al. the matrix $\mathbf{F}$ is replaced by a tree structure that defines the interaction between elements in the hierarchy. Our approach solves the radiosity system (Eq. 5.1) storing $\mathbf{F}$ with a sparse format.
- Importance-driven radiosity is specially designed to compute the illumination for a particular emission, while our method aims to take many thousands of solar configurations or long-wave emissions into account.
- Our proposal is capable of considering specular surfaces and multiple emitters of importance. These extensions will be described in the next sections.

5.3.3 Extension for treating specular surfaces

The use of materials with specular properties in exterior urban scenes has increased in the last decades. Furthermore, elements such as water (lakes, rivers) present a specular behavior that must be taken into account in the calculations to obtain realistic results [Ho et al., 2011]. We propose to use the approach presented by Sillion and Puech [Sillion and Puech, 1989] to handle specular reflections in our radiosity engine. This algorithm implies a combination of the classical hemicube

technique with an embedded ray tracing engine to follow specular paths. The advantage of this technique is that it allows to simulate any light phenomena that a regular ray-based engine handles, such as arbitrary BRDFs (Bidirectional Reflectance Distribution Functions). As a proof of concept, in this article we are going to consider mirror-like specular reflections with multiple bounces.

The calculation of extended form factors follows a two step approach for each patch. In the first place, five projections (one for each face of the hemicube) are generated using the z-buffer technique. The second step, responsible for the extended part, consists in casting rays only into those patches seen by the hemicube that have a specular component. Each ray is recursively traced until hitting a purely diffuse surface (Figure 5.3). The elementary form factor is distributed along the patches that were hit by the ray in accordance to their specular and diffuse indices. Although the inclusion of a ray tracing engine reduces the performance of the hemicube technique, this modification does not produce a critical slowdown in the overall execution time if the fraction of specular surfaces in the urban model is moderate.

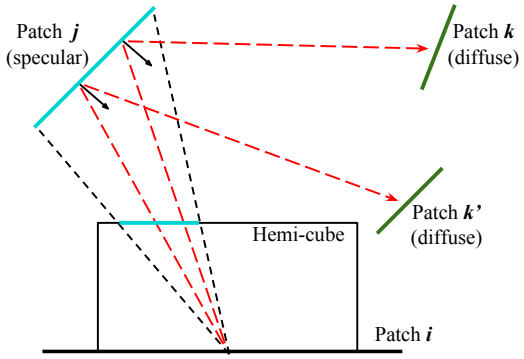

Figure 5.3: Calculation of extended form factors. A fraction of $\mathbf{F}(i,j)$ is distributed between $\mathbf{F}(i,k)$ and $\mathbf{F}(i,k')$, because patch j has specular properties.

This approach for handling specular surfaces is designed for radiosity computations. The next step consists in linking extended form factors with importance. Let us assume patch i is the target surface that emits importance. This importance bounces on patch j and reaches patch k. Then, both patches j and k are equally responsible for the radiation reaching i. In other words, if one of the patches is discarded, then the other loses its importance. The only difference is that the importance associated with j is, in some way, an indirect specular importance.

In order to incorporate this concept into our algorithm, we define a new specular importance vector ψ_s. Going back to line 3 in Algorithm 4, the extended form factors are now computed and stored in $\mathbf{F}(i,:)$. Here, a new vector S is generated, indicating a weight for each specular surface involved in the calculation of $\mathbf{F}(i,:)$. Every time a path $i \rightarrow j \rightarrow k$ (with j being the specular patch) is found, the elementary form factor is not only added to $\mathbf{F}(i,k)$, but also to $S(j)$. If the path has multiple specular bounces ($i \rightarrow j \rightarrow j' ... \rightarrow k$), then the value is added to the indices corresponding to all the traversed specular patches. The results in S should be incorporated into our global indirect specular importance vector:

$$\psi_s = \psi_s + S * \psi(i)$$

Now, two importance vectors are generated by the algorithm: the original ψ, which contains diffuse

importance and is renamed ψ_d, and ψ_s. The selection and refinement of patches (see Algorithm 5) is performed with the sum of both vectors, $\psi = \psi_d + \psi_s$.

5.3.4 Handling multiple target patches

In this section we analyze the case of an initial importance configuration emitted by multiple patches, composing a surface s. We categorize the multiple emission problems in two groups. In the first group (the linear case) a single vector θ_s determines ψ_s through Eq. 5.3. In the second group (the non-linear case), each patch i in s is used to calculate a vector ψ_i, and then these vectors are combined using a non-linear operation for computing ψ_s. In both cases, s must contain a relatively small number of patches when compared to the size of the city, to reduce the memory requirements of $\mathbf{F}$.

The linear case

Let us suppose that the problem consists in finding the total incident power P received by a surface s composed of multiple patches. This problem is expressed as:

$$P(s) = \sum_{i \in s} w_i B(i) \text{ , where } w_i = A_i/R_i \text{ (ratio between area and reflectivity index of patch } i)$$

$P(s)$ is a linear function in B. Thus, as expressed in Sec. 5.2.2:

$$P(s) = v_s = \theta_s^T B = \psi_s^T E \text{ , where } \theta_s(i) = \left\{ \begin{matrix} w_i \text{ when } i \in s \\ 0 \text{ otherwise} \end{matrix} \right\} \quad \forall i \in \text{scene}$$

In this equation, ψ_s is the importance vector corresponding to the calculation of $P(s)$. The previous scheme is useful for any other calculation that implies a linear function in B, such as total reflected power, total absorbed power, etc.

The calculation of radiosity for each patch in s is usually addressed as a linear problem, assigning an initial importance emission of 1 to each of these patches [Christensen, 2003]. The main drawback of this approach is that the final importance of every patch in the scene is the *sum of the importances* of all the contributing patches, reaching higher values than needed, and thus leading to over-refinement.

The non-linear case

We propose a different approach for the calculation of radiosity in each patch of s, to avoid the over-refinement of patches. This approach is similar to the ideas of Suykens and Willems [2000], because instead of using the sum of importances, the *maximum importance* value is found. The importance vectors ψ_i are computed independently using Eq. 5.3 for each patch i in s. Then, the output vector ψ_s is computed in the following way:

$$\psi_s(j) = \max_{i \in s} \left(\psi_i(j) \right) \quad \forall j \in \text{scene}. \tag{5.5}$$

This approach ensures that the importance of each patch j is lower than using the sum described before, but it is well-estimated for the calculation of B_i for each i in s.

The computation of ψ_i is expressed using Eq. 5.6, which is an extension of Eq. 5.3.

$$\begin{aligned}(\mathbf{I} - \mathbf{RF})^T \Psi_s = \Theta_s \text{ , where } \Theta_s = \left(\theta_{i_1}, \cdots, \theta_{i_k}\right), \\ \Psi_s = \left(\psi_{i_1}, \cdots, \psi_{i_k}\right) \text{, and } s = \{i_1, \cdots, i_k\}\end{aligned} \tag{5.6}$$

The unknown Ψ_s and the independent term Θ_s are $n \times k$ matrices. The column θ_{i_c} is a vector describing the initial emission of importance when patch i_c is the only source, built in the same way as described in Sec. 5.3.1. The column ψ_{i_c} is the correspondent importance vector. Algorithm 6 is a modification of Algorithm 3 to include above considerations.

Algorithm 6 Importance vector calculation for non-linear case.

Input: $\Theta_s, \varepsilon_{\min}$
Output: ψ_s
1: $\Psi_s^{(new)} \leftarrow \Theta_s$
2: **repeat**
3: $\quad \Psi_s \leftarrow \Psi_s^{(new)}$
4: $\quad \mathbf{F} \leftarrow$ computeFormFactors($\max_{\{\text{per row}\}}(\Psi_s)$, $\varepsilon_{\min}$)
5: $\quad \Psi_s^{(new)} \leftarrow (\mathbf{RF})^T \Psi_s + \Theta_s$
6: **until** $\| \Psi_s^{(new)} - \Psi_s \|_{Frobenius} < t$
7: $\psi_s = \max_{\{\text{per row}\}}(\Psi_s^{(new)})$

Under certain conditions, the use of the maximum importance increases the size of the scene (and thus the associated matrix $\mathbf{F}$) more than it is desired, especially when there are outliers in the set of importance values ($\psi_i(j)$ in Eq. 5.5). A practical solution to this issue is to ignore outliers, for instance discarding the tenth decile of all importance values.

Another possibility in the calculation of $\psi_s(j)$ consists in assigning weights Ω to the initial emitters of importance. If a patch $i_1 \in s$ is more significant or relevant (e.g. a window patch) than another patch $i_2 \in s$, then $\Omega i_1 > \Omega i_2$. Consequently, Eq. 5.5 should be transformed into:

$$\psi_s(j) = \max_{i \in s} \left(\Omega_i \psi_i(j) \right) \quad \forall j \in \text{scene.}$$

The inclusion of weights allows controlling the importance results, reducing the influence of unexpected outliers. Moreover, it provides a connection between the semantics of the patches in s and the importance results.

5.3.5 Importance for other radiometric units

The importance ψ of each patch is related to the radiometric unit used, because Eq. 5.3 is only valid for radiosity computations. In addition to radiosity, in this section we describe the importance scheme for reflected radiosity B_r (W/m^2), total irradiance I_t (W/m^2) and incident power P (W). Moreover, we show that Algorithm 3 can be used to compute importance for these radiometric units, by just selecting the correct initial source of importance. An analogous strategy is used for the non-linear case (Algorithm 6).

Reflected radiosity (B_r) is the fraction of total radiosity not emitted by a surface. The relation between B_r and radiosity B is defined by the equation B_r=B−E. The linear system of equations

for calculating B_r is:

$$(\mathbf{I} - \mathbf{RF})B_r = \mathbf{RF}E.$$

The corresponding importance adjoint equation is:

$$(\mathbf{I} - \mathbf{RF})^T \psi^{B_r} = (\mathbf{RF})^T \theta^{B_r}.$$

Therefore, the iterative process for the calculation of the importance vector ψ^{B_r} would be:

$$\psi^{B_r{}^{(new)}} \leftarrow (\mathbf{RF})^T \psi^{B_r} + (\mathbf{RF})^T \theta^{B_r}.$$

The implementation of this process implies a substitution of line 5 in Algorithm 3 by the above iteration. An alternative to this strategy consists in the modification of the input, in such way that $\theta = (\mathbf{RF})^T \theta^{B_r}$. In this case, the output of the algorithm would be ψ^{B_r}, because the only difference between the two iterations is the independent term.

Total irradiance (I_t) is the radiant flux received by a surface per unit area. The relation between I_t and radiosity is defined by the equation $I_t = \mathbf{F}B$. The equation related to this unit is:

$$(\mathbf{I} - \mathbf{FR})I_t = \mathbf{F}E.$$

The adjoint equation and iterative process needed to calculate ψ^{I_t} given θ^{I_t} are:

$$(\mathbf{I} - \mathbf{RF})^T \psi^{I_t} = \mathbf{F}^T \theta^{I_t}, \text{ and } \psi^{I_t{}^{(new)}} \leftarrow (\mathbf{RF})^T \psi^{I_t} + \mathbf{F}^T \theta^{I_t},$$

respectively. The alternative to compute ψ^{I_t} consists in selecting θ=$\mathbf{F}^T \theta^{I_t}$ as the input of Algorithm 3.

Incident power (P) is the radiant flux received by a surface. The relation with radiosity is defined by $P = \mathbf{AF}B$, where $\mathbf{A}$ is a diagonal matrix with $\mathbf{A}(i,i) = A_i$ (area of patch i). The equation related to this unit is:

$$(\mathbf{I} - \mathbf{FR})\mathbf{A}^{-1}P = \mathbf{F}E$$

and the adjoint equation and iterative process to calculate ψ^P given θ^P are:

$$(\mathbf{I} - \mathbf{RF})^T \psi^P = (\mathbf{AF})^T \theta^P, \text{ and } \psi^{P^{(new)}} \leftarrow (\mathbf{RF})^T \psi^P + (\mathbf{AF})^T \theta^P$$

respectively. The alternative to compute ψ^P consists in entering $(\mathbf{AF})^T \theta^P$ as input in Algorithm 3.

A final remark must be stated regarding the use of Algorithm 3 for computing importance of other radiometric units. The 3 different inputs proposed include the product between $\mathbf{F}^T$ and θ. This approach is useful when θ has few entries different to 0, in order to avoid the full computation of $\mathbf{F}$. A small zone of interest satisfies this condition.

5.4 Experimental analysis

In this section, we present the analysis conducted for measuring the performance of the algorithm. We focus on short wave radiation computations, but it is important to highlight that the analysis for

long wave radiation problems produces similar results. The importance-driven approach is compared with a full radiosity solution for a scene small enough to fit in system memory. Next, radiation is computed for a very large city to show the usefulness of the proposal.

5.4.1 Implementation and execution platform

The implementation of the algorithm proposed in this article was performed using C++ and OpenGL for the form factors computation and MATLAB [MATLAB, 2010] for matrix operations. Tests were conducted on a desktop computer composed of an Intel quad-core i7 processor, 16 Gbytes of RAM memory and a NVIDIA GeForce-1070 GPU.

5.4.2 Validation with standard radiosity

The presented algorithm aims to accelerate the calculation of urban context radiation. We compare the new scheme with a full radiosity solution, where the radiation computation needs to be performed for the whole city [Aguerre et al., 2017; Fernández et al., 2016a]. We select a medium-sized city scene to perform the comparison. Two different meshes are used: a coarse mesh composed of $\approx 9k$ patches, and a fine one, where each patch is subdivided into 16, leading to $\approx 142k$ elements. The coarse mesh is used as input to the importance-based approach, while the fine one is used in the previous algorithm. The diffuse reflectivity index is set to 0.3 for all surfaces, representing concrete material. The density and memory requirement of the form factors matrix associated with the fine mesh are 0.64% and 2.3GB, respectively. A global view of the city and the detail of both meshes are shown in Figure 5.4.

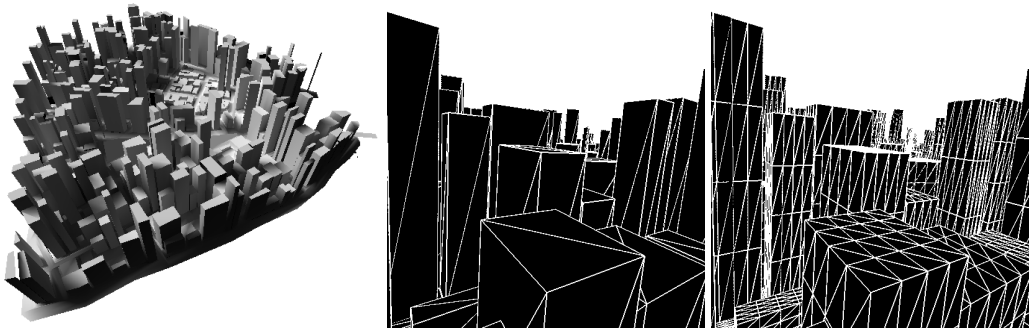

(a) Global view (b) Coarse mesh (c) Fine mesh

Figure 5.4: City scene used for comparison purposes. Coarse and fine meshes are shown.

The importance vector related to a patch depends highly on its position within the city. For example, the results may be very different for one patch located in a tall building and another located in a short house. The former probably sees a big part of its surroundings, while the latter sees only nearby patches. For this purpose, we select three patches in the city with different characteristics, which helps analyzing the performance of the algorithm under different test instances. Figure 5.5 shows the importance in the same scale for the three different target surfaces. The openness of the view increases from left to right.

The first step of the comparison consists in computing the radiation of the urban environment for the three selected patches. We compute radiosity using the algorithm proposed with different

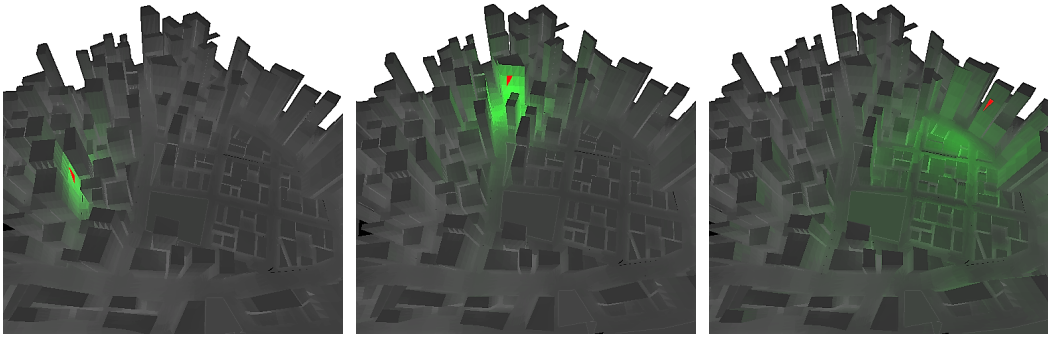

(a) Patch 1: occluded view (b) Patch 2: semi-open view (c) Patch 3: open view

Figure 5.5: Importance results (in green scale) for three different patches (in red).

input thresholds and compare the results with the previous algorithm. The emission configuration chosen for this test corresponds to 140 E vectors, corresponding to a simulation of solar radiation for 10 working hours a day for two weeks. After executing the algorithm, each emission generates a radiosity value for the target patch, which leads to a vector of 140 elements. Table 5.2 shows the results, where *size* represents the number of patches of the output city model and *error* is the relative error: $\|\mathbf{B}_{140} - \widetilde{\mathbf{B}_{140}}\|/\|\mathbf{B}_{140}\|$. $\mathbf{B}_{140}$ contains the radiosity results obtained with standard radiosity and $\widetilde{\mathbf{B}_{140}}$ is the approximation obtained with the importance-driven approach. It is important to highlight that the error in the radiosity value of the selected patch is a good average error measure, since it is closely related to the error in the view from the patch.

		$\varepsilon_{\min}$=10^{-7}		$\varepsilon_{\min}$=10^{-6}		$\varepsilon_{\min}$=10^{-5}	
	$\varepsilon_{\max}$	size	error	size	error	size	error
Patch 1	10^{-5}	5096	0.0008	4265	0.0021	3764	0.0183
	10^{-4}	2822	0.0027	1991	0.0029	1547	0.0179
	10^{-3}	1835	0.0105	1004	0.0104	560	0.0172
Patch 2	10^{-5}	8151	0.0005	6570	0.0013	5728	0.0059
	10^{-4}	4524	0.0015	2949	0.0020	2152	0.0058
	10^{-3}	3246	0.0061	1674	0.0062	889	0.0073
Patch 3	10^{-5}	17737	0.0004	15856	0.0005	14336	0.0040
	10^{-4}	7006	0.0023	5167	0.0021	3791	0.0037
	10^{-3}	4669	0.0049	2830	0.0048	1472	0.0044

Table 5.2: Results on relative errors and size of the modified mesh after applying the importance-driven algorithm. Original coarse and fine meshes are 8k and 142k, respectively.

Results in table 5.2 show that the number of patches on the urban model are drastically reduced without a significant increase in the relative error (always smaller than 2%). As $\varepsilon_{\max}$ and $\varepsilon_{\min}$ increase, the size of the mesh gets smaller, resulting in a reduction of the memory consumption and the execution time of the solar radiation simulation.

The worst case is observed at Patch 3 with $\varepsilon_{\min}$=10^{-7} and $\varepsilon_{\max}$=10^{-5}, where the size of the output mesh is 17737. In this case, the density of the refined form factors matrix is 6.6%. The rate between the memory requirements for the full and sparse representations of this matrix is 2400MB /327MB = 7.34×. The memory consumption is then reduced from 2.3GB to 327MB (6.7×), which is a considerable gain for a worst case scenario. In the best case (Patch 1 with $\varepsilon_{\min}$=10^{-5} and

ε_{max}=10^{-3}), the memory gain goes up to 718×. These results suggest that using importance to reduce the model allows considering scenes that otherwise cannot be used.

The produced error is not large for the tested scenes. Also, the errors are not directly related with the size of the resultant mesh, but with the respective configurations of ε_{max} and ε_{min}. More precise error results are observed in Table 5.3, which contains 4 fish-eye views representing the perspective seen from patch 3 using different ε_{min} and ε_{max} configurations. The color of the patches depicts the absolute error generated by the importance-driven approximation. 140 radiation results are computed with standard radiosity and the approximated algorithms. Then, for each city patch, the worst case among the 140 results is selected. These values are then transformed into the correspondent colors using the presented colormap.

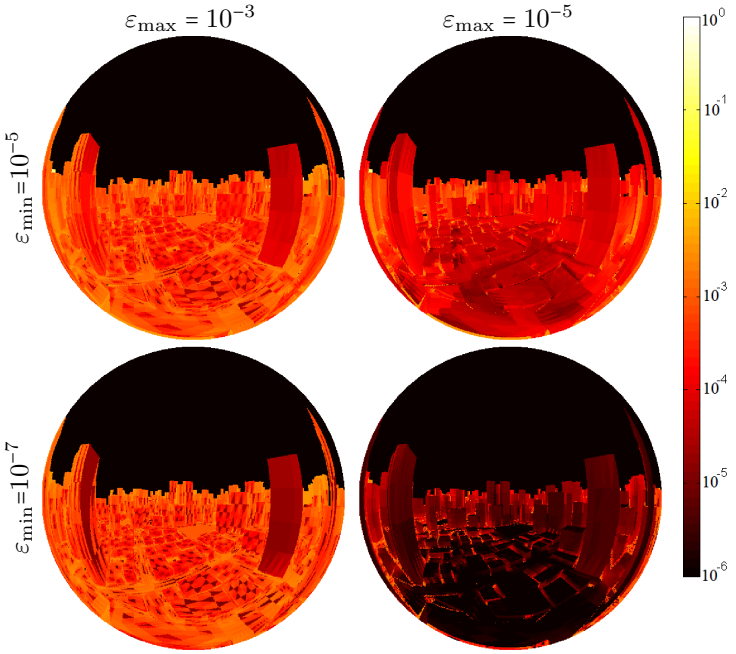

Table 5.3: Fish-eye views representing errors for patch 3 using different ε_{min} and ε_{max} configurations.

Taking a closer look into Table 5.3, it can be appreciated that the errors are not strictly related with the size (measured in solid angle) or closeness of the patches seen. In fact, the error in a patch depends on several aspects, like the portion of the sky seen from it, the number of buildings surrounding it, its orientation, etc. For example, patches in the roofs of the buildings tend to have lower error, because the influence of the city is smaller on them. On the other hand, patches with a big sky obstruction, like those in the streets, have larger error.

5.4.3 Testing the algorithm for multiple target patches

The previous test used a unique patch as target surface. Next, we propose a test that pushes the limits of the algorithm. Algorithm 6 is used for computing importance for multiple patches, increasing the computational effort needed. For example, if solar radiation must be studied for a whole block of buildings, then a fair number of elements should be selected as target patches.

For this test we select a block of buildings in the middle of the city scene, composed of approxi-

mately 2k patches. Figure 5.6 presents the importance diagram for this case. Comparing Figures 5.5 (a,b,c) with Figure 5.6, it is easily observed that, in the new test, the importance is distributed in a larger part of the city.

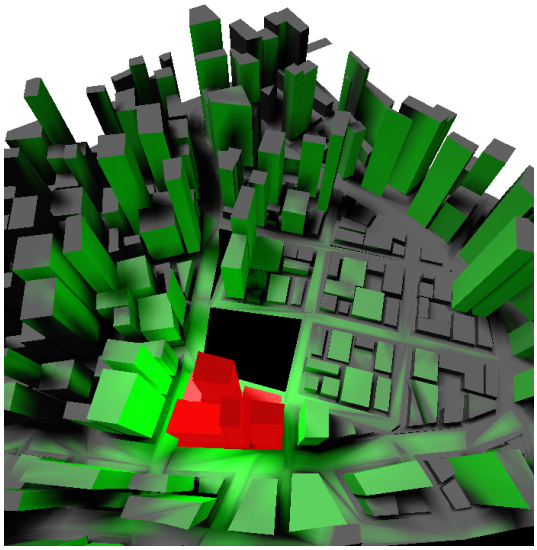

Figure 5.6: Importance results for a block of buildings. Selected patches are in red, while importance is in a green scale.

Table 5.4 shows results on executing Algorithm 6 for the selected block of buildings. It can be seen that for the same $\varepsilon_{\min}$ and $\varepsilon_{\max}$ as in Table 5.2, the size of the output mesh is larger, as expected. Nevertheless, the method allows reducing the memory consumption significantly, producing small errors in the radiosity calculations.

$\varepsilon_{\max}$			$\varepsilon_{\min}$=10^{-7}	$\varepsilon_{\min}$=10^{-5}
10^{-5}	size		35199	31640
	error	μ	7.6×10^{-5}	6.8×10^{-4}
		σ	1.1×10^{-4}	1.2×10^{-3}
	density		3.6%	4.5%
	gain		3.3×	3.6×
10^{-3}	size		9177	5780
	error	μ	1.8×10^{-3}	1.9×10^{-3}
		σ	1.6×10^{-3}	1.9×10^{-3}
	density		4.7%	9.2%
	gain		36.7×	45.6×

Table 5.4: Results on the application of the algorithm using multiple target patches. Different configurations of $\varepsilon_{\min}$ and $\varepsilon_{\max}$ are studied, showing the size of the output mesh, the mean μ and standard deviation σ of the error, the density of the resultant $\mathbf{F}$ matrix, and the gain in memory when comparing to the original fine mesh.

A more detailed view of the error produced is observed in Figure 5.7(a), where a colormap is used to show the errors produced for each patch. The errors in the patches on the roofs are lower than in those on the walls. Figure 5.7(b) shows the histogram for the errors in the 2k patches. In this test, 99.5% of the patches have a relative error below 0.01.

It is worth noting that the size reduction of the city model can be performed with other approaches

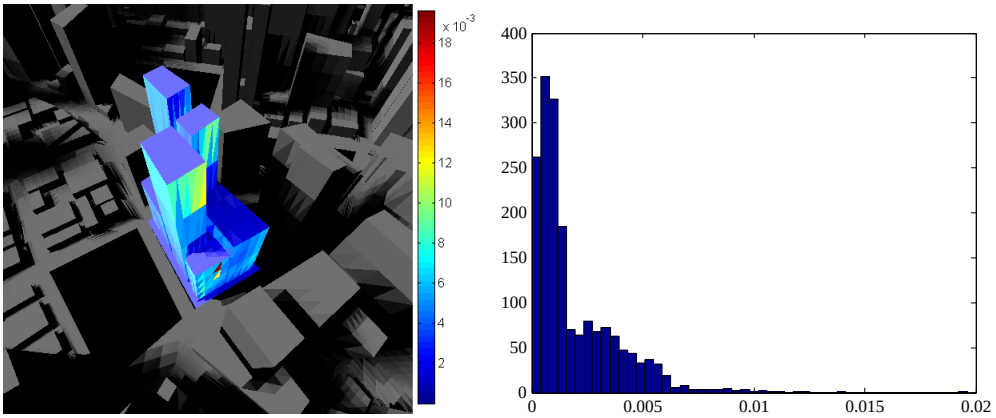

(a) Patches colored by their error.

(b) Histogram of the errors for the 2k patches.

Figure 5.7: Relative errors produced by the importance-driven approach in the block of buildings, using $\varepsilon_{\min} = 10^{-5}$ and $\varepsilon_{\max} = 10^{-3}$.

besides the importance-driven method. For example, the strategy followed by a regular user facing the obstacle of working with big urban environments could be to remove patches according to their distance to the region of interest. As a proof of concept, we implemented and measured the error generated by this kind of approach and the results are conclusive: the errors for daylighting computations grow by a factor of $100\times$ when using the same number of patches than the importance-based algorithm ($N = 5780$ and $N = 9177$). This experiment justifies the use of our proposal for handling big city models with low error, and provides a warning against using simpler algorithms without the appropriate precautions.

5.4.4 Test case with specular components

Sec. 5.3.3 presented an extension of the algorithm to consider specular surfaces. In order to analyze the extension, we use a test case where the building facade selected as the zone of interest has a specular facade in front of it. This example could be the case of a modern glass building. Figure 5.8 shows the importance distribution, where the sky blue facade is the specular surface. The effect of the specular reflections was augmented for the reader to understand the results. The specular part has a considerable effect on the importance distribution, generating a green stripe along the portion of the city that is symmetric to the zone of interest.

After testing the algorithm with multiple configurations of ε_{min} and ε_{max}, the resulting vector of specular importance ψ_s always indicates to select and subdivide the specular patches, which is the expected behavior. Multiple sky configurations were tested, and the results are very similar to those in the previous section, reaching low relative errors, and large gains in memory and execution time.

5.4.5 Example of application: irradiance over a wall in Venice

Solar radiation predictions are fundamental for thermal simulations, thus there are several software packages that can take advantage of our proposal. For example, CitySim [Robinson et al., 2009], EnergyPlus [Crawley et al., 2004], and ENVI-met [Huttner and Bruse, 2009] use a nodal method [Meyer, 1999] for simulating heat exchange at the urban level. The input data for this approach is

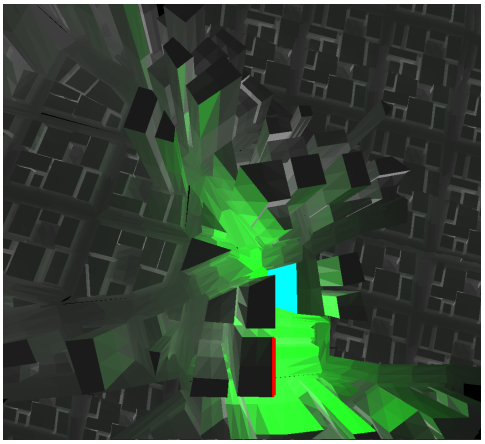

Figure 5.8: The facade highlighted in red is the emitter of importance, whereas the facade colored with sky blue has specular properties.

the incident power over each building facade or envelope. The strategy described at Sec. 5.3.5 can be used along with any of these software for simulating big urban scenes.

The global irradiance over surfaces in the city is also commonly used as a basis for heat exchange simulations. This quantity is useful because it describes the amount of solar energy that can be exploited for heating purposes more precisely. The global irradiance on a horizontal unobstructed plane consists of the sum of the direct irradiance and diffuse irradiance coming from the sky, which can be calculated using meteorological data [Perez et al., 1993]. On the other hand, predicting irradiance over tilted obstructed surfaces may need the inclusion of the energy reflected by the ground and other surrounding elements. This case is much more difficult to address, because inter-reflections must be taken into account. Moreover, in complex scenarios such as a city, the computational complexity easily scales to the point of being impractical.

In this test we propose to study the irradiance for the whole year over tilted surfaces in the city of Venice, Italy (45°26'). We use a 3D model generated using CityEngine [Parish and Müller, 2001], composed of 1.5 million patches (see Figure 5.9). The surfaces of the city are considered diffuse with a reflectivity index of 0.3, while the water on the canals is meshed with partly specular patches. The density of the form factors matrix of this coarse (unrefined) model is 0.016%, which requires 2.7GB of memory to be stored using a sparse representation. The computation of this matrix takes 30 hours of execution time. Furthermore, dividing each patch into 16 leads to a finer mesh composed of 24 million patches. In this case, the form factors would take at least 50GB to be stored, and around 500 hours to be computed.

The climate-based data is derived from the direct normal and diffuse horizontal irradiation data, extracted from Typical Meteorological Year data and a Reinhart 2305 sky tile discretization.

For this test, two patches are selected to study the irradiation pattern. The first one is the common case for this type of city, i.e. a vertically oriented patch in a building located at the typical narrow street. The second one corresponds to a patch in the Campanile of the Piazza San Marco, which represents a worst case scenario because this building is the tallest in the city.

The first step consists in computing the importance vector for the selected patches, which takes 6 minutes for each example. The algorithm is executed with $\varepsilon_{\min} = 10^{-7}$ and $\varepsilon_{\max} = 10^{-4}$. Figure

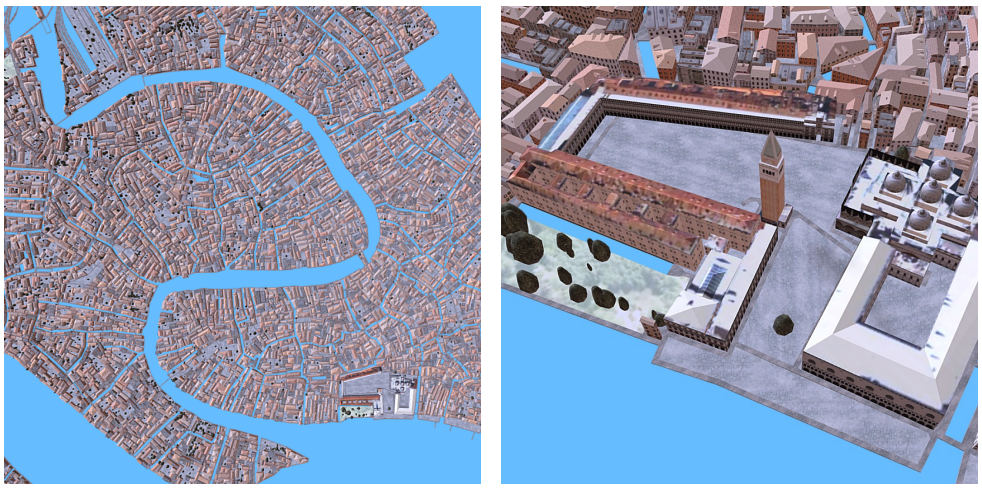

(a) Global view. (b) Piazza San Marco detail.

Figure 5.9: Venice 3D model, generated using ESRI's CityEngine. Zones colored in sky blue are water canals, which are partly specular surfaces.

5.10 presents the importance results for the case of the campanile.

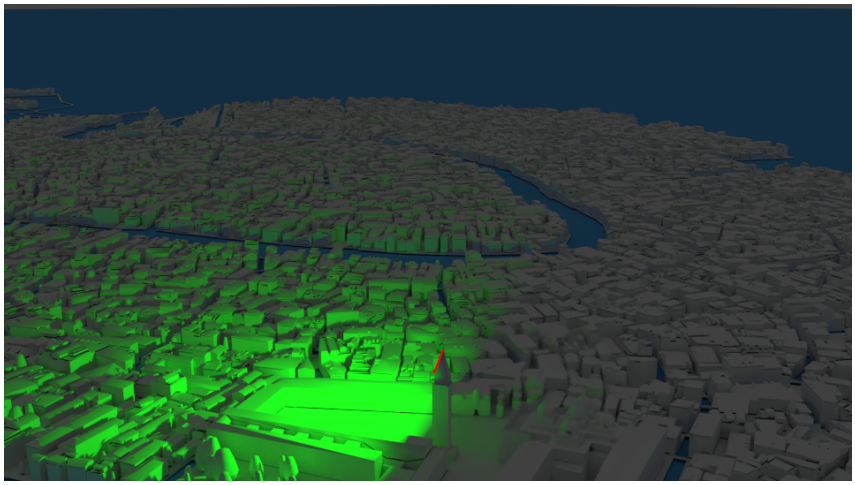

Figure 5.10: Importance results for the target patch in the Campanile of the Piazza San Marco.

After executing Algorithm 5, the size of the model is reduced to 7k patches for the occluded case, and 15k patches for the campanile. The computation of the form factors for the reduced model takes less than 1 minute for both cases, resulting in sparse matrices of density smaller than 3%. The gain in memory with respect to the finer Venice model is greater than $1000\times$. Solving radiosity for $365 \times 24 = 8760$ hours in the year takes 15 seconds. The overall execution time of the method is reduced by three orders of magnitude when compared to a standard radiosity engine that does not use importance.

The total irradiance value (I_t) for the selected patch is then computed as the ratio between its radiosity and reflectivity values: $I_{t_i} = B_i/R_i$. Figure 5.11 shows the results, measured in watts hour per square meter per day. The blue plot corresponds to the irradiation coming directly from the sky,

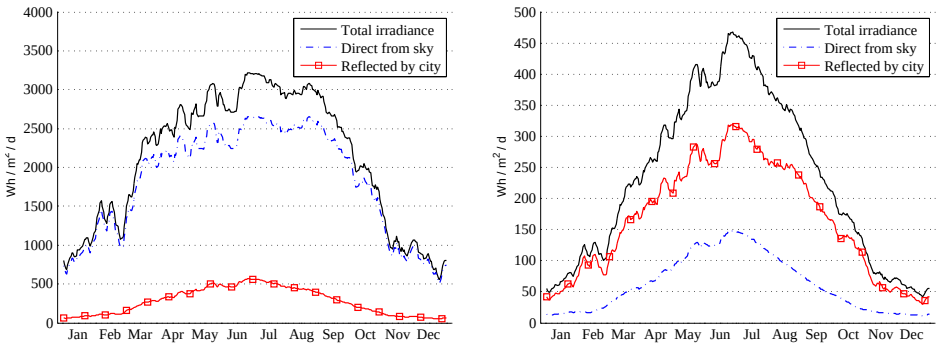

(a) Location: Campanile of the Piazza San Marco.

(b) Location: Building in narrow street.

Figure 5.11: Results for the vertical solar irradiation over a standard meteorological year in Venice.

while the red plot presents the irradiation reflected by the city environment. As expected, the total irradiation (black plot) is larger in the summer months of June, July and August. It can be seen that the irradiation in the campanile is greater than in the narrow street, mostly because of the greater sky view factor.

In the campanile, the influence of the city in the solar irradiation ranges between 7% and 18%, reaching its maximum value during summer days. Moreover, in the other case the influence is greater, ranging between 50% and 75%. This fact confirms that it is highly necessary to consider the urban environment in the calculations.

5.4.6 Validation with a standard ray tracing engine

In this section, a validation with RADIANCE software is presented. Both importance-driven and ray tracing engines are used to compute daylight coefficients using the Venice model. For this study, the zone of Campo San Maurizio is selected, which represents a typical square in this kind of city. 1502 sensors are placed in the zone, and daylight coefficients are computed. RADIANCE command *rfluxmtx* is used with a Reinhart sky subdivision composed of 2305 sky elements.

Several tests are conducted, using different number of rays in RADIANCE and varying the values of ε_{min} and ε_{max} in the importance-driven algorithm. The results are compared to a reference RADIANCE simulation that traces 10 million rays per sensor. In all the tests, a maximum of 4 diffuse bounces are allowed, which are the minimum values that show less than 1% of relative error. The radiosity solutions are executed with a hemicube resolution of 1024×1024 pixels.

Figure 5.12 shows the importance results for this test. The selected patches are painted in red, while the important patches are in white. As can be seen, a large number of the white patches are focused near the zone of interest. Nevertheless, there are many white patches that are very far away and still need to be considered in the computations. This fact shows that discarding far away patches is an unsuitable alternative strategy because of the potential error produced.

Relative errors to the reference simulation are measured for each sensor. Given a sensor s, the relative error is calculated as:

$$\frac{\|\mathbf{DC}(s,:) - \hat{\mathbf{DC}}(s,:)\|_2}{\|\mathbf{DC}(s,:)\|_2}$$

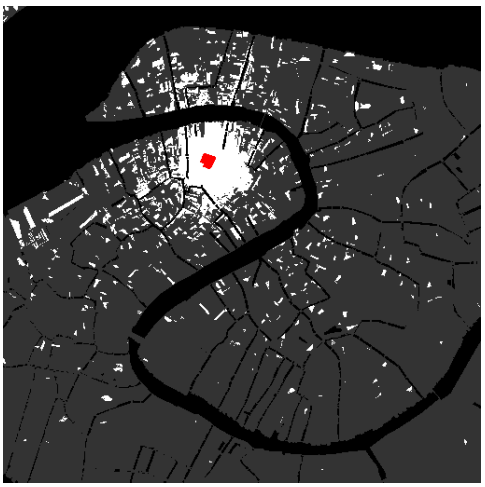

Figure 5.12: Campo San Maurizio in the model of Venice (red), and the selected important patches (white).

where $\mathbf{DC}$ is the reference daylight coefficient matrix, $\hat{\mathbf{DC}}$ its estimation, and $\|\|_2$ the 2-norm. Table 5.5 shows the mean μ and standard deviation σ of the error. Reported RADIANCE execution times correspond to a parallel execution with 6 threads.

	Relative error		Execution time
	μ	σ	
Radiance 10M rays	-	-	56122s
Radiance 1M rays	0.0099	0.0028	5677s
Radiance 250k rays	0.0252	0.0061	1578s
Radiance 100k rays	0.0479	0.0106	618s
Radiance 10k rays	0.2397	0.0437	82s
Importance-driven #1	0.0224	0.0067	302s
Importance-driven #2	0.0317	0.0082	150s

Table 5.5: Error results and execution time of the validation with RADIANCE. Importance-driven #1 was executed with ε_{min} =1×10^{-8} and ε_{max}=1×10^{-4}, resulting in a mesh composed of around 20k patches. Importance-driven #2 parameters are ε_{min} =1×10^{-7} and ε_{max}=1×10^{-3}, and the correspondent mesh is near 10k patches. The mean μ and standard deviation σ of the error are reported.

The previous results show that the importance-driven radiosity approach achieves very good error schemes in short execution times. The proposed technique is a viable alternative when aiming to quickly achieve low error results, for example when multiple material properties need to be evaluated with sufficient precision [Marschner and Greenberg, 1998]. Nevertheless, when higher errors are allowed, or when execution times are not critical, ray tracing engines can provide more flexible results.

Another advantage of using importance-driven radiosity in urban scenes is that the execution times tend to grow sublinearly with the number of sensors. If the set of sensors have spatial coherence, adding a new sensor with a similar view of the city does not add a significant portion of the city to the resulting model, therefore the computational effort increases at lower rates.

5.5 Conclusions and future work

This article presents an importance-driven approach for computing urban radiative exchange in an efficient manner. The proposed method accelerates solar radiative computations and reduces memory consumption without introducing a significant error. This approach allows studying local phenomena in city models that otherwise cannot be processed using radiosity.

The main contribution of the proposal is related to the use of importance in urban physics, an area that deals with huge city geometries and requires high precision simulations. The high occlusion factor of city models allows reducing the computational requirements of radiation calculations by exploiting the fact that a lot of the information contained in the model is not needed for simulations over a zone of interest. An algorithm for calculating the importance vector was implemented and tested, showing a remarkable performance for very large scene models. The method allows considering diffuse and specular materials.

When compared to standard radiosity, the new method presented a memory reduction of up to $718\times$, having a relative error of less than 2% when selecting a single patch as target surface. The case of selecting multiple patches showed considerable gains and even better resulting error. As an example of a real application, the irradiance over surfaces in the city of Venice was computed, using a model whose coarse mesh is composed of 1.5 million patches. The memory gains in this case were greater than $1000\times$, and the execution time was also reduced by three orders of magnitude. This reduction allows executing the whole simulation using a regular desktop PC in few minutes. A comparison between the proposed approach and a state-of-the-art ray-based system was also conducted to validate the results, showing that radiosity is an alternative algorithm to simulate urban models.

There are many pending research directions. Using importance for selecting which patches are removed can lead to unwanted errors when the city environment is too large, because a set of distant patches that are independently discarded can have an influence in the zone of interest when considered together. Clustering methods [Gibson and Hubbold, 1996; Smits et al., 1994] help avoiding this issue. Level of Detail [Luebke, 2003] techniques can be combined with our approach. For example, important facades or buildings can be replaced by more detailed models [Döllner and Buchholz, 2005], increasing the realism of the simulation. Implementing arbitrary BRDF properties can help improving the simulation conditions, although other strategies different than ray tracing can be studied to accelerate the extended form factors computations. Finally, embedding the proposed algorithm into a heat transfer software is required to test long wave computations.

Acknowledgements The work was partially supported by project FSE_1_2017_1_144731 from Agencia Nacional de Investigación e Innovación (ANII, Uruguay). The authors would like to express their gratitude to Per Christensen for his kind cooperation.

Chapter 6

A street in perspective: Thermography simulated by the Finite Element Method

---

The contents of this chapter were published in:
Aguerre, J. P., Nahon, R., Garcia-Nevado, E., La Borderie, C., Fernández, E., and Beckers, B. (2019). *A street in perspective: Thermography simulated by the finite element method*. Building and Environment, 148, 225-239. Elsevier.

Thermograms of urban perspective views provide an efficient way to analyze heat transfer phenomena in cities. The computational simulation of thermograms introduces more information into the analysis, allowing for the comparison of spatialized information to provide a better understanding of the involved physical parameters. The main objective of this work was to simulate thermograms at the urban scale using the finite element method (FEM). Geometrical properties and environmental and boundary conditions were carefully established. A comparison between a time sequence of thermograms on a real urban district and a set of simulated thermograms was developed. The computational model shows compelling results, reproducing the same order of magnitude and general appearance of the experimental data. Moreover, the results allow for the evaluation of the heat flux balance at various interesting points on the geometry, and the impact associated with the modification of scene parameters.

6.1 Introduction

Recent advances in measurement, particularly in long-wave radiation (thermography) and computer science (for instance, climate-based simulations), should promote the adaptation of standard simulation methods to the complex geometries of cities to enable more precise quantification of energy fluxes at the urban scale.

Infrared thermography is commonly used in civil engineering for building diagnostics [Kirimtat and Krejcar, 2018; Kylili et al., 2014; Lucchi, 2018], such as the detection and assessment of heat losses through thermal bridging [Asdrubali et al., 2012; Nardi et al., 2018; O'Grady et al., 2017], the evaluation of building material thermal properties [Barreira and de Freitas, 2007], or the identification of construction defects [de Freitas et al., 2014]. They are also used to calibrate numerical models, taking the observed surface temperatures as a reference to evaluate the simulation results at the building scale and, less frequently, at the urban scale [Charisi et al., 2018; Ghandehari et al., 2018; Lalanne et al., 2015; Rodler et al., 2018]. Thermal modeling of the building envelope is usually performed using simplified models such as resistance-capacitance methods, which offer a good compromise between accuracy and computational costs [Asawa et al., 2008; Groleau et al., 2003; Kramer et al., 2012; Krayenhoff and Voogt, 2007; Reinhart and Davila, 2016; Yang and Li, 2013]. The finite element method (FEM) allows a better approximation of the real wall behavior and was recently used to model multilayer building walls, coupling simulations and experimental measurements such as thermography [Evangelisti et al., 2018; Mayer et al., 2014].

Thermal images of urban perspective views provide an efficient way to gather the maximum possible amount of physical information [Beckers and Garcia-Nevado, 2018]. Their interpretation is not direct, hence, a faithful evaluation of the transient heat transfers using FEM allows for a better understanding of the concerned physical phenomena [Beckers et al., 2019; Morrison et al., 2018].

The physical properties of walls, particularly their short-wave reflectance and their thermal inertia, determine the rate at which energy is stored and released by buildings. Thermal modeling using numerical tools allows for the prediction of the impact of material choice on outdoor surface temperatures; for example, the assessment of urban heat island mitigation techniques such as the use of 'cool' coatings, with high short-wave reflectance and emissivity [Bozonnet et al., 2013; Guattari et al., 2018; Zhang et al., 2017].

The spatial distribution of the radiant power emitted by the urban surfaces has a strong impact on the outdoor thermal comfort [Lindberg et al., 2008; Nazarian et al., 2017]. Most of the models used to simulate the thermal behavior of buildings at the urban scale are not well-suited for studying the outside surface temperature spatial distribution. Recent studies have shown interest in simulating heat transfers using fine meshes [Idczak et al., 2010; Lagouarde et al., 2010; Roupioz et al., 2018].

In this study, a street of the Petit Bayonne, one of France's densest districts, was modeled using the Cast3m finite element software [Charras and Di Paola, 2011], which allows for precise calculation of the spatial distribution of the outside surface temperature over time. The main contribution of this study is to present a set of simulated thermograms of a street in perspective and their comparison to experimental data. The results were used for the evaluation of heat flux balance at different points on the geometry and the impact associated with the modification of scene parameters.

6.2 Modeling physical base

In this study, we focus on the three main types of heat transfer: conduction, convection, and radiation. Heat flux [W m^{-2}] refers to a vector quantity that defines the flux of energy per unit of area per unit of time.

6.2.1 Conduction

The steady state conduction equation is provided by Fourier's law, which indicates that the rate of heat transfer through a material per unit area is proportional to the negative temperature gradient:

$$\overrightarrow{q} = -k\overrightarrow{\nabla T} \tag{6.1}$$

$\overrightarrow{q}$ is the vector of heat flux [W m^{-2}], k is the conductivity of the material [W m^{-1} K^{-1}], and $\overrightarrow{\nabla T}$ is the temperature gradient [W K^{-1}]. The value of k is considered to be constant throughout the material.

The transient heat conduction is obtained applying the energy conservation law to differential volumes [Lewis et al., 2004]. In Eq. 6.2, thermal conductivity is isotropic and heat sources are ignored.

$$k\Delta T = \rho c_p \frac{\partial T}{\partial t} \tag{6.2}$$

ΔT is the temperature Laplacian, ρ the density [kg m^{-3}] and c_p [J kg^{-1} K^{-1}] the specific heat of the material.

6.2.2 Radiation

All surfaces with a temperature greater than the absolute zero emit energy as electromagnetic waves at different wavelengths. Plank's law establishes the density of electromagnetic radiation emitted by a blackbody at a given temperature [Howell et al., 2015]. The total radiated power per unit surface of a blackbody at a temperature T across all wavelengths, noted as φ [W m^{-2}], is given by the Stefan law:

$$\varphi = \sigma T^4 \tag{6.3}$$

where σ is the Stefan-Boltzmann constant, whose value is $\approx 5.6703 \times 10^{-8}$ W m^{-2} K^{-4}.

The Sun may be assimilated to a blackbody at 5778 K, which emits electromagnetic waves at short wavelengths (less than 4μm). Part of the radiation reaching the atmosphere is absorbed by the clouds (23%) and the Earth (47%) and is essentially returned in electromagnetic waves with long wavelengths (greater than 4 μm) [Beckers, 2013c].

Like the Sun, the atmosphere may be assimilated to a blackbody at a varying sky temperature T_{sky} [K]. It may as well be assimilated to a grey body at the air temperature T_a, characterized by the sky emissivity ε_{sky}, which exhibits its ability to absorb and emit long-wave radiative energy. Atmospheric radiation φ_{sky} [W m^{-2}], which is the long-wave radiation from the sky to the Earth, is given by the following expression:

$$\varphi_{sky} = \sigma {T_{sky}}^4 = \varepsilon_{sky} \sigma {T_a}^4 \tag{6.4}$$

A fraction of the radiation received by the outside surfaces at the Earth level is reflected. In an urban context, the multiple inter-reflections between built surfaces have an important impact on their temperature. In this study, all surfaces were assimilated to perfectly diffuse blackbody materials; the whole long-wave radiation reaching a surface is absorbed and a fraction of the incident short-wave

radiation is reflected following Lambert's cosine law.

6.2.3 Convection

Convection simulations are fundamental for obtaining precise results. In urban scenarios, the air is the fluid in contact with the target surfaces. The equation that models the heat flux by convection is given by Newton's law of cooling:

$$q_{conv} = h(T - T_a) \tag{6.5}$$

In Eq. 6.5, q_{conv} is the convective heat flux, T_a is the air temperature, T is the temperature of the surface, and h is the convective heat transfer coefficient [W m^{-2} K^{-1}].

The convective heat transfer coefficient depends on the wind speed and its direction, and the nature of the surface. The simulation of fluid dynamics is expensive due to its computational complexity. In the test presented here, the wind was relatively absent, allowing for the avoidance of the fluid dynamics simulation; the convective heat transfer coefficient was assumed to be constant for all the materials throughout the day.

6.3 Test case description

6.3.1 Site and experimental set-up

The present test case is built upon a measurement campaign developed in the *Rue des Tonneliers* in Bayonne (43.48º N). This narrow and deep street canyon is located in the *Petit Bayonne*, one of the densest districts in France and a representative example of a highly occluded urban tissue. Within such urban geometries, the simulation of energy exchanges between built surfaces faces significant challenges, primarily due to the multiple inter-reflections of short-wave radiation. From this perspective, the site is an interesting case study to test our current ability to comprehensively compute the energy exchanges taking place within a complex urban environment.

For this test case, the built environment of Tonnelier's street has been modeled as a set of four boxes (Figure 6.1). Individual buildings in the area have been grouped into just four blocks of uniform thickness (0.18 m). The spatial distribution and orientation of these blocks essentially respond to that of the studied area. All of the blocks have been modeled as boxes with a uniform height of 14.30 m, corresponding to the average value of the real buildings. An additional 1-meter-thick box has been included in the model to represent the ground surface bounded by the building blocks.

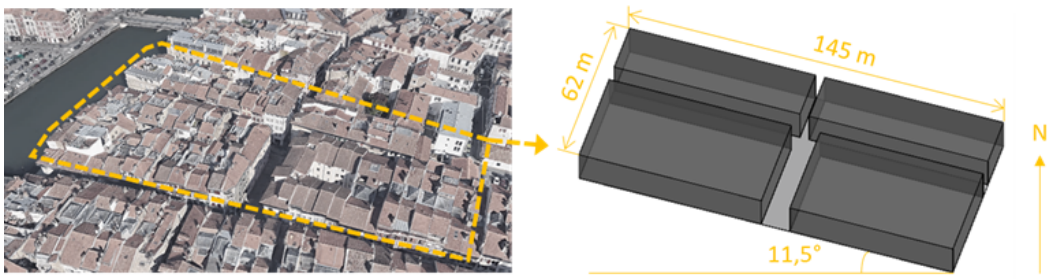

Figure 6.1: Aerial image of the study case and its geometrical model.

As is typical in urban environments, Tonnelier's street surfaces exhibit a remarkable material heterogeneity. For the sake of simplicity, just four surface types were considered in this test case: walls, roofs, floors, and street pavement (Figure 6.2). Thermal and optical properties were described using four parameters: reflection coefficient (r), emissivity (ε), thermal conductivity (k [W m^{-1} K^{-1}]), and volumetric heat capacity (c_v [J m^{-3} K^{-1}]).

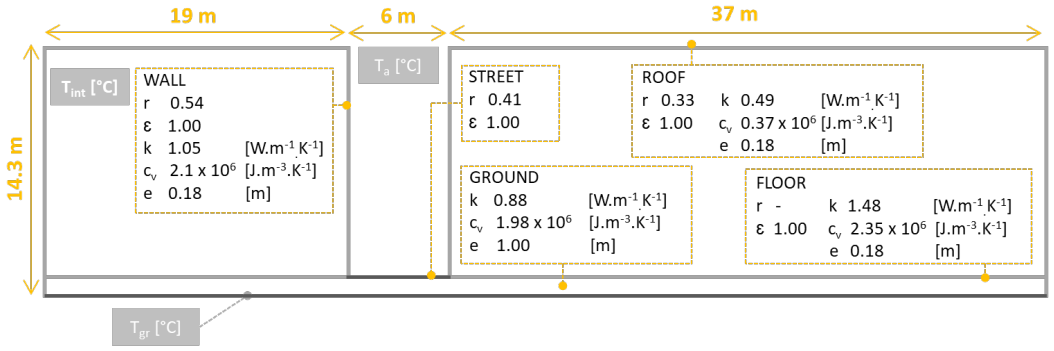

Figure 6.2: Surface types and material properties.

The material properties of built surfaces have been defined from both experimental data collection and assumptions based on in situ observations. Reflection coefficients of the exterior walls and street surfaces have been estimated from grayscale photographs, comparing the luminance of the region of interest to that of a reference surface with a known reflectance under the same lighting conditions. Thermal properties of the materials were estimated from material databases according to the most common building techniques observed in this urban area.

6.3.2 Experimental set-up

The experimental work consisted of a time-lapse sequence of photographs (short-wave) and thermograms (long-wave) taken on April 23rd, 2017, a cloudless day with very little wind, from 4:00 to 23:00 local solar time (ST). An infrared camera, FLIR B200, with a field of view of 25 x 19° was set on a tripod placed at the west entrance of the street. The camera view was aligned to the street axis with a tilt of 10° from the horizontal plane, so that the ground, the north and south facing façades, and a sky fraction were simultaneously captured (Figure 6.3). In this study, shots were intentionally framed with a perspective view of the street to maximize the amount of physical information captured by the images.

The infrared images obtained were calibrated according to the environmental data recorded during the measurement campaign (air temperature and relative humidity). The object emissivity was set to 1 and its distance to the camera to 0, to eliminate the influence of the surroundings on the measurements and to cancel the thermal absorption and radiation of the air layer between the object and the camera lens [Kruczek, 2015a]. Under these conditions, the observed apparent temperatures were directly deduced from the total radiant power emitted in the spectral range of the camera (7 to 13μm) that reached its lens.

Figure 6.3: Position of the infrared camera.

6.3.3 Environmental and boundary conditions

The environmental and boundary conditions were defined by combining information from several sources (Table 6.1). To enable comparability between the simulated and measured results, data were obtained whenever possible from the on-site measurements on April 23rd, 2017 in Bayonne. When unavailable, the values were modeled or estimated.

Parameters	Units	Measured	Modeled	Estimated
Global Horizontal Irradiance	W m^{-2}	X		
Direct Normal Irradiance	W m^{-2}		X	
Diffuse Horizontal Irradiance	W m^{-2}		X	
IR horizontal Irradiance	W m^{-2}		X	
Sky temperatures	°C		X	
Outside air temperature	°C	X		
Outside air relative humidity	%	X		
Wind speed	M s^{-1}	X		
Outside convection coefficient	W m^{-2} K^{-1}			X
Ground temperature	°C			X

Table 6.1: Input parameters of the test case.

The outside air temperature and relative humidity were measured on-site from 4:00 to 23:00 with a time interval of 30 minutes. The data from 23:00 to 4:00 were linearly interpolated to obtain a 24-hour period. The air temperature ranged from 9.5°C at 4:30 to 19.8°C at 11:00 and relative humidity from 68% at 6:00 to 52% at 11:00 (Figure 6.4). The inside air temperature was fixed at 20°C, common for the winter; however, this may be questionable at the end of April, when the outside air temperature often exceeds 20°C during the day.

Outside convection coefficients depend on the wind speed and direction. The average wind speed, measured in the middle of the street at a height of 2.2 m, was 0.2 m/s on the selected day, with values ranging from 0.05 to 0.3 m/s. Therefore, the outside convection coefficient was fixed at 10 m^{-2} K^{-1}, corresponding to the mean wind speed for most of the models available in the literature [Mirsadeghi et al., 2013]. Interior convection coefficients were set to a value of 0.7 m^{-2} K^{-1} for the ground, 2.5 W m^{-2} K^{-1} for vertical walls, and 5 W m^{-2} K^{-1} for the roof, as specified in the French thermal regulation [CSTB France, 2012].

The ground temperature at a depth of 1 m is not sensitive to the daily variation of temperature and solar radiation [Givoni and Katz, 1985] and its variation from one year to another can be neglected.

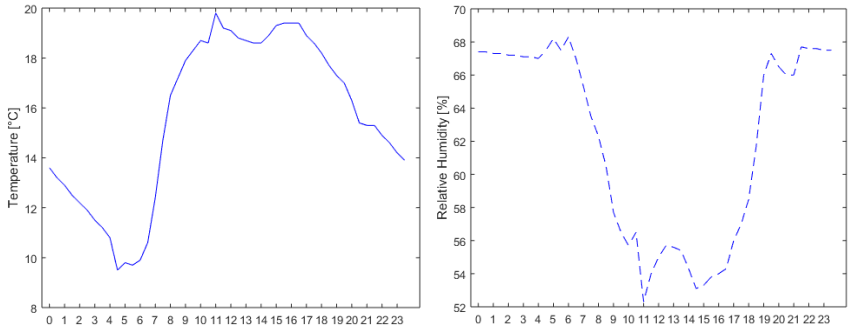

Figure 6.4: Outside measured air temperature and relative humidity - Bayonne, April 23rd 2017.

For this test case, this parameter was set to 11.1°C, corresponding to the mean ground temperature at a depth of 1 m in April for the city of Bayonne extracted from stochastically generated time series from the Meteonorm [Remund et al., 2010] global meteorological database.

Global horizontal irradiances were calculated on the basis of validated formulations from the literature for clear sky conditions, using measured data for calibration purposes. The direct normal and diffuse horizontal irradiances were calculated using the clear sky model described by Liu and Jordan [Liu and Jordan, 1960], which considered an atmospheric transmittance of 73% to match the global horizontal irradiance measured at a weather station located in Anglet, 3.4 km from the Tonneliers street. Under this assumption, the deviation between the measured and modeled global irradiance was lower than 1% for the selected day. The infrared horizontal irradiance was calculated with the Angström formula [Ångström, 1915], using the outside air temperature and relative humidity measured at the Biarritz-Anglet airport observatory, 5.5 km away from the studied location, assuming that the urban heat island has no effect on the incident atmospheric radiation.

The sky short-wave and long-wave radiances on a clear day are anisotropic; the short-wave radiance in each direction depends on its angle relative to the Sun's position and the zenith, and the long-wave radiance depends on the atmosphere thickness and decreases along with the zenithal angle. To compute the sky short and long-wave irradiances in this study, the sky vault was divided into tiles using the partition scheme described by Beckers [Beckers and Beckers, 2014]. This strategy allows the user to freely define the number of tiles, ensuring that each has the same solid angle and aspect ratio. The short-wave radiance of each tile is supposed to be uniform and was calculated at its center using the Perez all-weather model [Perez et al., 1993], which utilizes previously modeled theoretical direct normal and diffuse horizontal irradiances under a clear sky. The variation of long-wave radiance with the zenithal angle was estimated using the model described below. Figure 6.5 shows the radiance angular distribution pattern at different time steps on the selected day, both in short and long waves, for a 5000-tile partition of the sky.

The variation of the sky emissivity with the zenithal angle was estimated as recommended in [Nahon, 2017], and took the model described in [Bliss Jr, 1961] as its starting point:

$$\varepsilon_\zeta = 1 - \left(1 - \varepsilon_{sky}\right)^{1/(b-\cos(\zeta))} \tag{6.6}$$

with ζ being the zenithal angle [rad], ε_ζ the sky emissivity at the zenithal angle ζ, ε_{sky} the sky global emissivity and b a constant term of 1.8 in the original model.

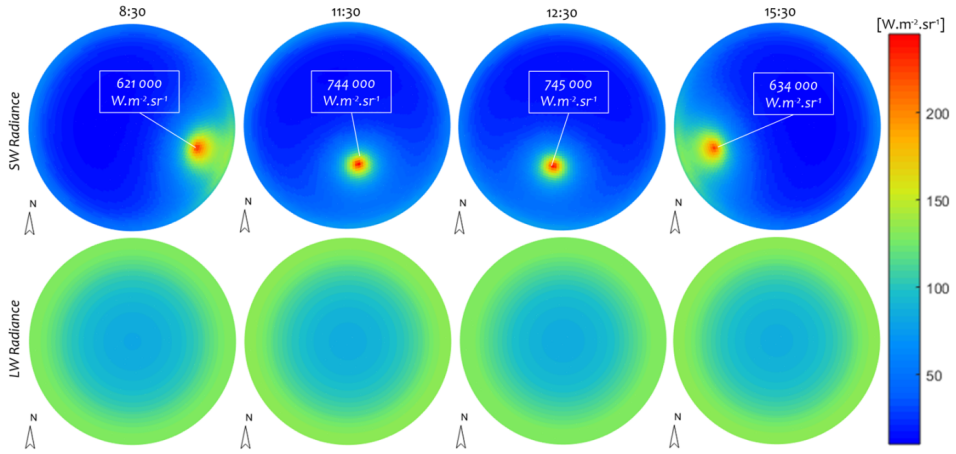

Figure 6.5: Modeled short-wave and long-wave radiance distribution on the 23rd of April 2017.

The integration of ε_ζ on the hemisphere, considering b as a constant, gives a new value of the sky global emissivity ε'_{sky} that is different of up to 5% from ε_{sky}. To ensure energy conservation, b should be a variable depending on the weather conditions, especially on the outside relative humidity. In this model, it was estimated over an iteration process; ε'_{sky} was calculated for b ranging from 1.15 to 1.95 with a step of 0.01 and compared to ε_{sky}, the value of b which minimizes the difference $\Delta\varepsilon = \varepsilon'_{sky} - \varepsilon_{sky}$ is taken for the computation of $\Delta\varepsilon$. The weather conditions were stable on the selected day and the value of b ranges from 1.48 to 1.49, with a difference $\Delta\varepsilon$ lower than 0.5%.

The sky temperatures obtained at different time steps are shown in Figure 6.6 using a partition of the sky vault in 5000 tiles. The gradient between the horizon and zenith depends on the weather

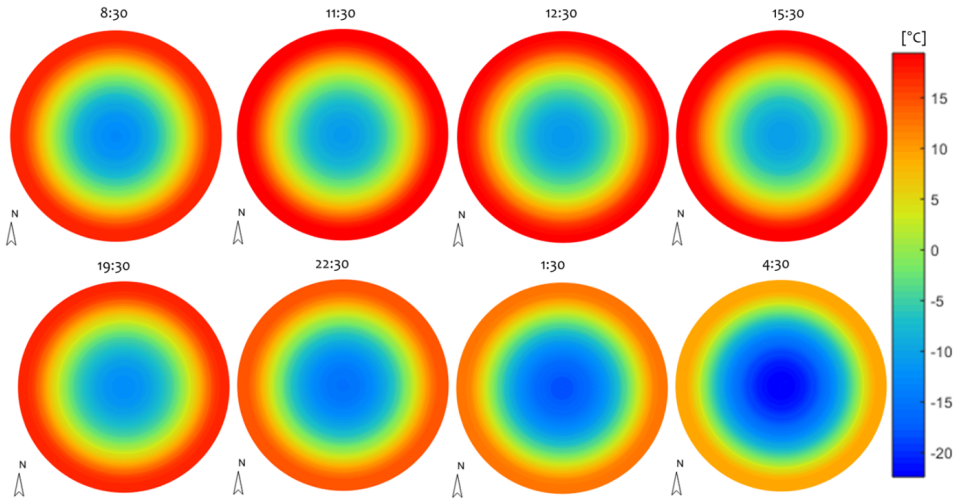

Figure 6.6: Modeled sky temperature on the 23rd of April 2017.

conditions—its variations were negligible on the selected day. The sky temperatures obtained using the proposed model match the observed sky temperatures at night under a clear sky. During daytime, the lack of data makes this result difficult to analyze, but the temperature differences between the zenith and the horizon are so important that it appears reasonable to prefer this distribution to an

isotropic one.

6.4 Computational model

In this section, the computational model used to perform the simulation of thermograms at the urban scale is described. For FEM computations, Cast3m was used [Charras and Di Paola, 2011], which benefits from an accurate treatment of long-wave radiation. For short-wave input fluxes, the radiosity method implemented in MATLAB was used [Aguerre et al., 2017].

Location Day Time	Bayonne, (43.545453 N, 1.188985 E) April 23^{rd} 00:00 to 24:00
Elements	8 nodes hexahedrons 4 nodes quadrilaterals for envelope 4 layers of hexahedrons within walls
Size of the geometry	113580 volumes 28395 exterior quads (radiation)
Simulation	10 minute time steps (144 steps)

Table 6.2: Summary of the main components of the computational model.

6.4.1 Characteristics of the mesh

FEM computations require the geometry to be discretized into elements. The resulting mesh must be congruent in order to ensure suitable simulation conditions. As shown in Figure 6.1, the scene contains four boxes, each one with six faces: a base, four walls, and a roof. The street must be connected to the buildings. Finally, a ground surrounding the structures was added to ensure accurate boundary conditions for both conduction and radiation.

The components of the scene are meshed with volumes for conduction and surfaces for the envelope that are subject to boundary conditions (radiation and convection). We chose to use hexahedrons to mesh the volume, which defines an envelope composed of quadrilaterals.

Regarding the interpolation functions, linear elements were used. Since the evolution of temperature through the different components may be non-linear, several layers of elements must be added to the walls to correctly simulate the surface temperatures. This approximation makes the mesh more complex but allows for more precise tracking of the temperatures within the volumes. Tests were made using one to four layers of hexahedrons in each wall; the results started to converge from two layers and we chose to use four layers of hexahedrons in each wall to ensure the validity of the results.

We started by meshing the buildings. Each of the six external faces is constructed separately, starting by the exterior surface (Figure 6.7a). As it can be seen, the surface is composed of many elements in the edges that account for the layers of the other surfaces that are in contact with it. The correspondent volume was then obtained by extruding the surface. The total volume of the building is constructed by joining the partial volumes and eliminating the duplicate nodes (Figure 6.7b).

After the buildings were meshed, the edges of the bases that face the urban canyon are joined to build the street surface and its volume by extrusion. Finally, a surrounding ground is added using

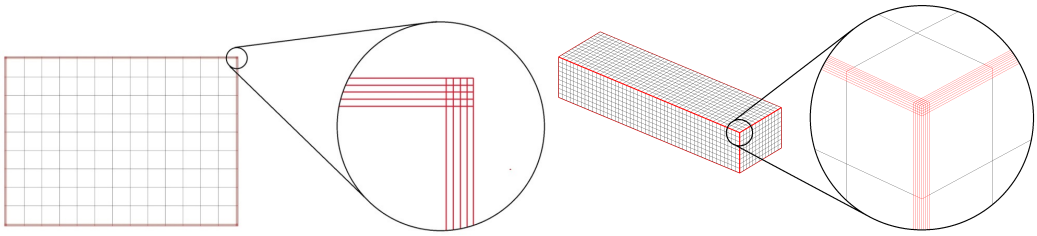

(a) Exterior surface of a wall (b) Volume of building

Figure 6.7: Parts of the geometry.

the contour of the bases and the street. The ground mesh gets finer near the buildings to have better precision in that area.

The mesh is built using elements of area 1.5 m x 1.5 m, except for the tiny elements along the edges, which are sized according to the wall width (0.18 m) and the number of layers (4 layers). The 4 buildings bring a total of 87904 volume elements and an exterior envelope of 21976 quadrilaterals. The street is composed of 2828 volumes and 707 surfaces, while the ground has 22848 and 5712, respectively. The total number of volume elements is 113580, while the exterior envelope is composed of 28395 quadrilaterals. Finally, a skydome was added to simulate the radiative exchange between the city and the sky, which is composed of 240 quadrilaterals.

6.4.2 Pre-computations

Short-wave Radiation

The computation of short-wave radiation is a fundamental step in the simulation as it is the main external flux of energy entering the model. Irradiance over a surface in the city model is composed of the sum of the direct and diffuse energies coming from the sky and the radiation reflected on other surfaces (surrounding buildings, ground, etc). Therefore, two major phenomena need to be simulated: the sky emission and the diffuse radiative exchange inside the city.

The radiative exchange between the surfaces in the city was computed using a radiosity algorithm, with the assumption that all surfaces are Lambertian reflectors [Cohen et al., 1986]:

$$(\mathbf{I} - \mathbf{RF})J = \xi \tag{6.7}$$

In this equation, $\mathbf{I}$ is the identity matrix, and $\mathbf{R}$ is a diagonal matrix containing the reflectance of each patch (Rii=ri). J is the radiosity vector to be found, and ξ is the emission vector; both are expressed in [W m^{-2}]. $\mathbf{F}_{ij}$ is a number between 0 and 1 known as the form factor between patches i and j. This value indicates the fraction of the radiation leaving i that reaches j. Matrices $\mathbf{I}$, $\mathbf{R}$, and $\mathbf{F}$ have dimension $n \times n$, while vectors J and ξ are $n \times 1$; n is the number of interacting patches.

The computation of matrix $\mathbf{F}$ was the most expensive part of the pre-computation stage. These calculations were performed using the hemi-cube algorithm, taking advantage of modern graphics hardware potential to determine visibility between the elements. Because the geometry is static, this computation was performed only once, allowing for an efficient evaluation of multiple radiation configurations [Aguerre et al., 2017].

After computing radiosity values, the radiant power absorbed by each element $\wedge_i$ was calculated from irradiance values E_i, and entered in Cast3m as imposed flux:

$$\Lambda_i = (1 - r_i)E_i \text{ with } E_i = \sum_{j=1}^{N} \mathrm{F}_{ij} J_j \tag{6.8}$$

Tests were conducted to analyze the importance of considering short-wave radiation bounces; it demonstrated that the reflected component is fundamental to avoiding the underestimation of short-wave irradiances. Walls in shadow are very sensitive to radiation bounces. Moreover, the number of elements in the sky is a very important parameter in the simulation. A sky divided into a few elements does not allow for an accurate estimation of direct radiation, while an over-tessellation of the elements reduces the computational performance of the algorithm. With 150 elements, sharp shadows tend to be replaced by a gradient that is not suitable for thermography simulation. The incorrect shadow representation only disappears with thousands of elements [Beckers and Beckers, 2014]. In this test, 2400 elements were used.

Cast3m uses form factors for long-wave radiation calculations over the same mesh. Because the emissivity of each element is set to 1, the radiosity J_i is only composed of the emitted component (σT_i^4). The current Cast3m implementation works with full matrix representations to store the matrix $\mathbf{F}$, which increases the memory consumption of the simulation. The sky subdivision for long-wave radiation can be reduced without a significant impact on the results; therefore, a dome composed of 240 elements was used.

Initial temperature

The initial conditions have a strong influence on the simulation results and a sufficiently long simulation period is necessary to capture the true solution [Kramer et al., 2012]. As stated in Sec. 6.3, the first thermogram was taken at 4:00. The initial temperatures correspond to the steady state solution obtained at 22:00 the previous day. The simulated surface temperatures are compared after periods of 6 and 30 hours, repeated the same day—the differences were less than one degree. Hence, a simulation period of 6 hours appears sufficient in this case.

6.4.3 FEM for heat transfer

The transient heat conduction equation (Eq. 6.2) can be solved with the finite element method (FEM) [Lewis et al., 2004]. FEM provides a solution of partial differential equations through a system of algebraic equations with a finite number of unknowns (points defined in the domain, hereafter called "nodes"). The discretization process involves:

1. subdivision of the computational domain into smaller parts, called *finite elements*,
2. local resolution of integrals and assembly into a global system of algebraic equations,
3. solution of the resulting system. When working with 3D geometries, conductive phenomena occur in the solid, while heat exchanges take place in some parts of the surfaces that enclose the domain.

A single element can be inside the domain, and consequently all its faces are shared with contiguous ones. When the element is situated along the border of the domain, it can contain one face

S_1 subjected to convection and/or another one S_2 loaded with a heat flux.

First, the variational principle of temperature [Lewis et al., 2004] is shown:

$$< \int_{\Omega} \left[\frac{k}{2} \nabla\tau \, . \, \nabla\tau \right] d\Omega + \frac{1}{2} \int_{S_1} h(\tau - \tau_a)^2 dS + \int_{S_2} q_e \tau \, dS > \; minimum \tag{6.9}$$

This functional is transformed into its discrete form by introducing an approximated temperature field. Inside the element, the temperature is given by the following expression:

$$\begin{aligned} \tau &= [N_1(x,y,z) \quad ... \quad N_i \quad ... \quad N_m] \{T\} = \{N\}^T \{T\} \; with \\ \{T\}^T &= [T_1 \quad ... \quad T_i \quad ... \quad T_m] \end{aligned} \tag{6.10}$$

The m weight functions N_i are related to the m nodal temperatures T_i of the element. They are continuous between elements, and equal to 0 on all the nodes except one, where they are equal to 1. Similarly, we can define the l weight functions on the face of the element counting l nodes. In this problem, to include the convective external node at temperature T_a, an extra weight function equal to -1 can be added.

$$(\tau - \tau_a)^{S_1} = [M_1(x,y,z) \quad ... \quad M_i \quad .... \quad M_l \quad -1] \begin{Bmatrix} T^{S_1} \\ T_a \end{Bmatrix} = M^T \begin{Bmatrix} T^{S_1} \\ T_a \end{Bmatrix} \tag{6.11}$$

The algebraic form of the principle is then:

$$\frac{1}{2} \{T\}^T \int_{\Omega} k(\nabla N)^T \cdot \nabla N \, d\Omega \; \{T\} + \frac{1}{2} \begin{Bmatrix} T^{S_1} \\ T_a \end{Bmatrix}^T \int_{S_1} h M^T M dS \; \begin{Bmatrix} T^{S_1} \\ T_a \end{Bmatrix} + \int_{S_2} q_e M^T dS \left\{ T^{S_2} \right\} \tag{6.12}$$

From this expression, the three contributions for the element are deduced. The first one corresponds to the classical conductivity matrix.

$$\mathbf{K}_{element}^{conduction} = \int_{\Omega_{element}} k(\nabla N)^T \cdot \nabla N \, d\Omega \tag{6.13}$$

The second integral leads to a second conductivity matrix defined on the S_1 part of the border [De Veubeke and Hugge, 1972].

$$\mathbf{K}_{element}^{convection} = \int_{S_1} h M^T M \, dS \tag{6.14}$$

The third one allows for the computation of the generalized heat loads (i.e. the weighted averages of the imposed heat flow q_e). This imposed heat flow can be any integrable function defined on S_2. This function can be discontinuous on S_2, for instance, it can correspond to partial Sun illumination. The component f_i of the heat flow is given by:

$$f_{i,element} = \int_{S_2} q_e M_i dS \tag{6.15}$$

With these definitions, at the element level, the discrete variational principle is:

$$\frac{1}{2}\{T\}^T \mathbf{K}_{element}^{conduction}\ \{T\} + \frac{1}{2}\begin{Bmatrix} T^{S_1} \\ T_a \end{Bmatrix}^T \mathbf{K}_{element}^{convection}\ \begin{Bmatrix} T^{S_1} \\ T_a \end{Bmatrix} + \left\{T^{S_2}\right\}^T \{f\} \tag{6.16}$$

Performing the derivation with respect to the parameters—nodal temperatures—we obtain:

$$\mathbf{K}_{element}^{conduction}\ \{T\} + \mathbf{K}_{element}^{convection}\ \begin{Bmatrix} T^{S_1} \\ T_a \end{Bmatrix} + \{f\} = 0 \tag{6.17}$$

This relation is the discrete form of the heat transfer equation limited to a domain composed of a single element and subjected to loads on S_2 and to convection on S_1.

The radiative heat transfer must be performed accurately for simulating urban scenarios, as the temperature difference between walls can be significant. Moreover, the sky plays an important role in the computations because the temperatures of some zones of the sky hemisphere can be much lower than those of the city elements.

Long-wave radiation is treated in a similar way as convective conditions. The radiative surfaces produce heat proportionally to the fourth power of their temperature. An important assumption is that all the surfaces are blackbody, i.e., their emissivity is 1, so there are no long-wave reflections. The flux at a given point on the boundary exchanged with the visible scene at temperature T_r is then expressed by:

$$q_{lw} = \sigma\left(T^4 - T_r^4\right) \tag{6.18}$$

In this relation, T_r is the average temperature of the surroundings, composed of the elements visible from the considered point. The fourth power of T defines a nonlinear system. An iterative scheme allows for solving the system by simulating radiation as a convective flux. Eq. 6.18 is modified in the following way:

$$\begin{aligned} &q_{lw} = h_{rad}(T - T_r), \\ &with\ h_{rad} = \sigma\left(\tilde{T}^2 + T_r^2\right)(\tilde{T} + T_r), \end{aligned} \tag{6.19}$$

where T is the unknown temperature and $\tilde{T}$ is the temperature at the previous iteration. The neighbor temperature is computed in each iteration by calculating irradiances E from $\tilde{T}$.

$$\begin{aligned} &T_r = (E_i/\sigma)^{\frac{1}{4}} \\ &with\ E_i = \sum_{j=1}^{N} F_{ij}(\sigma\tilde{T}_j^4) \end{aligned} \tag{6.20}$$

Good convergence schemes ensure $T \simeq \tilde{T}$ at the last iteration, hence Eq. 6.20 is equivalent to Eq. 6.18. The radiation conductivity matrix is then:

$$\mathbf{K}_{element}^{radiation} = \int_{S_r} h_{rad} M^T M\ dS \tag{6.21}$$

As previously seen for convection, the vector of shape functions on the face of the element is extended to include the temperature of the element to which radiative transfer is occurring.

The heat transfer differential equations involve second-order terms, and thus, require two boundary conditions to be solved:

1. Dirichlet (imposed temperature): T = Tb on a part of the boundary. In our simulation, the temperature was also imposed on the sky, the inner layer of the street and the ground. The air temperature used for convection can also pertain to this category of boundary condition.
2. Neumann (imposed flux): $q_e = -k\partial T/\partial n$ on the rest of the boundary. This kind of boundary conditions is used for imposing short-wave fluxes.

Time t appears as a first-order term in Eq. 6.2, so an initial value is necessary to solve the equation: T = T0 at t = 0. In the transient problem, a new element, matrix C, is introduced to describe the capacity of the material to store heat. At the elemental level, this matrix is simply defined by:

$$\mathbf{C}_{element} = \int_{\Omega_{element}} \rho c_p N^T N d\Omega \tag{6.22}$$

In this expression, ρ represents the specific mass (kg m^{-3}) and c_p the heat capacity (J kg^{-1} K^{-1}). By adding all of the element contributions, (Eqs. 6.17 and 6.22), we obtain the global equations to be solved.

$$\mathbf{C}\frac{\partial}{\partial t}\{T\} + \mathbf{K}\{T\} - \{f\} = 0 \tag{6.23}$$

In this equation, which is the discrete form of Eq. 6.2, $\mathbf{C}$ is the global capacitance matrix (mass matrix in elasticity) and $\mathbf{K}$ is the global conductivity matrix (stiffness matrix for elasticity), T is the unknown's vector, and f is the load (heat flow) vector. Each term of the above expression is expressed in watts.

The time temperature derivatives are discretized through a forward difference approach.

$$(\mathbf{C} + \theta\,\Delta t\,\mathbf{K}\,)\left\{T^{n+1}\right\} = (\mathbf{C} - (1-\theta)\,\Delta t\,\mathbf{K})\,\{T^n\} + \Delta t\,\left(\theta\left\{f^{n+1}\right\} + (1-\theta)\,\{f^n\}\right) \tag{6.24}$$

Each term of the above expression is expressed in joules. The variables θ , Δt, $\left\{f^{n+1}\right\}$ are imposed while $\{T^n\}$ and $\{f^n\}$ are computed at the previous step. The value θ = 1 corresponds to the implicit scheme considered as unconditionally stable.

$$(\mathbf{C} + \Delta t\,\mathbf{K})\left\{T^{n+1}\right\} = \mathbf{C}\,\{T^n\} \;+ \Delta t\left\{f^{n+1}\right\} \tag{6.25}$$

The resolution of this algebraic system of equations enables the unknown temperatures at each node to be obtained, which is the basis for simulating the thermography. In the study, the solution was obtained with time steps of 10 minutes. With 6 steps per hour, simulating 24 hours requires 144 steps.

6.5 Simulation results

Regarding the computational performance of the simulations, the algorithms were executed in short times on a standard desktop PC (see Table 6.3). The main limitation of the system was the memory consumption for storing the form factors matrix, used for radiation computations within the Cast3m

framework. In future simulations, higher levels of detail will lead to a larger number of elements; thus, the use of alternative matrix representations such as sparse formats must be studied.

Task	Execution time (minutes)	Memory consumption (Gbytes)
Short-wave pre-computation	3.2	1.5
Cast3m pre-computation	16.9	12.8
Step	1.3	-
Total	202.1	14.2

Table 6.3: Detail of the execution of the simulation.

6.5.1 Simulated thermograms

Simulated surface temperatures are compared to the actual thermograms on selected time steps in Figure 6.8. The overall temperature patterns are accurately predicted by the simulation, with bigger differences on the north facing wall than on the south one. At 7:00, the Sun reached the north facing wall and the surface temperatures began to rise. At 10:00, the street surface temperature was overestimated, which is explained by the geometrical simplification of flat roofs without overhangs; sunlight reaches the ground on the simulation, while in the corresponding photograph this zone is shadowed by the north facing buildings. From 13:00 onwards, the temperature of the wooden carpentry and joinery reaches up to 40°C; those elements, characterized by low reflectance and thermal inertia, were not considered in the simulation. At night, the points with lower surface temperatures were those with a higher sky view factor, both on the simulations and thermograms.

The measured thermograms show negligible differences in the surface temperatures between adjacent buildings under similar radiative conditions (SVF, solar radiation). This finding justifies grouping the building rows into unitary boxes. On the contrary, on-site thermograms reveal that the presence of a street intersection may be significant from a thermal point of view, making it necessary to model four boxes (as opposed to the two that are typically represented in classical urban canyon models). Nevertheless, the assumption of flat roofs with uniform building heights leads to some deviations between the simulation results and the thermograms, mainly due to differences in shadow patterns. Despite this bias, this modeling method enables the understanding of the main heat exchange phenomena in the street while simplifying the test case and simulation conditions. In summary, it allows the test case to be both instructive and easily replicable.

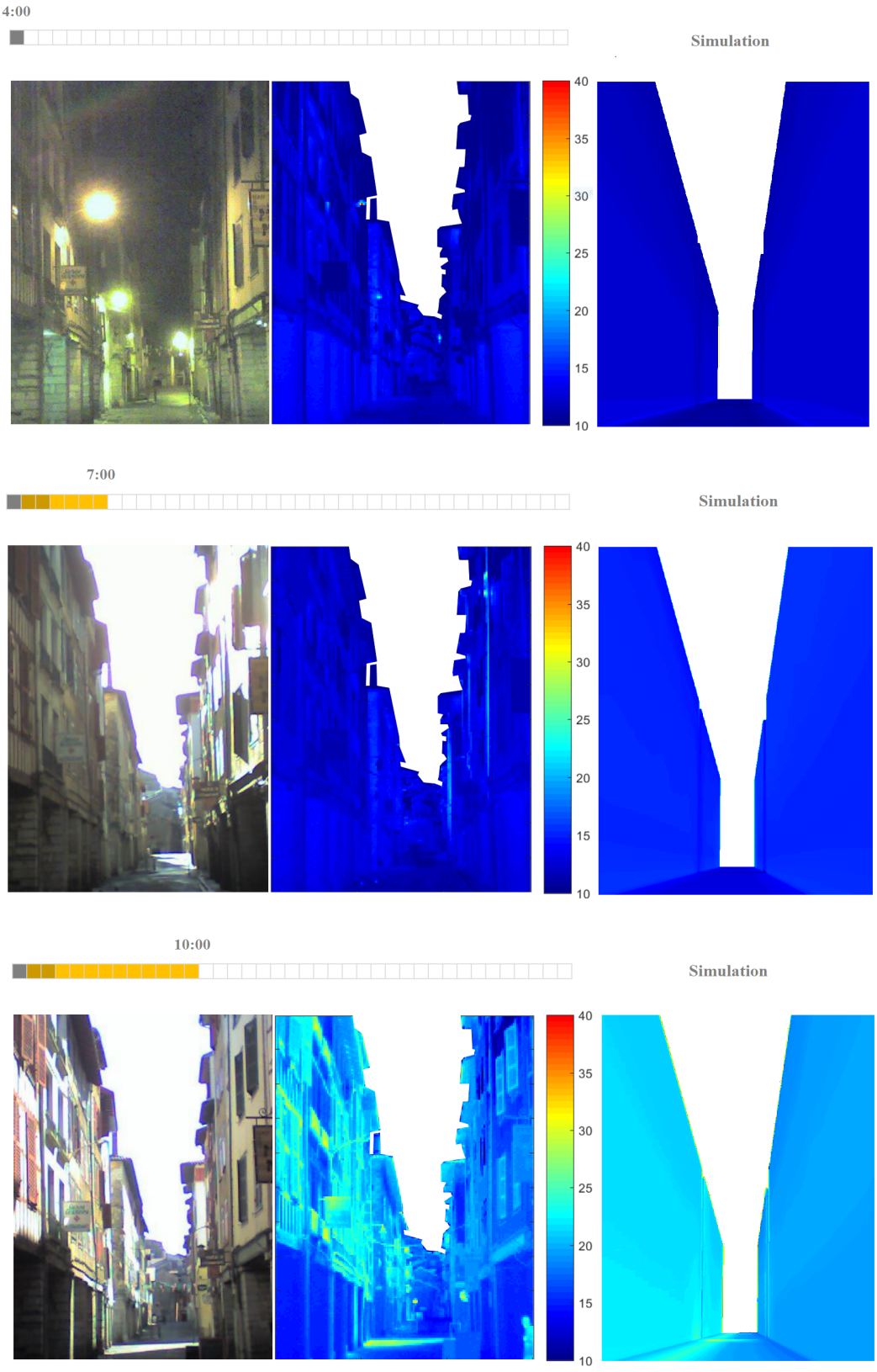

Figure 6.8: Time-lapse of the photographs, thermograms, and corresponding simulated results (at 4:00, 7:00, and 10:00 ST).

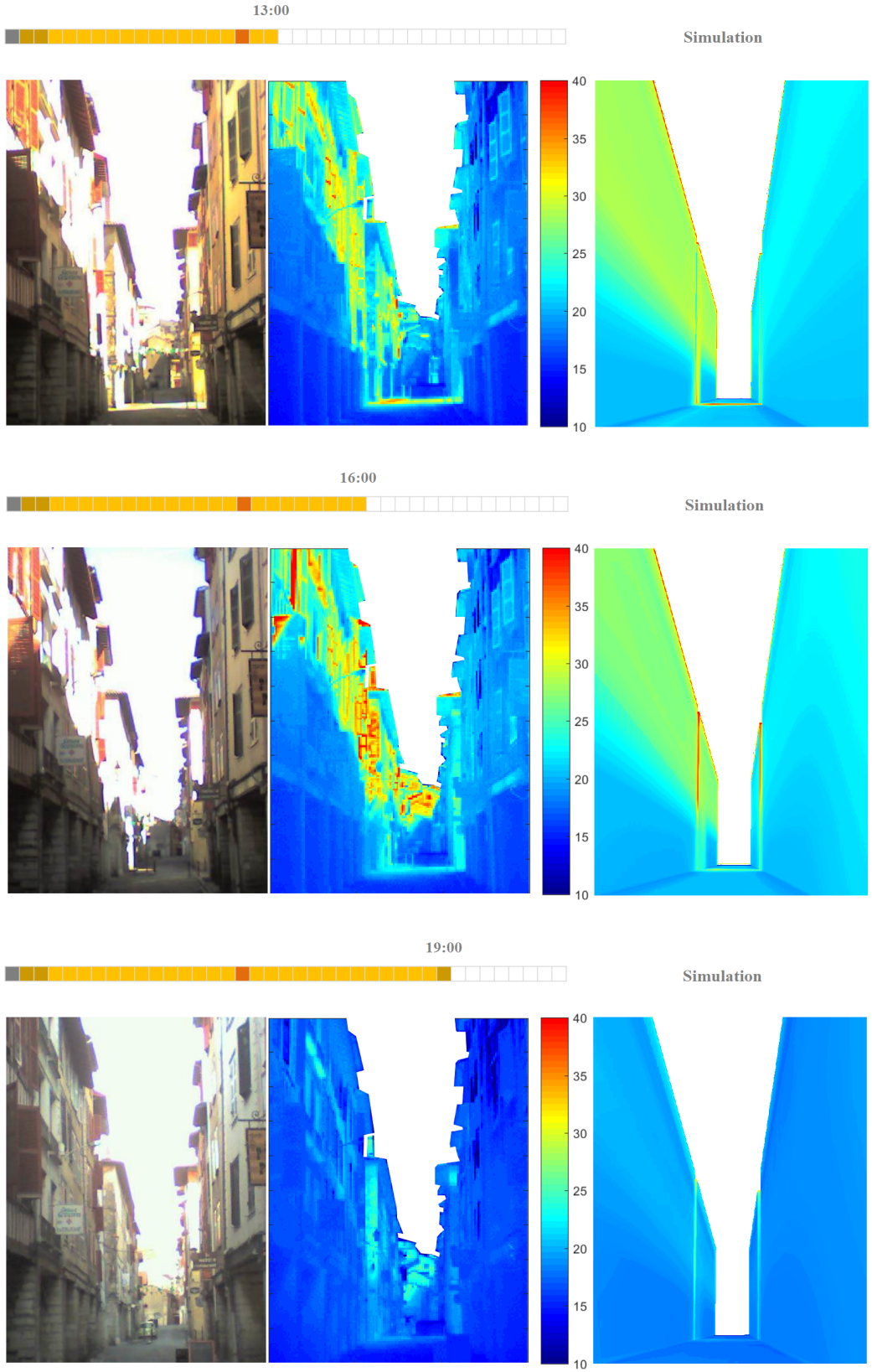

Figure 6.8: Time-lapse of the photographs, thermograms, and corresponding simulated results (at 13:00, 16:00, and 19:00 ST).

6.5.2 Temperature evolution for 3 points

To evaluate the results, three points were selected, and the evolution of the apparent surface temperature was plotted. The experimental plots were obtained by selecting pixels on the thermograms and matching their color with the respective temperature.

Figure 6.9 shows the points coordinates. Two points are selected at different heights on the south facing wall and one on the north facing wall.

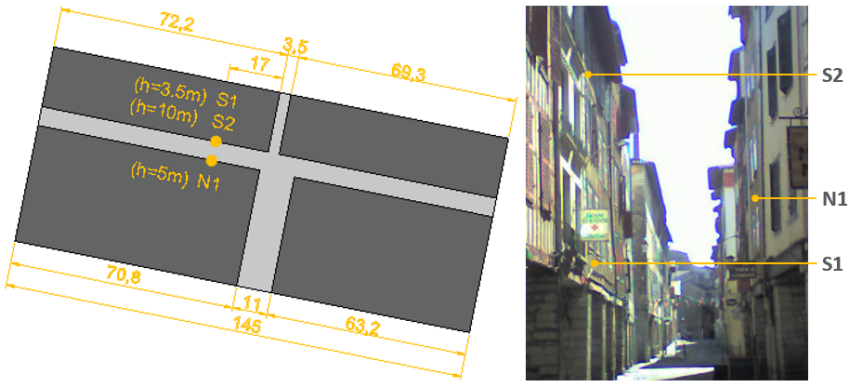

Figure 6.9: Selected points for evaluating the simulation results.

There is a strong correlation (Figure 6.10) between the simulated and observed surface temperatures for both points on the south facing wall (S1 and S2), with a difference smaller than 2°C from 10:00 to 23:00. The discrepancy is greater on the north facing wall, with a difference of nearly 5°C for most of the day.

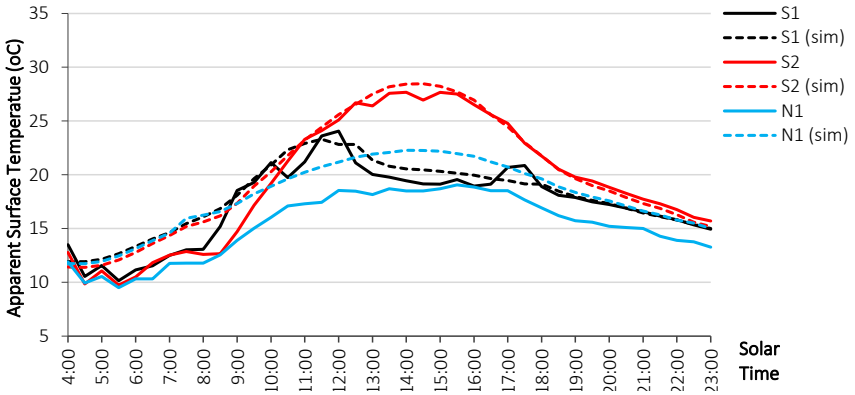

Figure 6.10: Temperature evolution at the selected points (dashed lines are the simulation results).

For a better interpretation of these results, the heat transfers at the interface of the wall and the air on the selected points are shown in Figure 6.11. The positive values reflect heat absorption by the wall surface. Short-wave absorbed radiant power is the input flux described in the above sections. The total long-wave heat balance is the difference between long-wave radiant power absorbed and emitted by the surface. It was divided into two components: sky and urban surfaces). Both were calculated at the barycenter of the concerned elements. For the sake of simplicity, the conductive and

convective heat transfers were also calculated at the barycenter of the same elements. The convective heat transfer was obtained at each time step by the Newton formula, Eq. 6.5. All of the heat absorbed by the surface was transmitted through the wall by conduction, thus the conductive heat transfer was obtained as the opposite of the sum of the convective and radiative heat transfers.

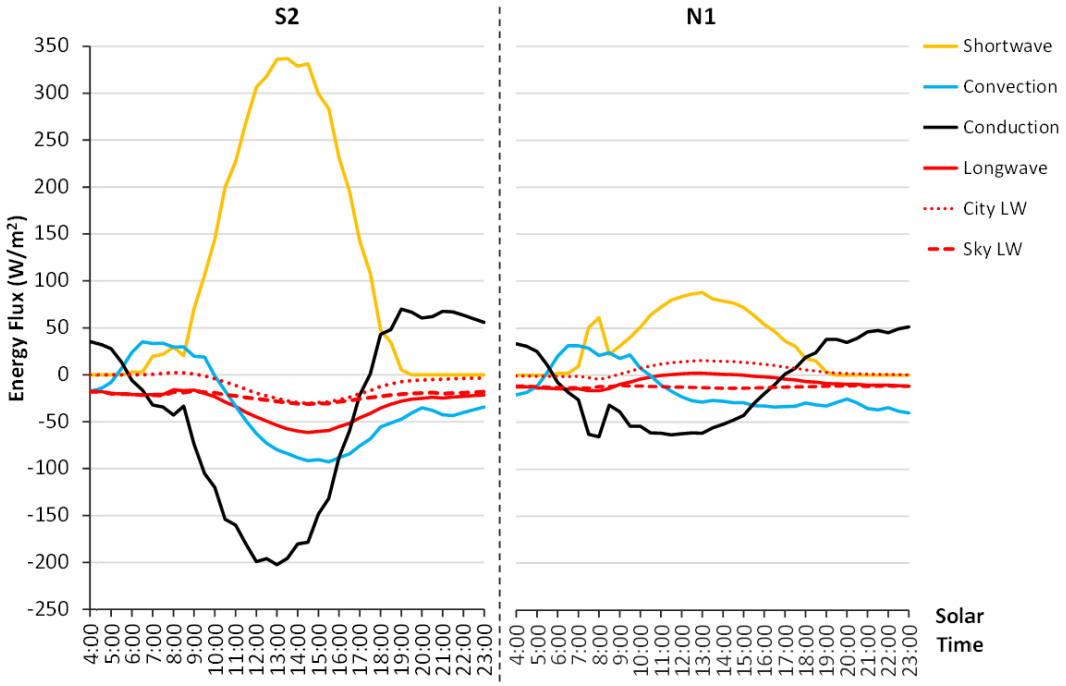

Figure 6.11: Heat balance at points S2 and N1.

The Sun reached the north facing point from 7:00 to 8:00 and the south facing point from 8:00 to 18:00. From 7:00 to 8:00, the short-wave radiant power absorbed by the north facing surface was due to the direct solar radiation. From 8:00 to 18:00, it was primarily due to the reflection of the south facing wall. Conversely, the short-wave radiant power absorbed by the south facing surface was due to reflections from 7:00 to 8:00 and direct radiation from 8:00 to 18:00. For the selected points, the conductive heat transfer was positive from 18:00 to 6:00 as the wall surface was heated by conduction during the night, regardless of the orientation. The long-wave radiative heat transfer with the sky was negative all day long for all of the selected points and induced a decrease in the street surface temperatures. The long-wave radiative heat transfer between the street surfaces was negative all day long for the south facing points and positive on the hottest hours of the days for the north facing point; the surface temperature of the south facing wall, when heated by the Sun, was higher than that of the north facing wall, and the long-wave radiant power emitted by the former is heating the latter. The convective heat transfer was positive from 5:00 to 10:00 and negative for the rest of the day regardless of the orientation; the exterior surface temperatures were higher than that of the air and the walls were cooled down by convection during most of the day, except for the first few hours after sunrise (5:00 to 10:00) when the air temperature increased rapidly.

Until 8:00, the simulated temperatures were higher than the observed ones, with differences of up to 5°C for both orientations. During this time, the wall surface was heated by conduction; the interior surface temperature of the wall was higher than that of the exterior surface, mostly due

to the assumption that a heating system ensures a constant interior air temperature of 20°C. The differences are explained by the fact that the buildings were not actually heated, or at least, that the setpoint temperature was overestimated for this time.

From 8:00 onwards, the simulated surface temperatures on the north facing wall were overestimated. During this time range, the selected point was not exposed to direct solar radiation and the short-wave radiant power absorbed by the north facing surface was mostly due to the reflected radiation. The differences between the simulated and observed surface temperatures show that the short-wave reflections reaching the north facing surface were overestimated, which can be explained by the simplification of the geometry, especially the assumptions of flat roofs without overhangs and the omission of ground floor arcades.

6.6 Modifying the urban scene

6.6.1 Impact of the thermal inertia

Thermal inertia reflects the resistance of materials to temperature changes; it is a key property for diurnal and seasonal surface temperature variations. It can be characterized by the diffusivity α of the material, which is the ratio of the thermal conductivity k to the product of the density ρ and specific heat c_p:

$$\alpha = \frac{k}{\rho c_p} \tag{6.26}$$

In the reference simulation, the walls were supposed to be made of cob, a mixture of clay, water, and straw that is commonly used in the historical center of the city of Bayonne. The actual proportion of each material may vary, resulting in different thermal characteristics. The density, specific heat, and thermal conductivity used for the simulation are representative of the cob traditionally used in Bayonne. To illustrate the impact of thermal inertia on the surface temperature variations, a heavy and a light cob with high and low thermal inertias, respectively, were tested. The heavy cob has a higher proportion of clay than the traditional one, resulting in a higher density, while the light cob has a higher proportion of straw, resulting in a lower density, conductivity, and specific heat (cf. Table 6.4). Figure 6.12 shows the evolution of the temperature for the points selected for those materials.

	ρ [kg m^{-3}]	k [W m^{-1} K^{-1}]	c_p [J kg $^{-1}$ K^{-1}]	α [m^2 s^{-1}]
traditional cob	1400	1.05	1500	5.00×10^{-7}
heavy cob	1800	1.05	1500	3.89×10^{-7}
light cob	600	0.50	900	9.26×10^{-7}

Table 6.4: Material properties.

The amplitude of the surface temperature variation was much higher for a low inertia material, with, for example, maximum and minimum temperatures of 34°C and 10°C at point S2 for the light cob, respectively, in contrast with 28°C and 12°C for the traditional cob. The differences between the heavy and traditional cobs are less important, which is explained by the small difference of diffusivity between the two materials. The peak temperature was delayed for a material with high inertia; the

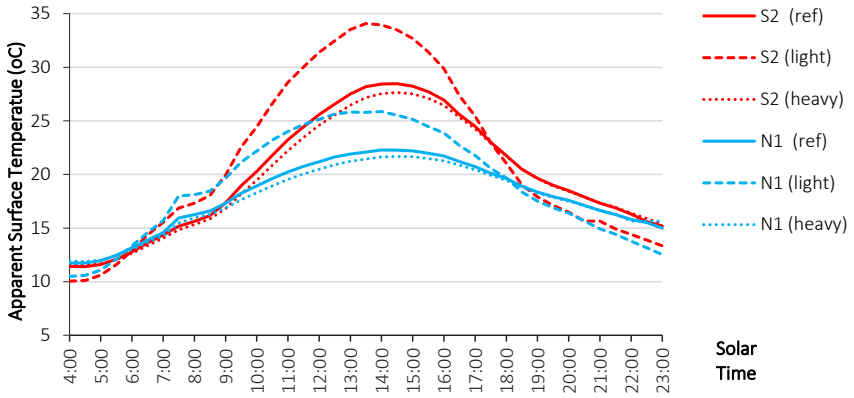

Figure 6.12: Temperature evolution at S2 and N1 for different kind of material inertia.

maximum surface temperature at point S2 was reached at 13:30 for light cob, corresponding to the maximum short-wave irradiance on the south facing wall, and at 14:30 for heavy cob. There is a phase difference of one hour between both materials.

6.6.2 Impact of the reflectance

The reflectance of a material expresses the fraction of the incident short-wave radiant power that is reflected by its surface. The remaining fraction is absorbed and induces a rise in the surface temperature, which explains the difference in the thermograms between the bright and dark parts of the wall. To illustrate this phenomenon, the surface temperatures were computed for reflectances of 40%, corresponding to the reflectance of the dark parts of the wall, and 90%, corresponding to the reflectance of a white wall, as can be found in cities with high levels of sunshine such as Seville or Cordoba in the south of Spain (cf. Figure 6.13).

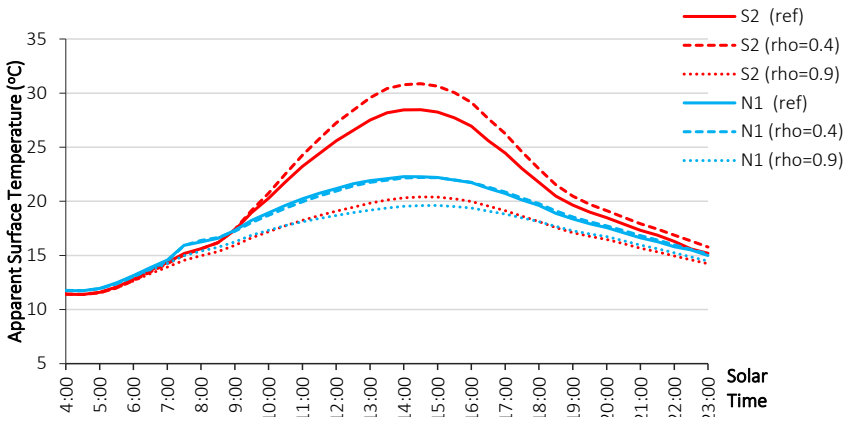

Figure 6.13: Evolution of the simulated temperature at S2 and N1 for different reflectances.

The temperature of the south facing surface was much higher for a reflectance of 40% than in the reference simulation, with a difference of 4°C between the maximum temperatures at S2. The differences on the north facing wall are less important as the short-wave radiant power absorbed at its surface is less important than convective and conductive fluxes. For a reflectance of 90%, the

short-wave radiant power is equally distributed between the south and north facing walls, thus, the surface temperature is nearly the same at the three selected points.

6.7 Conclusions

The main objective of this study was to demonstrate the possibility of simulating thermograms at the urban scale using FEM (i.e., providing precise physical solutions without losing the information on the geometry).

A real urban district was chosen (a quiet street with little traffic in the city of Bayonne) in which a time sequence of thermograms was produced using a standard thermal camera set on a tripod. A cloudless day with very little wind was selected to take benefit from simple weather conditions. The thermal images were all set to the same scale (from 10 to 40°C) to allow for comparison.

After the experimental step, a simple geometrical model (four regular boxes of uniform thickness) of the street was built to capture the main physical phenomena: the correct orientation of the street, average building heights, etc. The environmental and boundary conditions were carefully established using on-site measurement, data from a nearby weather station, and when necessary, estimations based on observations and the available literature. The set of these conditions has not been influenced by the simulation results.

The simulations, performed using the Cast3M software, provide compelling results, reproducing the same order of magnitude and general appearance of the measured thermograms. The main discrepancies are explained by the difference between the actual street and the model (i.e., the assumption of flat roofs without overhangs and uniform exterior coatings). The computations were made in a reasonable amount of time and could be reproduced using most of the existing FEM codes.

Thermography produces spatialized information; therefore, it is possible to choose the most interesting points of the geometry and assess the balance of energy fluxes at their localization through a complementary diagram. To do so, only the computed surface temperatures were used, i.e., the FEM simulation primary results. The flux analysis on representative and remarkable points of the geometry allowed for a better understanding of the simulated thermograms.

Simulations by means of FEM appear to be useful in accurately evaluating alternative scenarios for the urban canyon. To illustrate this potential, this study assessed the impact of modifying the outside coatings and thermal diffusivities of walls. It was demonstrated that changes at the street scale may significantly affect the thermal behavior of individual buildings. For instance, changing the facades reflectance from 60 to 90% in the studied canyon leads to a temperature difference of up to 10°C on the south surface.

The results of this paper highlight the interest aspects of performing a thermal analysis at a street level based on a perspective view. This spatial scale allows for the quantification of energy interactions between the buildings. Displaying results in perspective provides a comprehensive view of the scene and a deeper understanding of the physical phenomena.

Streets seem to be the smallest scale on which architectural interventions may have a real impact on the urban thermal environment, which simultaneously affects outdoor comfort and building energy demands. Besides, its representation in perspective is easily understandable to designers and may help to better incorporate thermal criteria into urban projects.

Acknowledgements The work was partially supported by project FSE_1_2017_1_144731 from Agencia Nacional de Investigación e Innovación (ANII, Uruguay). The authors would like to thank Nadia Coulon for her assistance with Cast3m programming. Contributions to this work carried out by Elena Garcia-Nevado were supported by a PhD fellowship granted by the FPU program of the Spanish Ministry of Education (FPU 13/03884).

Chapter 7

Improving FEM computations for the simulation of thermograms at the urban scale

---

The contents of this chapter were published in:
Aguerre, J. P., Nahon, R., Fernández, E., and Beckers, B. (2019). *Improving FEM computations for the simulation of thermograms at the urban scale*. Proceedings of Building Simulation 2019: 16th Conference of IBPSA.

Infrared cameras allow for the estimation of the temperature of urban surfaces. A time sequence of thermograms can be accurately simulated by computational techniques such as the finite element method (FEM) for transient heat transfer. The main objective of this work was to improve FEM convective and radiative boundary conditions, enabling a more precise analysis of an urban scene. The software Cast3m was used for performing the simulations, and the results were compared to a set of thermograms taken in the city of Bayonne through a clear-sky day. A street composed of two blocks was selected for the study, where the geometrical properties and boundary conditions were carefully established. The conducted experiments show that free internal air temperatures, rather than fixed, increase the realism of the simulation. Furthermore, the computational performance of the model was improved by exploiting specific properties of urban geometries.

7.1 Introduction

The analysis of thermograms of urban perspective views allows to obtain relevant information about the thermal behavior of buildings [Beckers and Garcia-Nevado, 2018]. Heat transfer simulation engines bring more information into the studies, because a clean comparison between accurate simulations and experimental results can reveal details about the occupants behavior and the thermal comfort of the urban scenario. The analysis of this spatialized information can help in the redesign of city elements, and even on the projection of future buildings. Nevertheless, the simulations need

to be as accurate as possible to perform a useful analysis.

The computational simulation of transient heat transfer involves dealing with several boundary conditions such as convection and radiation. Convection happens at both the exterior environment and interior spaces, having a significant effect on internal air masses and urban surfaces temperatures. On the other hand, radiation is emitted at different wavelengths by every surface with a temperature above the absolute zero. It can be studied at two levels: short wave radiation is emitted by the sun and refracted by the sky before reaching the urban surface, and long wave radiation is emitted and exchanged by the urban materials and the sky.

Thermal studies of urban elements are usually addressed using simplified models like electric circuit analogy methods, providing a balance between accuracy and algorithmic performance [Asawa et al., 2008; Kramer et al., 2012; Reinhart and Davila, 2016]. Nevertheless, the spatialized information shown in thermograms is difficult to simulate with these kind of methods due to the high level of detail and granularity needed. Other computational techniques for dealing with finer meshes are available, such as finite difference methods (FDM) or FEM [Lewis et al., 2004]. These kind of methods are not specifically designed for cities, thus adaptations must be done [Huttner and Bruse, 2009; Idczak et al., 2010; Lü, 2002]. A careful mix between these highly accurate techniques and certain modeling simplifications can enable reliable studies to be tackled using regular PCs in reasonable execution times.

In this work, a study was conducted for improving FEM boundary conditions at the urban scale using the software Cast3m [Charras and Di Paola, 2011]. Two problems were tackled. In the first place, a method inherited from previous electric analogy works [Fraisse et al., 2002; Nielsen, 2005] was adapted to FEM to address the interaction between the interior surfaces and internal air. Secondly, radiation computations, which are the most expensive part of the computations, were accelerated within Cast3m, taking advantage of the low density factor (which is the rate between non-zero elements and the total number of elements) of the involved sparse form factors matrices [Aguerre et al., 2017]. These modifications were applied to simulate the test case presented in [Aguerre et al., 2019], where a real thermography campaign was compared to FEM results. Higher accuracy is observed with the proposed modifications.

7.2 Methods

In this section, FEM for transient heat transfer is described, and the two proposed modifications for improving the computation of boundary conditions are presented.

7.2.1 Transient heat transfer

The behavior of heat conduction can be expressed by a differential equation that relies on the heat conservation law to describe the transient heat flow:

$$k\Delta T = \rho c_p \frac{\partial T}{\partial t} \tag{7.1}$$

In this equation, k ($Wm^{-1}K^{-1}$) is the thermal conductivity of the material, considered constant along the solid and isotropic (equal in all directions). Δ is the spatial temperature Laplacian. ρ (kgm^{-3}) and c_p ($Jkg^{-1}K^{-1}$) are the density and the specific heat of the material, respectively. This

differential equation has second order terms, thus requires two boundary conditions to be solved: Dirichlet (imposed temperature $T = T_b$ on part of the boundary Γ) and Neumann (imposed flux $q = -k\frac{\partial T}{\partial n}$, with n being the normal vector of the boundary geometry). Other heat transfer phenomena such as convection and radiation are expressed as boundary conditions of the conduction problem. Time t appears as a first order term in Eq. 7.1, hence an initial value is enough to solve the system.

The solution of the conduction equation in a three-dimensional complex geometry is a challenging problem in many aspects. Computational methods require the discretization of the domain (space and time), which implies the discretization of the equations. Two approaches are commonly used for this purpose: FDM or FEM. In this study, FEM was used as the main technique for treating the spatial domain Π, because it allows to deal with complex geometries. On the other hand, FDM was applied for the discretization of time (transient scheme).

7.2.2 FEM for spatial discretization of conduction

FEM provides a solution to partial differential equations through a system of algebraic equations with a finite number of unknowns in the domain [Lewis et al., 2004]. A set of elements with known shape (2D: triangles, quadrilaterals, etc; 3D: tetrahedrons, hexahedrons, etc) is defined, within which the temperature variation is described by a polynomial of first, second or higher order. Hence, the temperature can follow constant, linear, parabolic and other behaviors. The functions that describe this interpolation are the *shape functions*. For example, given a two-dimensional quadrilateral, the temperature at any point p inside the element can be expressed as:

$$T(p) = N_1(p)T_1 + N_2(p)T_2 + N_3(p)T_3 + N_4(p)T_4 \tag{7.2}$$

where T_i is the temperature at node i and N_i the correspondent shape function. By replacing the continuous temperature field in Eq. 7.1 with its discretized form, and minimizing the energy balance using the Galerkin method, a system of equations is defined:

$$\mathbf{C}\left\{\frac{\partial T}{\partial t}\right\} + \mathbf{K}\{T\} = \{f\} \tag{7.3}$$

In this equation, $\mathbf{C}$ is the capacitance matrix (diagonal matrix) and $\mathbf{K}$ is the conductivity matrix (sparse matrix). $\{T\}$ is the vector of unknowns, and $\{\mathrm{f}\}$ is the load vector. $\left\{\frac{\partial T}{\partial t}\right\}$ is the vector of temperature derivatives over time, which is not yet discretized. Eq. 7.4 shows the value of each element of the matrices. Remaining derivatives and integrals are solved using a combination of analytical and numerical methods.

$$\begin{gathered}\mathbf{C}_{ij} = \int_{\Pi} \rho c_p N_j N_i dp, \;\; \mathbf{K}_{ij} = \int_{\Pi} k \nabla N_j \nabla N_i dp \\ \{f\}_i = -\int_{\Gamma_q} N_i q dp\end{gathered} \tag{7.4}$$

7.2.3 FDM for time discretization

The time-temperature derivatives are discretized using a forward difference approach. Using Taylor series, a first order approximation of the derivatives is:

$$\frac{\partial T_{t_i}}{\partial t} \approx \frac{T_{t_{i+1}} - T_{t_i}}{\Delta t} \tag{7.5}$$

Assuming a linear variation of temperature inside a short timestep length Δt, it can be said that:

$$f_t = \theta f_{t_{i+1}} + (1-\theta) f_{t_i} \tag{7.6}$$

Replacing and rearranging Eqs. 7.5 and 7.6 in Eq. 7.3, the following system is obtained:

$$\begin{gathered}\big(\mathbf{C} + \theta\Delta t\mathbf{K}\big)\big\{T_{t_{i+1}}\big\} = \big(\mathbf{C} - (1-\theta)\Delta t\mathbf{K}\big)\big\{T_{t_i}\big\} + \\ \Delta t\big\{\theta f_{t_{i+1}} + (1-\theta) f_{t_i}\big\}\end{gathered} \tag{7.7}$$

The value $\theta = 1$ was used in this study, corresponding to an implicit scheme (unconditionally stable):

$$\big(\mathbf{C} + \Delta t\mathbf{K}\big)\big\{T_{t_{i+1}}\big\} = \mathbf{C}\big\{T_{t_i}\big\} + \Delta t\big\{f_{t_{i+1}}\big\} \tag{7.8}$$

Δt and $\big\{f_{t_{i+1}}\big\}$ are imposed, while $\big\{T_{t_i}\big\}$ is computed in the previous step.

7.2.4 Convection

A pure FEM treatment of heat transfer does not allow for the calculation of complex air movements within the city. Computational fluid dynamics can be incorporated into the model, but these bring much harder computational challenges and complicate the study. In this work, convection was simplified with the use of the heat transfer coefficient, commonly represented by the letter h. This approximation works properly when wind is not dominant in the system, i.e. a calm day is being studied. The equation that represents the heat flux by convection is presented in Eq. 7.9, which is provided by Newton's law of cooling.

$$q_c = h(T - T_{air}) \tag{7.9}$$

where T_{air} is the air temperature, and h is measured in $Wm^{-2}K^{-1}$.

Fixed air temperature. When T_{air} is input data (for example if the air temperature was measured in situ), then convection is treated as a Neumann boundary condition. Two terms are added to the system of Eq. 7.4:

$$\mathbf{K}_{ij}^{conv} = \int_{\Gamma_c} hN_jN_i dp \quad , \quad \big\{f\big\}_i^{conv} = \int_{\Gamma_c} N_i h T_{air} dp \tag{7.10}$$

Free air temperature. When T_{air} is not known (for example, if the internal air temperature was not measured) it is possible to calculate the interaction between the surface temperature of the boundary and the air. In this way, T_{air} is a new variable in the system, and an initial air temperature at t_0 is enough for computing it. Because Cast3m does not support this variation, some coding must be implemented.

A first approach for addressing this problem is the following. A new virtual node is added to the geometry, representing the air mass. All the boundary nodes are connected to the virtual node, and the air-surface interaction is modeled as a conduction problem within the FEM engine. The main advantage of this approach is that, as long as other nonlinearities (such as radiation) are not introduced, the problem remains linear. However, the computational performance for solving the system can be affected because the density factor of $\mathbf{K}$ is increased, and its sparse structure can change [Karimi et al., 2014].

In this study, a different approach was implemented, based on the techniques used in electric analogy systems [Reinhart and Davila, 2016]. In contrast with the method described in last paragraph, the surface-air interaction can be uncoupled from the FEM engine, and treated as part of the discretization of time with FDM. An iterative solver was used for solving the system of equations at each timestep.

Let us study this interaction for the case of an air mass enclosed in a room with a varying surface temperature. It is important to define the notion of the *time constant* τ, which is the parameter characterizing the response to a step input of a first-order, linear time-invariant system. The inverse of this constant (s^{-1}) is:

$$\frac{1}{\tau} = \frac{hS}{\rho c_p V} \tag{7.11}$$

where ρ and c_p are the density and specific heat of air, V is the volume of the air (m^3) and S is the surface in contact with the air (m^2).

Given an initial air temperature and the current internal surface temperatures, the goal is to compute the new air temperature and a new surface temperature. Using Newton's law of cooling, with the assumption that all the internal surfaces have the same h coefficient, the next differential equation is obtained:

$$\frac{dT_{air}(t)}{dt} = -\frac{1}{\tau}\Big(T_{air}(t) - T_S(t)\Big), \text{ with a given } T_{air}(0) \tag{7.12}$$

where $T_S(t)$ is the mean surface temperature at time t. Because a FDM is being used, the evolution of internal surface temperature follows a linear behavior within the timestep of length Δt:

$$T_S(t) = (1 - t/\Delta t)T_S^{prev} + (t/\Delta t)T_S^{cur} \tag{7.13}$$

where T_S^{prev} is the surface temperature of the previous timestep, and T_S^{cur} is the current solution of the iterative solver.

Joining Eqs. 7.12 and 7.13, a new differential equation is obtained:

$$\frac{dT_{air}}{dt} = -\frac{1}{\tau}T_{air}(t) - \frac{1}{\tau}\left(\frac{T_S^{prev} - T_S^{cur}}{\Delta t}\right)t + \frac{1}{\tau}T_S^{prev} \tag{7.14}$$

This equation has an analytical solution, which simplifies the computational effort. For each timestep, the equation is solved multiple times in the iterative solver, until reaching surface and air temperature convergence. The extension of Eq. 7.14 for various different h coefficients (for instance for each wall, roof and floor, totaling six surfaces) implies the following re-definition of the time constant: $\frac{1}{\tau} = \sum_{i=1}^{6} \frac{h_i S_i}{\rho c_p V}$.

7.2.5 Adding support for windows

Electric analogy systems allow for the simulation of windows without increasing the geometrical complexity of the model. In this study, a similar approach was used for adding this features to the FEM system.

Windows have a dual effect on convective heat exchange. In the first place, ventilation and air filtrations imply a direct exchange between external and internal air. In the second, the low thermal inertia of the thin glass present in windows causes a much faster heat flow. Therefore, two components were added to Eq. 7.12 to account for the effect of windows:

$$\begin{gathered}\frac{dT_{air}}{dt} = -\frac{1}{\tau}\Big(T(t) - T_S(t)\Big) \\ -\frac{U_V A_V}{\rho c_p V}\Big(T_{air}(t) - T_{ext}(t)\Big) - \frac{H_V}{\rho c_p V}\Big(T_{air}(t) - T_{ext}(t)\Big)\end{gathered} \tag{7.15}$$

In this equation, several terms are introduced. U_V is the thermal transmittance of the window ($Wm^{-2}K^{-1}$). A_V is the surface area of the window. This term is related to the concept of window to wall ratio, which is a measure of the total glazed area with respect to the total envelope area. H_V is the heat transmission coefficient due to ventilation (WK^{-1}):

$$H_V = \frac{\eta \rho c_p V}{3600}$$

where η is the air change rate (ACH, h^{-1}). Finally, T_{ext} is the external air temperature, which is a function of time and grows linearly between two timesteps (in a similar way than Eq. 7.13):

$$T_{ext}(t) = (1 - t/\Delta t)T_{ext}^{(i-1)} + (t/\Delta t)T_{ext}^{(i)} \tag{7.16}$$

where $T_{ext}^{(i-1)}$ and $T_{ext}^{(i)}$ are the external air temperatures of the previous and current timestep, respectively. For the sake of clarity, a new parameter is defined, which is the inverse of the time constant with respect to the effect of windows in the system:

$$\frac{1}{\tau_V} = \frac{U_V A_V + H_V}{\rho c_p V} \tag{7.17}$$

Joining Eqs. 7.15, 7.16, and 7.17, a new differential equation is obtained:

$$\begin{gathered}\frac{dT_{air}}{dt} + aT_{air} + bt - c = 0, \text{ with a given } T_{air}(0) \\ \text{where } a = \tfrac{1}{\tau} + \tfrac{1}{\tau_V} \\ b = \frac{1}{\tau}\left(\frac{T_S^{prev} - T_S^{cur}}{\Delta t}\right) + \frac{1}{\tau_V}\left(\frac{T_{ext}^{(i-1)} - T_{ext}^{(i)}}{\Delta t}\right) \\ c = \tfrac{1}{\tau}T_S^{prev} + \tfrac{1}{\tau_V}T_{ext}^{(i-1)}\end{gathered} \tag{7.18}$$

The analytical solution of this equation is:

$$T_{air}(t) = \frac{c - bt}{a} + \frac{b - e^{-at}(-T_{air}(0)a^2 + ca + b)}{a^2} \tag{7.19}$$

7.2.6 Long wave radiation

Thermal studies of cities must address long wave radiative exchange accurately because temperature differences between the involved elements can be large. In particular, low sky temperatures play a major role in the urban cooling process [Morakinyo et al., 2017].

Assuming that all the surfaces are blackbody emitters (their emissivity value is 1), the radiative flux at a given point on the boundary is expressed by:

$$q_{lw} = \sigma(T^4 - T_r^4) \tag{7.20}$$

where T_r is the mean temperature of the environment visible from the point, and σ is the Stefan-Boltzmann constant ($\approx 5.6703 \times 10^{-8} W m^{-2} K^{-4}$).

With the presence of radiation, the FEM system becomes non-linear. The computational simulation of radiative boundary conditions works in a similar way than a convective flux, but adding an iterative scheme to solve the non-linearity:

$$q_{lw} = h_{rad}(T - T_r), \text{ with } h_{rad} = \sigma(\tilde{T}^2 + T_r^2)(\tilde{T} + T_r) \tag{7.21}$$

where T is the temperature to be found, and $\tilde{T}$ is result of the previous iteration. When the iterative process converges, $T = \tilde{T}$, and thus Eqs. 7.20 and 7.21 are the same. The most complicated stage of each iteration is finding the mean visible environment temperature T_r, which involves the use of form factors:

$$T_r = (E_i/\sigma)^{\frac{1}{4}}, \text{ with } E_i = \sum_{j=1}^{N} F_{ij}(\sigma \tilde{T}_j^4) \tag{7.22}$$

Because the city geometry is static throughout the entire simulation, matrix $\mathbf{F}$ can be precomputed and stored. Following [Aguerre et al., 2017], $\mathbf{F}$ can be stored in sparse format to avoid excessive memory usage and to accelerate the sum in Eq. 7.21. This enables refined geometries (composed of tens of thousands of elements) to be processed in regular desktop PCs. In this study, the density factor of the involved matrix $\mathbf{F}$ were studied, and the results are presented in the experimental section.

7.2.7 Short wave radiation

The low density factor of $\mathbf{F}$ was also exploited to compute short wave radiation, which is the radiation emitted by the sun and sky that reaches the surfaces after a limited number of scene bounces. The assumption of working with diffuse concrete materials allows use of the radiosity method for computing irradiance flux over the surfaces of the city. The following linear system must be solved:

$$(\mathbf{I} - \mathbf{RF})J = \xi \tag{7.23}$$

where $\mathbf{I}$ is the identity matrix, $\mathbf{R}$ a diagonal matrix of short wave reflectivity coefficients, J the radiosity values and ξ the emission. The strategy described at [Aguerre et al., 2017] was used to compute climate-based radiation with multiple reflections. After the radiosity values J are computed for each element, the absorbed radiation is inputted as an imposed flux (Neumann boundary condition) in the right hand side of Eq. 7.3.

7.3 Test case and model

The modifications proposed in this study were evaluated using the test case described in [Aguerre et al., 2019], which is summarized in this section.

A measurement campaign was carried out in Bayonne, France (43.48 N°), in *Rue des Tonneliers*. A set of thermograms were taken on April 23rd 2017 using an infrared FLIR B200 camera. The idea was to maximize the amount of physical information contained in the pictures, thus the street was captured in perspective (Figure 7.1). The test case used a simplified geometry composed of four boxes that represent the set of buildings captured in the thermograms. The thickness of walls and roofs was 0.18m. Material properties used are presented in Figure 7.2.

Figure 7.1: Camera location and model description of the test case. The square and dashed lines indicate the position of the thermal camera and the perspective angle. S1, S2 and N1 are points selected for the study.

Regarding environmental conditions, several parameters were experimentally measured, whereas others were modeled or estimated. A clear sky day was selected for the imaging campaign. Very low wind values were measured in situ, allowing for the estimation of a proper value for the external h coefficient, which was set to 10 $Wm^{-2}K^{-1}$. The interior h coefficients were extracted from the French thermal regulation [CSTB France, 2012]: 0.7 for the ground, 2.5 for vertical walls, and 5 for the roof (values in $Wm^{-2}K^{-1}$). Outside air temperature (see Figure 7.5) and relative humidity were

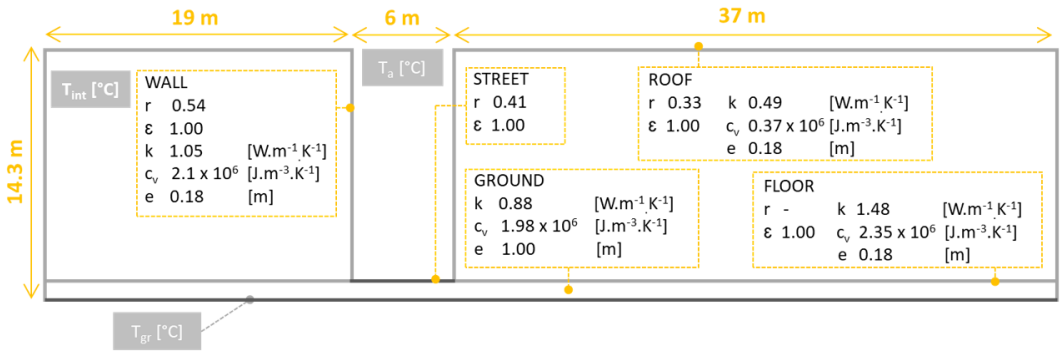

Figure 7.2: Material properties of the test case. Extracted from [Aguerre et al., 2019]

measured in situ.

Global horizontal irradiance was measured in a weather station located 3.4 km away from the experiments location. Using this data, direct and diffuse irradiances were modeled using Liu-Jordan clear sky model [Liu and Jordan, 1960]. Perez All-weather sky model [Perez et al., 1993] was used to compute short wave irradiances, using a sky dome geometry divided into 2400 elements [Beckers and Beckers, 2014].

Infrared horizontal irradiance and sky temperatures were modeled using Angström formula [Ångström, 1915]. Sky emissivity and directional temperatures were modeled based on the work described by [Nahon, 2017]. A sky dome geometry discretized into 130 elements was used for computing long wave radiation.

Data was extracted from Meteonorm [Remund et al., 2010] global meteorological database to estimate the ground temperature at 1m deep (11.1 ^{o}C), value that can be considered constant for a day period.

The internal air temperature of buildings was proposed to be fixed at 20^{o}C, which was highlighted as a questionable supposition by the authors. This assumption was changed in the study presented in this paper, where these temperatures were also simulated using the method described above. Results can be observed in the next section.

The implementation of this test case in a FEM engine like Cast3m requires meshing the geometry to obtain a discretized version of the problem. The geometry was meshed using hexahedrons of linear shape functions, with four layers of elements along the thickness of each wall. The boundary elements are quadrilaterals of area 1.5m x 1.5m (see Figure 7.3). The total model is composed of four boxes, street, ground, and sky dome for long wave radiation. The number of volume elements is 113580, and the number of boundary elements is 28395.

Because the series of thermograms were taken during one day, the aim of this study was to simulate 24 hours. Accurate simulation results depend highly on initialization conditions. A strategy commonly used in electric analogy systems was adopted: the simulated period was repeated several times. The results for the first day differ considerably from the second, but they converged for the third day. Hence, a three day repetition was enough to obtain the initial temperatures of the surfaces. The results presented in the next section correspond to the third day of simulation.

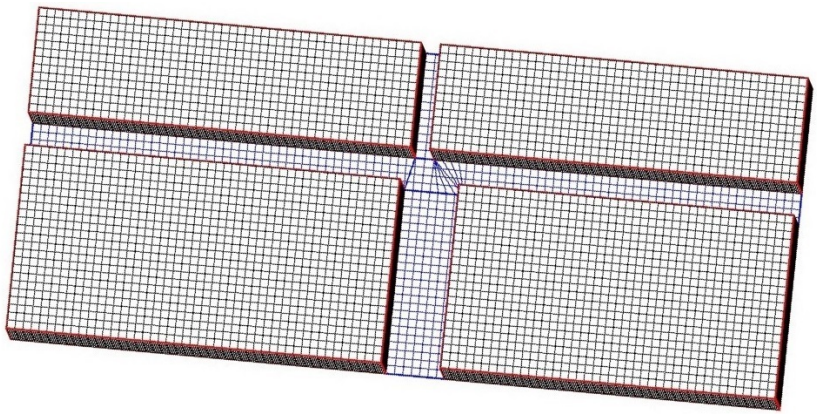

Figure 7.3: Mesh representing the environment of Rue des Tonneliers, used for the FEM simulation.

7.4 Results and discussion

Table 7.1 shows the thermography campaign and the correspondent simulated results. Temperature patterns are similar in both experimental and simulated images. Higher accuracy is reached for the wall that receives direct sunlight through most of the day. In the other wall, as well as in the street, temperatures are overestimated due to lower short wave radiation values, which can be explained by the geometrical simplifications (flat roofs, no overhangs, etc) . It is important to highlight that the red parts observed at 16:00 in the thermograms correspond to wooden carpentry and joinery, elements that are not present in the simulation.

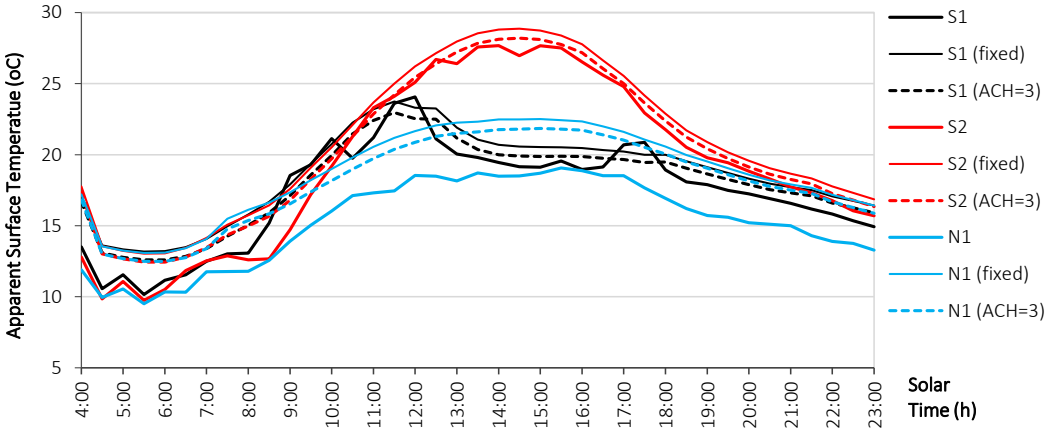

Figure 7.4: Comparison between simulated and measured temperatures at the selected points.

The simulation with free internal air temperature is more accurate than the one with fixed air at 20^oC. Because the difference between both set of images is not easy to appreciate, an image showing the absolute difference (from 0^oC to 1.5^oC) is presented. The impact of the internal air temperature on the surface temperature of the walls is greater than on the street, due to conduction along the thickness of walls. To enable a better evaluation of the results, three points were selected in the geometry (see Figure 7.2). The evolution of the experimental apparent surface temperature was obtained by selecting pixels on the thermograms and matching their color with the respective

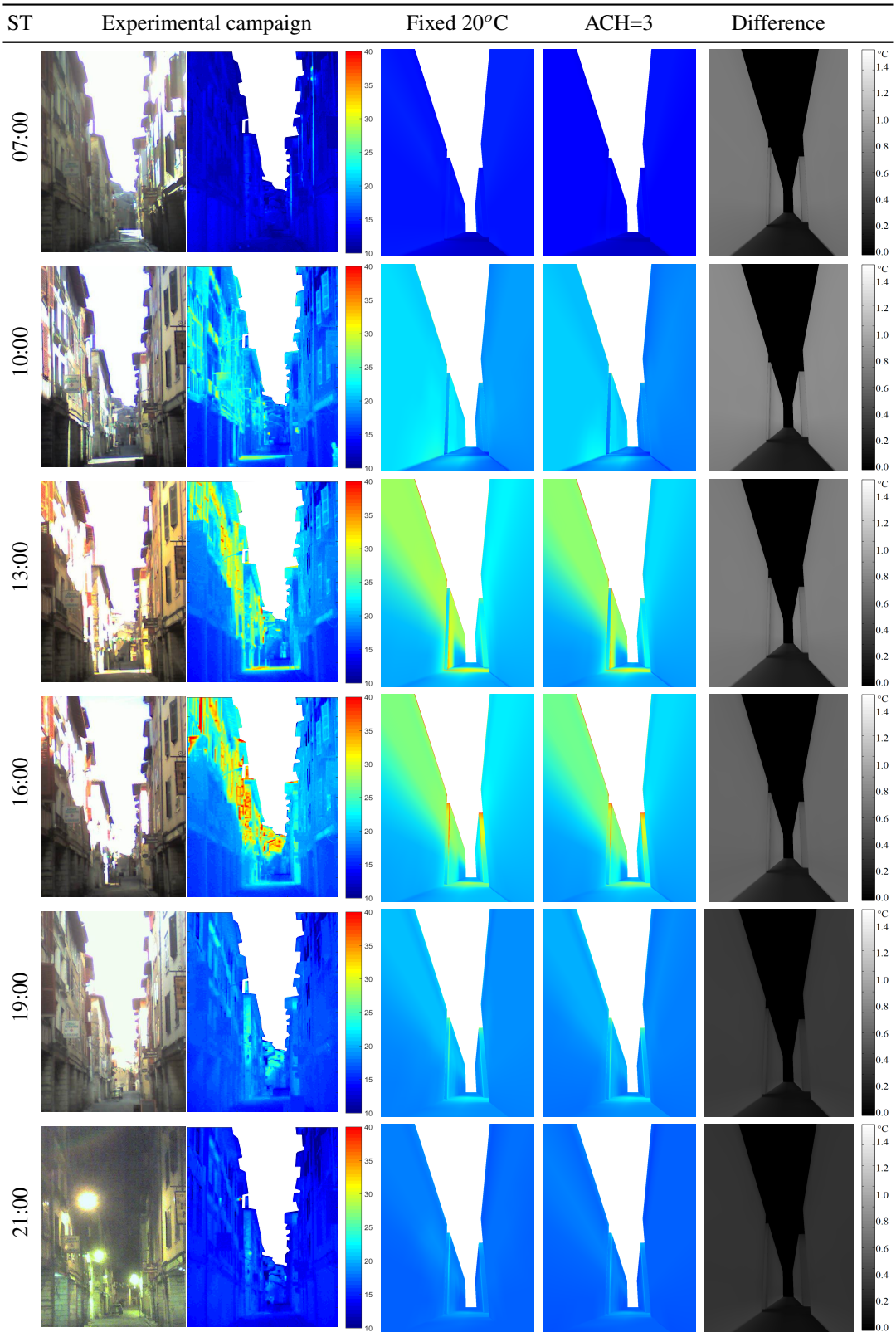

Table 7.1: Time-lapse (in solar time ST) of the photographs, thermograms, and corresponding simulated results for fixed and free internal air temperature. Column 5 corresponds to the absolute difference between the two simulated thermograms in columns 3 and 4.

temperature. These results are presented in Figure 7.4, along with the correspondent simulations. The results with ACH=3 are closer to the experimental data than those with fixed air temperature.

The modifications of FEM implemented in this study allow for the estimation of internal air temperature. Figure 7.5 shows the evolution of the internal air temperature using different configurations of ACH, along with the external air temperature. The three plots correspond to the internal results of one of the studied blocks. The results showed no significant differences for the rest of the blocks. Thermal inertia of air is observed, where the minimum of the three curves is always hotter than the minimum external temperature. An analogous behavior is shown for the maximum temperature. Larger ACH values implied a greater similarity between the evolution of internal and external temperatures.

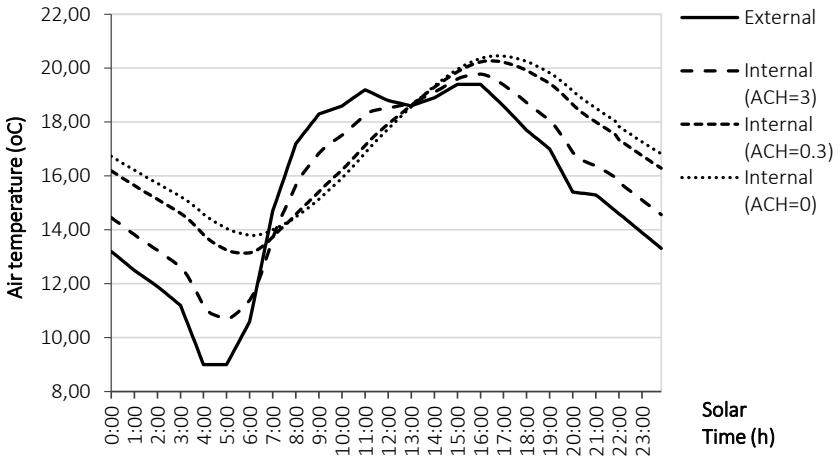

Figure 7.5: Evolution of external and internal air temperatures using different air change rates.

The results shown in Figure 7.5 explain the differences observed in column 5 of Table 7.1. An internal air temperature fixed at 20^oC was far away from the computed one, where the maximum gap with ACH=3 is observed around 05:00 ($\approx 9^oC$). Due to the thermal inertia of the wall, this difference takes some time to be reflected on the outside surface temperature, which reached its maximum difference around 10:00.

7.4.1 Computational performance

The simulations presented in this study were executed on a standard desktop PC (core i7 processor and 16GB of RAM memory). The code implemented for the computation of internal air temperatures did not affect the computational performance of the model, because an iterative solver was already being used to account for the non-linearities associated with radiation. The number of iterations needed to converge in each timestep is the same with fixed and varying internal air temperatures.

The memory consumption of Cast3m depends highly on the size of the geometry (number of elements). In particular, matrix $\mathbf{F}$ from Eq. 7.23 is a square matrix of dimensions $\approx 23k \times 23k$. Using full matrix representations, which is the current Cast3m implementation, the memory requirement to store $\mathbf{F}$ was $\approx 4GB$. Because of the geometrical properties of the scene, the density factor of $\mathbf{F}$ is equal to 4.16%, which justified the use of sparse representations. The memory consumption was

reduced to $331MB$, and the radiation step was considerably accelerated. Table 7.2 shows results for the entire FEM model.

Version	Execution time (minutes)	Max. memory consumption (GB)
Original Cast3m	572	4.6
Sparse matrix	61	0.9

Table 7.2: Execution time and memory usage details.

Around $9\times$ speedup was reached in total execution times. The memory consumption was reduced by a factor of 5.1.

Sparse form factors matrices enable dealing with larger geometries, which can be an important results for future simulations. For example, the size of the geometry can easily scale to hundreds of thousands elements if a higher level of detail is modeled, and/or if a larger zone wants to simulated.

7.5 Conclusion

In this study, a set of thermograms were simulated using FEM, and the results were compared to an experimental thermography campaign. The computational techniques used were presented, and two improvements regarding convective and radiative boundary conditions were implemented in Cast3m.

The results showed that a simplified geometry can generate accurate results if the computational model is highly precise. In particular, using free internal air temperatures increased the realism of the simulation, reaching accurate results when compared to experimental data. In periods where occupants do not make use of artificial temperature conditioners, measuring the air temperature can also serve as trustful information about thermal comfort.

Furthermore, the computational performance of the algorithm was optimized by using sparse matrix representations for storing form factors. The entire simulation was executed in a standard desktop PC in reasonable times, enabling the simulation of much longer periods of time.

Acknowledgments This work was partially funded by project FSE_1_2017_1_144731 from Agencia Nacional de Investigación e Innovación (ANII, Uruguay).

Chapter 8

Physically-based simulation and rendering of urban thermography

---

The contents of this chapter are currently under review in ACM Transactions on Graphics (TOG): Aguerre, J. P., Garcia-Nevado, E., Paz y Miño, J., Fernández, E., and Beckers, B. *Physically-based simulation and rendering of urban thermography*. Submitted to ACM Transactions on Graphics (TOG).

Urban thermography is a non-invasive measurement technique commonly used for building diagnosis and energy efficiency evaluation. The physical interpretation of thermal images is a challenging task because they do not necessarily depict the real temperature of the surfaces, but one estimated from the measured incoming radiation. In this sense, the computational rendering of a thermal image can be useful to understand the results captured in a measurement campaign. The computer graphics community has proposed techniques for light rendering that are used for its thermal counterpart. In this work, a physically-based simulation methodology based on a combination of the Finite Element Method (FEM) and ray tracing is presented. The proposed methods were tested using a highly detailed urban geometry. Directional emissivity models, glossy reflectivity functions, and importance sampling were used to simulate the temperature of urban surfaces and to render thermal images. The simulation results were compared with a set of measured thermograms, showing good agreement between them.

8.1 Introduction

Just as digital photographic cameras capture incoming light radiation and transform it into colors, thermal cameras capture incoming thermal radiation and transform it into temperatures [Vollmer and Möllmann, 2017]. In a real-world environment, light is typically emitted by few surfaces (the Sun or artificial sources such as a lamp) and reflected by the rest of the scene. Thermal radiation, on the other hand, is emitted by every surface at a temperature above the absolute zero, and it is also reflected by the objects. Hence, in this part of the spectrum, the urban surfaces become radiation

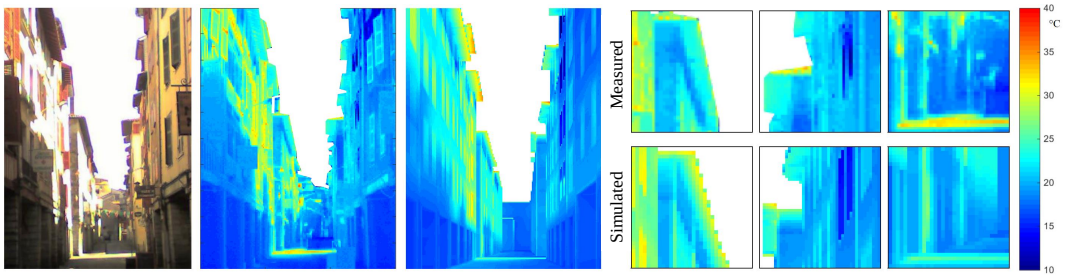

Figure 8.1: Urban scene of *Tonneliers* street in Bayonne, France. From left to right: photography in a perspective view of the street, measured thermogram of the scene, rendered thermogram using the proposed methodology, and different quadrants showing the details of the results. All the images were built over the same colormap.

sources. Thermograms display an estimated temperature of the surfaces that is derived from the combined emitted and reflected radiation arriving at the lens.

Thermography is widely used in many industries and scientific areas. Civil engineers and architects use thermal cameras for building diagnostics and energy efficiency evaluation [Evangelisti et al., 2018]. Thermal imaging of urban scenes has become a recent topic of interest because it provides spatialized information about the thermal behavior of the city [Beckers and Garcia-Nevado, 2018]. However, the interpretation of the resulting images is a difficult task [Datcu et al., 2005], and therefore numerical simulations have been developed for assessing the reliability of measurements [Aguerre et al., 2019; Poglio et al., 2006].

The computational simulation of photography has long been subject of study for both physics and computer graphics communities [Ward, 1994]. Material properties such as reflectivity, transparency, and absorptivity in the visible spectrum have been widely researched, looking for more realistic simulation conditions. Nevertheless, its thermal counterpart, namely *thermography simulation*, has not been addressed with the same intensity, although it is gaining attention in the graphics community [Haraké and Burkard, 2018; Kottler et al., 2019; Muñoz et al., 2018].

In the context of thermal simulation with FEM-based solvers, it is of particular interest to analyze the integration of high level of detail geometries [Nishida et al., 2016] and its impact on the computational performance. Furthermore, for thermography rendering, working with suitable infrared material characteristics such as directional emissivities and reflectivity functions [Snyder and Wan, 1998] and their effect on the results must be studied.

In this work, a physically-based simulation methodology built on a combination of the FEM code Cast3m [Charras and Di Paola, 2011] and the ray tracing kernel Embree [Wald et al., 2014] is presented for rendering urban thermography. The simulated thermograms were compared to the results of an measurement campaign performed in the city of Bayonne, France, where a sequence of thermal images was captured throughout a clear sky day [Garcia-Nevado, 2019]. A directional emissivity model was estimated from thermographic observations, and a glossy reflectivity function was used in the simulations to account for infrared radiation reflections. The main contribution of this study is to present a set of methods that enable rendering thermal images in urban scenes. Compared with measurements, the methodology exhibits accurate precision and good computational performance.

8.2 Physical basis

The temperature of a body is an expression of its energetic state, which is the result of its energy balance. The urban energy balance problem can be formulated as a conduction-dominant transient problem, where the conductivity properties of the scene greatly influence its thermal behavior through time. Nevertheless, several boundary conditions must be considered in an urban study, which complicates the analysis and the involved computational methods [Garcia-Dorado et al., 2017; Maréchal et al., 2010]. The transient energy balance is described using Fourier's law of heat conduction:

$$\begin{aligned} \rho_m c_p \frac{\partial T}{\partial t} &= k\Delta T \;\text{ subject to: }\; T = T_b \;\text{ on }\; \Gamma_b, \\ \text{and }\; -k\frac{\partial T}{\partial n} &+ q_s + h(T - T_{air}) + \varepsilon\sigma(T^4 - T_{env}^4) = 0 \;\text{ on }\; \Gamma_q \end{aligned} \tag{8.1}$$

This equation is a non-linear second-order partial differential equation. The first part represents heat conduction, while the subsequent terms account for boundary conditions. Dirichlet conditions are imposed temperatures T_b in the interface Γ_b. Neumann conditions are imposed fluxes in Γ_q, in the form of absorbed short-wave radiation q_s (W m^{-2}), long-wave radiative exchange, and convective heat transfer exchanged with the air. The vector n denotes the outward normal to the boundary Γ_q. T is the temperature of the surface in K, t represents time, while Δ is the Laplace operator. ρ_m (kg m^{-3}), c_p (J kg^{-1} K^{-1}) and k (W m^{-1} K^{-1}) are the mass density, specific heat, and conductivity of the material. h is the convective heat transfer coefficient in W m^{-1} K^{-1}, and T_{air} is the air temperature. ε is the emissivity of the material, and T_{env} is the average temperature of the environment. An initial temperature T_0 at t = 0.0s is necessary for solving this differential equation. The urban heat transfer problem is diagrammed in Fig. 8.2.

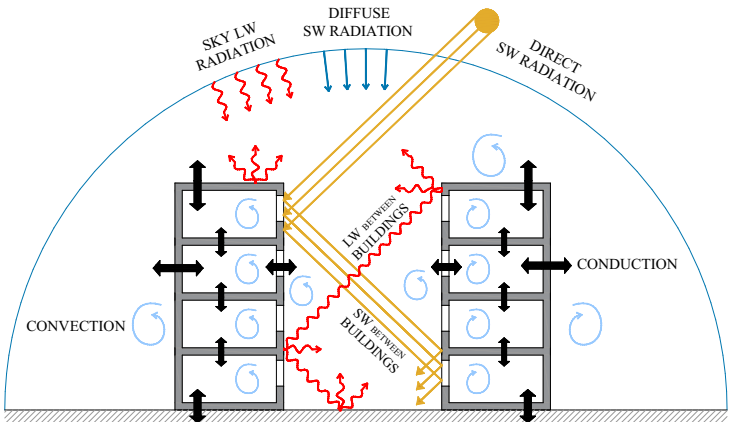

Figure 8.2: Diagram of heat transfer at the urban scale.

Every body at a temperature above the absolute zero emits and absorbs radiation. Radiation is energy in the form of electromagnetic waves that is propagated through vacuum or material mediums at the speed of light. The spectral distribution (wavelength) of the radiation emitted by a blackbody depends solely on its temperature (Planck's law). A blackbody can be defined as an ideal body that absorbs all of the incident radiation no matter the direction and, to stay in thermal equilibrium, emits radiation at the same ratio (as a Lambertian emitter). Integrating over the whole spectrum, Stefan's

law describes the total radiative density flux of the blackbody as:

$$\Phi^{black}(T) = \sigma T^4 \tag{8.2}$$

where σ is the Stefan-Boltzmann constant ($\approx 5.6703 \times 10^{-8}$ W m^{-2} K^{-4}) and T the blackbody temperature.

The Sun, which can be approximated as a blackbody at a temperature of around 5778 K, emits most of its radiation at short wavelengths (under 4 micrometers μm). This radiation reaches the Earth, passes through the atmosphere, and heats the planet's surface. A building within a city context receives light directly from the Sun, diffusely from the atmosphere, and reflected by surrounding elements. Urban surfaces emit thermal radiation (at long wavelengths, above 4μm), and this radiation is exchanged with other urban elements and with the sky. Nevertheless, urban surfaces cannot always be assumed as blackbody emitters because of the wide variety of materials used in construction.

The notion of gray body is defined as a body whose spectral emissivity and absorptivity properties are independent of wavelength [Modest, 2003]. A gray body emits a fraction of the total radiation emitted by the blackbody. This fraction (a number between 0 and 1) is called the emissivity ε. The total density of the gray body radiative flux is:

$$\Phi^{gray}(T) = \varepsilon \sigma T^4 \tag{8.3}$$

The emissivity depends on several factors, such as radiation wavelength, material roughness, geometrical imperfections, and incidence angles. Regarding the emissivity wavelenght dependence, a common assumption in studies involving solar radiation is to consider two well-defined regions: short and long spectra. In this case, materials are often called *semigray* [Howell et al., 2015], and they are approximated using two different set of properties that are uniform within each region. This assumption is used in the present work for urban elements.

Two kinds of ideal directional emissivity models are described in the literature for non-conductive materials in the thermal spectrum: optically smooth surfaces such as glass are usually modeled using Fresnel's relations (following Schlick's approximation from the normal emissivity $\varepsilon_\perp$ [Schlick, 1994]), where the emissivity reaches its maximum value near the normal direction and shows smaller values for larger angles of incidence. On the other hand, very rough materials can be approximated with a perfectly diffuse emission model, which implies a unique emissivity value for every direction. Figure 8.3 shows examples of ideal models. A common assumption is that the emissivity values depend only on the zenith angle of view, i.e. it has the same behavior for different directions in the azimuthal angle.

Kirchhoff's law of thermal radiation states that the emissivity ε and the absorptivity α of any body in thermodynamic equilibrium are the same. For a gray, diffuse and opaque (i.e. without transmission) body, it can be stated that:

$$\varepsilon = \alpha = 1 - \rho \tag{8.4}$$

where ρ is the reflectivity of the material. Kirchhoff's law is also true *directionally*: the directional emissivity is equal to the directional absorptivity for all directions.

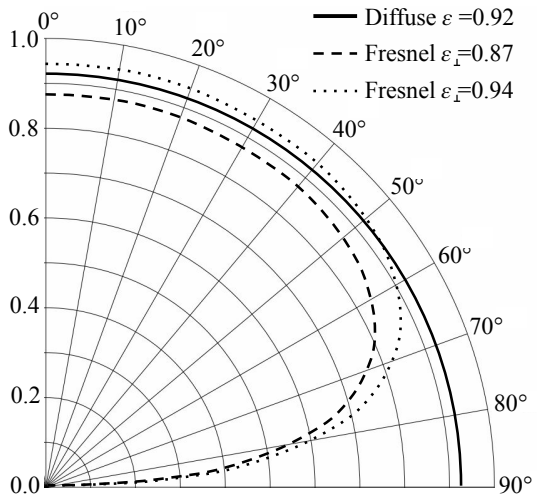

Figure 8.3: Ideal directional emissivity models using Fresnel equations in the case of smooth surfaces (with $\varepsilon_\perp$ the normal emissivity of the material) and perfectly diffuse approximations for very rough surfaces.

The reflective properties of materials depend greatly on the wavelength of study. At the long-wave spectrum, surfaces tend to behave more specularly than in the visible spectrum. Perfectly smooth materials that follow Fresnel's emissivity model are completely specular reflectors, while diffuse emitters can present different reflectivity patterns, depending on their surface roughness. Construction materials such as concrete, mortar, or wood are usually not smooth, making it is necessary to study the emissivity and reflectivity models that approximate their behavior.

Current scientific knowledge on the behavior of materials in the infrared spectrum is limited. Directional emissivity and reflectivity at the long-wave spectrum are still a matter of study for experimental physics [Peeters et al., 2016]. Literature provides little information about these properties for construction materials [Vollmer and Möllmann, 2017] and tests to determine them are complex to perform outside a lab environment.

8.3 Literature review

8.3.1 Urban thermal simulation

The urban heat transfer problem has been solved using different computational approaches, such as electric-analogy approximations [Reinhart and Davila, 2016], finite difference methods (FDM) [Rodler et al., 2018], and finite element methods (FEM) [Evangelisti et al., 2018]. Physically-based studies must address all the involved boundary conditions that are present in urban scenes. Convection energy exchanges have been simulated using Computational Fluid Dynamics (CDF) at the city scale [Van Hooff and Blocken, 2010]. Under calm wind conditions, setting an approximate value of h from literature references or empirical correlations has proved to be accurate enough for thermal simulations [Mirsadeghi et al., 2013].

Regarding short-wave radiation, the computer graphics community offers several methods that have been adapted to daylighting simulations [Carroll, 1999]. Radiosity-based systems [Cohen and Wallace, 1993] allow for direct integration with meshed geometries. Ray tracing techniques,

on the other hand, offer better simulation conditions for dealing with arbitrary material properties [Lawrence et al., 2004]. Urban daylight simulations have been commonly addressed using RADIANCE software [Saratsis et al., 2017] or its alternative hardware-accelerated implementations [Jones and Reinhart, 2016]. The typical steps that are required to simulate urban short-wave radiation loads include the computation of daylight coefficients, the integration of sky models, and the usage of weather data [Mardaljevic, 2000; Muñoz-Pandiella et al., 2017].

Long-wave radiation simulation is not as widely studied as its short-wave counterpart. This fact is partly explained by the differences between these two phenomena. On the one hand, the balance of thermal radiation at a point implies a self-dependence, because the incoming radiative flux depends on the temperature of the point, and vice-versa [Howell et al., 2015]. On the other hand, infrared radiation is emitted by every surface in the city, which brings the question of how to model the behavior of multiple emitters and their energy exchange. The self-dependence issue is usually tackled by linearizing the flux and using last timestep temperatures to compute the current timestep radiation, treating it as an imposed flux [Evins et al., 2014]. This approach does not ensure flux equilibrium because the temperatures can differ greatly between the previous and current timesteps. Using short timesteps helps reducing radiative flux differences but implies an increment in the computational costs. The radiation exchange between multiple emitters is commonly solved using Sky View Factor (SVF) based approaches, which assume a uniform temperature of the urban context and an isotropic temperature distribution of the sky.

A second level of complexity for long-wave exchange simulations consists of accounting for the diffuse exchanges between the elements of the scene. In this context, radiosity becomes the most used technique for computing long-wave radiation in FDM or FEM systems (e.g. COMSOL multiphysics [COMSOL Inc., 2018], ANSYS [Stolarski et al., 2018], and Cast3m [Charras and Di Paola, 2011])). Greater detail in radiation exchange simulations requires modeling the optical properties of materials, which implies the integration of more complex graphical methods [Modest, 2003] that are not implemented in these kind of software solutions.

8.3.2 Previous works

Thermography has been used for comparison and validation of thermal simulations. Hénon et al. [2012] used the SOLENE-microclimat model to perform thermal simulations of a set of buildings. The results were compared with temperature measurements obtained from an airborne thermal camera, showing differences of around 2-5°C in the generated images. This bias was attributed to the geometric and material simplifications made in the 3D model. Rodler et al. [2018] presented a computational model based on FDM to analyze the thermal behavior of a building and its environment. The results were compared with measured thermograms and contact temperature sensors, obtaining some uncertainties related to the adopted simplifications in the building energy model. Aguerre et al. [2019] showed that FEM is a suitable tool for urban thermography simulation. The simulation results were compared to infrared images captured with a perspective view of the street, obtaining differences of up to 5°C, due to the low geometrical detail used, as well as the simplification of blackbody radiation for long-wave simulations.

Works that focus in the geometrical modeling and meshing strategies for physical simulations have been developed. Van Hooff and Blocken [2010] presented a grid generation strategy for per-

forming urban studies in a multiscale context, where large differences in geometrical length scales were present. Although intented for CFD simulations, this work provided a detailed study on how the urban meshing selection can have a significant effect on the simulation results. Garcia-Dorado et al. [2017] explored the procedural generation of urban models using a physically-based design tool to study the interaction of the scene with different weather conditions. The high level of detail modeling allowed obtaining accurate results from both physical and graphical perspectives.

Regarding long-wave radiation simulations, Evins et al. [2014] showed the importance of an accurate consideration of long-wave exchanges in urban thermal studies. The authors improved to the long-wave processes in the EnergyPlus engine, showing differences of up to 6°C in the surface temperatures when compared to the default simplified model. In this context, few works have presented simulations adopting a non-diffuse behavior of thermal radiation. The integration of directional emissivities and reflectivities into the simulation is necessary under some circumstances [Haraké and Burkard, 2018], especially when perspective views of the scene are captured [Garcia-Nevado, 2019]. Van Eekelen [2013] presented a FEM approach to simulate satelite surface temperature considering non-gray surfaces and specular reflections. By using different simulation configurations, the author showed that the thermo-optical properties of the surfaces are an important tool for the thermal control of a satellite. Snyder et al. [1998; 1997] and Li et al. [1999] introduced a variety of Bidirectional Reflectance Distribution Function (BRDF) models for studying land surface temperatures. Li et al. [2009] performed a set of ray-tracing simulations of the thermal response of a cup for mid-wavelength infrared (1.3-3 μm) using a simplified global illumination model to consider reflections. Military studies are particularly interested in rendering mid-wave and long-wave radiation of fields for motion-detection; hence some approaches were presented using ray-tracing and empirical BRDF models [Kwan et al., 2008; Latger et al., 2007]. Wu et al. [2015] proposed a mid-wavelength BRDF and compared it with a thermal image of a set of buildings. Lagouarde et al. [2010] modeled the directional anisotropy of a large-scale city center based on airborne acquisition. To this day, no work has addressed the directional properties of long-wave radiation in a simulation with a detailed urban geometry as it was performed in the present study.

8.4 Simulation Methodology

This section presents a methodology to simulate urban surface temperatures and to render thermal images. This methodology starts from a set of inputs that are necessary to model reality. The 3D model of the scene and its associated material properties are used in all the stages of the simulation. *In situ* measurements or alternative physically-based models are needed to estimate boundary conditions accurately. For example, short-wave horizontal irradiances and air temperatures must be measured or estimated because the system is strongly dependent on them.

The simulation process can be divided into three main steps (Figure 8.4). The pre-processing stage carries out computations that are independent of temperature values, such as the calculation of short-wave loads and long-wave view factors. The processing stage uses the previous results to compute surface temperatures. Finally, post-processing is necessary to obtain the rendered thermograms.

We propose using FEM to address the processing stage, because it allows for the simulation of urban geometries using different types and sizes of elements, and because the results provide

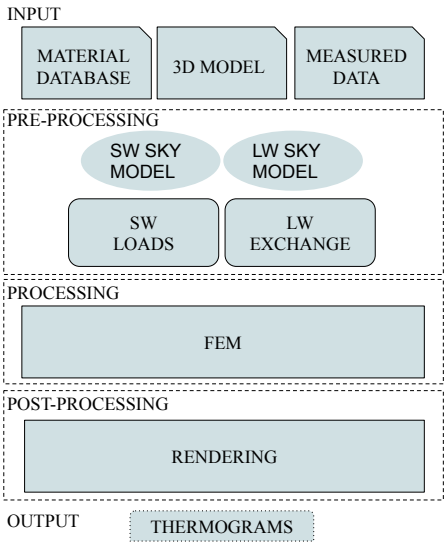

Figure 8.4: Scheme of the computational model

the temperature distribution across every surface based on the selected shape functions. This stage requires the heaviest computations because several physical phenomena must be incorporated in the calculations. The involved boundary fluxes (Neumann boundary conditions) are convection, short-wave radiation, and long-wave radiation. Imposed temperatures (Dirichlet boundary conditions) are used to fix the ground temperature at a given depth. The FEM discretization of the heat transfer partial differential equations (Eq. 8.1) results in the following system of equations [Lewis et al., 2004]:

$$\mathbf{C}\left\{\frac{\partial T}{\partial t}\right\} + (\mathbf{K} + \mathbf{K}^{conv} + \mathbf{K}^{lw})\{T\} = (\{f\}^{sw} + \{f\}^{conv} + \{f\}^{lw}) \tag{8.5}$$

In Eq. 8.5, $\mathbf{K}$ is the global conductivity matrix (assemblage of elementary matrices), while $\mathbf{K}^{conv}$ and $\mathbf{K}^{lw}$ are the convective and radiative terms of the conductivity. $\mathbf{C}$ is the capacitance matrix, $\{f\}^{sw}$, $\{f\}^{conv}$ and $\{f\}^{lw}$ are the load vectors of short-wave radiation, convection and long-wave radiation, respectively. $\{T\}$ is the vector of unknown temperatures of the nodal points, and $\left\{\frac{\partial T}{\partial t}\right\}$ is the vector of temperature derivatives over time, which is discretized using FDM. The entries of the previous vectors are calculated following Eq. 8.6.

$$\begin{aligned} \mathbf{C}_{ij} &= \int_{\Pi} \rho_m c_p N_i N_j dp, \\ \mathbf{K}_{ij} = \int_{\Pi} k \nabla N_i \nabla N_j dp, \;\; \mathbf{K}_{ij}^{conv} &= \int_{\Gamma_c} h N_i N_j dp \\ \{f\}_i^{sw} = -\int_{\Gamma_q} N_i q_s dp, \;\; \{f\}_i^{conv} &= \int_{\Gamma_c} N_i h T_{air} dp \end{aligned} \tag{8.6}$$

where the only new terms (besides those already presented in Eq. 8.1) are the total volume domain Π, and the surface domains subject to boundary conditions Γ_c and Γ_q. N_i represents the shape function of node i [Lewis et al., 2004], which is a continuous function that describes the evolution of temperature within the elements. The terms q_s, $\mathbf{K}^{lw}$ and $\{f\}^{lw}$ are described in the following sections.

8.4.1 Short-wave radiation

The term q_s presented in Eq. 8.6 corresponds to the absorbed short-wave flux of each surface. Radiation is received and exchanged at the boundary of the volume mesh, which is a flat mesh that represents the exterior envelope. For instance, if hexahedral volumes are used, the envelope is composed of quadrilateral elements. For a given element in the exterior, the short-wave flux depends on both the light emitted by the scene that arrives directly, and the light reflected by the surrounding elements. Therefore, two steps are necessary to account for q_s: the estimation of the emitted light and the radiative exchange between the city objects.

During daylight hours, the sky is the only emitter of short-wave radiation. Several anisotropic sky models are available in the literature, which can be used to consider all kinds of meteorological conditions. The proposed methodology was tested under clear sky situations, which leads to using Liu and Jordan model [1960] to estimate the direct and diffuse sky emissions, taking the measured global horizontal irradiances as input. A sky vault partition [Beckers and Beckers, 2014] with 2400 tiles is used to account for the anisotropy of the emission. The radiance value for each tile is calculated with Perez all-weather model [Perez et al., 1993].

After the sky emission is estimated, the radiosity method is used to compute the radiative exchange, which is a well-suited algorithm for dealing with urban environments composed of mainly diffuse surfaces at the short-wave spectrum. Extended form factors [Sillion and Puech, 1989] are used to enable other kinds of reflections, such as the behavior of window glasses (specular surfaces). This approach provides short computational times and negligible error when compared to classical ray-based approaches, as shown by Aguerre et al. [2018].

Once the incoming radiation results are obtained for each element and for each timestep of the simulation, the absorbed short-wave fluxes are computed using the absorptivity value of each material, which is equal to 1 minus its reflectivity (Eq. 8.4). These results are then considered as the nodal imposed flux q_s by averaging the values of all the adjacent elements of each node.

8.4.2 Long-wave radiation

A typical approach followed by FEM systems is to integrate long-wave radiation in a similar way than convection, but using an iterative solver for dealing with the non-linearities and self-dependences associated with long-wave exchanges. The correspondent h coefficient, namely h_{rad}, is recalculated several times for each timestep based on the emissivities and surrounding temperatures of each element. Most of the FEM packages work in this way, assuming gray-diffuse materials and using the radiosity algorithm for solving the exchange process [Coulon, 2006].

Non-diffuse surfaces properties are harder to integrate into the system. In this context, radiosity cannot be used to compute the incoming radiation. Typical construction materials are not perfect diffuse emitters/reflectors, which means that they emit and reflect different amounts of energy depending on the angle of incidence. In the present work, a linear combination of the ideal emissivity models presented in Figure 8.3 (Fresnel and diffuse) is used for this purpose, where greater surface roughness implies greater contribution of the diffuse part (Figure 8.5). In this way, smooth construction materials like glass are modeled with values closer to the Fresnel model and very specular reflectivities. Rough surfaces, such as wood or stone, follow a more diffuse emission pattern and a glossy reflectivity behavior, which is approximated with a specular lobe around the reflected direc-

tion. These assumptions allow modeling the material behavior of rough non-conductive materials at the long-wave spectrum as presented in Torrance and Sparrow [1965] for emission and Yang and Buckius [1995] for reflections.

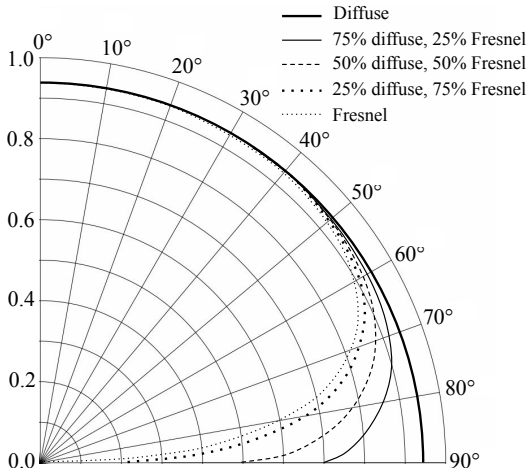

Figure 8.5: Directional emissivity interpolated from two ideal models.

The net radiative fluxes are calculated by estimating sky temperatures and computing the total emitted and absorbed radiation for each timestep and for each element of the radiative boundary. These methods are described next.

Long-wave sky model

The first step for computing long-wave radiation consists in meshing the sky vault using the same kind of partition than for short-wave [Beckers and Beckers, 2014] but with 230 elements instead of 2400. Fewer elements are enough because the distribution of long-wave sky radiances is smoother than short-wave ones. Berdhal and Fromberg clear sky model [Berdahl and Fromberg, 1982; Evangelisti et al., 2019] is used to estimate the anisotropic distribution of sky temperatures, based on measured air temperatures and relative humidity.

Total emitted radiative flux

The total emitted flux ϕ_i^{ε} of the barycenter of element i is:

$$\phi_i^{\varepsilon} = \varepsilon_i^h \sigma T_i^4 \tag{8.7}$$

where ε_i^h is the total hemispherical emissivity of the material of element i, which depends on the directional emissivity presented in Figure 8.5. The total hemispherical emissivity is calculated by an integration on the zenith angle:

$$\varepsilon^h = 2 \int_0^{\pi/2} \varepsilon(\theta)\, cos\theta\, sin\theta\, d\theta \tag{8.8}$$

Total absorbed radiative flux

The computation of the total absorbed flux is performed at the barycenter of each element. Since the geometry is permanent, a pre-computation of the inter-element relations that are exclusively geometry-dependent is performed, in order to accelerate the simulation process. An absorption matrix, namely $\mathbf{A}$, is pre-computed. $\mathbf{A}_{ij}$ contains a number between 0 and 1 that expresses the fraction of the blackbody radiant power of element j (σT_j^4) that is absorbed by element i. This number is difficult to obtain, because it depends on the directional absorptivity of i, and on the directional emissivity of j. Moreover, there is a fraction of this radiation that bounces on other elements before reaching i, and therefore the directional reflectivities of surrounding elements must be considered. A backward ray tracing method (presented in Alg. 7) is used to calculate $\mathbf{A}$, considering non-diffuse absorptions and emissions, and glossy reflections.

Figure 8.6 illustrates the algorithm. To compute the absorbed radiation at the receiver point, it is necessary to consider the directional emissivity, absorptivity, and glossy reflections [Jensen, 2001]. The sky is the only part of the scene that is treated as a blackbody. A large number m of rays is casted from the barycenter of each element of the city following the distribution presented in [Beckers and Beckers, 2016]. Hence, the contribution ΔA assigned to each direction is equal to $1/m$. This contribution is first weighted by the directional absorptivity, obtained with the ray direction and the emissivity curve of the material of the receiver element. Then, this contribution is distributed into the element that is directly seen and those elements reached through glossy reflections. In Figure 8.6, $\mathbf{S}_i$ corresponds to the set of elements that contribute radiation after reflections, which means that their emitted radiation reaches the receiver element after bouncing on another element. $\mathbf{S}_3$ has a greater contribution than $\mathbf{S}_1$ because element **k** is seen at a shallower angle than element **j**: the weight of $\mathbf{S}_3$ is equal to the absorptivity of the correspondent direction (0.85) times the reflectivity of patch k in the correspondent direction (0.35), totaling $0.85 \times 0.35 \approx 0.3$. On the other hand, the weight of $\mathbf{S}_1$ is equal to $0.91 \times 0.08 \approx 0.07$.

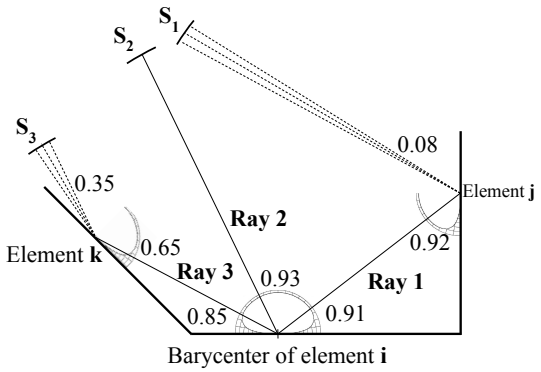

Figure 8.6: Example of backward ray tracing with non-diffuse surfaces. Dashed lines correspond to specularly reflected rays.

To compute the direction of the reflected rays, the following energy-conserving probability density function is used [Lafortune and Willems, 1994]:

$$p(\omega) = \frac{e+2}{2\pi}\cos^e\alpha \tag{8.9}$$

In this equation, ω is a direction sampled around $(0,0,1)$, with α its zenith angle. The higher the value of e, the smaller the specular lobe. Following Lafortune and Willems [1994], importance sampling is used to cast rays around the specular lobe, assigning a higher probability to directions that are closer to $(0,0,1)$. Starting from two numbers r_1 and $r_2 \in$ [0,1], the polar coordinates of the direction are computed with:

$$\omega = (\alpha, \phi) = \left(\arccos r_1^{\frac{1}{e+1}}, 2\pi r_2\right) \tag{8.10}$$

The ray direction in Cartesian coordinates is:

$$\omega = (x_\omega, y_\omega, z_\omega) = \left(\sin\alpha\cos\phi, \sin\alpha\sin\phi, \cos\alpha\right) \tag{8.11}$$

Hammersley sampling [Suffern, 2016] is used to obtain r_1 and r_2, avoiding the noise related with randomness. After computing the direction centered in $(0,0,1)$, a rotation towards the specularly reflected vector is performed to obtain the final direction.

Alg. 7 presents a pseudocode that describes the computation of the absorption matrix $\mathbf{A}$, which is initialized as a matrix of zeros. For each element i of the boundary mesh (which relates to each row of $\mathbf{A}$), m rays are casted from its barycenter, in order to sample the directional absorptivity of the corresponding material. A fraction of the total ray contribution is added to the directly seen element j, represented by the entry $\mathbf{A}$(i , j). After this, L rays are casted to sample the specular lobe of the reflection. Each reflected direction generates a different path (using FOLLOWSPECULARPATH procedure) to distribute the ray contribution into the reflected elements using multiple radiation bounces. After the glossy sampling, the paths are built over the simplification of perfectly specular reflections. This simplification allows for reasonable computational performance of the algorithm without producing a significant absolute error to the calculations.

Once matrix $\mathbf{A}$ is precomputed, the total absorbed radiation can be computed for every element multiplying the matrix by a vector of the blackbody radiant power of each element, based on its current temperature:

$$\phi_i^\alpha = \sum_{j=1}^{n} A_{ij}(\sigma T_j^4) \tag{8.12}$$

Combining Eqs. 8.7 and 8.12, the net radiative flux in the barycenter of element i is:

$$\phi_i = \phi_i^\varepsilon - \phi_i^\alpha = \sigma\left(\varepsilon_i^h T_i^4 - \sum_{j=1}^{n} A_{ij} T_j^4\right) \tag{8.13}$$

In order to integrate this equation in the FEM system, the flux is expressed in the form of a convective boundary condition:

$$\begin{gathered} \phi_i = h_{lw}^{[k]}\left(T_i^{[k+1]} - T_{env}^{[k]}\right) \\ \text{where } h_{lw}^{[k]} = \varepsilon_i^h \sigma\left((T_i^{[k]})^2 + (T_{env}^{[k]})^2\right)\left(T_i^{[k]} + T_{env}^{[k]}\right) \\ \text{and } T_{env}^{[k]} = \left(\frac{1}{\varepsilon_i^h}\sum_{j=1}^{n} A_{ij}(T_j^{[k]})^4\right)^{1/4} \end{gathered} \tag{8.14}$$

where T_{env} is the apparent temperature of environment as seen from the barycenter of i, and h_{lw} is

Algorithm 7 Calculate absorption matrix $\mathbf{A}$.

```
A=getZerosMatrix(n,n);
for each element i ∈ 1...n do
    p=getElementBarycenter(i)
    for each ray r ∈ 1...m do
        dir=getHemisphereDirection(r)          ▷ using Beckers and Beckers[2016]
        [j, p2]=castRay(p,dir)                 ▷ returns intersected point p2 and element j
        ε_i = getDirectionalEmissivity(i,dir)  ▷ Figure 8.5
        α_i = ε_i                              ▷ Directional absorptivity, Eq. 8.4
        rayCon = α_i * 1/m                     ▷ get ray contribution
        ε_j = getDirectionalEmissivity(j,dir)
        A( i , j ) += ε_j * rayCon
        for each reflected ray l ∈ 1...L do
            reflDir=getGlossyDirection(j,dir)  ▷ Eq. 8.11+rotation
            ρ_j=1 − ε_j                        ▷ Directional reflectivity, Eq. 8.4
            rayCon *= ρ_j * 1/L
            FOLLOWSPECULARPATH(A, rayCon, p2, reflDir)
        end for
    end for
end for
```

```
procedure FOLLOWSPECULARPATH(A, rayCon, p2, reflDir)
    while rayCon > t do                        ▷ t is a threshold ≈ 0
        [j , p2]=castRay(p2,reflDir)
        ε_j=getDirectionalEmissivity(j,reflDir)
        A( i , j )+= ε_j * rayCon
        reflDir=getSpecularDirection(j,reflDir)
        ρ_j = 1 − ε_j
        rayCon *= ρ_j
    end while
end procedure
```

the correspondent radiative heat transfer coefficient. Note that the computed elemental fluxes must be averaged to obtain the correspondent nodal fluxes.

The superscript k refers to the current step of the non-linear solver that must be used to account for radiation, which means that several h_{lw} and T_{env} values are calculated for each timestep of the simulation. Because of the pre-computational effort spent to compute $\mathbf{A}$, T_{env} can be calculated using a single matrix-vector multiplication. Then, going back to Eq. 8.5, the new terms related to long-wave radiation, $\mathbf{K}_{ij}^{lw}$ and $\left\{f\right\}_i^{lw}$, are added to $\mathbf{K}$ and $\left\{f\right\}$, respectively, where:

$$\begin{aligned} \mathbf{K}_{ij}^{lw^{[k]}} &= \int_{\Gamma_r} h_{lw}^{[k]} N_i N_j dp \\ \left\{f\right\}_i^{lw^{[k]}} &= \int_{\Gamma_r} N_i h_{lw}^{[k]} T_{env}^{[k]} dp \end{aligned} \tag{8.15}$$

The iterative scheme used to overcome the non-linear relations implies solving the linear system of equations (Eq. 8.5) several times for each timestep , until reaching convergence ($T^{[k]} \approx T^{[k+1]}$).

8.4.3 Thermography rendering

Once the surface temperatures are obtained, post-processing is needed to simulate the thermal camera. The final rendered thermograms are simulated by placing a virtual thermal camera inside the

geometric model. This section describes the model used by real thermal cameras first, and then an algorithm for simulating the virtual camera is proposed.

Thermal cameras

Thermal cameras are composed of a collection of infrared sensors that gather the incoming infrared radiative flux arriving in directions within the field of view (FOV) of the lens [Vollmer and Möllmann, 2017]. These sensors measure radiation with a wavelength between 7 and 14 μm, which is a mixture of three different components: radiation emitted by the captured object, radiation emitted by other bodies and reflected by the object, and radiation emitted by the atmospheric layer between the camera and the object (Figure 8.7).

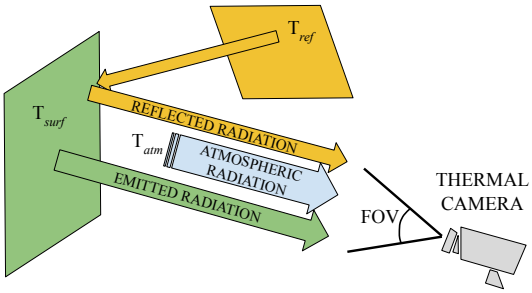

Figure 8.7: Components of the radiation captured by a thermal camera.

This simplified physical model is then used by the camera software to obtain an estimated temperature for each pixel. The model is based on the measured radiative flux and some data that must be entered to the camera: the emissivity ε, reflected temperature T_{ref}, air temperature, and the relative humidity of the scene. The measured radiative flux is first used to estimate a total radiant power ϕ_{in}, following the spectral distribution of a blackbody. Then, the blackbody radiant power of the captured surface $\Phi^{black}(T_{surf})$ is estimated by subtracting the atmospheric and reflected components [Vollmer and Möllmann, 2017]:

$$\begin{aligned}\Phi^{black}(T_{surf}) = \frac{\phi_{in}}{\tau_{atm}\varepsilon} - \frac{1-\varepsilon}{\varepsilon}\Phi^{black}(T_{ref}) \\ - \frac{1-\tau_{atm}}{\tau_{atm}\varepsilon}\Phi^{atm}(T_{atm})\end{aligned} \tag{8.16}$$

where T_{surf} is the unknown surface temperature, and τ_{atm} is the atmospheric transmittance estimated using an atmospheric model with the input data. $\Phi^{atm}(T_{atm})$ is the radiant power of the atmosphere at temperature T_{atm}, output of the atmospheric model.

For a sufficiently close measurement distance, the atmospheric radiation can be neglected ($\tau_{atm} = 1$). Under these conditions, and taking into account that $\Phi^{black}(T_{surf})$ is equal to σT_{surf}^4 (Eq. 8.2), the surface temperature is calculated using the following expression:

$$T_{surf} = \sqrt[4]{\frac{\phi_{in}}{\sigma\varepsilon} - \frac{1-\varepsilon}{\varepsilon}T_{ref}^4} \tag{8.17}$$

Moreover, if the input emissivity is set to be 1, the output temperatures are called *apparent surface temperatures* (T_{surf}^{app}). In this context, blackbody behavior of materials is assumed, and the

atmospheric radiation source is neglected:

$$T_{surf}^{app} = \sqrt[4]{\frac{\phi_{in}}{\sigma}} \tag{8.18}$$

Virtual thermal camera

The goal of thermography rendering is not to show the real surface temperature of the scene, but to imitate the image captured by a real camera. In this sense, the most important calculation is the estimation of the virtual incoming radiative flux ϕ_{in}^{virt} for each pixel. In our study, this estimation is performed using the reverse of the real camera's approach (the reverse of Eq. 8.17):

$$\phi_{in}^{virt} = \varepsilon\sigma T_p^4 + (1-\varepsilon)\sigma T_{ref}^4 \tag{8.19}$$

The virtual flux ϕ_{in}^{virt} is computed based on the simulated temperature of the directly seen point (T_p), the reflected temperature (T_{ref}), and the corresponding pixel emissivity ε. The properties of the virtual camera must be set to be the same as the real thermal camera used in the measurement campaign (same FOV, pixel resolution, position and direction of view). The emissivity ε associated with each pixel is obtained using a directional emissivity model such as those described in Figure 8.5. Finally, the estimated temperature is calculated by replacing the computed ϕ_{in}^{virt} in Eq. 8.18 to simulate the calculations done by the real thermal camera.

Ray tracing is used to obtain T_p and T_{ref}. One primary ray is casted for each pixel, and the temperature of the intersected point T_p is obtained. The reflected temperature is the average of the temperatures of the points reached through the glossy reflected paths that follow the specular lobe (Eq. 8.11). This process is graphically shown in Figure 8.8, and it is performed for each pixel of the image. Reflections take a greater importance in the case where the angles of incidence are large, which happens very often in the case of a small camera FOV and perspective views of the scene.

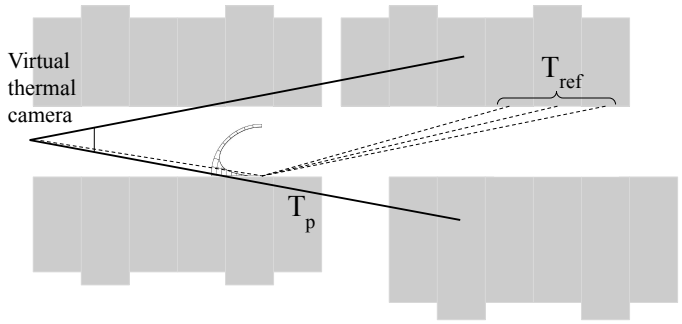

Figure 8.8: Ray tracing for rendering a thermal image using a virtual camera.

Under clear sky conditions, the atmospheric transmissivity is high in the spectral range of the camera, because of the atmospheric window [Kruczek, 2015b]. This fact leads to an underestimation of the apparent sky temperature captured in thermography, which is affected by the much colder space background. In urban thermograms, the built surfaces can reflect the sky radiation. Hence, a new sky model, different to the one used in FEM, must be included in the rendering stage to reproduce the effect of the atmospheric window on the rendered thermograms. The model described by Bliss [Bliss Jr, 1961] is used in this study.

8.5 Case of study

The proposed simulation method was evaluated on a real case study, which was *Tonelliers* street in the city of Bayonne, France (Figure 8.9). The selected environment is characterized by a high complexity from both a material and geometrical point of view. A highly detailed 3D model was developed (Sec. 8.5.1) taking into account the requirements for a FEM simulation, as described in Acuña et al. [2018]. The simulations were compared with measured data retrieved from the urban thermographic campaign [Garcia-Nevado, 2019] summarized in Sec. 8.5.2.

Figure 8.9: Satelite view of Rue des Tonneliers, Bayonne, France. Extracted from Google Maps on July 31, 2019.

8.5.1 3D geometry

The urban model used for the simulations corresponds to an urban tissue mostly composed of eighteenth-century buildings. The preponderant construction technique in this urban area is a timber-framed system over a ground floor built of stone masonry. Wood, mortar and stone are therefore the predominant materials in the scene, although some other materials such as asphalt and glass windows are also present. The geometric modeling of this scene was based on an *in situ* survey by means of drones and LIDAR techniques; the model was manually built using Computer Aided Design tools. A high level of geometrical detail was used, which was important in the validation of the results with measured thermograms. The walls and inner floors were modeled with a constant thickness, which was set to $0.18m$ following the average value obtained from *in situ* inspections.

The FEM simulations required a specific geometric modeling strategy called conformal meshing [Zienkiewicz et al., 2013]. A conformal mesh is one in which no node of an element is on an edge or face of another element, and in which all adjacent elements share full edges. Regular hexahedrons and a small number of triangular prisms were used. The skin of the model, which is the part of the geometry subject to convective and radiative boundary conditions, is then composed of quadrilateral and triangular elements. The final model (Figure 8.10) is meshed with 192911 volume elements and 104377 surface elements.

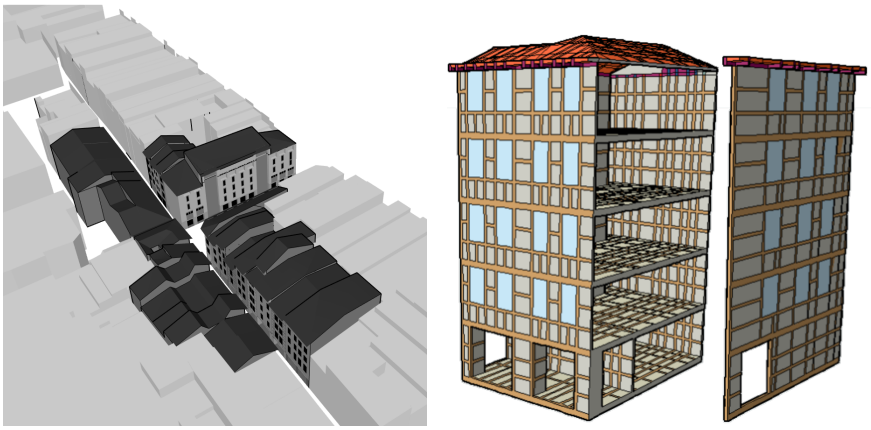

(a) Overall geometry. (b) Building model and mesh detail.

Figure 8.10: Geometry model of Tonneliers street, Bayonne.

Building parts were modeled seeking for constructive realism. For example, wood and mortar elements together form the typical timber frame constructions that are present in Bayonne. Some windows were modeled with glass (if wooden blinds were opened during the campaign) and the rest of them with wood.

8.5.2 Measurement campaign and parameter set-up

The results from a measurement campaign were used to validate the simulations. The campaign was carried out during April 23^{rd} (spring), a day with clear sky and calm wind conditions. A thermal camera (FLIR B200, 240 x 180 pixels, FOV: 25°×19°) was placed on the *Tonneliers* street, and a series of thermograms were taken during a period of 18 hours (6 am to 12pm). The camera was set to capture the apparent surface temperature: the emissivity was set to 1 and the distance to 0m.

Figure 8.11 shows the position of the camera and the surface captured by the camera lens. A perspective view of the scene was selected in order to acquire a maximal amount of physical information in a single frame. An example of photograph and correspondent thermogram can be observed in Figure 8.1.

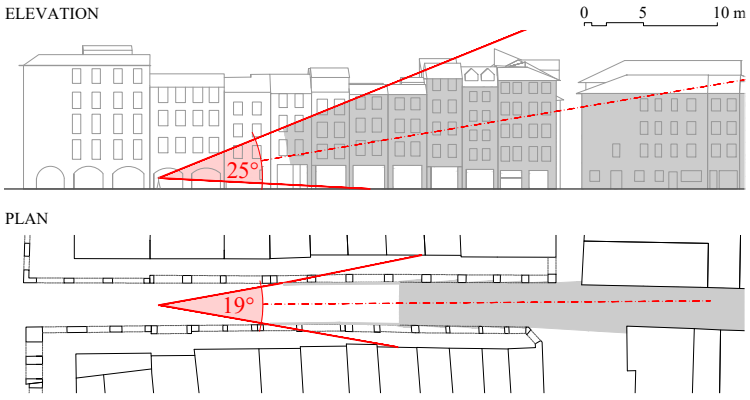

Figure 8.11: Position and view of the thermal camera in the measurement campaign.

Other environmental conditions were measured to estimate the correct boundary conditions in the simulations. The wind velocity was captured by an anemometer placed at 2.5m from the ground. Street air temperatures and relative humidity were measured *in situ* (see Figure 8.12). A weather station located at 3.4 km away from the location provided the global horizontal irradiances. Short-wave reflectivities of the materials in the street (wood, mortar, stone, asphalt, roof tiles, and glass) were estimated by measuring the luminance differences between each material and a baseline tape with a known reflectance, under the same lighting conditions. Finally, Meteonorm [Remund et al., 2010] data was used to define the ground temperature 1m in depth, which was estimated to be 11.1°C, and constant for the period of measurement.

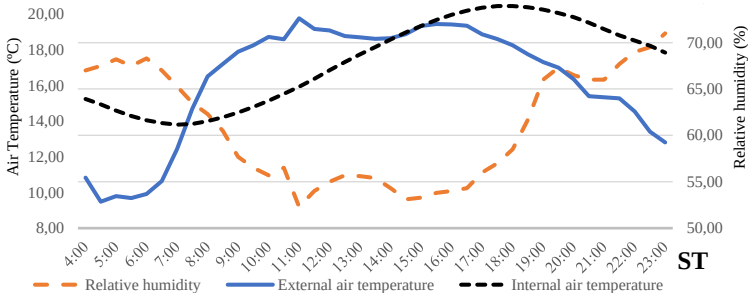

Figure 8.12: Measured outside air temperature and relative humidity, along with the estimated internal air temperature.

The parameter set-up is shown in Table 8.1. The values for the conductivity components (k, ρ and c_p) were extracted from a reference material database [CSTB France, 2012], while short-wave reflectivity values r were averaged for each material.

Material	k	ρ_m	c_p	r
mortar	1.05	1400	1500	0.53
wood	0.21	800	1255	0.45
stone	3.50	2750	880	0.49
asphalt	1.48	2267	1035	0.41
roof tile	0.49	394	937	0.48
glass	0.95	2500	836	0.1

Table 8.1: Parameter set-up for material properties.

Finally, the convective coefficient of the outside surfaces was set to h = 10 W m^{-2} K^{-1} , based on the low wind values that were measured *in situ* (lower than 1 m/s). For inside surfaces, the values extracted from the French thermal regulation [CSTB France, 2012] were 0.7 W m^{-2} K^{-1} for the ground, 2.5 W m^{-2} K^{-1} for vertical walls, and 5 W m^{-2} K^{-1} for roofs.

8.5.3 Emissivity estimations

The emissivity of urban surfaces plays a key role on the physically-based simulation and rendering process. Measured directional emissivity models for urban materials are not available in the literature. In this work, following the process described in Figure 8.5, the directional emissivities were estimated using combination of ideal Fresnel and diffuse models. This assumption is based on *in situ* observations of material roughness (Figure 8.13), as well as on a second measurement campaign

in the same street [Beckers and Garcia-Nevado, 2018], where two thermal cameras were used (the first one with a perspective view and the second one with a frontal view).

Figure 8.13: Detail of the urban scene, showing the roughness of the studied materials.

Table 8.2 shows the parameters chosen for the generation of directional emissivity curves. The Fresnel and diffuse percentages were estimated from the observations, and the normal emissivity values $\varepsilon_\perp$ were extracted from [Fronapfel and Stolz, 2006].

Material	$\varepsilon_\perp$	Fresnel	Diffuse	e
mortar	0.91	15%	85%	300
wood	0.95	10%	90%	200
stone	0.96	30%	70%	500
asphalt	0.92	20%	80%	400
roof tile	0.90	50%	50%	1000
glass	0.92	90%	10%	10^4

Table 8.2: Emissivity parameters for different materials, along with the specular lobe parameter e (Eq. 8.9).

The emissivity captured by the virtual camera placed in the same position than in the campaign is presented in Figure 8.14. The surfaces observed under grazing angles present lower emissivities (e.g. side façades on the background and the ground). In materials that are mostly-specular, such as glass, this effect is further accentuated. This is the case of the open windows, which present the lowest emissivities of the scene. Notice that the lower the emissivity value, the greater the importance of the reflected component.

8.6 Implementation

The surface temperatures were simulated using the Cast3m code [Charras and Di Paola, 2011] as the base FEM engine. A total of 24 hours was simulated (midnight to midnight) with a timestep of 10 minutes (144 steps). Linear shape functions were used. The input outside air temperatures used were those presented in Figure 8.12, which also presents the internal air temperatures that were obtained in the FEM simulation. The initial temperature conditions were obtained using a steady state simulation for the first hour (00:00) under the imposed boundary conditions that were described above.

The algorithm for computing the long-wave radiation absorption matrix (Alg. 7) was implemented using Embree high performance ray tracing kernels [Wald et al., 2014] with different sizes

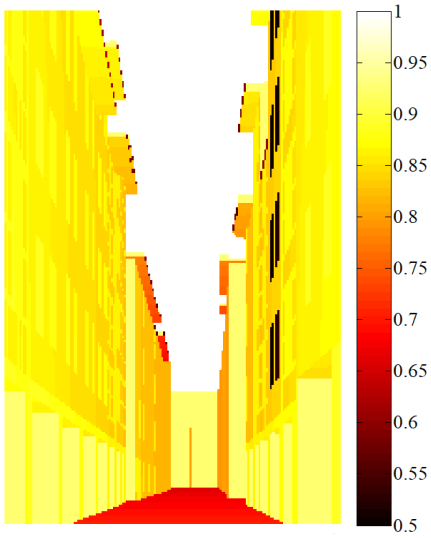

Figure 8.14: Emissivity of the scene as captured by the virtual camera.

of the specular lobes (see Eq. 8.9) depending on the material roughness. The values for e are presented in Table 8.2. The number of reflected rays was set to be $L = 20$, and the threshold was $t = 10^{-5}$. Note that matrix $\mathbf{A}$ is a n×n matrix of floating point numbers, with n≈100k. Following [Aguerre et al., 2018], sparse representations were used to reduce the memory requirements of such matrix, leading to a total consumption of around 8GB. Then, the non-diffuse long-wave radiation boundary conditions were implemented in Cast3m using the precomputed matrix $\mathbf{A}$.

The implementation of the post-processing stage was also performed with the Embree kernel. The reflected temperatures are estimated using importance sampling with the probability density function of Eq. 8.9, and multiple bounces to account for radiation reflections. After computing ϕ_{in}^{virt} from the direct and reflected temperatures, Eq. 8.18 was used to obtain the simulated apparent surface temperatures, following the same behavior than the real camera in the measurement campaign.

8.7 Results and discussion

This section presents the result of the simulations and a comparison with the measured thermograms. All tests were executed on an Intel i7-7700 processor with 4 cores and 16GB of ram. In the preprocessing stage, the computation of short-wave loads took around 7 minutes, while the extended view factors matrix $\mathbf{A}$ using Embree took 11 minutes. FEM simulation (Cast3m) had the longest execution time, which was 62 minutes. With these results, the post-processing stage took less than 2 seconds to render each thermogram.

The first results are shown in Table 8.3 and correspond to the surface temperatures obtained with the FEM simulation. The results are presented for the north and south street façades at four different times of the day. The results show cold surfaces in the morning (11:00hs), mainly driven by the air temperatures. The surface temperatures begin to rise as the sunlight starts to impinge directly (15:00hs). The thermal inertia of the walls keeps them hot during the evening (19:00hs), while at night (23:00hs) the simulation shows colder roof temperatures due to long-wave radiation exchanges with the sky. This behavior agrees with the one expected for an urban scene during a windless sunny

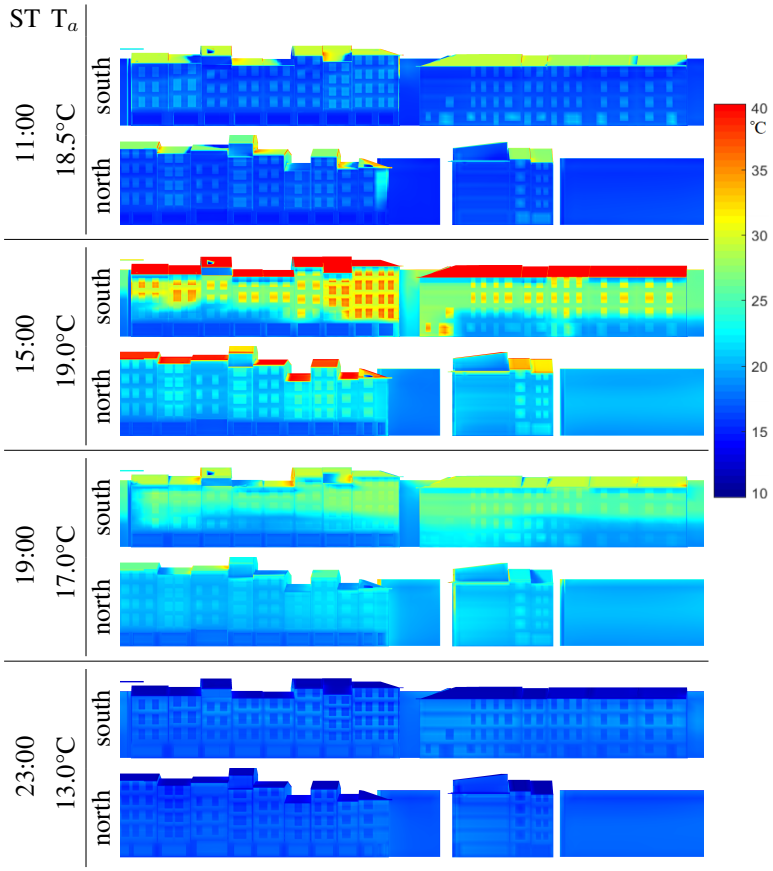

Table 8.3: Surface temperatures simulated with FEM. The results are separated into the north and south facing walls.

day.

8.7.1 Impact of directional emissivity

For the next experiment, the virtual thermal camera was placed in the same position as in the measurement campaign. Two hours of the day were selected, one during daylight hours (15:00hs) and the second one at night (23:00hs). Thermal images were rendered using different directional emissivity models, in order to show the effect of this parameter on the results. Table 8.4 depicts the rendering results (rows 1-4) and corresponding thermograms from the measurement campaign (last row).

The first row was generated using a blackbody model ($\varepsilon = 1$). Under this assumption, the wooden blinds on the south wall present higher temperatures than in the measurements, as well as the entire surface of the north facing wall.

When the emissivity is set below 1 (as done in rows 2-4), the radiation reflections start having an effect on the results. Hence, to help the analysis, the glossy reflected temperatures captured by the virtual camera are shown in Table 8.5, obtained by following the glossy reflected paths as described in Sec. 8.4.3. Two different colormap intervals were used for a better visualization of the reflected sky temperatures, which are much colder than the urban surfaces.

The results are more similar to the measurements when using a diffuse emission approximation

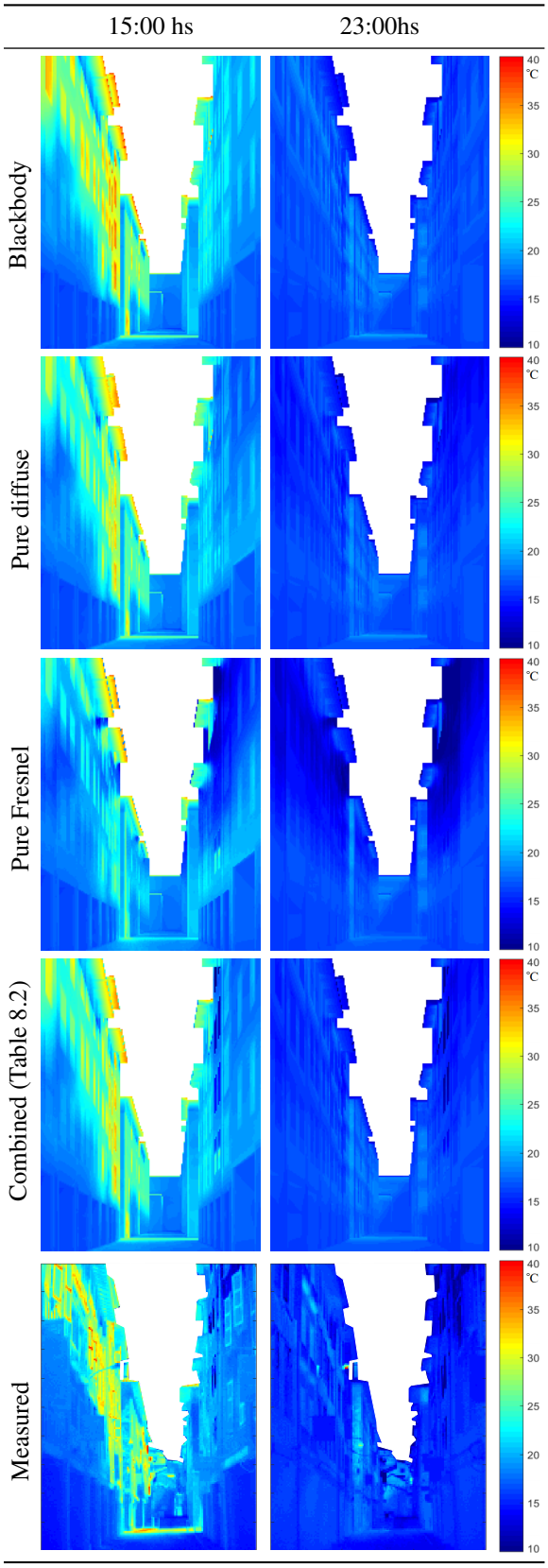

Table 8.4: Several rendered thermograms using different emissivity models along with measured results.

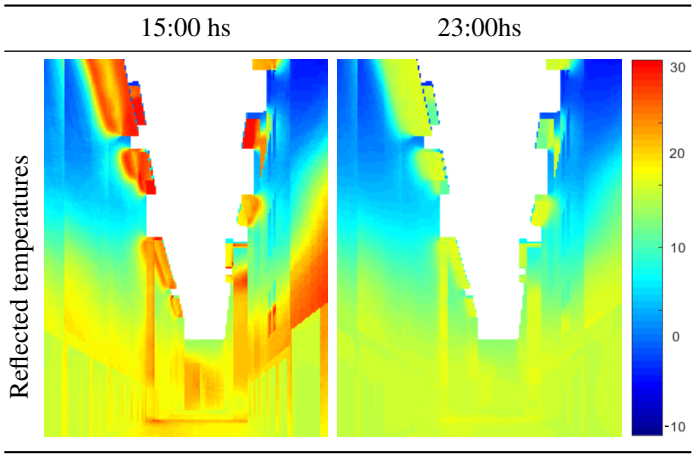

Table 8.5: Reflected temperatures of each pixel associated with the same camera position and two different hours. A new colormap interval is used to visualize the colder reflected temperatures of the sky.

(row 2 of Table 8.4), where the surfaces are considered gray-body emitters. Here, the normal emissivity ($\varepsilon_\perp$) values from Table 8.2 were used as the constant emissivity for each material. In this case, the colder reflected temperatures of the sky start having an effect in the results, allowing for better results in the south wall, but non-rough surfaces (e.g. glass windows in the north wall) still present an overestimated emissivity. The third row was generated using the Fresnel emissivity model (Figure 8.3). In this case, the reflected temperatures have a major effect in the rendered images, which are much colder than in the measurements. These images are especially influenced by the large incidence angles of the perspective view, resulting in lower emissivity values. The images in the fourth row were generated using the mix of diffuse and Fresnel emissivity models with the percentages presented in Table 8.2. This model allows for the simulation of both smooth surfaces and diffuse ones: the wooden blinds show colder temperatures as in the third row, and the glass on windows reflect the sky temperatures. Upon comparison with the measurement results, the combined model proved to be the most accurate one. Therefore, this model was used in the rest of the analysis.

8.7.2 Time sequence of measured and rendered thermograms

The time-lapse of measured and simulated results is presented in Tables 8.6 and 8.7. Thermal images are shown with the same colormap to facilitate the comparison. Temperature patterns are very similar between both set of images. During the day, the short-wave shadowing pattern drives the temperature distribution on the south walls, which is also observed in the simulations. Direct sunlight strikes these walls more perpendicularly around noon, resulting in a temperature rise. After 14:00hs, the temperature of some elements that were not considered in the simulations (e.g. opened wooden blinds) rises. These elements, which have low reflectance and thermal inertia, produce higher maximal temperatures in the real thermogram than in the simulation (see the results for 17:00hs).

After the sunset (around 20:00), surface temperatures are very dependent on the sky view factor, resulting in colder temperatures for surfaces that see bigger portions of the sky. This phenomenon is due to the key role of radiative cooling of surfaces towards the sky. The simulations show some differences in ground temperatures, probably due to an estimation bias in the sky temperatures or

ST	Measurement campaign	Simulation
08:00	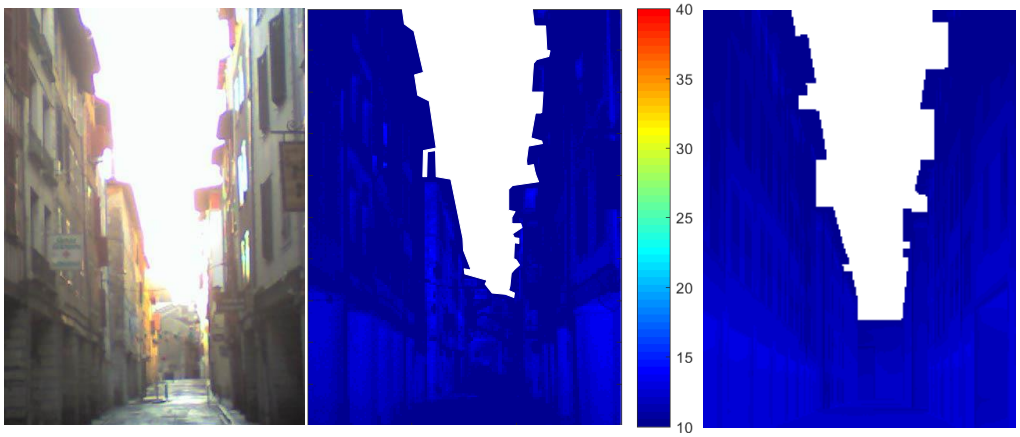	
11:00	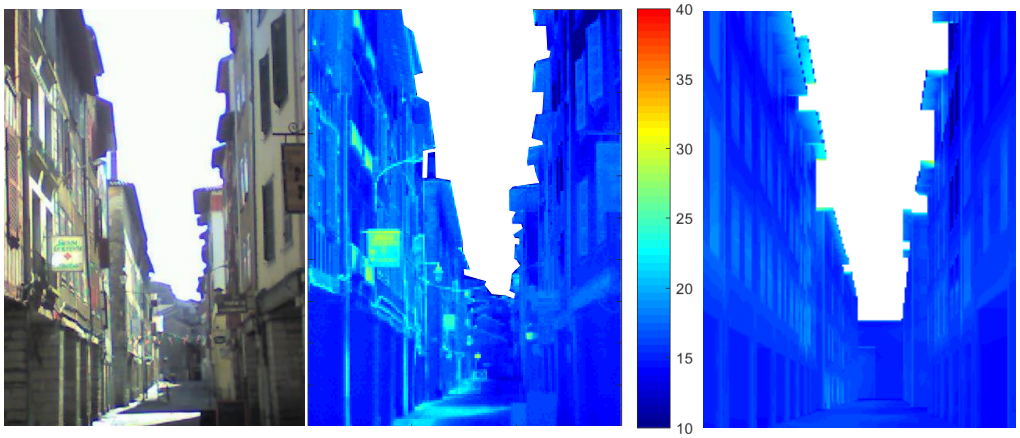	
14:00	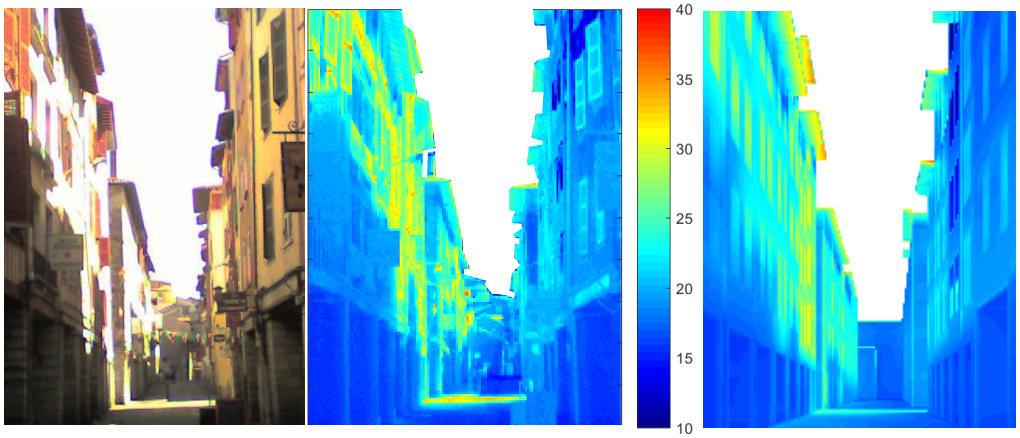	

Table 8.6: Set of photographs, thermograms, and the simulated results between 08:00 and 14:00, Solar Time (ST)

ST	Measurement campaign	Simulation
17:00	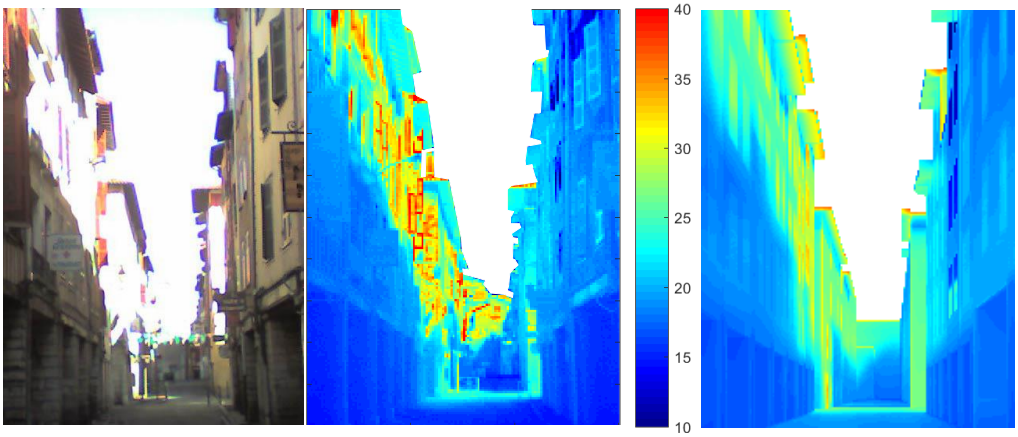	
21:00	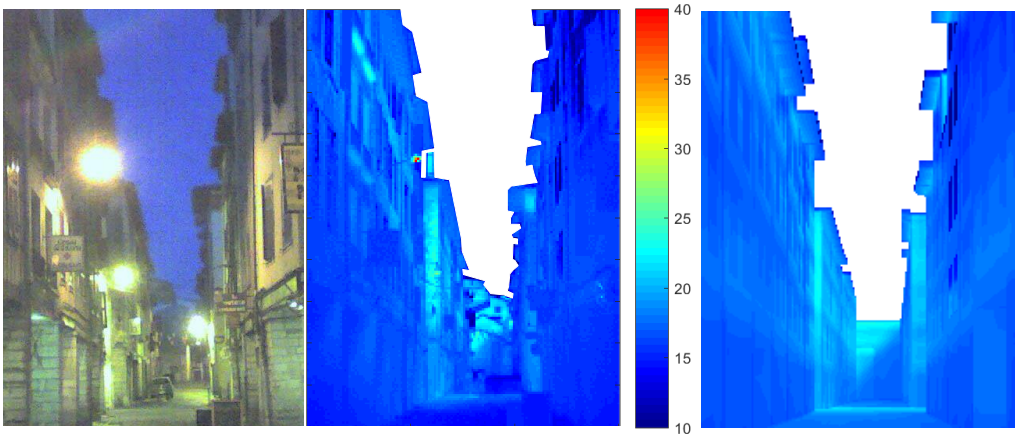	
23:00	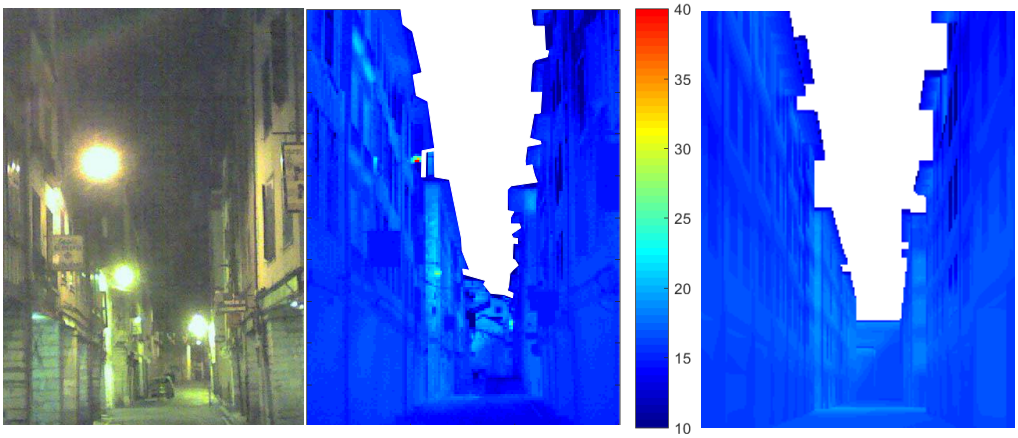	

Table 8.7: Set of photographs, thermograms, and the simulated results between 17:00 and 23:00, Solar Time (ST)

short-wave reflectivity. Both measurements and simulations show that the roof overhangs reduce the effect of long-wave cooling, resulting in higher temperatures in the top parts of walls.

In order to get a better visualization of the results and to analyze the differences between measurement campaign and simulations, two thermograms were studied with greater detail: one at daytime (14:00), where short-wave fluxes were dominant, and the second one at night (23:00), where the influence of long-wave radiation is greater. Both images are shown in Figure 8.15, where three quadrants and two lines were selected in the measured images. The corresponding quadrants and lines were selected in the simulated thermograms, looking to cover the same area of the real images that can be slightly deformed by the lens.

The content of the quadrants was extracted and zoomed-in in Table 8.8. In this table, Dx means quadrant x of daytime thermogram, while Ny means quadrant y of nighttime thermogram. D1 shows the temperature patterns caused by short-wave shadowing. The roofs are hotter in the simulation because a single material (roof tile) was considered, while in reality they have multiple layers with different properties. Windows reflecting the cold sky are observed in D2, and similar temperature patterns can be seen in D3. The section of the street that receives direct sunlight is colder in the simulation. N1 and N2 show the effect of the long-wave cooling process of the buildings at night, where the parts protected by the roof overhangs are hotter. Finally, D3 details a section of the street and a wall which were heated by short-wave radiation throughout the day and remain warmer than the rest of the street due to thermal inertia.

The temperature plots for each pixel of the lines are shown in Figure 8.16, which also contains the mean and standard deviation of the absolute error between both plots. DV stands for daytime vertical, while NH means nighttime horizontal. The plots show that accurate temperature estimations were obtained for both daytime and nighttime thermograms. The temperature profiles have similar behaviors, showing larger biases in sections where the geometrical differences between the real scene and the 3D model are greater. For instance, the first pixels of DV cover parts of the wooden blinds that were opened in the measurement campaign. This kind of detail was neglected in the 3D model, leading to a deviation in the temperature profiles. The overall mean of the absolute error reaches its maximum value of 1.12°C in DH, which is expected because the horizontal line covers built surfaces with a wide geometrical variety.

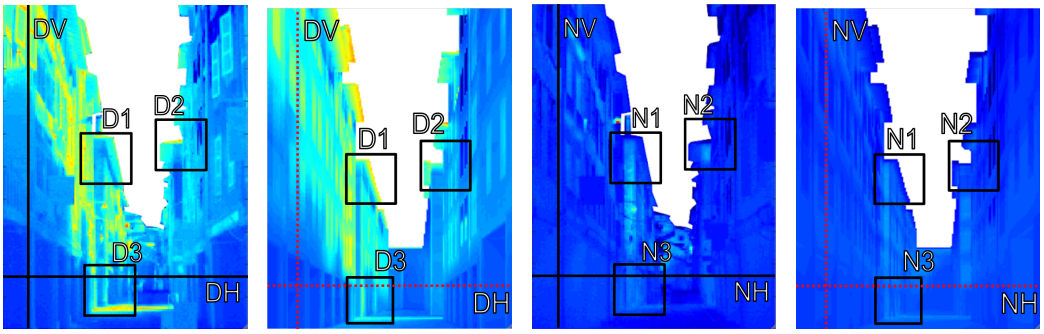

(a) Measured (14:00) (b) Simulated (14:00) (c) Measured (23:00) (d) Simulated (23:00)

Figure 8.15: Two measured and two simulated thermograms. For each image, three quadrants were selected and zoomed-in, and two lines of pixels were plotted.

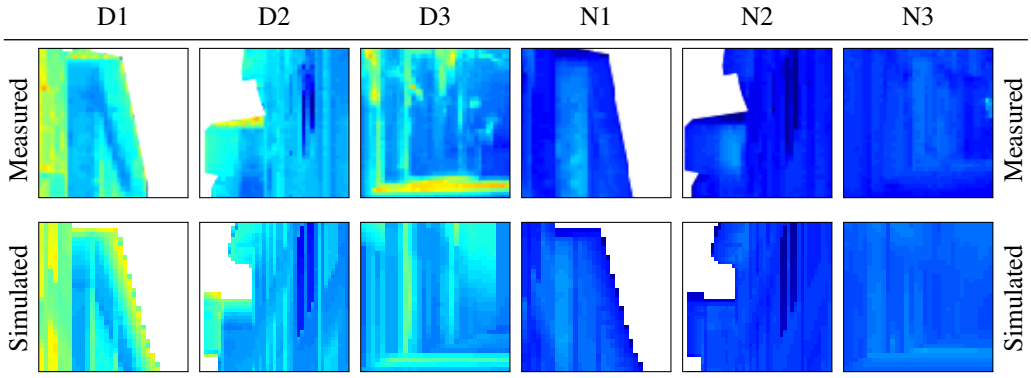

Table 8.8: Details of the measured and simulated thermograms.

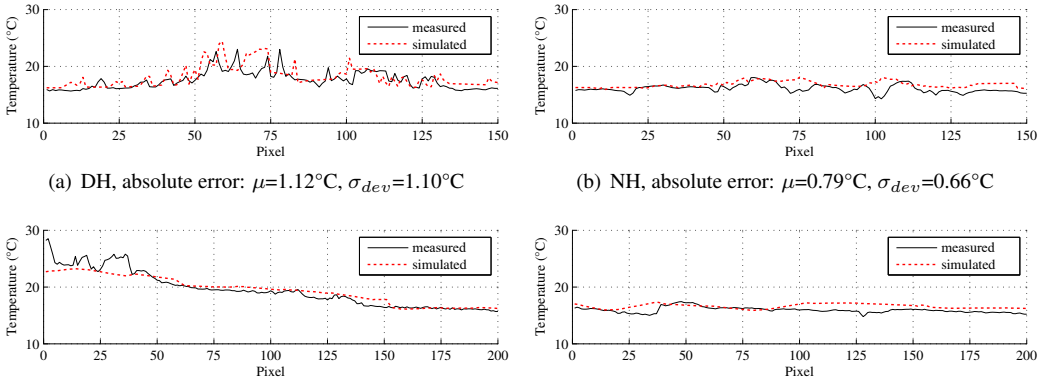

(a) DH, absolute error: μ=1.12°C, σ_{dev}=1.10°C (b) NH, absolute error: μ=0.79°C, σ_{dev}=0.66°C

(c) DV, absolute error: μ=0.81°C, σ_{dev}=0.91°C (d) NV, absolute error: μ=0.75°C, σ_{dev}=0.51°C

Figure 8.16: Temperature plots of horizontal and vertical lines of the selected thermograms.

8.8 Conclusion

A methodology for the simulation and rendering of urban thermography was presented, providing a set of accurate methods to account for the radiative boundary conditions that are involved in urban heat transfer studies. The methodology is based on a combination of FEM to discretize the heat conduction differential equations, and ray tracing to address the radiation modules.

The comparison of simulated and measured data shows that very accurate results were obtained by the proposed algorithms. The computational model showed good performance, allowing for the analysis of results under different parameter configurations. The use of directional emissivities was necessary in the rendering stage, because the measured results were affected by the large incidence angles of perspective views.

Urban thermography rendering can be of fundamental help in the interpretation of a time sequence of thermal images. For example, the simulation results showed the significant influence of the low sky temperatures in the urban apparent surface temperatures, which is otherwise difficult to appreciate in measured thermograms captured with a single camera. In this context, thermography rendering appears as an interesting tool to understand the main physical phenomena of an urban scene.

The graphical approach adopted in this study, where a set of thermal images were compared in detail, pushed the limits of urban thermal simulation methods. The results showed that rendering complex urban scenes, involving both rough and smooth materials, requires a precise treatment of directional emissivities and the proper reflectivity functions. Computer graphics algorithms provide many solutions to treat these kind of behaviors, but these properties are still a matter of study for physics. Therefore, thermography rendering provides a promising future avenue in the collaboration between both communities.

Chapter 9

Conclusions and future work

This chapter presents the conclusions and final remarks of this thesis. After this, the main lines of future work emerged during its development are outlined.

9.1 Conclusions

This thesis addressed the study of a set of methods for the simulation of heat transfer in urban scenes. The methodology is based on a combination of FEM to discretize the heat conduction differential equations, and radiosity and ray tracing to address the radiation modules. The comparison of simulated and experimental data showed that very accurate results were obtained by the proposed algorithms. The studies depended greatly on the level of detail of the geometry as well as on the physical models used to account for radiation and convection.

9.1.1 Radiation techniques

Radiosity has proved to be a well-suited global illumination algorithm to compute radiation exchanges in urban environments. It was found to be efficient for dealing with many diffuse materials. At the street scale, computing multiple diffuse bounces was key to obtaining accurate estimations, especially at the lower parts of the buildings.

The main problem with radiosity is the memory consumption associated with storing view factors. This issue was addressed using sparse matrix representations, exploiting the fact that city environments present a high occlusion factor in the inter-element's visibility. In Chapter 4, it was shown that there is a strong correlation between the geometrical characteristics of a city and the density of its view factors matrix. A method for obtaining a sparse approximation of the inverse of the radiosity matrix was presented, enabling the acceleration of daylighting calculations in up to two orders of magnitude when compared to standard radiosity, and showing low relative errors.

After the success of the approach presented in Chapter 4, sparse view factors matrices were used in Chapter 5 for daylighting in larger urban scenes, in Chapter 6 for the computation of short-wave loads in a smaller model, in Chapter 7 for long-wave radiation computations in the same smaller model, and in Chapter 8 for both short and long-wave calculations in a model with higher geometrical detail. Sparse matrices not only accelerated the calculations, but also allowed for the

processing of large models with a significant reduction in the memory requirements.

A second conclusion regarding radiation is that importance-driven methods can be used for computing energy exchange in geometries representing large urban districts. Chapter 5 presented an algorithm for reducing the models based on selecting the parts of the geometry that influence the radiation of a zone of interest. The main conclusion of this chapter was the fact that importance can be used for dealing with big city scenes in the context of urban physics. This idea can bring about a renewed interest in importance-driven methods in the near future.

Chapter 5 also provided two important results. In the one hand, the use of extended view factors allowed for the inclusion of specular materials in the urban geometry, increasing the realism of the results by implementing an efficient combination between radiosity and ray tracing. On the other hand, the methods were compared with the RADIANCE package to validate the results, showing accurate precision and shorter execution times. The proposed technique was shown to be an interesting alternative in scenes with many diffuse objects and a smaller set of specular materials.

In the following chapters, importance was not used for radiative calculations because such large urban geometries were not simulated with FEM. Although the original idea was to integrate this kind of technique to the full thermal analysis methodology, street-scale studies were selected, and importance was not necessary for reducing radiation computations.

9.1.2 FEM for urban thermal analysis

One of the main objectives of this thesis was to use FEM for urban thermal analysis. The first approach to this end was addressed in Chapter 6, using a simple test case as a starting point. A real urban district was chosen, and a simplified geometry based on four boxes was designed. A street-scale study was selected because it was simpler to validate with the available measurement techniques, and because it allowed for an easier interpretation of the results extracted from the combined experimental-simulation approach taken. The simulations, performed using the software Cast3m, provided compelling results, reproducing the same order of magnitude and general appearance of the measured data. The main discrepancies were explained by the adopted geometric simplifications, such as the use of flat roofs without overhangs and uniform exterior coatings.

FEM allowed to represent and simulate the urban geometry using a fine mesh, obtaining very detailed temperature profiles. Starting from the volume mesh used in FEM, the skin exterior mesh was extracted to calculate short-wave loads. This mesh was directly entered into a radiosity engine to perform the calculations, showing that FEM and radiosity are intrinsically compatible and allow for a straightforward integration. Long-wave calculations were also performed with view factors but based on the Cast3m implementation, which does not use sparse matrix representations.

In Chapter 7, two improvements to the previous model were presented. Sparse matrices were entered in Cast3m to enhance the computational performance of the long-wave part. With this modification, the entire simulation was accelerated by a factor of 9×. The second improvement was the implementation of a technique to enable free internal air temperatures. This method increased the realism of the study, reaching more accurate results when compared to experimental data.

The simulations performed in Chapters 6 and 7 were limited by the geometrical representation of the scene. The idea of repeating a similar study using a detailed model appeared as a direct line of work but brought many problems that had to be addressed. The first issue was to design

a geometry and a mesh compatible with FEM, as well as to insert it into Cast3m, as presented in Chapter 8. A greater variety of material properties were introduced, leading to a much complex simulation in which FEM proved to be a flexible method with an outstanding capacity for dealing with sophisticated scene characteristics.

9.1.3 Thermography and infrared rendering

The data extracted from a thermography campaign performed in Bayonne, France, during a spring day was used in Chapters 6, 7 and 8. The spatialized results provided by FEM analysis allowed for the simulation of street-scale thermograms. The comparison between measured and simulated data was shown to be an innovative validation strategy. Moreover, it proved to be an interesting analysis methodology, since simulations offer complementary information that is not visible in the thermal images.

Blackbody materials were simulated in Chapters 6 and 7. This assumption simplified the algorithms in the post-processing module but limited the phenomena that could be represented in the rendered images. Therefore, in Chapter 8, computer graphics techniques were used to simulate a virtual thermal camera, in order to compare the spatialized results with a greater detail. The implementation of this rendering module was developed with the ray tracing library Embree. Thermography rendering appeared as an interesting tool to understand the infrared behavior of the urban scene. For example, both measured and rendered results showed the significant influence of the low sky temperatures in the urban apparent surface temperatures captured by thermal cameras. Ray tracing proved to be efficient for such task, and the Embree library allowed for the generation of each rendered thermal image in less than two seconds.

The infrared rendering of non-blackbody materials required the proper definition of directional emissivity and reflectivity models. In this context, the current scientific knowledge on the behavior of construction materials in the infrared spectrum was found to be very limited. A combined emissivity model was proposed, using a mix of diffuse and Fresnel models. Glossy reflectivity functions were used to represent the reflected portion of the radiation that reaches the thermal camera. This combination allowed for the simulation of both smooth and rough surfaces, which proved to be accurate upon comparison with the measurements.

The computer graphic strategies used in this chapter pushed the limits of the urban thermal simulation methodology. The results showed that rendering complex urban scenes requires a precise treatment of directional emissivities and the proper reflectivity functions. Computer graphics provides many solutions for rendering, but the physical description of these properties must be studied with greater detail in order to obtain better simulation conditions. In this sense, thermography rendering provides a promising future avenue in the collaboration between both communities.

9.1.4 Computational performance

Finally, regarding computational performance, it must be stated that all the calculations presented in this thesis were executed in short times, with a maximum of two hours in Chapter 8. FEM is occasionally presented as a heavy computational method in the literature, but this thesis showed that it can be used for urban simulations in an efficient manner. The short execution times provided the possibility of evaluating the thermal impact of the modification of reflectivity and diffusivity

material properties in Chapter 6, as well as using different infrared properties in Chapter 8. Assessing different design options is one of the possible applications of the methods proposed in this thesis, and hence it is very important to provide reasonable execution times.

The most expensive part of the model was found to be the long-wave radiation calculations. Using sparse view factors matrices not only reduces the memory consumption, but also accelerates the process significantly. In Chapter 8, the model was executed with a mesh of ≈100k elements, which was only possible with sparse matrices. An important conclusion of this thesis is that, in the context of urban FEM analysis, long-wave calculations should be addressed with special care, trying to reduce the size of the mesh and/or to improve the computational performance of the algorithms by exploiting specific properties of the problem.

Although only 24hs periods were simulated in the experiments performed, only a standard PC was used as the main hardware. The computation of larger periods such as yearly timeframes can be addressed using other available computer hardware such as larger CPUs, GPUs or computer clusters, using high performance computing techniques to develop parallel algorithms and more efficient solutions.

9.2 Future works

Many simplifications were adopted in the course of development of this thesis, some related with limitations of the framework used (Cast3m), and other associated with physical assumptions that were made to provide good simulation conditions and to enable an easier interpretation of the results. In this sense, there are many lines of future work that must be covered to improve and extend the current state of the model.

9.2.1 Geometry for FEM

Due to limitations in the current implementation of Cast3m (Cast3m 18), the usage of higher order elements such as quadratic shape functions [Lewis et al., 2004] was not tested. The introduction of these kind of elements can simplify the meshing process of the urban geometry. For example, this strategy can be an efficient alternative to using several layers of linear elements in the thickness of the walls. The compatibility between quadratic elements and long-wave radiation exchange is not currently supported by Cast3m, so an alternative is to modify this framework or to use other FEM codes.

A similar limitation brought by Cast3m was the inability of using shell elements in the urban mesh. Shell elements are flat three-dimensional elements used to represent solids in which one of the dimensions is significantly smaller than the other ones. This representation allows to simplify the geometrical design. A thickness value must be indicated for each element, which is used in mathematical formulation of the problem. Using shell elements can reduce the computational costs of the problem by reducing the number of nodes, as well as improving the numerical stability of the solution [Zienkiewicz et al., 1977]. Replacing the solid elements used in this thesis (of size ≈ 1.5m × 1.5m × 0.18m) by shell elements can drastically simplify the urban mesh. Cast3m provides shell elements, but its compatibility with long-wave radiation exchange is not yet implemented.

Another line of future work is to use procedural modeling to generate urban meshes that are

suitable for FEM simulations. The computer graphics area has developed many algorithms to generate urban 3D scenes from a set of grammatic rules and other specifications [Musialski et al., 2013]. These methods can consider different level of detail to control the creation of the model [Besuievsky and Patow, 2013]. In this way, it should be possible to adapt these kinds of algorithms to generate congruent volume meshes that provide good simulation conditions for FEM. This task can facilitate the design process of urban meshes, which is particularly difficult when a high level of detail is required [Acuña Paz y Miño et al., 2018]. Moreover, it can ease the integration processes of a CAD mesh into a FEM framework [Duport et al., 2019].

9.2.2 Integration of fluid dynamics

Another topic that was not addressed in this thesis is the modeling of wind movements and natural convection within the urban environment. Air flow is an important factor in the heat transfers of the city [Blocken, 2015]. Under the presence of strong wind velocities, the urban surface temperatures can be significantly affected by convection. Real-scale experiments and reduced-scale wind tunnel measurements can help assessing the impact of the air dynamics to study ventilation, pedestrian comfort and thermal exchanges.

In the last decades, Computational Fluid Dynamics (CFD) has been used to avoid the high cost of experimental analysis, replacing it by numerical modeling. This strategy requires meshing the air volume around the buildings and setting the correct boundary conditions of the problem [Van Hooff and Blocken, 2010]. A very large number of elements must be used to solve the Navier-Stokes equations [Chorin, 1968], which describe the behavior of fluids. In this context, the numerical accuracy of CFD regarding geometry, grid generation, solver selection, and the proper interpretation of the results, becomes a major concern. The integration of CFD can be an important step for assessing relevant problems such as the urban heat island effect [Wang and Li, 2016], yearly building energy consumption [Mirsadeghi et al., 2013] and pollutant dispersion [Di Sabatino et al., 2013].

Thermal and CFD solutions can be coupled by joining the algorithms in a unique solver. For example, a system with FEM for heat conduction and CFD for air movements can be implemented to solve urban heat transfer problems that present strong wind conditions. In this approach, CFD outputs air temperatures and heat exchange coefficients, which are used to compute a new surface temperature with FEM. These last results are used in a new CFD step, and so on. A simpler approach would be to use CFD for computing a set of heat transfer coefficients only considering forced convection, i.e. discarding natural convection, and hence de-coupling both problems. These coefficients can then be entered into the FEM code without the need of an iterative process.

9.2.3 Large-scale studies

Chapters 4 and 5 provided short-wave methods for large urban scenes. In the next chapters, these methods were applied to a street scale scene in which the thermography measurements were performed. One line of future work is to develop a similar study in a larger urban geometry [Beckers, 2016]. This goal brings new challenges from both measurement and simulation perspectives, because such highly complex test case pushes the limits of the proposed methodologies.

Infrared measuring of larger environments is not a simple issue. A drone with a thermal camera can be an interesting option to tackle this problem [Entrop and Vasenev, 2017]. Another alternative

is to use a thermal camera from a high spot in the city, in order to capture more information in one frame [Meier et al., 2011]. Figure 9.1 presents an example of large-scale infrared measurement. The images were taken from a high building in the city of Montevideo, Uruguay. The captured scene includes several buildings of different heights, vegetation, streets, and other elements. This scale can enable the study of the thermal interaction between a set of buildings, including inter-building shadows, different sky view factor proportions, and a wide material variety.

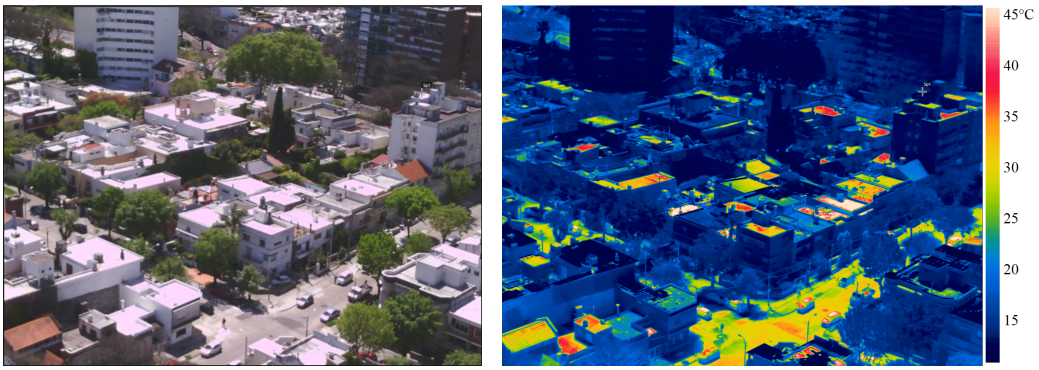

(a) Photo (b) Thermogram

(c) CAD geometry representing the urban scene

Figure 9.1: Photo and thermogram of an apple of buildings in Montevideo, Uruguay. Images captured using a FLIR T1020 thermal camera on October 8, 2019.

From a computational perspective, extending the simulations to a larger scale can require new algorithmic optimizations and methodological advances. The integration of a scene like the one presented in Figure 9.1 implies dealing with a larger mesh. A clustering method can be used to reduce the storage requirements of the view factors matrix [Péniguel and Rupp, 2004]. Combining this approach with sparse matrices can be an efficient choice for this purpose. Another option for computing radiation in such scales can be to reduce the memory requirements by avoiding the computation of the full view factor matrix, which can be accomplished using a progressive radiosity approach [Cohen et al., 1988]. The idea of this algorithm is to compute the form factors on demand, to gather radiosity on an element, or to expand the power from an element into the scene. This tech-

nique can be combined with importance to select the next shooting elements [Bekaert and Willems, 1995; Sbert, 1997]. Adapting this approach to long-wave computations should be studied, because in this context all the patches become radiation sources and the convergence of the progressive approach can be affected. Finally, at this scale, the wind becomes more difficult to predict with local measurements. Using CFD calculations becomes unavoidable for an accurate study.

Figure 9.1(c) shows a 3D model of the scene captured with the thermal camera. It can be seen that the geometry is much more complex that in the previous studies. The integration of such model into a FEM software requires a lot of manual work. A good alternative is to use procedural modeling to generate the mesh in a format that is readable by FEM geometry packages.

The computational requirements of a study like this can be considerably larger than before, leading to the possibility of using cluster computers to reduce the execution times. The same idea can be used if a larger time period is to be computed, such as annual simulation periods.

Bibliography

Acuña Paz y Miño, J., Lefort, V., Lawrence, C., and Beckers, B. (2018). Maquette numérique d'une rue du vieux bayonne pour son étude thermique par éléments finis. *A la pointe du BIM: Ingénierie et architecture, enseignement et recherche*, 1:103.

Aguerre, J. P., Fernández, E., and Beckers, B. (2018). Importance-driven approach for reducing urban radiative exchange computations. *Building Simulation*, 12(2):231–246.

Aguerre, J. P., Fernandez, E., Besuievsky, G., and Beckers, B. (2017). Computing urban radiation: A sparse matrix approach. *Graphical Models*, 91:1–11.

Aguerre, J. P., Nahon, R., Garcia-Nevado, E., La Borderie, C., Fernández, E., and Beckers, B. (2019). A street in perspective: Thermography simulated by the finite element method. *Building and Environment*, 148:225–239.

Ångström, A. K. (1915). *A study of the radiation of the atmosphere: based upon observations of the nocturnal radiation during expeditions to Algeria and to California*, volume 65. Smithsonian Institution.

Asawa, T., Hoyano, A., and Nakaohkubo, K. (2008). Thermal design tool for outdoor spaces based on heat balance simulation using a 3d-cad system. *Building and Environment*, 43(12):2112–2123.

Asdrubali, F., Baldinelli, G., and Bianchi, F. (2012). A quantitative methodology to evaluate thermal bridges in buildings. *Applied Energy*, 97:365–373.

Ashdown, I., Jackson, C., Spahn, J., and Saemisch, T. (2017). Licaso and daysim. Technical report, Lighting Analysts Inc.

Baker, N. and Steemers, K. (2014). *Daylight design of buildings: A handbook for architects and engineers*. Routledge.

Barreira, E. and de Freitas, V. P. (2007). Evaluation of building materials using infrared thermography. *Construction and building materials*, 21(1):218–224.

Beckers, B. (2013a). *Solar energy at urban scale*. John Wiley & Sons.

Beckers, B. (2013b). Taking advantage of low radiative coupling in 3d urban models. In *Proceedings of the Eurographics Workshop on Urban Data Modelling and Visualisation*, pages 17–20. Eurographics Association.

Beckers, B. (2013c). Worldwide aspects of solar radiation impact. *Solar Energy at Urban Scale, John Wiley & Sons*, pages 99–118.

Beckers, B. (2016). Multiscale analysis as a central component of urban physics modeling. In *Computational Methods for Solids and Fluids*, pages 1–27. Springer.

Beckers, B., Aguerre, J. P., Besuievsky, G., Fernández, E., Garcia-Nevado, E., Laborderie, C., and Nahon, R. (2019). Visualizing the infrared response of an urban canyon throughout a sunny day. In *Sustainable Building for a Cleaner Environment*, pages 277–284. Springer.

Beckers, B. and Beckers, P. (2014). Sky vault partition for computing daylight availability and shortwave energy budget on an urban scale. *Lighting Research & Technology*, 46(6):716–728.

Beckers, B. and Beckers, P. (2016). Fast and accurate view factor generation. In *FICUP, An International Conference on Urban Physics*, volume 9, pages 249–259.

Beckers, B. and Garcia-Nevado, E. (2018). Urban planning enriched by its representations, from perspective to thermography. In *Sustainable Vernacular Architecture*, pages 165–180. Springer International Publishing.

Beckers, B. and Masset, L. (2006). Heliodon2, software and users' guide. Technical report, http://www.heliodon.net.

Bekaert, P. and Willems, Y. D. (1995). Importance-driven progressive refinement radiosity. In *Rendering Techniques' 95*, pages 316–325. Springer.

Berdahl, P. and Fromberg, R. (1982). The thermal radiance of clear skies. *Solar Energy*, 29(4):299–314.

Besuievsky, G. and Patow, G. (2013). Customizable lod for procedural architecture. In *Computer Graphics Forum*, volume 32, pages 26–34. Wiley Online Library.

Bliss Jr, R. (1961). Atmospheric radiation near the surface of the ground: a summary for engineers. *Solar Energy*, 5(3):103–120.

Blocken, B. (2015). Computational fluid dynamics for urban physics: Importance, scales, possibilities, limitations and ten tips and tricks towards accurate and reliable simulations. *Building and Environment*, 91:219–245.

Borel, C. C., Gerstl, S. A., and Powers, B. J. (1991). The radiosity method in optical remote sensing of structured 3-d surfaces. *Remote Sensing of Environment*, 36(1):13–44.

Bourgeois, D., Reinhart, C. F., and Ward, G. (2008). Standard daylight coefficient model for dynamic daylighting simulations. *Building Research & Information*, 36(1):68–82.

Bozonnet, E., Musy, M., Calmet, I., and Rodriguez, F. (2013). Modeling methods to assess urban fluxes and heat island mitigation measures from street to city scale. *International Journal of Low-Carbon Technologies*, 10(1):62–77.

Brown, M. J., Grimmond, S., and Ratti, C. (2001). Comparison of methodologies for computing sky view factor in urban environments. Technical report, Los Alamos National Lab., NM (US).

Bruse, M. (2004). Envi-met 3.0: updated model overview. *University of Bochum. Retrieved from: www. envi-met. com*.

Carroll, W. (1999). Daylighting simulation: methods, algorithms, and resources. Technical report, Ernest Orlando Lawrence Berkeley NationalLaboratory, Berkeley, CA (US).

Chakraborty, A. (2005). Impact of orography on the simulation of monsoon climate in a general circulation model. *Centre for Atmospheric and Oceanic Sciences (CAOS)*.

Chappuis, C., Rassineux, A., Breitkopf, P., and Villon, P. (2004). Improving surface meshing from discrete data by feature recognition. *Engineering with Computers*, 20(3):202–209.

Charisi, S., Thiis, T. K., Stefansson, P., and Burud, I. (2018). Prediction model of microclimatic surface conditions on building façades. *Building and Environment*, 128:46–54.

Charras, T. and Di Paola, F. (2011). Utiliser cast3m: la procédure pasapas. Technical report, Commissariat á l'énergie atomique.

Chelle, M. and Andrieu, B. (1998). The nested radiosity model for the distribution of light within plant canopies. *Ecological Modelling*, 111(1):75–91.

Chen, S. E., Rushmeier, H. E., Miller, G., and Turner, D. (1991). A progressive multi-pass method for global illumination. In *ACM SIGGRAPH Computer Graphics*, volume 25, pages 165–174. ACM.

Chorin, A. J. (1968). Numerical solution of the navier-stokes equations. *Mathematics of computation*, 22(104):745–762.

Christensen, P. H. (2003). Adjoints and importance in rendering: An overview. *IEEE Transactions on Visualization and Computer Graphics*, 9(3):329–340.

Christensen, P. H., Stollnitz, E. J., Salesin, D. H., and DeRose, T. D. (1996). Global illumination of glossy environments using wavelets and importance. *ACM Transactions on Graphics (TOG)*, 15(1):37–71.

Clarke, F. and Parry, D. (1985). Helmholtz reciprocity: Its validity and application to reflectometry. *Lighting Research & Technology*, 17(1):1–11.

Cohen, M. and Wallace, J. (1993). *Radiosity and Realistic Image Synthesis*. Academic Press Professional, Inc., San Diego, CA, USA.

Cohen, M. F., Chen, S. E., Wallace, J. R., and Greenberg, D. P. (1988). A progressive refinement approach to fast radiosity image generation. *SIGGRAPH Comput. Graph.*, 22.

Cohen, M. F. and Greenberg, D. P. (1985). The hemi-cube: A radiosity solution for complex environments. In *ACM SIGGRAPH Computer Graphics*, volume 19, pages 31–40. ACM.

Cohen, M. F., Greenberg, D. P., Immel, D. S., and Brock, P. J. (1986). An efficient radiosity approach for realistic image synthesis. *IEEE Computer graphics and Applications*, 6(3):26–35.

Collier, C. (2006). The impact of urban areas on weather. *Quarterly Journal of the Royal Meteorological Society*, 132(614):1–25.

COMSOL Inc. (2018). Comsol multiphysics 5.4: Heat transfer module user's guide.

Coulon, N. (2006). Nouvel algorithme pour traiter le rayonnement thermique en milieu transparent dans cast3m. Technical report, Commissariat á l'énergie atomique.

Cramer, V., Torgersen, S., and Kringlen, E. (2004). Quality of life in a city: The effect of population density. *Social Indicators Research*, 69(1):103–116.

Crawley, D. B., Lawrie, L. K., Pedersen, C. O., Winkelmann, F. C., Witte, M. J., Strand, R. K., Liesen, R. J., Buhl, W. F., Huang, Y. J., Henninger, R. H., et al. (2004). EnergyPlus: New, capable, and linked. *Journal of Architectural and Planning Research*, pages 292–302.

Crawley, D. B., Lawrie, L. K., Winkelmann, F. C., Buhl, W. F., Huang, Y. J., Pedersen, C. O., Strand, R. K., Liesen, R. J., Fisher, D. E., Witte, M. J., et al. (2001). Energyplus: creating a new-generation building energy simulation program. *Energy and buildings*, 33(4):319–331.

Croft, D. R. and Lilley, D. G. (1977). *Heat transfer calculations using finite difference equations*. Applied Science Publishers London:.

CSTB France, C. (2012). Régles th-u – fasicule 4: Parois opaques.

Datcu, S., Ibos, L., Candau, Y., and Mattei, S. (2005). Improvement of building wall surface temperature measurements by infrared thermography. *Infrared physics & technology*, 46(6):451–467.

de Cougny, H. L. and Shephard, M. S. (1996). Surface meshing using vertex insertion. In *Proceedings of the 5th International Meshing Roundtable*, pages 243–256. Citeseer.

de Freitas, S. S., de Freitas, V. P., and Barreira, E. (2014). Detection of façade plaster detachments using infrared thermography–a nondestructive technique. *Construction and Building Materials*, 70:80–87.

De Veubeke, B. M. F. and Hugge, M. A. (1972). Dual analysis for heat conduction problems by finite elements. *International Journal for Numerical Methods in Engineering*, 5(1):65–82.

Devabhaktuni, V., Alam, M., Depuru, S. S. S. R., Green II, R. C., Nims, D., and Near, C. (2013). Solar energy: Trends and enabling technologies. *Renewable and Sustainable Energy Reviews*, 19:555–564.

Di Sabatino, S., Buccolieri, R., and Salizzoni, P. (2013). Recent advancements in numerical modelling of flow and dispersion in urban areas: a short review. *International Journal of Environment and Pollution 7*, 52(3-4):172–191.

Döllner, J. and Buchholz, H. (2005). Continuous level-of-detail modeling of buildings in 3d city models. In *Proceedings of the 13th annual ACM international workshop on Geographic information systems*, pages 173–181. ACM.

Duff, I. S. (1977). A survey of sparse matrix research. *Proceedings of the IEEE*, 65(4):500–535.

Duport, N., Acuña Paz y Miño, J., and Beckers, B. (2019). Handling 3d model of a street for an urban thermal study with the finite element method. In *Proceedings of the 16th IBPSA Conference*, pages 310–319.

Dutre, P., Bala, K., Bekaert, P., and Shirley, P. (2006). *Advanced Global Illumination*. AK Peters Ltd.

Ebrahimpour, A. and Maerefat, M. (2010). A method for generation of typical meteorological year. *Energy Conversion and Management*, 51(3):410–417.

EnergyPlus, M. (2012). Energyplus engineering reference. *The reference to EnergyPlus calculations*, 1.

Entrop, A. and Vasenev, A. (2017). Infrared drones in the construction industry: designing a protocol for building thermography procedures. *Energy procedia*, 132:63–68.

Evangelisti, L., Guattari, C., and Asdrubali, F. (2019). On the sky temperature models and their influence on buildings energy performance: A critical review. *Energy and Buildings*, 183:607–625.

Evangelisti, L., Guattari, C., Gori, P., and Asdrubali, F. (2018). Assessment of equivalent thermal properties of multilayer building walls coupling simulations and experimental measurements. *Building and Environment*, 127:77–85.

Evins, R., Dorer, V., and Carmeliet, J. (2014). Simulating external longwave radiation exchange for buildings. *Energy and Buildings*, 75:472–482.

Fernández, E. (2009). Low-rank radiosity. In *Proceedings of the IV Iberoamerican symposium in computer graphics. Sociedad Venezolana de Computación Gráfica*, pages 55–62.

Fernández, E., Aguerre, J. P., Beckers, B., and Besuievsky, G. (2016a). Optimizing window shape for daylighting: An urban context approach. In *Eurographics Workshop on Urban Data Modelling and Visualisation*. Eurographics Association.

Fernández, E., Beckers, B., and Besuievsky, G. (2016b). A fast daylighting method to optimize opening configurations in building design. *Energy and Buildings*, 125:205 – 218.

Fernández, E. and Besuievsky, G. (2012). Inverse lighting design for interior buildings integrating natural and artificial sources. *Computers & Graphics*, 36(8):1096–1108.

Fraisse, G., Viardot, C., Lafabrie, O., and Achard, G. (2002). Development of a simplified and accurate building model based on electrical analogy. *Energy and buildings*, 34(10):1017–1031.

Freitas, S., Catita, C., Redweik, P., and Brito, M. C. (2015). Modelling solar potential in the urban environment: State-of-the-art review. *Renewable and Sustainable Energy Reviews*, 41:915–931.

Fronapfel, E. and Stolz, B. (2006). Emissivity measurements of common construction materials. In *InfraMation 2006 Proceedings*, pages 212–220. FLIR Systems, ITC.

Garcia-Dorado, I., Aliaga, D., Bhalachandran, S., Schmid, P., and Niyogi, D. (2017). Fast weather simulation for inverse procedural design of 3d urban models. *ACM Transactions on Graphics (TOG)*, 36(2):21.

Garcia-Nevado, E. (2019). *Termografía del cañón urbano: uso de la perspectiva para una evaluación térmica global de la calle*. PhD thesis, Universitat Politècnica de Catalunya.

Geisler-Moroder, D., Lee, E. S., and Ward, G. J. (2017). Validation of the five-phase method for simulating complex fenestration systems with radiance against field measurements. *15th International Conference of the International Building Performance Simulation Association*.

Ghandehari, M., Emig, T., and Aghamohamadnia, M. (2018). Surface temperatures in new york city: Geospatial data enables the accurate prediction of radiative heat transfer. *Scientific reports*, 8(1):2224.

Gibson, S. and Hubbold, R. J. (1996). Efficient hierarchical refinement and clustering for radiosity in complex environments. In *Computer Graphics Forum*, volume 15, pages 297–310. Wiley Online Library.

Gillingham, K., Newell, R. G., and Palmer, K. (2009). Energy efficiency economics and policy. *Annu. Rev. Resour. Econ.*, 1(1):597–620.

Givoni, B. and Katz, L. (1985). Earth temperatures and underground buildings. *Energy and Buildings*, 8(1):15–25.

Glickman, T. (2000). Ams glossary of meteorology. *American Meteorology Society, Boston, USA*.

Goel, N. S., Rozehnal, I., and Thompson, R. L. (1991). A computer graphics based model for scattering from objects of arbitrary shapes in the optical region. *Remote Sensing of Environment*, 36(2):73–104.

Goral, C. M., Torrance, K. E., Greenberg, D. P., and Battaile, B. (1984a). Modeling the interaction of light between diffuse surfaces. In *ACM SIGGRAPH computer graphics*, volume 18, pages 213–222. ACM.

Goral, C. M., Torrance, K. E., Greenberg, D. P., and Battaile, B. (1984b). Modeling the interaction of light between diffuse surfaces. In *Proceedings of the 11th annual conference on Computer graphics and interactive techniques*, SIGGRAPH '84, pages 213–222, New York, NY, USA. ACM.

Gortler, S. J., Schröder, P., Cohen, M. F., and Hanrahan, P. (1993). Wavelet radiosity. In *Proceedings of the 20th annual conference on Computer graphics and interactive techniques*, pages 221–230. ACM.

Groleau, D., Fragnaud, F., and Rosant, J.-M. (2003). Simulation of the radiative behaviour of an urban quarter of marseille with the solene model. In *Fifth International Conference on Urban Climate, Lodz, Pologne*, pages 1–5.

Guattari, C., Evangelisti, L., and Balaras, C. A. (2018). On the assessment of urban heat island phenomenon and its effects on building energy performance: A case study of rome (italy). *Energy and Buildings*, 158:605–615.

Hall, M. R. (2010). *Materials for energy efficiency and thermal comfort in buildings*. Elsevier.

Haraké, L. and Burkard, E. (2018). Towards Physically Based Material Appearance in the Thermal Infrared Spectrum: A Short Survey. In Klein, R. and Rushmeier, H., editors, *Workshop on Material Appearance Modeling*, pages 37–40. The Eurographics Association.

Hay, J. E. and Davies, J. A. (1980). Calculation of the solar radiation incident on an inclined surface. In *Proc. of First Canadian Solar Radiation Data Workshop (Eds: JE Hay and TK Won), Ministry of Supply and Services Canada*, volume 59.

Hénon, A., Mestayer, P., Lagouarde, J.-P., and Voogt, J. (2012). An urban neighborhood temperature and energy study from the capitoul experiment with the solene model. *Theoretical and applied climatology*, 110(1-2):177–196.

Ho, C. K., Ghanbari, C. M., and Diver, R. B. (2011). Methodology to assess potential glint and glare hazards from concentrating solar power plants: analytical models and experimental validation. *Journal of Solar Energy Engineering*, 133(3):031021.

Hottel, H. and Woertz, B. (1942). Performance of flat-plate solar-heat collectors. *Trans. ASME (Am. Soc. Mech. Eng.);(United States)*, 64.

Howell, J., Menguc, P., and Siegel, R. (2015). *Thermal Radiation Heat Transfer, 6th Edition*. CRC Press.

Huttner, S. (2012). *Further development and application of the 3D microclimate simulation ENVI-met*. PhD thesis, Mainz University, Germany.

Huttner, S. and Bruse, M. (2009). Numerical modeling of the urban climate–a preview on ENVI-met 4.0. In *7th International Conference on Urban Climate ICUC-7, Yokohama, Japan*, volume 29.

Hviid, C. A., Nielsen, T. R., and Svendsen, S. (2008). Simple tool to evaluate the impact of daylight on building energy consumption. *Solar Energy*, 82(9):787–798.

Idczak, M., Groleau, D., Mestayer, P., Rosant, J.-M., and Sini, J.-F. (2010). An application of the thermo-radiative model solene for the evaluation of street canyon energy balance. *Building and Environment*, 45(5):1262–1275.

Igawa, N., Koga, Y., Matsuzawa, T., and Nakamura, H. (2004). Models of sky radiance distribution and sky luminance distribution. *Solar Energy*, 77(2):137 – 157.

Immel, D. S., Cohen, M. F., and Greenberg, D. P. (1986). A radiosity method for non-diffuse environments. In *ACM SIGGRAPH Computer Graphics*, volume 20, pages 133–142. ACM.

Jensen, H. W. (2001). *Realistic image synthesis using photon mapping*. AK Peters/CRC Press.

Johnson, T. (1981). *Solar architecture: the direct gain approach*. McGraw Hill Book Company.

Jones, N. and Reinhart, C. (2016). Parallel multiple-bounce irradiance caching. *Computer Graphics Forum*, 35(4):57–66.

Jones, N. L. (2017). *Validated interactive daylighting analysis for architectural design*. PhD thesis, Massachusetts Institute of Technology.

Jones, N. L. and Reinhart, C. F. (2014). Irradiance caching for global illumination calculation on graphics hardware. In *Proceedings of 2014 ASHRAE/IBPSA-USA Building Simulation Conference*, pages 111–120.

Kajiya, J. T. (1986). The rendering equation. *SIGGRAPH Comput. Graph.*, 20(4):143–150.

Kämpf, J. H. and Robinson, D. (2007). A simplified thermal model to support analysis of urban resource flows. *Energy and buildings*, 39(4):445–453.

Karimi, R., Akhtari, A. A., and Seyedashraf, O. (2014). Implementation of the skyline algorithm in finite-element computations of saint-venant equations. *Journal of Applied Research in Water and Wastewater*, 1(2):61–65.

Kirimtat, A. and Krejcar, O. (2018). A review of infrared thermography for the investigation of building envelopes: Advances and prospects. *Energy and Buildings*, 176:390–406.

Kirk, D. B. and Hwu, W.-m. W. (2010). *Programming Massively Parallel Processors: A Hands-on Approach*. Morgan Kaufmann Publishers Inc., San Francisco, CA, USA, 1st edition.

Kontkanen, J., Turquin, E., Holzschuch, N., and Sillion, F. X. (2006). Wavelet radiance transport for interactive indirect lighting. In *Rendering Techniques 2006 (Eurographics Symposium on Rendering)*, pages 161–171.

Kottler, B., Burkard, E., Bulatov, D., and Haraké, L. (2019). Physically-based thermal simulation of large scenes for infrared imaging. In *Proceedings of the 14th International Joint Conference on Computer Vision, Imaging and Computer Graphics Theory and Applications*, pages 53–64. SCITEPRESS - Science and Technology Publications.

Kramer, R., Van Schijndel, J., and Schellen, H. (2012). Simplified thermal and hygric building models: A literature review. *Frontiers of architectural research*, 1(4):318–325.

Krayenhoff, E. S. and Voogt, J. A. (2007). A microscale three-dimensional urban energy balance model for studying surface temperatures. *Boundary-Layer Meteorology*, 123(3):433–461.

Kruczek, T. (2015a). Conditions for the use of infrared camera diagnostics in energy auditing of the objects exposed to open air space at isothermal sky. *Archives of Thermodynamics*, 36(1):67–82.

Kruczek, T. (2015b). Use of infrared camera in energy diagnostics of the objects placed in open air space in particular at non-isothermal sky. *Energy*, 91:35–47.

Kwan, Y.-T., Sawtelle, S., Bernstein, U., Pereira, W., and Less, D. (2008). A simulation for hyperspectral thermal IR imaging sensors. In Shen, S. S. and Lewis, P. E., editors, *Algorithms and Technologies for Multispectral, Hyperspectral, and Ultraspectral Imagery XIV*, pages 65–75. SPIE.

Kylili, A., Fokaides, P. A., Christou, P., and Kalogirou, S. A. (2014). Infrared thermography (irt) applications for building diagnostics: A review. *Applied Energy*, 134:531–549.

Lafortune, E. (1996). Mathematical models and monte carlo algorithms for physically based rendering. *Department of Computer Science, Faculty of Engineering, Katholieke Universiteit Leuven*, 20:74–79.

Lafortune, E. and Willems, Y. (1994). Using the modified phong reflectance model for physically based rendering. Report CW 197, Departement Computerwetenschappen, KU Leuven, Celestijnenlaan 200A, 3001 Heverlee, Belgium.

Lagouarde, J.-P., Henon, A., Kurz, B., Moreau, P., Irvine, M., Voogt, J. A., and Mestayer, P. G. (2010). Modelling daytime thermal infrared directional anisotropy over toulouse city centre. *Remote Sensing of Environment*, 114(1):87–105.

Lalanne, N., Krapez, J.-C., Le Niliot, C., Briottet, X., Pierro, J., and Labarre, L. (2015). Development and validation of a numerical tool for simulating the surface temperature field and the infrared radiance rendering in an urban scene. *Quantitative InfraRed Thermography Journal*, 12(2):196–218.

Latger, J., Cathala, T., Douchin, N., and Goff, A. L. (2007). Simulation of active and passive infrared images using the SE-WORKBENCH. In Holst, G. C., editor, *Infrared Imaging Systems: Design, Analysis, Modeling, and Testing XVIII*, pages 35–45. SPIE.

Lawrence, J., Rusinkiewicz, S., and Ramamoorthi, R. (2004). Efficient BRDF importance sampling using a factored representation. *ACM Transactions on Graphics*, 23(3):496.

Lewis, R. W., Nithiarasu, P., and Seetharamu, K. N. (2004). *Fundamentals of the finite element method for heat and fluid flow*. John Wiley & Sons.

Li, H., Bai, T., Ma, S., Lv, X., Gao, P., Yang, W., and Feng, J. (2009). An infrared imaging computation model and its validation. In Puschell, J., mei Gong, H., Cai, Y., Lu, J., and dong Fei, J., editors, *International Symposium on Photoelectronic Detection and Imaging 2009: Advances in Infrared Imaging and Applications*, pages 252–262. SPIE.

Li, X., Strahler, A. H., and Friedl, M. A. (1999). A conceptual model for effective directional emissivity from nonisothermal surfaces. *IEEE Transactions on Geoscience and Remote Sensing*, 37(5):2508–2517.

Lighting Analysts, I. (2019). Licaso: Annual daylight simulation software for agi32 and elumtools.

Lindberg, F., Holmer, B., and Thorsson, S. (2008). Solweig 1.0–modelling spatial variations of 3d radiant fluxes and mean radiant temperature in complex urban settings. *International journal of biometeorology*, 52(7):697–713.

Liu, B. Y. and Jordan, R. C. (1960). The interrelationship and characteristic distribution of direct, diffuse and total solar radiation. *Solar energy*, 4(3):1–19.

Longcore, T. and Rich, C. (2004). Ecological light pollution. *Frontiers in Ecology and the Environment*, 2(4):191–198.

Loyer, F. L. (1988). *Paris nineteenth century: Architecture and urbanism*, volume 711: 72 (44). Abbeville Press Publishers,.

Lü, X. (2002). Modelling of heat and moisture transfer in buildings: I. model program. *Energy and buildings*, 34(10):1033–1043.

Lucchi, E. (2018). Applications of the infrared thermography in the energy audit of buildings: A review. *Renewable and Sustainable Energy Reviews*, 82:3077–3090.

Luebke, D. P. (2003). *Level of detail for 3D graphics*. Morgan Kaufmann.

Maréchal, N., Guérin, E., Galin, E., Mérillou, S., and Mérillou, N. (2010). Heat transfer simulation for modeling realistic winter sceneries. *Computer Graphics Forum*, 29(2):449–458.

Mardaljevic, J. (2000). *Daylight simulation: validation, sky models and daylight coefficients*. PhD thesis, © John Mardaljevic.

Marschner, S. R. and Greenberg, D. P. (1998). *Inverse rendering for computer graphics*. Citeseer.

Martin, M. and Berdahl, P. (1984). Summary of results from the spectral and angular sky radiation measurement program. *Solar Energy*, 33(3-4):241–252.

MATLAB (2010). *version 7.10*. The MathWorks Inc., Natick, Massachusetts.

Mayer, R., Enache-Pommer, E., Parsons, G., Mazor, M., Hansbro, J., Lastovica, J., Buck, C., and Maurer, M. (2014). Finite element thermal modeling and correlation of various building wall assembly systems. *Energy and Buildings*, 75:410–418.

McNeil, A. and Lee, E. (2013). A validation of the radiance three-phase simulation method for modelling annual daylight performance of optically complex fenestration systems. *Journal of Building Performance Simulation*, 6(1):24–37.

Meier, F., Scherer, D., Richters, J., and Christen, A. (2011). Atmospheric correction of thermal-infrared imagery of the 3-d urban environment acquired in oblique viewing geometry. *Atmospheric Measurement Techniques*, 4(5):909–922.

Meyer, R. X. (1999). *Elements of space technology*. Academic Press.

Miller, C., Thomas, D., Kämpf, J., and Schlueter, A. (2015). Long wave radiation exchange for urban scale modelling within a co-simulation environment. In *Proceedings of International Conference CISBAT 2015 Future Buildings and Districts Sustainability from Nano to Urban Scale*, pages 871–876. LESO-PB, EPFL.

Mirsadeghi, M., Cóstola, D., Blocken, B., and Hensen, J. L. (2013). Review of external convective heat transfer coefficient models in building energy simulation programs: Implementation and uncertainty. *Applied Thermal Engineering*, 56(1-2):134–151.

Modest, M. (2003). *Radiative Heat Transfer*. Elsevier.

Morakinyo, T. E., Dahanayake, K. K. C., Ng, E., and Chow, C. L. (2017). Temperature and cooling demand reduction by green-roof types in different climates and urban densities: A co-simulation parametric study. *Energy and Buildings*, 145:226–237.

Morrison, W., Kotthaus, S., Grimmond, C., Inagaki, A., Yin, T., Gastellu-Etchegorry, J.-P., Kanda, M., and Merchant, C. J. (2018). A novel method to obtain three-dimensional urban surface temperature from ground-based thermography. *Remote sensing of environment*, 215:268–283.

Muñoz, D., Besuievsky, G., and Patow, G. (2018). A procedural approach for thermal visualization on buildings. In *Proceedings of the XXVIII Spanish Computer Graphics Conference*, pages 109–117. Eurographics Association.

Muñoz-Pandiella, I., Bosch, C., Mérillou, N., Pueyo, X., and Mérillou, S. (2017). Real-time solar exposure simulation in complex cities. In *Computer Graphics Forum*, volume 36, pages 554–566. Wiley Online Library.

Muñoz, D., Beckers, B., Besuievsky, G., and Patow, G. (2018). A technique for massive sky view factor calculations in large cities. *International Journal of Remote Sensing*, 39(12):4040–4058.

Musialski, P., Wonka, P., Aliaga, D. G., Wimmer, M., Gool, L. v., and Purgathofer, W. (2013). A survey of urban reconstruction. In *Computer graphics forum*, volume 32, pages 146–177. Wiley Online Library.

Nahon, R. (2017). *Modélisation des échanges radiatifs à l'échelle urbaine pour un urbanisme bioclimatique*. PhD thesis, Lille 1.

Nahon, R., Acuña Paz y Miño, J., and Beckers, B. (2019). Exploring the sky longwave radiance distribution in the french basque country. In *Proceedings of the 16th IBPSA Conference*, pages 1310–19.

Nardi, I., Lucchi, E., de Rubeis, T., and Ambrosini, D. (2018). Quantification of heat energy losses through the building envelope: A state-of-the-art analysis with critical and comprehensive review on infrared thermography. *Building and Environment*, 146:190–205.

Nazarian, N., Fan, J., Sin, T., Norford, L., and Kleissl, J. (2017). Predicting outdoor thermal comfort in urban environments: A 3d numerical model for standard effective temperature. *Urban climate*, 20:251–267.

Neumann, A., Neumann, L., Bekaert, P., Willems, Y. D., and Purgathofer, W. (1996). Importance-driven stochastic ray radiosity. In *Rendering Techniques' 96*, pages 111–121. Springer.

Nielsen, T. R. (2005). Simple tool to evaluate energy demand and indoor environment in the early stages of building design. *Solar Energy*, 78(1):73–83.

Nishida, G., Garcia-Dorado, I., Aliaga, D. G., Benes, B., and Bousseau, A. (2016). Interactive sketching of urban procedural models. *ACM Transactions on Graphics (TOG)*, 35(4):130.

Nunez, M. and Oke, T. (1976). Long-wave radiative flux divergence and nocturnal cooling of the urban atmosphere. *Boundary-Layer Meteorology*, 10(2):121–135.

O'Grady, M., Lechowska, A. A., and Harte, A. M. (2017). Infrared thermography technique as an in-situ method of assessing heat loss through thermal bridging. *Energy and Buildings*, 135:20–32.

Oliveti, G., Arcuri, N., and Ruffolo, S. (2003). Experimental investigation on thermal radiation exchange of horizontal outdoor surfaces. *Building and environment*, 38(1):83–89.

Overby, M., Willemsen, P., Bailey, B. N., Halverson, S., and Pardyjak, E. R. (2016). A rapid and scalable radiation transfer model for complex urban domains. *Urban Climate*, 15:25–44.

Parish, Y. I. and Müller, P. (2001). Procedural modeling of cities. In *Proceedings of the 28th annual conference on Computer graphics and interactive techniques*, pages 301–308. ACM.

Parker, S. G., Bigler, J., Dietrich, A., Friedrich, H., Hoberock, J., Luebke, D., McAllister, D., McGuire, M., Morley, K., Robison, A., et al. (2010). Optix: a general purpose ray tracing engine. In *Acm transactions on graphics (tog)*, volume 29, page 66. ACM.

Pattanaik, S. N. and Mudur, S. P. (1993). Efficient potential equation solutions for global illumination computation. *Computers & Graphics*, 17(4):387–396.

Paulescu, M. and Badescu, V. (2013). Territorial and urban measurements. *Solar Energy at Urban Scale, John Wiley & Sons*, pages 13–35.

Peeters, J., Ribbens, B., and Steenackers, G. (2016). Determining directional emissivity: Numerical estimation and experimental validation by using infrared thermography. *Infrared Physics & Technology*, 77:344–350.

Péniguel, C. and Rupp, A. (2004). Syrthes 3.4—manuel théorique. *EDF R&D, Paris, France*.

Perez, R., Ineichen, P., Seals, R., Michalsky, J., and Stewart, R. (1990). Modeling daylight availability and irradiance components from direct and global irradiance. *Solar energy*, 44(5):271–289.

Perez, R., Seals, R., and Michalsky, J. (1993). All-weather model for sky luminance distribution—preliminary configuration and validation. *Solar energy*, 50:235–245.

Pharr, M., Jakob, W., and Humphreys, G. (2016). *Physically based rendering: From theory to implementation*. Morgan Kaufmann.

Poglio, T., Mathieu-Marni, S., Ranchin, T., Savaria, E., and Wald, L. (2006). Osiris: a physically based simulation tool to improve training in thermal infrared remote sensing over urban areas at high spatial resolution. *Remote sensing of environment*, 104(2):238–246.

Prikryl, J., Bekaert, P., and Purgathofer, W. (2000). Importance-driven hierarchical stochastic ray radiosity. In *WSCG*. Citeseer.

Radhouani, M. and Daouas, N. (2013). *Exercice résolus de thermique: Rayonnment thermique.* Editions Technip.

Rahimi, M. and Sabernaeemi, A. (2010). Experimental study of radiation and free convection in an enclosure with a radiant ceiling heating system. *Energy and Buildings*, 42(11):2077–2082.

Rassineux, A. and Beckers, B. (2016). A robust smoothed voxel representation for the generation of finite element models for computational urban physics. In *Proceedings of the First International Conference on Urban Physics*, pages 249–259. Heliodon.

Reinhart, C. (2014). *Daylighting Handbook: fundamentals, designing with the sun*. Number v. 1 in Daylighting Handbook. Christoph Reinhart.

Reinhart, C. F. and Davila, C. C. (2016). Urban building energy modeling–a review of a nascent field. *Building and Environment*, 97:196–202.

Reinhart, C. F. and Herkel, S. (2000). The simulation of annual daylight illuminance distributions—a state-of-the-art comparison of six radiance-based methods. *Energy and Buildings*, 32(2):167–187.

Reinhart, C. F., Mardaljevic, J., and Rogers, Z. (2006). Dynamic daylight performance metrics for sustainable building design. *LEUKOS*, 3(1):7–31.

Remund, J., Mueller, S., Kunz, S., and Schilter, C. (2010). Meteonorm handbook part i: software. Technical report, Switzerland, Tech. Rep.

Robinson, D., Haldi, F., Leroux, P., Perez, D., Rasheed, A., and Wilke, U. (2009). Citysim: Comprehensive micro-simulation of resource flows for sustainable urban planning. In *Proceedings of the Eleventh International IBPSA Conference*, pages 1083–1090.

Robinson, D. and Stone, A. (2005). A simplified radiosity algorithm for general urban radiation exchange. *Building services engineering research and technology*, 26(4):271–284.

Rodler, A., Guernouti, S., Musy, M., and Bouyer, J. (2018). Thermal behaviour of a building in its environment: Modelling, experimentation, and comparison. *Energy and Buildings*, 168:19–34.

Roupioz, L., Kastendeuch, P., Nerry, F., Colin, J., Najjar, G., and Luhahe, R. (2018). Description and assessment of the building surface temperature modeling in laser/f. *Energy and Buildings*, 173:91–102.

Salisbury, J. W. and D'Aria, D. M. (1992). Emissivity of terrestrial materials in the 8–14 μm atmospheric window. *Remote sensing of Environment*, 42(2):83–106.

Saratsis, E., Dogan, T., and Reinhart, C. (2017). Simulation-based daylighting analysis procedure for developing urban zoning rules. *Building Research & Information*, 45(5):478–491.

Sbert, M. (1997). Optimal source selection in shooting random walk monte carlo radiosity. In *Computer Graphics Forum*, volume 16, pages C301–C308. Wiley Online Library.

Schlick, C. (1994). An inexpensive brdf model for physically-based rendering. *Computer graphics forum*, 13(3):233–246.

Shamir, A. (2008). A survey on mesh segmentation techniques. In *Computer graphics forum*, volume 27, pages 1539–1556. Wiley Online Library.

Shao, M.-Z., Peng, Q.-S., and Liang, Y.-D. (1988). A new radiosity approach by procedural refinements for realistic image sythesis. In *ACM SIGGRAPH Computer Graphics*, volume 22, pages 93–99. ACM.

Sillion, F. and Puech, C. (1989). A general two-pass method integrating specular and diffuse reflection. *SIGGRAPH Comput. Graph.*, 23(3):335–344.

Sillion, F. X., Arvo, J. R., Westin, S. H., and Greenberg, D. P. (1991). A global illumination solution for general reflectance distributions. In *ACM SIGGRAPH Computer Graphics*, volume 25, pages 187–196. ACM.

Sillion, F. X., Puech, C., et al. (1994). *Radiosity and global illumination*, volume 1. Springer.

Smits, B., Arvo, J., and Greenberg, D. (1994). A clustering algorithm for radiosity in complex environments. In *Proceedings of the 21st annual conference on Computer graphics and interactive techniques*, pages 435–442. ACM.

Smits, B., Arvo, J. R., and Salesin, D. H. (1992). An importance-driven radiosity algorithm. In *ACM SIGGRAPH Computer Graphics*, volume 26, pages 273–282. ACM.

Snyder, W. and Wan, Z. (1998). Brdf models to predict spectral reflectance and emissivity in the thermal infrared. *IEEE Transactions on Geoscience and remote Sensing*, 36(1):214–225.

Snyder, W., Wan, Z., Zhang, Y., and Feng, Y.-Z. (1997). Thermal infrared (3–14 μm) bidirectional reflectance measurements of sands and soils. *Remote Sensing of Environment*, 60(1):101–109.

Stolarski, T., Nakasone, Y., and Yoshimoto, S. (2018). *Engineering analysis with ANSYS software*. Butterworth-Heinemann.

Strømann-Andersen, J. and Sattrup, P. A. (2011). The urban canyon and building energy use: Urban density versus daylight and passive solar gains. *Energy and Buildings*, 43(8).

Suffern, K. (2016). *Ray Tracing from the Ground up*. AK Peters/CRC Press.

Suykens, F. and Willems, Y. D. (2000). Density control for photon maps. In *Rendering Techniques 2000*, pages 23–34. Springer.

Torrance, K. E. and Sparrow, E. M. (1965). Biangular reflectance of an electric nonconductor as a function of wavelength and surface roughness. *Journal of Heat Transfer*, 87(2):283–292.

Tregenza, P. R. (1987). Subdivision of the sky hemisphere for luminance measurements. *Lighting Research & Technology*, 19:13–14.

Tregenza, P. R. and Waters, I. M. (1983). Daylight coefficients. *Lighting Research and Technology*, 15(2):65–71.

United Nations, Department of Economic & Social Affairs, P. D. (2018). The world's cities in 2018. Data Booklet ST/ESA/SER.A/417, United Nations, Department of Economic & Social Affairs, Population Division.

van Eekelen, T. (2013). Radiation modeling using the finite element method. *Solar Energy at Urban Scale, John Wiley & Sons*, pages 237–257.

Van Hooff, T. and Blocken, B. (2010). Coupled urban wind flow and indoor natural ventilation modelling on a high-resolution grid: a case study for the amsterdam arena stadium. *Environmental Modelling & Software*, 25(1):51–65.

Veach, E. and Guibas, L. J. (1997). Metropolis light transport. In *Proceedings of the 24th annual conference on Computer graphics and interactive techniques*, pages 65–76. ACM Press/Addison-Wesley Publishing Co.

Vollmer, M. and Möllmann, K.-P. (2017). *Infrared thermal imaging: fundamentals, research and applications*. John Wiley & Sons.

Wald, I., Usher, W., Morrical, N., Lediaev, L., and Pascucci, V. (2019). Rtx beyond ray tracing: Exploring the use of hardware ray tracing cores for tet-mesh point location. *Proceedings of High Performance Graphics*.

Wald, I., Woop, S., Benthin, C., Johnson, G. S., and Ernst, M. (2014). Embree: a kernel framework for efficient cpu ray tracing. *ACM Transactions on Graphics (TOG)*, 33(4):143.

Wang, X. and Li, Y. (2016). Predicting urban heat island circulation using cfd. *Building and Environment*, 99:82–97.

Ward, G. (1994). The RADIANCE lighting simulation and rendering system. In *Proceedings of the 21st Annual Conference on Computer Graphics and Interactive Techniques*, SIGGRAPH '94, pages 459–472, New York, NY, USA. ACM.

Ward, G. J., Rubinstein, F. M., and Clear, R. D. (1988). A ray tracing solution for diffuse interreflection. *ACM SIGGRAPH Computer Graphics*, 22(4):85–92.

Whitted, T. (1979). An improved illumination model for shaded display. In *ACM SIGGRAPH Computer Graphics*, volume 13, page 14. ACM.

Wilkinson, J. (1971). The algebraic eigenvalue problem. In *Handbook for Automatic Computation, Volume II, Linear Algebra*. Springer-Verlag New York.

Wu, X., Zhang, J., Chen, Y., and Huang, X. (2015). Real-time mid-wavelength infrared scene rendering with a feasible brdf model. *Infrared Physics & Technology*, 68:124–133.

Yang, X. and Li, Y. (2013). Development of a three-dimensional urban energy model for predicting and understanding surface temperature distribution. *Boundary-layer meteorology*, 149(2):303–321.

Yang, Y. and Buckius, R. O. (1995). Surface length scale contributions to the directional and hemispherical emissivity and reflectivity. *Journal of Thermophysics and heat transfer*, 9(4):653–659.

Yunus, A. C. et al. (2003). Heat transfer: a practical approach. *MacGraw Hill, New York*.

Zhang, X., Estoque, R. C., and Murayama, Y. (2017). An urban heat island study in nanchang city, china based on land surface temperature and social-ecological variables. *Sustainable cities and society*, 32:557–568.

Zienkiewicz, O., Taylor, R., and Zhu, J. (2013). *The finite element method: its basis and fundamentals, 7th edition*. Elsevier.

Zienkiewicz, O. C., Taylor, R. L., Nithiarasu, P., and Zhu, J. (1977). *The finite element method*, volume 3. McGraw-hill London.